

Investigation of the effect of different post-weld heat treatment procedures on pipe strength and integrity

Calibration of numerical plasticity for modeling damage accumulation for verification of different post weld heat treatment procedures, material parameters extracted from experimental tests performed for welded AISI 4130 steel pipes.

EVEN ENGLUND

SUPERVISED BY
Dr. Dmitry Vysochinskiy

University of Agder, 2020
Faculty of Engineering and Science
Department of Engineering sciences

Obligatorisk egenerklæring/gruppeerklæring

Den enkelte student er selv ansvarlig for å sette seg inn i hva som er lovlige hjelpemidler, retningslinjer for bruk av disse og regler om kildebruk. Erklæringen skal bevisstgjøre studentene på deres ansvar og hvilke konsekvenser fusk kan medføre. Manglende erklæring fritar ikke studentene fra sitt ansvar.

1. Jeg/vi erklærer herved at min/vår besvarelse er mitt/vårt eget arbeid, og at jeg/vi ikke har brukt andre kilder eller har mottatt annen hjelp enn det som er nevnt i besvarelsen.

2. Jeg/vi erklærer videre at denne besvarelsen:
 - ikke har vært brukt til annen eksamen ved annen afdeling/universitet/høgskole innenlands eller utenlands.
 - ikke refererer til andres arbeid uten at det er oppgitt.
 - ikke refererer til eget tidligere arbeid uten at det er oppgitt.
 - har alle referansene oppgitt i litteraturlisten.
 - ikke er en kopi, duplikat eller avskrift av andres arbeid eller besvarelse.

3. Jeg/vi er kjent med at brudd på ovennevnte er å betrakte som fusk og kan medføre annullering av eksamen og utestengelse fra universiteter og høgskoler i Norge, jf. Universitets- og høgskoleloven §§4-7 og 4-8 og Forskrift om eksamen §§ 31.

4. Jeg/vi er kjent med at alle innleverte oppgaver kan bli plagiatkontrollert.

5. Jeg/vi er kjent med at Universitetet i Agder vil behandle alle saker hvor det forligger mistanke om fusk etter høgskolens retningslinjer for behandling av saker om fusk.

6. Jeg/vi har satt oss inn i regler og retningslinjer i bruk av kilder og referanser på biblioteket sine nettsider.

Publiseringsavtale

Fullmakt til elektronisk publisering av oppgaven

Forfatter(ne) har opphavsrett til oppgaven. Det betyr blant annet enerett til å gjøre verket tilgjengelig for allmennheten (Åndsverkloven. §2).

Alle oppgaver som fyller kriteriene vil bli registrert og publisert i Brage Aura og på UiA sine nettsider med forfatter(ne)s godkjenning.

Oppgaver som er unntatt offentlighet eller tausehetsbelagt/konfidensiell vil ikke bli publisert.

Jeg/vi gir herved Universitetet i Agder en vederlagsfri rett til å gjøre oppgaven tilgjengelig for elektronisk publisering:

JA NEI

Er oppgaven båndlagt (konfidensiell)?

JA NEI

(Båndleggingsavtale må fylles ut)

- Hvis ja:

Kan oppgaven publiseres når båndleggingsperioden er over?

JA NEI

Er oppgaven unntatt offentlighet?

JA NEI

(inneholder taushetsbelagt informasjon. Jfr. Offl. §13/Fvl. §13)

Acknowledgements

This study was part of the Master program in Civil and Constructional engineering at the University of Agder and Department of Engineering Sciences. This subject for the Master thesis was chosen due to the interesting and challenging subject of numerical simulation and material behavior of welded connections.

I would like to thank my supervisor Dr. Dmitry Vysochinskiy, who has guided me through the project.

I would thank Dmitri Rybakov, who has been the company contact from MHWirth and who supplied the materials for the experimental tests that were performed, and for being supportive with other information and relevant topics regarding this study.

I would also like to thank Rino Nilsen at Østfold University College, who was able to process and mill the tensile test specimens from the pipe sample that was used for this study.

I would also thank Cesilie Ødegår, who operated the machines during the experimental testing.

The goal of this study was to identify to what degree the strength will change after different post-weld heat treatments (PWHT) performed for AISI 4130 steel pipes. The background for this investigation was the change of PWHT procedure made in 2014 in the ASME Code (ASME B31.3) for welded pipes.

Due to the current situation and crisis regarding Covid-19, it must be mentioned that there were plans for more samples for experimental tension testing, metallurgical microscopy and new sets of hardness tests of the different welded sections of the tested pipe to be conducted for this thesis, but this was unfortunately not possible to complete. Due to the uncertainty regarding experimental testing, the study was initially based on the available material certificates and hardness tests performed in a previous study on the exact same pipe material. Fortunately, there was an opportunity to process and perform a small number of tensile tests, so the outcome became two different approaches to extract material data for the numerical simulations for this study.

It has been an enriching process and I'm looking forward to finalizing my Master's degree in the spring of 2020.

Grimstad, June 2020.

Even Englund

Summary

This Master thesis has been composed as part of the final year in the Master program of Civil and Constructional engineering at the University of Agder. This report was written during the spring semester of 2020. The background for the thesis was the need to analyze and investigate the changes in the properties for welded steel pipes after the changes to the ASME Code (ASME B31.3) for Pressure piping systems made in 2014. This study was conducted in collaboration with the leading provider of first-class drilling solutions MHWirth and the University of Agder (UiA).

The objective of this study is to look further into the effect different procedures for post-weld heat treatment (PWHT) of welded steel pipes can affect strength and failure mechanisms. Simulations using the finite element software package Abaqus were employed to analyze the strength and damage initiation of the welded pipe segments with the different PWHT procedures.

The importance of studying behavior and strength of post-weld heat treated steel structures and pipes in a wider perspective is also part of this study, as will be mentioned in the chapter "Significance of the work". The theory behind post-weld heat treatment is explained in this study, and the material behavior of steel subjected to welding and heat treatment is also explained.

The method used is done by extracting experimental results for analyzing the welded part of the pipe and simulating the damage behavior until final failure using finite element analysis software for testing of strength and failure. Explicit analysis has been used for simulating the damage behavior of the welded pipe by calibration of the chosen damage model using the experimental material results.

The study is done for AISI 4130 steel pipe and use two different approaches of extraction of material data for the numerical simulation in the chosen finite element software Abaqus. One approach has been performed using different material data taken from material hardness tests and material certificates, and post-processed by using numerical formulas for estimation of the proposed heat affected parts of the pipe. The second approach was performed using material data from experimental tensile tests of steel specimens applied with different heat treatment, simulating the material properties after different PWHT procedures. The reason for applying the first approaches was the uncertainty performing the experimental tests in the lab, due to the current virus restrictions. In this study there is one type of specimen that was tensile tested for extraction of material parameters for the welded and heat affected area as can be seen in the "Case" chapter.

Towards the end, there is a comparison between the different approaches and PWHT procedures including suggestions for further work.

Table of Contents

Obligatorisk egenerklæring/gruppeerklæring.....	i
Publiseringsavtale.....	ii
Acknowledgements.....	iii
Summary	iv
Table of Contents	v
List of Figures.....	ix
List of Tables.....	xiii
List of Symbols.....	xiv
1. Introduction.....	1
2. Significance of the work	2
3. Theory.....	5
3.1. Phase-diagrams	5
3.2. Austenite-Ferrite transformation.....	7
3.3. Bainite.....	9
3.4. Martensite	10
3.5. Tempering of Martensite	12
3.6. Heat treatment – Time-Tempering	12
3.7. Alloying contributions	14
3.8. Heat Affected Zone.....	15
3.9. Residual stresses and stress concentrations	16
3.10. Hydrogen cracking.....	18
3.11. Welding of Low Alloy Steels	19
3.12. Preheating of welds.....	20
3.13. PWHT of steel	21
3.14. Hardness testing and Hardness-Strength relation	23
3.15. Stress analysis of piping systems.....	26
3.16. Numerical analysis in Abaqus.....	29
3.17. Ductile damage in Abaqus.....	30
3.18. Mesh density	34
3.19. Mass scaling.....	34
4. Research question	36
5. Case	37
5.1. Design criteria for the pipe.....	39
5.2. Hardness data.....	39
5.3. Welded Steel pipe	40

5.4.	Test specimens	42
5.5.	Hydraulic Tensile test machine	44
5.6.	Extensometer	44
5.7.	Digital sliding gauge.....	44
5.8.	Furnace.....	45
5.9.	Numerical simulation tool.....	45
6.	Methods	46
6.1.	Material parameters based on hardness	47
6.2.	Design of experiments.....	51
6.2.1.	Preparation of specimens.....	51
6.2.2.	Heat treatment procedure	52
6.2.3.	Quality assurance of tests	54
6.2.4.	Calibration of equipment	54
6.2.5.	Execution of experiments.....	56
6.2.6.	Processing of experimental results	56
6.3.	Numerical setup and procedure.....	57
6.3.1.	Geometry and boundary conditions.	57
6.3.2.	Meshing of elements.....	59
6.3.3.	Material parameters in Abaqus.....	62
6.3.4.	Step definition and Mass scaling.....	62
6.3.5.	Amplitude and loading	63
6.4.	Pressure checks of pipe.....	66
7.	Results	67
7.1.	Analysis based on material data from hardness tests.....	67
7.1.1.	Results from calculation of material parameters.....	67
7.1.2.	Results sensitivity study	73
7.1.3.	Numerical results for weak electrode	75
7.1.4.	Numerical results from strong electrode	77
7.1.5.	Comparison of results.....	80
7.2.	Analysis based on material data from tensile tests	81
7.2.1.	Results from tension tests.....	81
7.2.2.	Numerical results based on weak electrode	87
7.2.3.	Numerical results based on strong electrode	90
7.2.4.	Comparison of results.....	93
7.3.	Results from pressure check	95
8.	Discussion.....	99
8.1.	Material parameters from hardness tests	99

8.2.	Material parameters from tensile test	100
8.3.	Numerical setup	101
8.4.	Numerical simulations	101
8.5.	Comparison of material parameters	102
8.6.	Sources of error	103
9.	Conclusion	104
10.	Suggestions for further work.....	105
	Bibliography.....	106
	Appendix A	110
	Appendix B	111
	Appendix C.....	112
	Appendix D	113
	Appendix E.....	114
	Appendix F.....	116
	Appendix G	117
	Appendix H	118
	Appendix I.....	121
	Appendix J	124
	Appendix K.....	125
	Appendix L.....	128
	Appendix M	129
	Appendix N	130
	Appendix O	137
	Appendix P.....	139
	Appendix Q.....	143
	TASKS	143
	TASKS	143
	TASKS	144
	TASKS	144
	TASKS	145
	TASKS	145
	TASKS	146
	TASKS	146
	TASKS	147

TASKS	147
TASKS	148
TASKS	148
TASKS	149
TASKS	149
TASKS	150
TASKS	150
TASKS	151
TASKS	151
TASKS	152
TASKS	152

List of Figures

Figure 1: Criteria for hydrogen induced cracking (HIC) [5].....	3
Figure 2: The iron-iron carbide phase diagram [11].....	5
Figure 3: TTT- and CCT-diagram for AISI 4130 steel investigated in this study [12].	6
Figure 4: Schaeffler diagram for predicting weld ferrite content and solidification mode [13].....	7
Figure 5: Growth of pro-eutectoid ferrite and hyper-eutectoid cementite: a) 0.34 wt% C, 12 minutes at 790°C. GB allotriomorphs of ferrite. b) 0.34 wt% C, 15 minutes at 725°C. Widmanstätten ferrite growing from GB ferrite. c) 0.34 wt% C, 12 minutes at 790°C. GB allotriomorphs and intragranular idiomorphs of ferrite. d) 0.34 wt% C, 15 minutes at 725°C. Intragranular Widmanstätten ferrite plates. e) 1.2 wt% C, 10 minutes at 730°C. GB allotriomorphs and intragranular idiomorphs of cementite. f) 1.2 wt% C, 10 minutes at 730°C. Widmanstätten cementite [14].	8
Figure 6: Ferritic body-centered cubic crystal structure (BCC) [11].	9
Figure 7: Transmission electron micrograph showing the structure of bainite. A grain of bainite passes from lower left to upper right corners; it consists of elongated and needle-shaped particles of Cementite (Fe_3C) within a ferrite (α) matrix. The phase surrounding the bainite is martensite [11].	10
Figure 8: Austenitic face-centered cubic structure (FCC) [11].	11
Figure 9: The body-centered tetragonal (BCT) unit cell for martensitic steel showing iron atoms (circles) and sites that may be occupied by carbon atoms (Xs). For this triagonal unit cell, $c > a$ [11]. .	11
Figure 10: (HRC) Rockwell hardness vs. (Hp) Holloman-Jaffe Time-Temperature parameter for tempering fully quenched 0.31% carbon steel [20].	13
Figure 11: Effect of elements on the hardness of martensite tempered for 1 hour at different temperatures (650°C and 705°C) [20].	14
Figure 12: Effect of Molybdenum Content on Tempered Hardness for 0,35% carbon content [14]. ..	14
Figure 13: Heat Affected Zone Regions in Relation to Equilibrium Iron-Carbon Phase Diagram [23]. .	15
Figure 14: (a) Longitudinal and (b) transversal residual stress distribution in a weld [28].	17
Figure 15: Schematic sketch of multipass welding. Note that the root pass has the highest dilution ratio [13].	17
Figure 16: Stress raisers in a V-groove [13].	18
Figure 17: Typical weld joint – V-groove [13].	18
Figure 18: Thermal cycle representing a PWHT schedule [23].	21
Figure 19: Correlation between measured and calculated grain-coarsened HAZ elongation, A35 [41].	26
Figure 20: Ductile fracture process [46].	30
Figure 21: Stress-strain curve with progressive damage degradation [51].	32
Figure 22: Linear damage evolution [51].	33
Figure 23: PWHT ASME B31.3-2012 [54].	37
Figure 24: PWHT ASME B31.3-2014 [33].	38
Figure 25: Alternate PWHT Requirements - ASME B31.3-2014 [33].	38
Figure 26: Specific design pressure from Piping Class Sheet KX10MH.	39
Figure 27: Calculation of the effects of welding and PWHT of previous study done in Weld Note.	40
Figure 28: Photo of the type of welded steel pipe under study [1].	41
Figure 29: (A) Raw steel pipe sample and (B) Uniform test specimens that were tested in this study.	43
Figure 30: Si-Plan Extensometer.	44
Figure 31. Digital sliding gauge.	44
Figure 32: Furnace used for heat treatment of the steel samples.	45
Figure 33: Check of microstructure in the welded area of the weld before PWHT using the Schaeffler diagram.	49
Figure 34: Cutting of the raw steel pipe sample.	52
Figure 35: Time tempering procedure for creation of martensite.	52
Figure 36: PWHT diagrams.	54

Figure 37: Tensile test frame with a specimen attached in the grip and extensometer attached to the specimen.	55
Figure 38: Modeled welded pipe segment.....	58
Figure 39: Design of the welded connection of the pipe. 1): unaffected base material, 2): PWHT base material, 3): HAZ, 4): Melted zone (Weld).	58
Figure 40: Applied boundary conditions for the modeled pipe segment.	59
Figure 41: Mesh definition for the pipe segment.	60
Figure 42: Applied 10mm mesh on the modeled pipe segment.....	60
Figure 43: Applied 7mm mesh on the modeled pipe segment.....	61
Figure 44: Applied 5mm mesh on the modeled pipe segment.....	61
Figure 45: Applied 4mm mesh on the modeled pipe segment.....	62
Figure 46: Time period of the defined step.....	63
Figure 47: Mass scaling for the numerical simulation of the pipe model.....	63
Figure 48: Pressure load applied in the pipe model.....	64
Figure 49: Load definition for the numerical pressure simulation.....	64
Figure 50: Time- Displacement amplitude for the applied pressure load in Abaqus.....	65
Figure 51: Loading amplitude for the pressure simulations.	65
Figure 52: Tempered Hardness of HAZ for AISI 4130 steel - Tempered in 20min, constant $c = 19,5$	68
Figure 53: Stress-strain diagram for base-material calculated from material certificate for the pipe.	69
Figure 54: True stress-strain diagram for PWHT 600.	70
Figure 55: True stress-strain diagram for PWHT 650.	70
Figure 56: True stress-strain diagram for PWHT 705.	70
Figure 57: (a) Base material parameter plotted for Ductile Damage in Abaqus. (b) Showing the Damage evolution from necking to fracture, using linear damage evolution, plotted Displacement at Failure.....	71
Figure 58: Visualization of calibration of strength coefficient K for unaffected base metal of the pipe.	72
Figure 59: Plotted plasticity data for the unaffected base material along with the calibrated strength coefficient K at the end that decides the start/behavior of the linear damage evolution.	73
Figure 60: Pressure vs mesh size diagram for the pipe due to pressure load.....	74
Figure 61: Pressure vs strain curve mesh sensitivity.....	74
Figure 62: Numerical results for PWHT 600 weak electrode.	75
Figure 63: Numerical results from PWHT 650 weak electrode.	75
Figure 64: Numerical results from PWHT 705 weak electrode.....	76
Figure 65: Resulting burst pressure based on weak electrode.	76
Figure 66: Highest stresses for pipe based on hardness data with weak electrode.	77
Figure 67: Pipe with pressure load until failure PWHT600 strong electrode.....	77
Figure 68: Pipe with pressure load until failure – PWHT650 strong electrode.....	78
Figure 69: Pipe with pressure load until failure – PWHT705 strong electrode.....	78
Figure 70: Burst pressure for simulations based on strong electrode.	79
Figure 71: Highest stresses for pipe based on hardness data with strong electrode.	79
Figure 72: Weak vs strong electrode – Burst pressure results in pipe.....	80
Figure 73: Weak vs strong electrode – Comparison of max stresses in pipe at fracture.....	81
Figure 74: Engineering stress-strain diagram – Uniform specimen Base 2.....	83
Figure 75: Illustration of determination of yield point from the experimental tensile tests – Here representing base material (Base 2).	83
Figure 76: True stress-strain diagram – Uniform specimen Base 2.....	84
Figure 77: True stress strain diagram for PWHT 600 based on experimental tests – Material parameters for the electrodes are estimated from certificates.	84
Figure 78: True stress strain diagram for PWHT 650 based on experimental tests – Material parameters for the electrodes are estimated from certificates.	85

Figure 79: True stress strain diagram for PWHT 705 based on experimental tests – Material parameters for the electrodes are estimated from certificates.	85
Figure 80: True stress strain diagram for PWHT 746 based on experimental tests – Material parameters for the electrodes are estimated from certificates.	86
Figure 81: Numerical results for PWHT 600 weak electrode.	87
Figure 82: Numerical results from PWHT 650 weak electrode.	87
Figure 83: Numerical results from PWHT 705 weak electrode.	88
Figure 84: Numerical results from PWHT 746 weak electrode.	88
Figure 85: Resulting burst pressure based on material data from experiments and weak electrode..	89
Figure 86: Highest stresses for pipe based on tensile experiment data with weak electrode.	89
Figure 87: Numerical results from PWHT 600 strong electrode.	90
Figure 88: Numerical results from PWHT 650 strong electrode.	90
Figure 89: Numerical results from PWHT 705 strong electrode.	91
Figure 90: Numerical results from PWHT 746 strong electrode.	91
Figure 91: Resulting burst pressure based on material data from experiments and strong electrode.	92
Figure 92: Highest stresses for pipe based on tensile experiment data with strong electrode.	92
Figure 93: Weak vs strong electrode – Burst pressure based on material data from tensile tests.	93
Figure 94: Weak vs strong electrode – Comparison of max stresses in pipe at fracture based on material data from tensile tests.	94
Figure 95: Presentation of burst pressure for all simulations, both based on hardness and tensile tests.	94
Figure 96: Calculation of material and temperature coefficient, Y.	95
Figure 97: Calculation of the stress acting on the pipe with the estimated design pressure.	95
Figure 98: Calculation of the test pressure for the pipe with the estimated design pressure.	95
Figure 99: Calculation of the stresses acting on the pipe under the estimated test pressure.	95
Figure 100: Visualization of service pressure and test pressure vs material burst pressure for the estimated and experimental hardness data collected.	97
Figure 101: Visualization of service stress and test stress vs material stress capacity for the estimated and experimental hardness data collected.	98
Figure 102: Hardness conversion table [21].	110
Figure 103: Hardness test results for PWHT procedure at 650°C [1].	111
Figure 104: Hardness test results for PWHT procedure at 705°C [1].	111
Figure 105: Some of the welded pipe sections that were hardness tested in the previous study [1].	111
Figure 106: PWHT procedure ASME B31.3-2012-Page 68[54].	112
Figure 107: PWHT procedure ASME B31.3-2012-Page 69[54].	112
Figure 108: PWHT procedure ASME B31.3-2014-Page 70[33].	113
Figure 109: Material Certificate.	114
Figure 110: Material Certificate.	114
Figure 111: Material Certificate.	115
Figure 112: Weak electrode 48.08 electrode used for the welded pipe [1].	116
Figure 113: Strong electrode – 74.86 electrode used for the simulation of the welded pipe.	117
Figure 114: Stress-strain diagram for the weak weld calculated from the electrode data sheet.	118
Figure 115: Stress-strain diagram for the strong weld calculated from the electrode data sheet.	118
Figure 116: HAZ Stress-strain diagram for the approximated results for PWHT 600.	119
Figure 117: HAZ Stress-strain diagram for the approximated results for PWHT 650.	119
Figure 118: HAZ Stress-strain diagram for the approximated results for PWHT 705.	120
Figure 119: Visualization of calibration of strength coefficient K for the weak electrode.	121
Figure 120: Visualization of calibration of strength coefficient K for the strong electrode.	121
Figure 121: Visualization of calibration of strength coefficient K for the HAZ with PWHT temperature 600°C.	122

Figure 122: Visualization of calibration of strength coefficient K for the HAZ with PWHT temperature 650°C.	122
Figure 123: Visualization of calibration of strength coefficient K for the HAZ with PWHT temperature 705°C.	123
Figure 124: Material course test samples.	125
Figure 125: Check list for tensile testing.	126
Figure 126: Test data sheet -There is one test data sheet that is filled out for each sample.	127
Figure 127: Drawing of the tested specimen -The total length varies between 150 and 170mm, but the gauge section is always centered accordingly.	128
Figure 128: Time temperature rate noted for each of the PWHT procedures.	129
Figure 129: Engineering stress-strain diagram – Uniform specimen Base 1.	130
Figure 130: True stress-strain diagram – Uniform specimen Base 1.	130
Figure 131: Engineering stress-strain diagram – Uniform specimen Base 2.	130
Figure 132: True stress-strain diagram – Uniform specimen Base 2.	131
Figure 133: Engineering stress-strain diagram – Uniform specimen HAZ - Quenched.	131
Figure 134: True stress-strain diagram – Uniform specimen HAZ - Quenched.	131
Figure 135: Engineering stress-strain diagram – Uniform specimen HAZ 600.	132
Figure 136: True stress-strain diagram – Uniform specimen HAZ 600.	132
Figure 137: Engineering stress-strain diagram – Uniform specimen Base 650.	132
Figure 138: True stress-strain diagram – Uniform specimen Base 650.	133
Figure 139: Engineering stress-strain diagram – Uniform specimen HAZ 650.	133
Figure 140: True stress-strain diagram – Uniform specimen HAZ 650.	133
Figure 141: Engineering stress-strain diagram – Uniform specimen Base 705.	134
Figure 142: True stress-strain diagram – Uniform specimen Base 705.	134
Figure 143: Engineering stress-strain diagram – Uniform specimen HAZ 705.	134
Figure 144: True stress-strain diagram – Uniform specimen HAZ 705.	135
Figure 145: Engineering stress-strain diagram – Uniform specimen Base 746.	135
Figure 146: True stress-strain diagram – Uniform specimen Base 746.	135
Figure 147: Engineering stress-strain diagram – Uniform specimen HAZ 746.	136
Figure 148: True stress-strain diagram – Uniform specimen HAZ 746.	136
Figure 149: Visualization of calibration of strength coefficient K for the tensile tested base material.	139
Figure 150: Visualization of calibration of strength coefficient K for the tensile tested HAZ 600.	139
Figure 151: Visualization of calibration of strength coefficient K for the tensile tested base material affected by PWHT temperature of 650°C.	140
Figure 152: Visualization of calibration of strength coefficient K for the tensile tested HAZ 650.	140
Figure 153: Visualization of calibration of strength coefficient K for the tensile tested base material affected by PWHT temperature of 705°C.	141
Figure 154: Visualization of calibration of strength coefficient K for the tensile tested HAZ 705.	141
Figure 155: Visualization of calibration of strength coefficient K for the tensile tested base material affected by PWHT temperature of 746°C.	142
Figure 156: Visualization of calibration of strength coefficient K for the tensile tested HAZ 746.	142

List of Tables

Table 1: Chemical composition of AISI 4130 steel from material certificate.	40
Table 2: Chemical composition of the “weak” OK 48.08 electrode found in the certificate.	42
Table 3: Chemical composition of the “strong” OK 74.86 Tensitrode electrode found in the certificate.....	42
Table 4: Heat treatment matrix for the tensile tested specimens and number of specimens.	43
Table 5: Comparison of hardness vs strength using hardness of 20HRC (238HV) as reference.	48
Table 6: Test Matrix based on hardness and numerical approximation.....	49
Table 7: Heat treatment to make the martensitic test specimens.	53
Table 8: Heat treatment matrix for the test specimen.	53
Table 9: Boundary conditions for the welded pipe segment analyzed for pressure in Abaqus.	59
Table 10: Element sizes in sensitivity procedure.	60
Table 11: Numerical pressure simulation matrix for the Hardness and Tensile test properties.	63
Table 12: Calculation of mean hardness values for the different zones of the weld before PWHT, calculated from values shown in Appendix B, the tensile stresses is found by using equation (15)....	67
Table 13: Calculation of mean hardness values for the different zones of the weld after PWHT, calculated from values shown in Appendix B, the tensile stresses are found by using equation (15). 68	68
Table 14: Material hardness for HAZ using Holloman-Jaffe and hardness tests correlation.....	68
Table 15: Material parameters calculated for HAZ.	69
Table 16: Stress Strain results for Base-material calculated from material certificate for the pipe.....	69
Table 17: Damage parameters calculated from certificates and hardness tests.....	71
Table 18: Calibrated Strength coefficient, K values and hardening exponent, n.....	72
Table 19: Sensitivity results from pressure load at fracture.	74
Table 20: Reaction forces on pipe with weak electrode.	76
Table 21: Reaction forces on pipe with strong electrode.	79
Table 22: Comparison of burst pressure for the pipe.	80
Table 23: Comparison of max stress for the fracture initiation of the pipe.....	80
Table 24: Collected experimental Normal/Engineering stress strain data.	82
Table 25: Collected experimental true stress strain data.	82
Table 26: Damage parameters calculated and run from tensile tests.....	86
Table 27: Calibrated Strength coefficient, K values and hardening exponent, n for tensile test data. 86	86
Table 28: Reaction forces on pipe weak electrode.	88
Table 29: Reaction forces on pipe with strong electrode.	91
Table 30: Comparison of burst pressure for the pipe.	93
Table 31: Comparison of max stress for the fracture initiation of the pipe.....	93
Table 32: Comparison of burst pressure and design pressure of 51.7 MPa.	96
Table 33: Comparison of max stress and design stress of 237.75 MPa.	96
Table 34: Comparison of burst pressure and test pressure of 77.55 MPa.....	96
Table 35: Comparison of max stress and test stress of 356.70 MPa.....	97
Table 36: Comparison of stress at ultimate tensile strength for HAZ.	103
Table 37: Stress-strain results for the weak electrode calculated from the electrode data sheet.....	118
Table 38: Stress-strain results for the strong electrode calculated from the electrode data sheet... 118	118
Table 39: Approximated HAZ Stress-strain results for PWHT 600.	119
Table 40: Approximated HAZ Stress-strain results for PWHT 650.	119
Table 41: Approximated HAZ Stress-strain results for PWHT 705.	120

List of Symbols

PWHT	Post weld heat treatment
HIC	Hydrogen induced cracking
HAZ	Heat affected zone
CGHAZ	Coarse grain heat affected zone
FGHAZ	Fine grain heat affected zone
ICHAZ	Intercritical heat affected zone
SCHAZ	Subcritical heat affected zone
Hp	Holloman-Jaffe parameter
c	Holloman-Jaffe constant
SCC	Stress corrosion cracking
A_1, A_1	Lower transformation temperature (eutectoid temperature)
A_3, A_3	Upper transformation temperature
HV	Vickers hardness number
HRC	Rockwell hardness number (150 kg. force - 120° diamond spheroconical)
t_m	Minimum required thickness of strait section of pipe
P	Design pressure
P_T	Minimum test gauge pressure
D	Outer diameter
d	Internal diameter
S	Allowable stress
S_T	Allowable stress at test temperature for the prevalent pipe material
C	Corrosion allowance
Y	Material and temperature coefficient
R_m	Ultimate strength/stress, tensile stress
$R_{0,2}, R_e$	Yield stress
FEM	Finite element method
FEA	Finite element analysis
A	Cross-section area
A_f	Final cross-section area
A_0	Initial cross-section area
D	Damage parameter
E	Young modulus
ν	Poisson's ratio
F	Force
K	Strength coefficient
$\bar{\epsilon}^{pl}$	Equivalent plastic strain
$\bar{\epsilon}_D^{pl}$	Equivalent plastic strain at the point of damage initiation
\bar{u}^{pl}	Fracture displacement
\bar{u}_f^{pl}	Fracture displacement at fracture
$\dot{\bar{\epsilon}}^{pl}$	Equivalent plastic strain rate
$\dot{\epsilon}_i$	Strain rate
ϵ^*	True fracture strain
η	Stress triaxiality
ρ	Material density
σ	Stress
$\sigma_1, \sigma_2, \sigma_3$	Principal stress
σ_c, σ_e	Von-Mises equivalent stress
TS, σ_u	Ultimate strength/stress, tensile stress

σ_y , σ_{y0}	Yield stress
σ_{true}	The true stress in the material
n	Hardening exponent
ϵ	Strain, Engineering strain
ϵ^{el}	Elastic strain
ϵ^{pl}	Plastic strain
ϵ_{true}	True/logarithmic strain
L, l	Length
l^e	Element length
l_0	Initial length
t	Time
u	Displacement
\bar{u}^{pl}	Fracture displacement
\bar{u}_f^{pl}	Fracture displacement at fracture
m	Material dependent constant
σ_T	True stress
ϵ_T	True strain
σ_f	Fracture strength
ϵ_f	True strain at final fracture

1. Introduction

Welding is an indispensable tool that allows for the construction and manufacture of piping, pressure vessels, pressure-containing parts and structural steel members. During this process, the molten pool often experiences sudden and extreme temperature increases. As it begins to cool, the metal will be subject to shrinking caused by the sudden thermal stress. This can have a negative impact on quality, and can chemically alter the structure of the steel. If this problem is not addressed, the weldment can fail to perform its function, potentially leading to disastrous effects.

Post weld heat treatment (PWHT) after welding is used to improve the properties after welding, and the need for PWHT is driven by code and applications. For Process pipes in the oil and gas industry the ASME code (ASME B31.3) is used and followed in terms of PWHT, and in 2014 the procedures for PWHT were changed. The maximum temperature was lowered approximately 50°C from 746-704°C to 705-650°C as the PWHT temperature range.

The motivation behind this study is to investigate what effects this change may have had on the strength and integrity of welded pipes. This study is performed in collaboration with the leading provider of first-class drilling solutions MHWirth and the University of Agder (UiA) as a final master thesis in Civil and Construction Engineering. The specific case in this study is piping systems used for drilling fluid in the offshore drilling industry that have been subjected to different PWHT procedures.

Experimental tensile and hardness tests were performed to characterize the AISI 4130 steel pipe under study when subjected to four different PWHT procedures. The procedure temperatures of 600°C, 650°C, 705°C and 746°C were investigated. The results from these tests allowed for the derivation of material constants for constitutive modeling, and led to a better understanding of the damage behavior of the welded pipe and possible differences in the material due to different PWHT procedures. This study also builds on an earlier study conducted for *Post weld heat treatment of welded low alloyed steel pipes*, done by Dimitri Rybakov [1]. And as the same steel pipes are used in this study, the earlier results done for hardness testing are also used in this study.

In order to determine and investigate the effects that different PWHT procedures have on a pipe, a pipe segment has been modeled and analyzed numerically. The material data extracted from the earlier hardness tests and the experimental tensile tests done in this study have been plotted numerically for verification of the different procedures. This has been achieved through data processing, with the final result in the form of input parameters for the material constitutive models in the finite element software Abaqus/Explicit. Implementation of the proposed damage behavior of internal pressure has been done by testing of the strength and integrity through a set of simulations to failure. A pressure check has also been performed for the welded pipe according to ASME B31.3 to see if there are any concerns in terms of highest allowed pressure.

The results of the numerical simulations done for the two different approaches of extraction of material data that were used are compared, in addition to the strength and behavior of the pipe when subjected to the different PWHT procedures.

2. Significance of the work

Welding is one of the most important techniques in the fabrication industries to join metals of different geometries and sizes with cost-effective and reliable assembly. The development of modern welding technology began in the latter half of the nineteenth century when electrical energy became commercially available [2]. Welding is a reliable and efficient joining process in which the coalescence of metals is achieved by fusion. The use of a welded structure, whether a crane structure, ship or pipeline, involves consideration of residual stresses and the effects of this factor in terms of load-bearing capacity of the structure in addition to the general consideration of stresses and strength. Localized heating during welding, followed by rapid cooling, can generate residual stresses in the weld and in the base metal [2].

The nature of residual stresses in welded structures is discussed in terms of their magnitude, directionality, spatial distribution, range and variability. The effects of the following factors on the residual stresses are considered [3]: material properties, material manufacture, structural geometry, fabrication procedure, welding procedure, post-weld treatments, and service conditions. These illustrate the different magnitudes and distributions of residual stress that can be found in different joint geometries, and demonstrate the effects of the mechanical, thermal and metallurgical properties of the constituent materials and the sensitivity of residual stresses to the pass sequence and to the restraints applied during welding [3]. Typical examples for the common case of circumferential butt welds in pipes and pressure vessels are used to illustrate the extent of residual stresses as a function of distance from the weld and the effects of post-weld heat treatment [3].

A high level of residual stresses can occur in weldment due to restraint by the parent metal during weld solidification [4, 5]. The stresses may be as high as the yield strength of material itself [4]. In order to ensure the material strength of a part is retained after welding, a process known as Post Weld Heat Treatment (PWHT) is regularly performed. PWHT can be used to reduce residual stresses, as a method of hardness control, or even to enhance material strength [4, 5]. If PWHT is performed incorrectly, or neglected altogether, residual stresses can combine with load stresses to exceed a material's design limitations. This can lead to weld failures, higher cracking potential, and increased susceptibility to brittle fracture [4, 5].

PWHT encompasses many different types of potential treatments; two of the most common types are post heating and stress relieving [4, 5]:

- **Post Heating:** Hydrogen-induced cracking (HIC) often occurs when high levels of ambient hydrogen permeate a material during welding. By heating the material after welding, it is possible to diffuse hydrogen from the welded area, thus preventing HIC. This process is known as post heating and should begin immediately after the weld is completed. Rather than being allowed to cool, the material needs to be heated to a certain temperature depending on the type and thickness of the material. It should be held at this temperature for a number of hours dependent on the thickness of the material.

- **Stress Relieving:** By the time it is complete, the welding process can leave a large number of residual stresses in a material, which can lead to an increased potential for stress corrosion and hydrogen induced cracking. PWHT can be used to release these residual stresses and reduce this potential. This process involves heating the material to a specific temperature and then gradually cooling it.

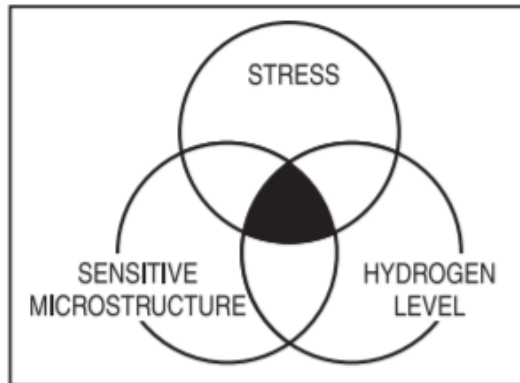


Figure 1: Criteria for hydrogen induced cracking (HIC) [5].

The need for PWHT is driven by code and application requirements as well as the service environment. In general, when PWHT is required, the goal is to increase the resistance to brittle fracture and relaxing residual stresses. Other desired results from PWHT may include hardness reduction, and material strength enhancements [2, 5]. The last two decades of improvement in steel metallurgy and pipe manufacturing, leading to high steel grade pipes, the development of new welding procedures as well as advanced and more reliable nondestructive testing (NDT) technology, have almost completely removed the failure modes associated with brittle material behavior, at last when operating temperatures are not severe [6].

With the above in mind, a simple description of the science behind the weld will give us a better glimpse into the importance and potential challenges involved in PWHT [7]:

- Grain structures of the HAZ differ from those of the base metal because it has been heated to a temperature just below the melting point of the material and then cooled quicker than the adjacent base metal. The maximum temperature reached, time at temperature and cooling rate all determine the grain structure of the HAZ.
- Grain structures of the weld metal differ from the HAZ because it too has been heated and cooled at a rate different from the HAZ and because it is a “casting” with a much different thermal and working history. With each successive weld bead, additional heat is applied to the weld below it, so each pass cools at a slower rate.

Unfortunately, mechanical, physical, and chemical properties within the HAZ are not always predictable or desirable and frequently cause problems. For example, in carbon steel and low alloy steel, the HAZ can be very hard [8]. As a result, this area can be brittle and commonly succumbs to various damage mechanisms (Caustic Stress Corrosion Cracking, Amine Stress Corrosion Cracking, sulfide stress cracking, stress-accelerated corrosion and many more mechanisms). This can lead to a phenomenon called weld-decay, wherein the HAZ corrodes rapidly (i.e., stress accelerated

corrosion/sensitization)[7]. Proper post-weld heat treatment (PWHT) removes or minimizes the effects of these undesirable properties inherent in the HAZ. PWHT does this by changing the residual stresses and microstructure in the weld area [8].

As a general rule, the fabrication codes dictate when post weld heat treatment is required and the particular post -weld heat treatment cycle. They also generally state the requirements in terms of the methods that can be used and the maximum heating and cooling rates and the maximum thermal gradients that are allowable. Examples of such codes would be ASME VIII, BS 5500 or AS 4458 for pressure vessels and ASME B31.3 or AS 4458 for piping [9]. Although various code and service requirements can dictate a variety of temperatures and holding times, the knowledge of change of microstructure and the effect this has on strength and hardness must be taken into consideration. This is important for understanding damage behavior, to avoid brittle fracture and failure and for improving the service life of welded steel structures as well as welded steel pipes.

3. Theory

This chapter will explain the theoretical background for this thesis in more detail in order to provide the reader with knowledge of mechanisms around the subject of post-weld-heat treatment (PWHT). First, theory surrounding different phases and microstructures of steel is presented, followed by heat treatment of steel and the effects and issues around welding. The theory behind design procedures and PWHT procedures of piping system according to the applicable standard is also presented. Finally, the last section will explain some of the theory behind the numerical analysis used in this study. The theory behind numerical damage modeling and also tensile testing can be read in the pre-study for this thesis " *Experimental calibration of continuum damage models* "[10].

3.1. Phase-diagrams

The iron-carbon phase diagram shows at what temperature the metal composition melts and what microstructure is present. For classification of steel, the carbon content is in the range of 0.08-2.14wt%, and carbon composition from 2.14-6.7wt% is classified as cast iron [11]. Time-temperature transformation (TTT) and Continuous cooling transformation (CCT) -diagrams provide a visualized connection between thermodynamics and kinetics. They show which phases will form during heat treatment at given times and temperature/cooling rates. Figure 3 shows both TTT and CCT diagrams for AISI 4130 steel investigated in this study. Highest and most critical tempering temperature, A1, is approximately 727°C (eutectoid temperature for AISI 4130 steel), where there is shift between phases, as can be seen from the TTT-diagram Figure 3 and the iron-iron carbide phase diagram in Figure 2.

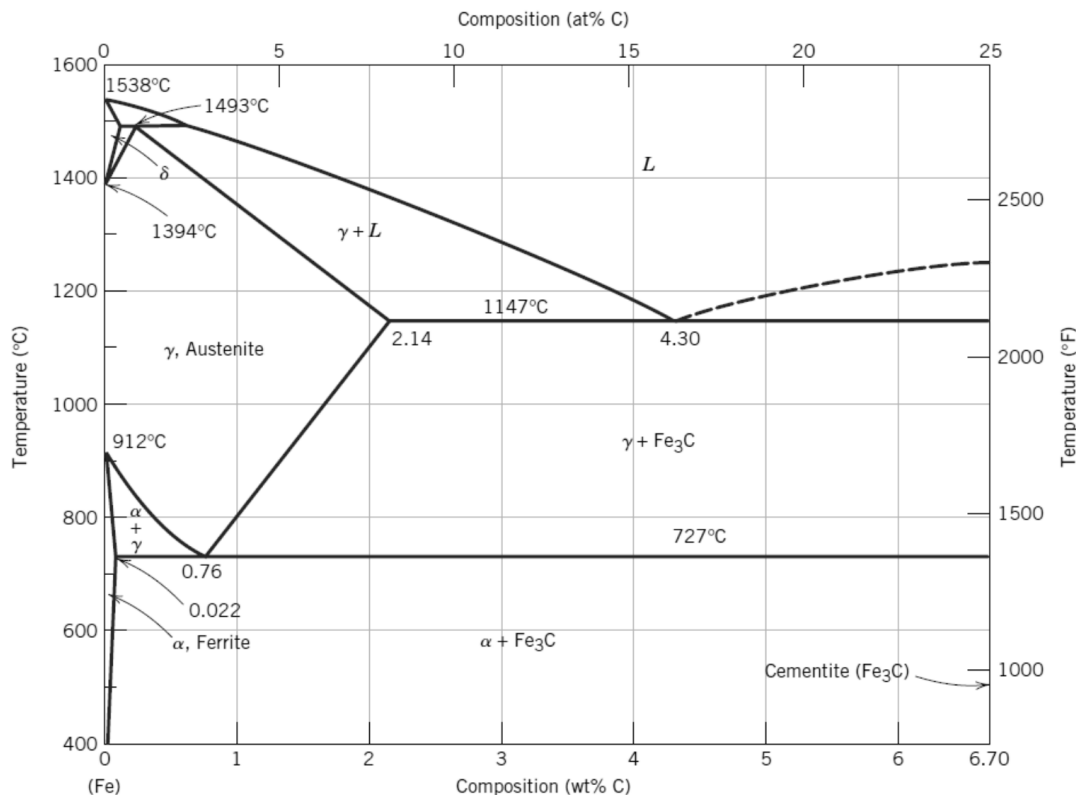
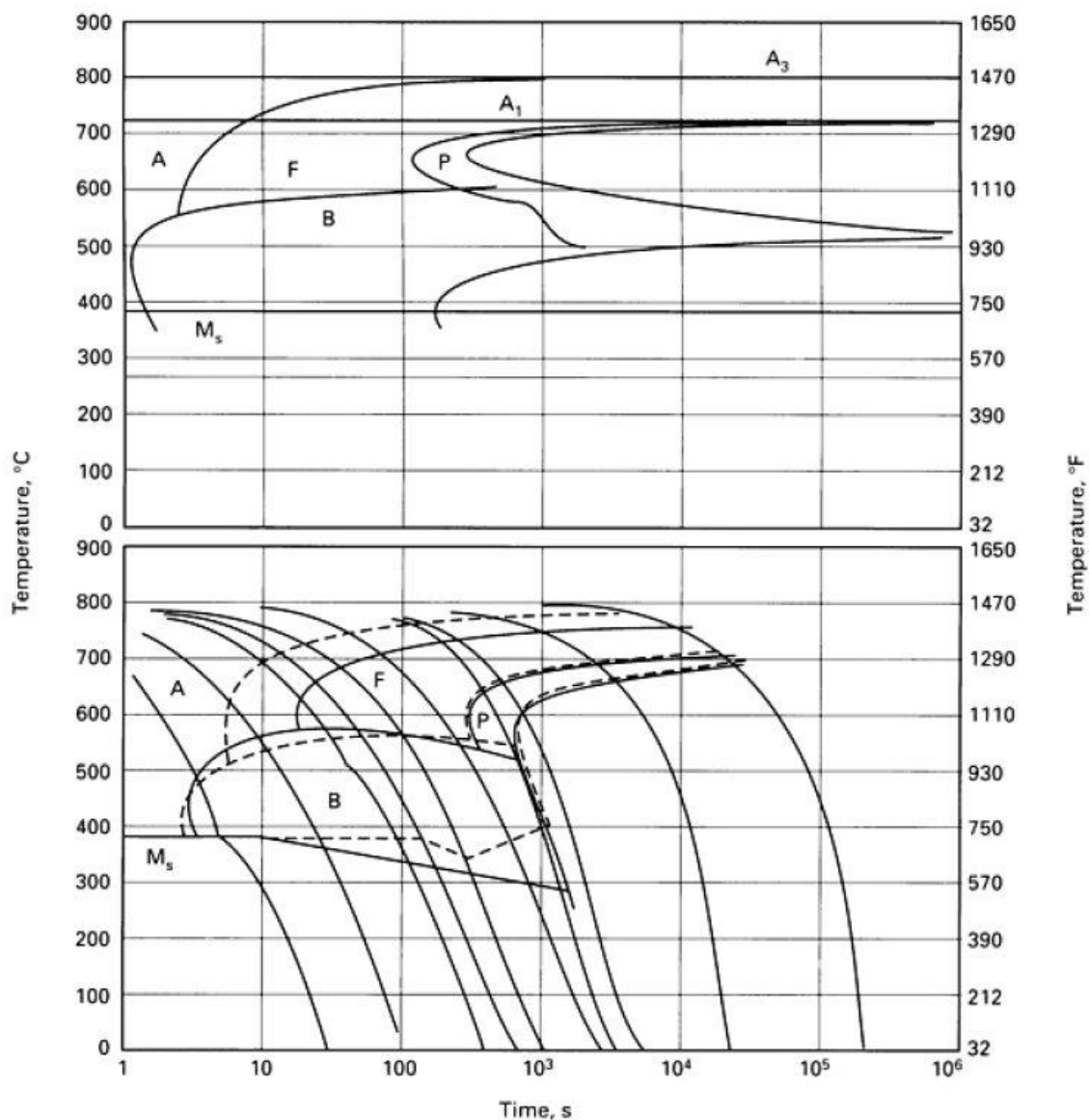


Figure 2: The iron-iron carbide phase diagram [11]

When structural steel is heated above A_1 , a transition takes place from ferrite to austenite[11]. At A_3 the transition is fulfilled. This process takes place in the structural steel every time a new weld pass is put into the groove. The reason is the special conditions in the Fe-lattice[8]. Fe is an allotropic material, meanings it changes microstructure in solid state as a function of the temperature. This is fundamental for a normalizing process, and normalization is only possible in allotropic material [8]. Fe and Ti have such properties. Every time the phase line is passed, a new grain -structure builds up. In this way, it is possible to eliminate rough grains and promote fine-grain practice. The corresponding heat treatment is called[8] a normalizing process. When welding structural steel, the normalizing process is especially important, which is one of the reasons for using multi-pass welds. Through multi-pass welds, the structure in HAZ is normalized[8].



No. 4970

Figure 3: TTT- and CCT-diagram for AISI 4130 steel investigated in this study [12].

In order to estimate the phases present in a steel alloy, one can also utilize a Schaeffler-diagram, shown in Figure 4. Such a diagram utilizes the concentration of alloy elements in order to estimate the phases present in the material. The Schaeffler-diagram was originally developed in order to analyze welds and weld beads. Therefore, the diagram attempts to describe the microstructure after melting and rapid cooling, i.e. equivalent to hardening and quenching [13]. By using a standardized set of equations, one calculates the coordinates of the material in the corresponding diagram. These coordinates are referred to as nickel- and chrome-equivalents (Ni_{eq} and Cr_{eq}), respectively [13]:

$$Ni_{eq} = \%Ni + 30 \cdot \%C + 0,5 \cdot \%Mn \quad (1)$$

$$Cr_{eq} = \%Cr + \%Mo + 1,5 \cdot \%Si + 0,5 \cdot \%Nb \quad (2)$$

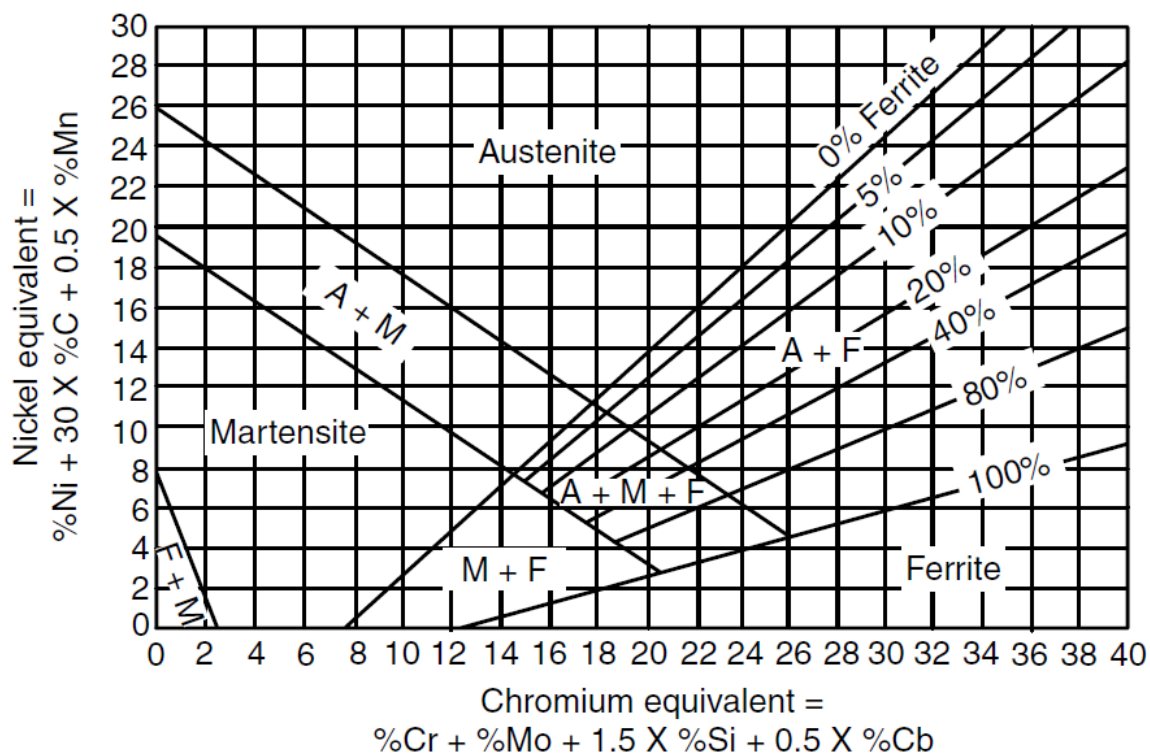


Figure 4: Schaeffler diagram for predicting weld ferrite content and solidification mode [13].

3.2. Austenite-Ferrite transformation

Under equilibrium conditions, pro-eutectoid ferrite will form in iron-carbon alloys containing up to 0,8wt% carbon. The reaction occurs at 910°C in pure iron but takes place between 910°C and 723°C in iron-carbon alloys. However, by quenching from the austenitic state to temperatures as low as 600°C. Ferrite-pearlite is the equilibrium microstructure obtained during slow cooling of steels containing up to 0.8 wt% carbon. Growth of ferrite starts at the austenite grain boundaries (GB), and with lowering α/γ transformation temperatures, four different morphologies of ferrite can be identified, as presented by Dubé [14]:

1. Grain boundary allotriomorphs: Grow along austenite GB, stretching into both the surrounding austenite grains. Random orientation with one austenite grain, more coherent orientation with the other grain. Can therefore be faceted on one side and curved on the other.
2. Widmanstätten ferrite plates or laths: Nucleate at austenite GB and grow along well-defined austenite planes. Will not cross austenite GB. Primary Widmanstätten ferrite forms directly on austenite GB, while secondary Widmanstätten ferrite grows from other allotriomorphs of ferrite.
3. Intragranular idiomorphs: Equi-axed ferrite that nucleate inside austenite grains, often on non-metallic inclusions. Will have some crystallographic facets.
4. Intragranular plates: Similar to Widmanstätten plates, but nucleate inside austenite grains without being in contact with GB.

Usually, combinations of the different morphologies are present. An example of this is the growth of ferrite during continuous cooling, where formation of grain boundary allotriomorph ferrite comes first, followed by growth of secondary Widmanstätten ferrite from the grain boundary allotriomorph, and finally the formation of intragranular idiomorphs or plates. This effect is illustrated in Figure 5, where different morphologies are shown together in the same picture[14].

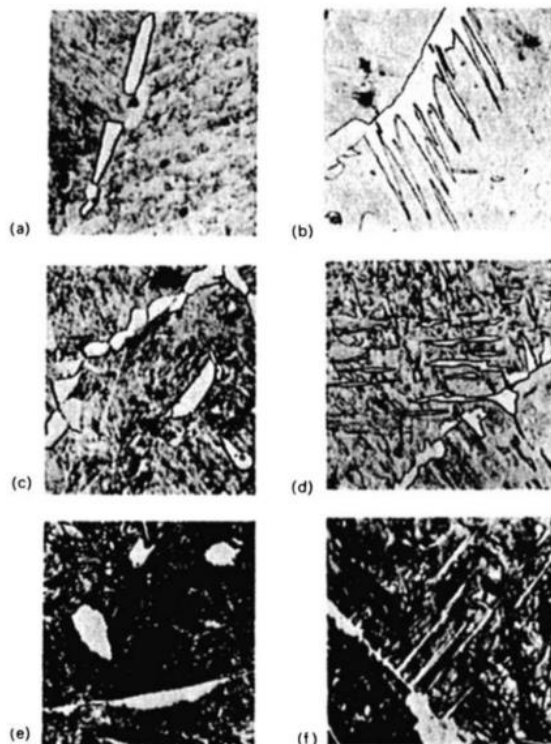


Figure 5: Growth of pro-eutectoid ferrite and hyper-eutectoid cementite: a) 0.34 wt% C, 12 minutes at 790°C. GB allotriomorphs of ferrite. b) 0.34 wt% C, 15 minutes at 725°C. Widmanstätten ferrite growing from GB ferrite. c) 0.34 wt% C, 12 minutes at 790°C. GB allotriomorphs and intragranular idiomorphs of ferrite. d) 0.34 wt% C, 15 minutes at 725°C. Intragranular Widmanstätten ferrite plates. e) 1.2 wt% C, 10 minutes at 730°C. GB allotriomorphs and intragranular idiomorphs of cementite. f) 1.2 wt% C, 10 minutes at 730°C. Widmanstätten cementite [14].

Diffusion during growth of ferrite leads to accumulation of carbon in the austenite. This eventually results in the formation of pearlite. A microstructure that forms through the eutectoid reaction, as shown in Equation 3 [11].



Pearlite is a lamellar structure consisting of parallel lamellae of cementite (θ - carbide or Fe_3C) and ferrite (α) layered in a sandwich structure. The formation of pearlite enables continued growth of the equilibrium phases while minimizing diffusion distance during growth. Because of its high strength, pearlite is an important constituent in steels [14]. However, pearlite is not favored in offshore engineering because of its low impact toughness.

Due to kinetics, the growth temperature will determine the thickness of the pearlitic lamellae. Low cooling rates or high transformation temperatures will result in coarse lamellae, while high cooling rates or low transformation temperature will produce fine lamellae due to lower diffusivity [11].

Obtaining a ferrite/pearlite microstructure is dependent on slow cooling. This is shown in Figure 3, where it can be seen that only very slow cooling will produce a ferrite-pearlite structure in AISI 4130 steel.

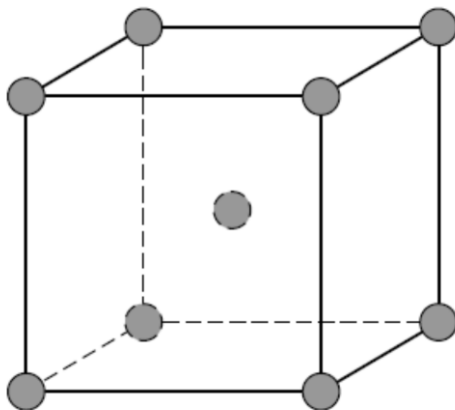


Figure 6: Ferritic body-centered cubic crystal structure (BCC) [11].

3.3. Bainite

Bainite is a microstructure formed in the intermediate between ferrite-pearlite and martensite. This is shown in Figure 3, where both the TTT- and CCT-diagram show the bainite nose. A bainitic microstructure can be obtained by a cooling rate too low to produce pure martensite, while still too high to produce ferrite-pearlite. Bainite can also be produced through isothermal heat treatment. The bainite microstructure consists of ferrite plates or laths. These are separated by residual phases like retained austenite, martensite or cementite. The bainitic plates are called subunits, which grow in clusters called sheaves, see Figure 3. Within each sheaf, the subunits are separated by low-misorientation grain boundaries or residual phases. Sheaves are also referred to as “packets” of bainite [15].

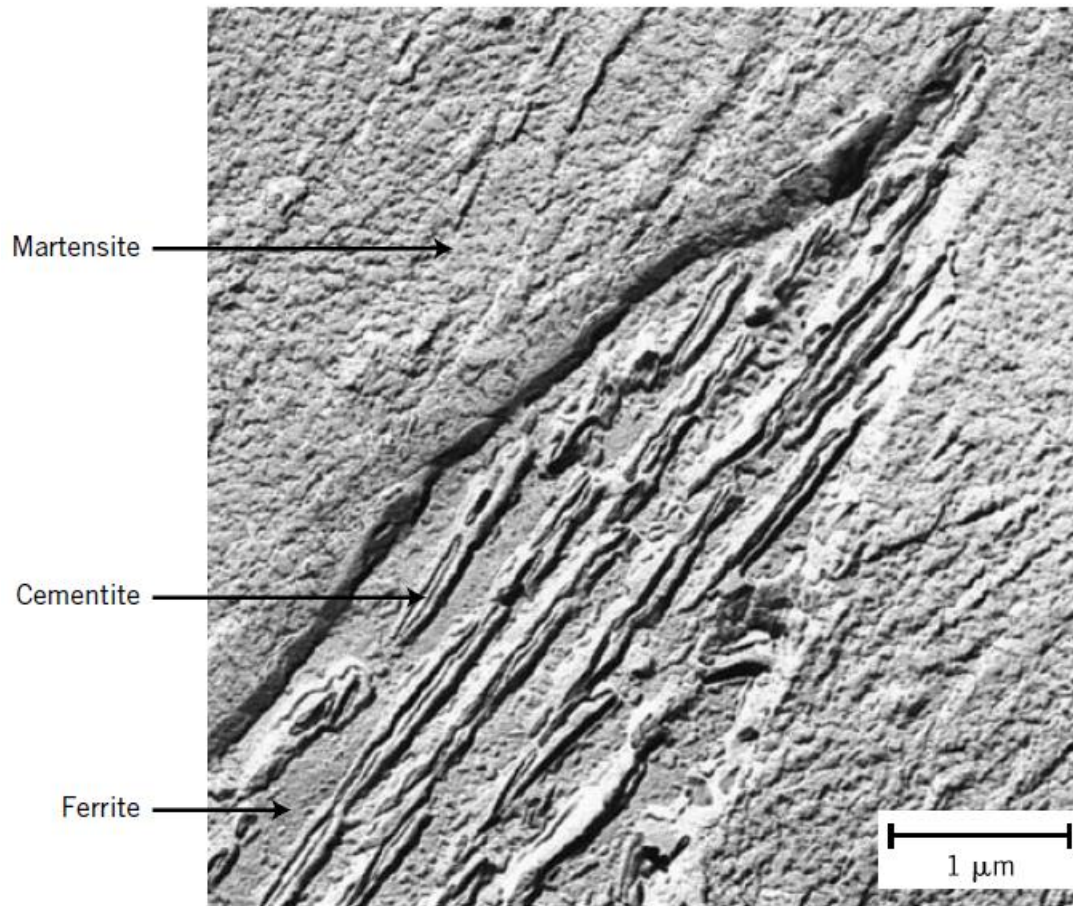


Figure 7: Transmission electron micrograph showing the structure of bainite. A grain of bainite passes from lower left to upper right corners; it consists of elongated and needle-shaped particles of Cementite (Fe_3C) within a ferrite (α) matrix. The phase surrounding the bainite is martensite [11].

3.4. Martensite

Martensite is a hard and brittle phase that forms when austenite is cooled too fast to form bainite [11]. Martensite is obtained with cooling rates high enough to avoid the bainite nose, see Figure 3. The martensite reaction is often referred to as a diffusion-less, shear transformation, which induces a shape change in the transformed region. The transformation is dependent on maintaining a high degree of coherency in the transformation interface. This results in an invariant-line strain, where one line in the transformation interface is unrotated and undistorted. The diffusion-less nature of the martensite reaction leaves carbon trapped in interstitial positions, which introduce lattice strains. In order to reduce strain energy from the surroundings, martensite forms as thin plates or laths [11, 14].

The martensite reaction is athermal. This means that the fraction transformed is only dependent on the undercooling below the martensite-start temperature (M_s). Carbon, having been in solid solution in the austenite, will remain in solid solution in the martensite as well due to the high cooling rate and fast transformation [14].

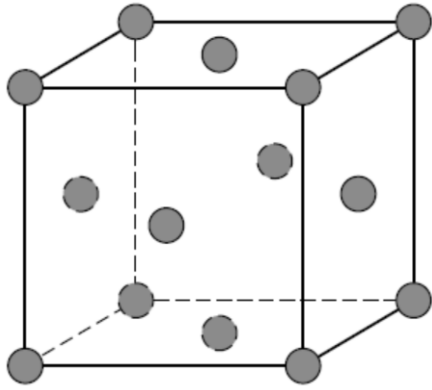


Figure 8: Austenitic face-centered cubic structure (FCC) [11].

Austenite has an FCC structure. The martensite that forms from it can have various crystal structures, dependent on the content of alloying elements. Martensitic steel consists mainly of BCT structure but bcc and hcp structures can also be found in martensite [11, 16]. The martensitic microstructure consists of laths in low- or medium-carbon steels, while the martensite forms as plates in high-carbon steels. The laths formed in low-carbon steels are fine, form at the grain boundaries and can stretch across an entire former austenite grain. The laths group together in sheaves or packets, like bainite (Figure 7). Each lath has a substructure consisting of a high density of dislocations arranged in cells, where one lath contains many cells. The cells have an average width of 2500 Å, and typical dislocation densities are estimated to be between 0.3 and $0.9 \cdot 10^{12}$ cm/cm³ [16].

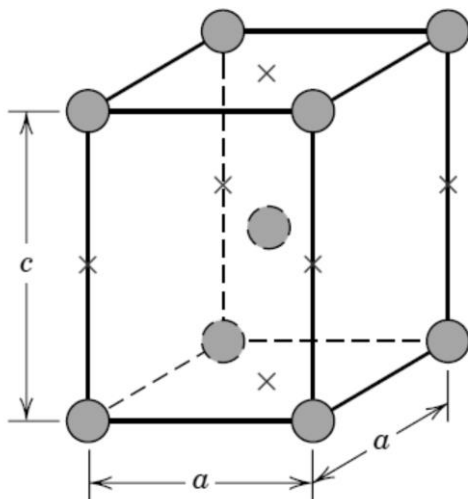


Figure 9: The body-centered tetragonal (BCT) unit cell for martensitic steel showing iron atoms (circles) and sites that may be occupied by carbon atoms (Xs). For this tetragonal unit cell, $c > a$ [11].

3.5. Tempering of Martensite

As explained, martensite in steels can be very hard and at the same time very brittle. It is therefore often necessary to temper the martensite, in order to improve its usability in structural and mechanical components. Tempered martensite provides one of the best combinations of strength and toughness obtainable in low carbon steels. The tempering process allows the microstructure to move incrementally towards an equilibrium, under the influence of thermal activation. Thus, the tempering ability of a material depends on the distance the microstructure has from its equilibrium state. Certain structures contain higher levels of stored free energy than others do. For example, for a typical alloy steel with a composition of Fe-0.2C-1.5Mn wt%, the reference (zero energy) state contains an equilibrium mix of ferrite, graphite and cementite. With a miniscule increase in stored energy (70 J mol⁻¹), the graphite is no longer present. The alloy steel has a phase mixture consisting of supersaturated ferrite at 1414 J mol⁻¹, and pure martensite at 1714 J mol⁻¹. Tempering a pure martensitic steel with said alloy composition can thus eventually alter the microstructure by releasing the free energy stored in it [14].

For pure martensitic steels, the tempering of martensite normally includes the diffusion of interstitially locked carbon. However, the substitutional solutes do not diffuse during this stage. If held at the tempering temperature for a sufficient amount of time, the structure can evolve into a dispersion of coarse carbides in a ferritic matrix, which bears little resemblance to the original martensitic structure. For martensitic ferritic steels, however, the quenching process yields a fully martensitic/ferritic structure. There is no indication that tempering induces the development of further ferritic content, or cementite. If tempering at temperatures above 550 °C, one can expect to see a development of austenite, finely dispersed in the martensitic structure [17]. This austenite is commonly referred to as reversed austenite, as it reverts to its pre-quenched form due to the reception of thermal energy. The effect this reversed austenite has on mechanical properties is proportional with ΔT (where ΔT is the difference in temperature between 550 °C and the actual temperature used in the tempering process).

3.6. Heat treatment – Time-Tempering

Tempering is the process whereby a material is reheated after hardening and quenching. The temperature used in this process is normally far below the critical temperature. The goal is not to repeat the hardening process, but to relieve stresses in the lattice structure, while simultaneously increasing the toughness and ductility of the material [11]. The tempering process will normally decrease the hardness of the material. Tempering usually consists of heating the material to a specified temperature, holding it at said temperature for a specified amount of time, and allowing it to fully cool in air to ambient temperature. The exact temperature used determines the resulting decrease in hardness and depends on the desired properties of the finished product. As an example, machining tools are usually tempered at very low temperatures, while springs are tempered at much higher temperatures [18].

It is empirically proven that the tempering temperature and the duration of the tempering process have direct effects on mechanical properties such as hardness. First described in 1945, the most statistically proven relation between tempering temperature and resulting effects is known as the Holloman-Jaffe Parameter, Equation (4) (also known as the Larson and Miller equation) [19]:

$$Hp = \frac{T \cdot [c + \log(t)]}{1000} \quad (4)$$

Where the T is temperature in kelvin, c is a constant depending on the steel alloy composition of carbon content and where t is the tempering time in hours. With this relation, they determined that the hardness (HRC) decreased linearly with increasing Hp . According to their results they determined that as long as the Hp was the same, the hardness resulting from a higher temperature, short time heat treatment would be the same as that from a lower temperature, longer time tempering. The constant (c) was found to decrease relatively linearly with increasing carbon content and they recommended a value of 19.5-20 for regular carbon and alloy steels. Through comparison with the literature available at the time, they determined this relationship to be valid independent of the starting microstructural constituents or secondary hardening effects for compositions from 0.31-1.15 wt% C, 0-5 wt% Mo and up to 5 wt% Cr. The valid tempering conditions ranged from 100°C to 710°C (not valid over A1 temperature) for times from 6 seconds to 1000 hours. Note that the tempering temperature has a more substantial impact than the time parameter [19].

Several diagrams for hardness versus Holloman- Jaffe parameter has been made for steels with a carbon content of 0.31-1.15% and with various alloying elements [20]. Figure 10 shows the effect of heat treatment of a martensitic microstructure in relation to the Rockwell hardness (HRC) and the Holloman-Jaffe parameter in terms of carbon content of 0.31% with a corresponding c value of 15.9.

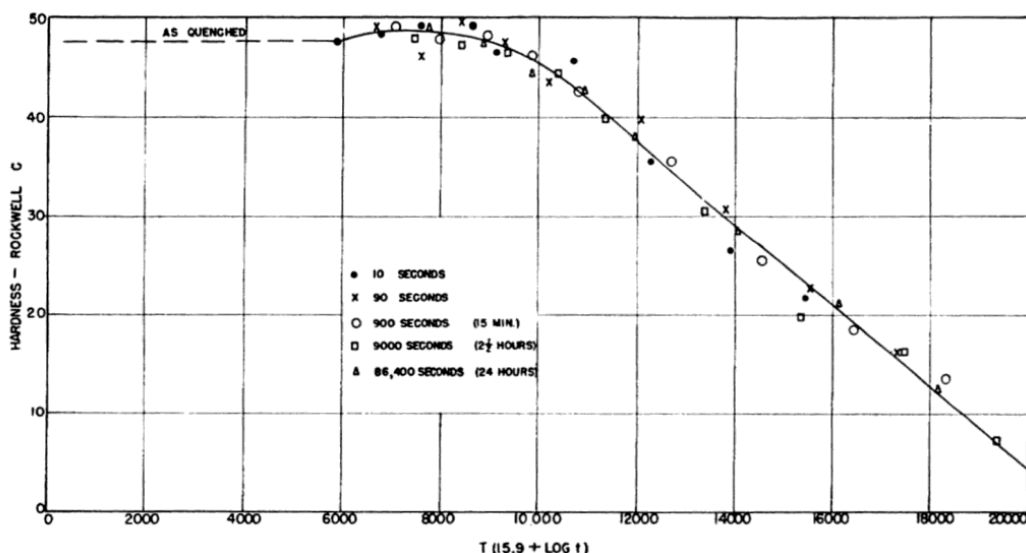


Figure 10: (HRC) Rockwell hardness vs. (Hp) Holloman-Jaffe Time-Temperature parameter for tempering fully quenched 0.31% carbon steel [20].

3.7. Alloying contributions

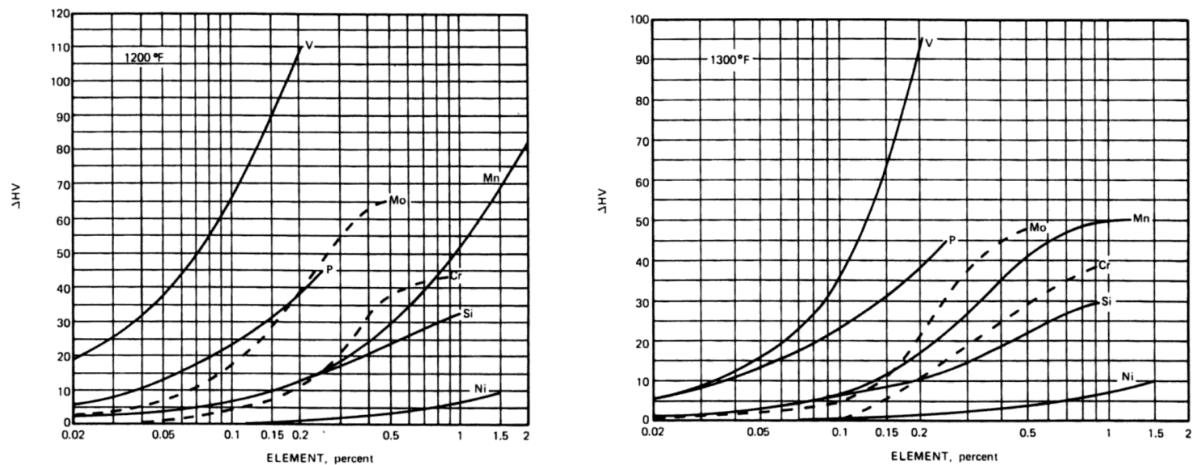


Figure 11: Effect of elements on the hardness of martensite tempered for 1 hour at different temperatures (650°C and 705°C) [20].

The main role of alloying elements in tempered tool steels is to compensate for the drop in strength and hardness that is seen in heat-treated carbon steels through a process called secondary hardening, and this is done primarily through two hardening mechanisms, precipitation and solution hardening. This increase in hardening may even be larger than that of the original peak hardness after quenching [14].

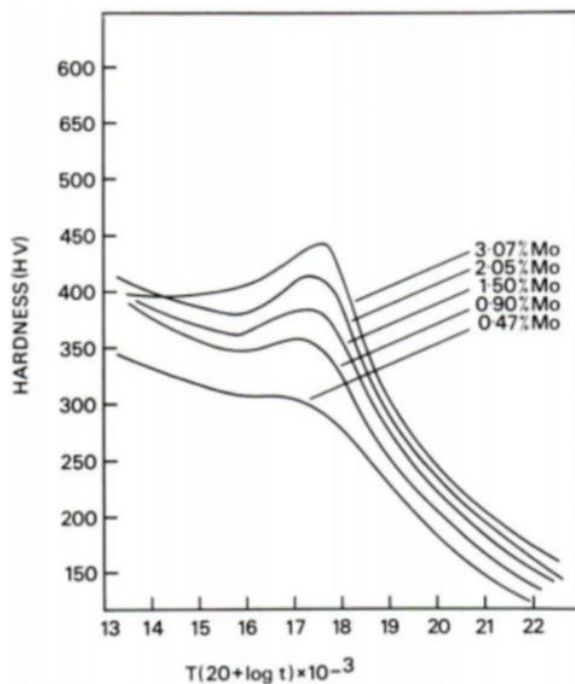


Figure 12: Effect of Molybdenum Content on Tempered Hardness for 0,35% carbon content [14].

Secondary hardening is an effect to take into consideration when tempering steels containing chromium, molybdenum, titanium, tungsten or vanadium. These elements are strong carbide formers and will precipitate as alloy carbides in preference to cementite at temperatures from 500-600°C. Due to their slow, substitutional diffusion, these elements will in most practical applications

form fine, dispersed carbides. Aided by higher thermodynamic stability, the dispersed alloy carbides will replace coarser cementite particles, and because of their “sluggish” diffusion, they will remain small and dispersed even at elevated temperatures [14, 16].

In an updated steel certificate, we will find many alloying elements; the majority are represented in such small amounts that we call them: micro alloying elements. Most of the micro alloying elements create chemical connection and belong to the following two groups: Carbides (with Carbon) and Nitrides (with Nitrogen)[21].

The carbides are primarily created in the ferrite (under A1) and they are located at the grain boundary [21]. A great amount of carbides results in brittle area; they are not a metal bonding and are therefore missing the plastic property. Such brittle areas reduce the ductility of the steel. There are some metals that have a high tendency to form carbides in steel: V, Ti and Nb. Some have a medium tendency: Mo, W and Cr. In fact, we must be aware of these carbide-formers when we propose PWHT [21].

3.8. Heat Affected Zone

Since carbon and low alloy steels undergo an allotropic phase transformation, the HAZ is an area in which drastic changes occur during the welding thermal cycle [22]. As can be seen in Figure 13, the regions of the HAZ can be related to the equilibrium iron-carbon phase diagram.

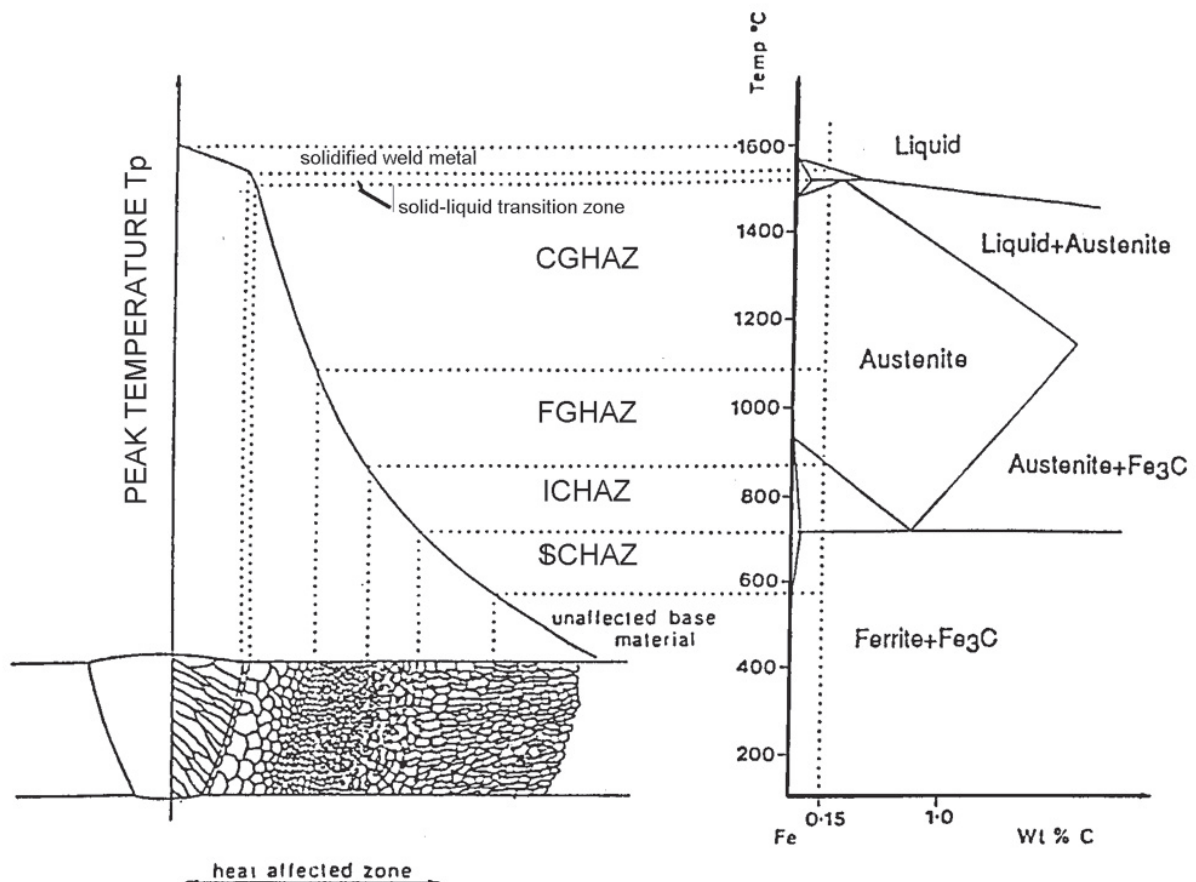


Figure 13: Heat Affected Zone Regions in Relation to Equilibrium Iron-Carbon Phase Diagram [23].

The HAZ can be further divided into coarse grain heat-affected zone (CGHAZ), fine grain heat-affected zone (FGHAZ) and the intercritical heat-affected zone (ICHAZ). The CGHAZ is a region in which the temperature reaches high into the austenite phase field, resulting in pronounced grain growth. This is the result of the reduction in free energy by the decreasing grain boundary area (and curvature) and the dissolution of carbides and nitrides, that act to pin boundaries and restrain growth [22, 24]. The FGHAZ is the region that reached a temperature slightly above the upper critical transformation temperature (A_3), which allows for recrystallization and results in grain refinement. Because it is only above this threshold for a short time, the ferrite present in this region does not completely transform to austenite and refines the grain structure on cooling [13]. In the ICHAZ, the temperatures range between the A_3 and lower critical (A_1) temperatures. Because of this, there is partial transformation to austenite during the welding thermal cycle [13].

During cooling from welding, phase transformations can play a large role in the properties and microstructure in the HAZ. Regions of the HAZ that were transformed to austenite will transform to a wide variety of phases based on welding parameters and material hardenability. In applications such as corrosion resistant cladding, the dilution of the weld filler metal by the base material must be controlled carefully in order to maintain the appropriate properties [25]. For this reason, the heat inputs used in these welding processes are typically very low and result in extremely fast cooling rates that lead to a near completely martensitic microstructure in the HAZ. Other applications, such as joining power generation boiler tubes, call for much higher heat input conditions that result in slower cooling conditions and microstructures consisting of bainite, ferrite and possibly martensite [26].

3.9. Residual stresses and stress concentrations

The cooling of a localized volume of material from its melting point to ambient temperature involves a significant reduction in volume and cause shrinkage of the weldment [13]. Since the welded structure remains continuous, there must be a mechanism whereby this difference in strain is accommodated. This is achieved in part through plastic strain of the material. The balance is accommodated through elastic strain. This results in a stress field distributed throughout the material after cooling, known as residual stress.

In welds of thick sections, the residual stresses that develop in the weldment often exceed the yield strength of the material. Therefore, the material yields and the remaining residual stress can be at the level of the yield stress, as the full elastic strain limit has been reached [3, 27].

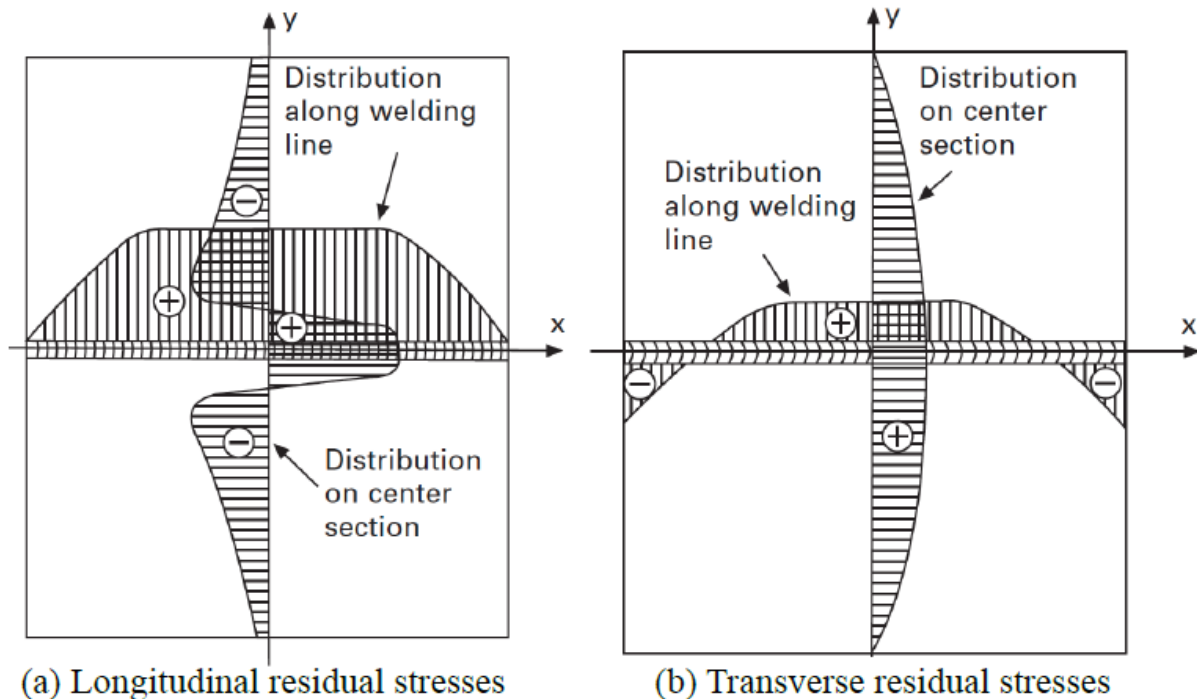


Figure 14: (a) Longitudinal and (b) transversal residual stress distribution in a weld [28].

In a multi-pass weld the residual stress field produced is triaxial. Since the weld metal is sufficiently constrained by the parent metal in each principal direction, the residual stresses also act in these three directions. This residual stress field can considerably decrease the strength of a weldment [3, 13].



Figure 15: Schematic sketch of multipass welding. Note that the root pass has the highest dilution ratio [13].

It is well known that stress raisers tend to reduce fatigue life namely, the what is known as notch effect. Stress raisers can be mechanical, such as toes with a high reinforcement, lack of penetration, and deep undercuts. They can also be metallurgical, such as micro fissures (microcracks), porosity, inclusions, and brittle and sharp intermetallic compounds [13]. These are factors that need to be taken into consideration when designing and approving the weld.

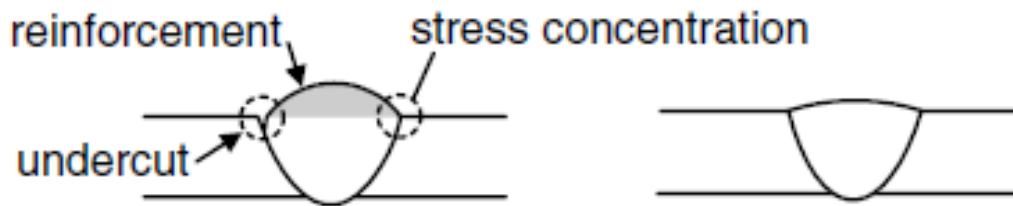


Figure 16: Stress raisers in a V-groove [13].

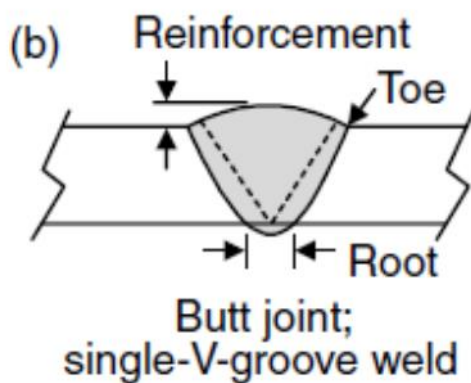


Figure 17: Typical weld joint – V-groove [13].

3.10. Hydrogen cracking

One of the chief weldability concerns in low alloy steels is hydrogen induced cracking (HIC). This form of cracking, also referred to as cold cracking occurs after cooling of the weldment. The welding process invariably introduces dissolved hydrogen into the weldment [27]. Several mechanisms by which this dissolved hydrogen leads to cracking have been proposed, without widespread agreement on the most likely mechanism [13].

Hydrogen cracking often involves a significant incubation period before the cracking is either detected or causes the component to fail. This incubation period is associated with the diffusion of hydrogen and can be of the order of several weeks [27].

The cracking proceeds in a step-wise fashion typically in the HAZ. There is a strong dependence on notch intensity to initiate the cracking. Such stress concentration in a weldment is usually supplied by the geometry of the weld toe. Any defects included in the weld structure such as slag, pores etc. could also contribute to stress concentration [13].

While the exact mechanism involved in hydrogen cracking is subject to conjecture, the factors that contribute to its appearance are widely accepted [27]. The most significant of these factors are:

- Hydrogen content
- Residual stress
- Microstructure

The most common region for hydrogen crack initiation is the CGHAZ. The increased size of prior austenite grains increases the segregation at grain boundaries [27]. It would appear that the role of hydrogen in the cold cracking mechanism is to decohere the matrix-particle interfaces of both precipitates and inclusions [13].

For a microstructure to be considered 'susceptible', it should exhibit the following properties [27]:

- Relatively hard grains (martensite or bainite)
- Coarse prior austenite grain size
- Grain boundary particles (Carbide precipitates or slag inclusions)
- High dislocation density

The properties of weldments (harden able, dispersion strengthened) render it susceptible to hydrogen cracking and for this reason, most weld procedures require the use of low hydrogen electrodes and thermal treatments to encourage H effusion [13, 27].

As described in the study done by Dimitri Rybakov [1], conducted for the same pipes used for drilling fluid in the drilling industry, the risk of cracking and failure due to Hydrogen Sulfide in the drilling fluid can be of major concern. This problem is caused by the Hydrogen Sulfide in the drilling fluid entering the impurity pockets and metallic voids in the steel pipe for so to expand to a crack as the hydrogen ions diffuse in the metal pocket or void [1].

3.11. Welding of Low Alloy Steels

For joining steel pipes in the oil and gas industry, fusion welding is the most commonly used form of welding. A fusion weld joint is broken into several regions, as identified by Savage et al.; the fusion zone (which contains both the composite region and the unmixed zone), the partially melted zone, and the true heat-affected zone (HAZ) [29]. The fusion zone is the region in which the temperature has exceeded the liquidus temperature and hence has fully melted. The partially melted zone is the region in which the temperature was between the liquidus and solidus temperature, resulting in an area that did not completely melt but had areas that formed liquid. The true HAZ is the region in which temperatures do not exceed the solidus and therefore all reactions are solid state type [23]. One of the reasons for developing low-carbon steel ($0.06\% < C < 0.12\%$) was the wish for a better weldability with special focus on the problems in HAZ[16, 23]:

- Stress corrosion
- Hydrogen-induced cracks (HIC)

These problems were related to the amount of martensite in HAZ[23]. In ordinary C-Mn-steel the tendency to form martensite was strong and the “eye of the needle” was the hardness test. Unannealed martensite is a structure with a high level of residual stresses and very little plasticity, hence a great danger of hydrogen-induced cracks[23]. In micro-alloyed low-carbon steel the hardness problem is almost eliminated, with the exception of steel for special purposes such as the NACE class[30, 31]: "Sour Service" equivalent a H_{max} requirement = 22 HRC (250 HV). However, the tendency to create brittle zones with rough grain size of so-called side-plate ferrite/ -Widmanstätten (SP) close to Fusion Line can be a risk. These areas have low toughness values, as explained at the beginning of this chapter.

Another point is that PWHT sometimes reduces the toughness value, in contrast to what can be expected with ordinary C-Mn-steel[23]. The development of low-carbon steel has in fact moved the current problem from a hardness problem in HAZ to a toughness problem in HAZ[23]. The relation between microstructure and the mechanical properties has been a focus during welding of structural steel [16]. Many investigations has been done to understand the amount and effect of the different micro-alloyed elements[16, 19].

3.12. Preheating of welds

The temperature of steel as soon as a weld run is started is the third major factor affecting weld cooling: for the first run, this is the preheat temperature; for subsequent runs, the interpass temperature. To avoid hydrogen cracking, steels are often preheated to temperatures up to 250°C before welding. To control weldment properties, maximum interpass temperatures (usually up to 300°C) may also be specified. These temperatures should be measured close (up to 50 mm) to the weld line immediately before a weld run is deposited. If the preheating is applied from one side only by a gas flame, the temperatures should preferably be measured on the side that is not heated. If this is not possible, the flame should be removed shortly before the temperature is measured: a waiting time of 1 min/25 mm of individual steel thickness is recommended.

Preheat and interpass temperatures within the ranges given above have less effect on the cooling rates at high temperatures than at low temperatures. Consequently, preheating a simple C or C:Mn steel, which transforms at a relatively high temperature, will not have much effect on the cooling rate through the transformation range, and on the resultant microstructure and hardness. However, it will considerably slow the cooling at lower temperatures, when hydrogen diffusion from the steel will be a major consideration in avoiding hydrogen cracking. On the other hand, low alloy steels transforming at lower temperatures can undergo significant changes to their HAZ microstructures and properties (not always favorably) by preheating to a higher temperature. Adverse effects on HAZ microstructure and properties may require maximum controls on preheat and interpass temperatures: the latter may lead to slower joint completion rates than are economically desirable and can give rise to problems, for example when automatically welding circumferential seams in small diameter thick-walled pipes.

3.13. PWHT of steel

The main difficulty in welding is the prevention of an abrupt deterioration of properties as a result of the appearance of structures, that reduce the resistance to brittle fracture in the heat-affected zone (HAZ)[25]. Post weld heat treatment (PWHT) is conducted on weldments for several reasons, including relief of residual stress, Hydrogen diffusion, homogenization, and dissolution of undesirable secondary phases that may have formed in the fusion zone or HAZ [25].

After PWHT, a weldment should be tougher and also should resist such service hazards as stress corrosion cracking (SCC) and in-service hydrogen cracking more readily than in the as-welded condition. The selection of PWHT temperatures is often aided or limited by the appropriate application standard, and is usually within the temperature range 550-750°C. It should be remembered that PWHT at a lower temperature will not undo any excessive softening that may have resulted from the use of too high a temperature. However, if a weldment has been under-tempered by PWHT, a further heat treatment at a higher temperature is always possible [8].

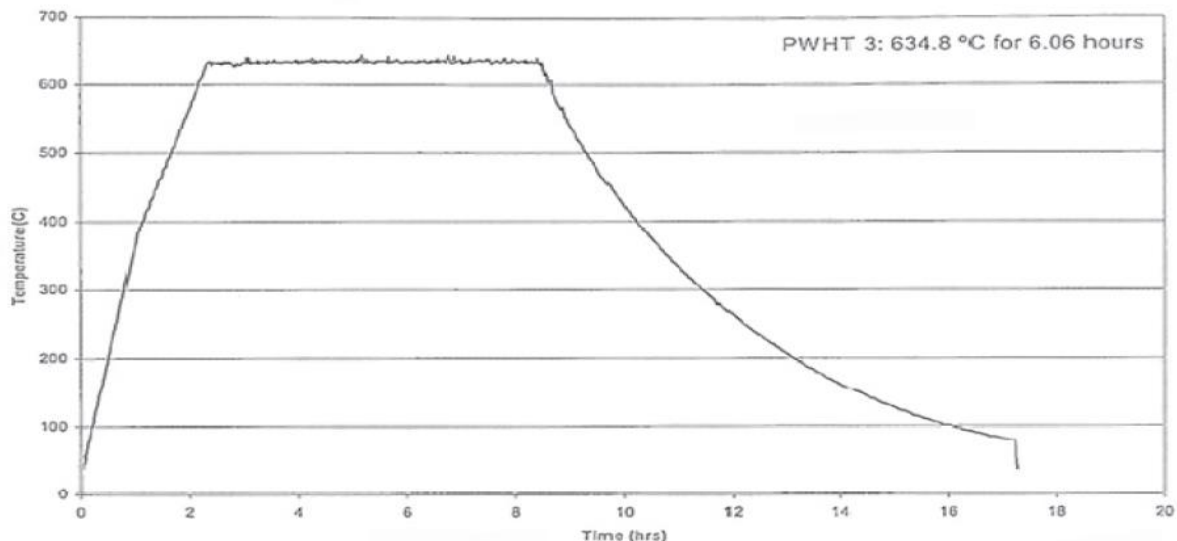


Figure 18: Thermal cycle representing a PWHT schedule [23].

Low alloy steels containing chromium generally require PWHT temperatures at or above 650°C[8], the temperature depending on the required properties and the application. The lower temperatures are used when the highest strength is required[8]: optimum creep resistance results from an intermediate temperature, whilst the highest temperature within the range is used to obtain maximum softening and stress relaxation. With alloy steels, two important points should be noted [8].

- The selected PWHT temperature should always be below the A_1 temperature of the steel, that is the temperature above which the steel begins to transform to austenite [8].

- When welding quenched and tempered steels that have been tempered to a particular strength or hardness level, it is important not to exceed the tempering temperature that was originally used, otherwise the whole component will be softened and weakened below its required level. It is normal to set the maximum of the PWHT temperature some 20°C below the actual tempering temperature [8].

Unfortunately, it is not always easy to discover the previous heat treatment history of a piece of steel, although it should be on the material certificate. Some steelmakers give such a wide range for the tempering temperature of a particular steel as to be useless, for example 530-680°C[8]. In such cases, the supplier or steelmaker should be carefully questioned. If this fails to provide the actual tempering temperature, the only action is to remove a small piece of steel from an unimportant area and subject it to careful hardness measurements after laboratory heat treatments at progressively higher temperatures in order to estimate the original tempering temperature. These tests should start at the bottom of the steelmakers' range and finish either where the steel starts softening, or at a temperature such as 650°C where a high degree of stress relief will be obtained [8].

During PWHT, care should be taken to ensure uniform heating of the components that may be of a very complex structure. Most heat treatment specifications give guidance on heating and cooling rates and temperature differentials. The penalties for exceeding these limits include distortion, cracking and also the re-imposition of residual stresses (albeit not in exactly the same configuration, but possibly up to the same maximum level) as that which the PWHT is intended to reduce. Although PWHT is preferably applied to completed fabrications, there are times when this is not possible. For example, available furnaces may be too small, the weld may be a repair in a structure too large to heat treat, or there may be a component in the vicinity that would be damaged by the heating. Local PWHT is acceptable in such cases, always provided precautions are taken to maintain low temperature gradients between the heated and unheated regions and to avoid distortion or buildup of high local stresses on cooling. Again, guidance is usually given in the appropriate application standard [8].

In terms of PWHT procedure of process piping systems the ASME B31.3 has become the world's most widely used standard, and the Norwegian offshore industry follows this standard for designing offshore piping systems. ASME B31.3 (Sect. 331.2.6) explains that welds may be subjected to local PWHT by means of a circumferential band around the entire component, with the weld located in the center of the band. The width of the band heated to the specified temperature range shall be at least three times the wall thickness at the weld of the thickest part of the part being joined [32]. There are different types of procedures for each type of alloy determining the thickness, where the PWHT procedure, temperature, holding time and heating and cooling rates are explained.

From the ASME code B31.3 heat treatment temperature shall be checked by thermocouple pyrometers or other suitable methods to ensure that the welding procedure specification (WPS) requirements are met. If used, the heat treatment furnace shall be calibrated such that the PWHT can be controlled within the required temperature range. For welds that require PWHT in accordance with Table 331.1.1 (see Figure 23 and Figure 24), the temperature of the material during PWHT shall be within the range specified [33]. However, if specified by the designer, the range may be extended as permitted by Table 331.1.2 (see Figure 25), provided the lower critical temperature A_1 , of the material is not exceeded [33].

3.14. Hardness testing and Hardness-Strength relation

Hardness tests have long been a standard method for material characterization since they provide an easy, inexpensive, non-destructive, and objective method of evaluating basic properties from a small volume of materials. In addition to resistance to plastic deformation, stiffness, strength of thin coatings, residual stresses near the surface, and the fracture toughness of the material are some basic properties that can be measured by the hardness tests. Hardness measurements are popular due to their flexibility where the products are not appropriate for standard material testing experiments such as simple tension, simple compression, or simple torsion. In this study, hardness data will be used to supply new increased yield strength distribution of cold-formed products and verify or compare the data obtained by FEM simulations in Abaqus.

Vickers hardness number (HV) has been the most popular in investigation of the relationship between hardness and the flow stress of materials such as steel for two reasons. Firstly, its superior resolution as compared to spherical indenters, and secondly, the Vickers indenter is self-similar, through which the hardness is ideally independent of the indentation load and indentation depth [34]. Therefore, in this study, as Vickers indentation and hardness test was used in the study done by Dimitri Rybakov [1], the same steel pipe with the same PWHT the same results will be used in this study for hardness measurement.

In literature, various authors have investigated the relationship between Vickers hardness number and the yield stress of material. A review of the first results is covered by Tabor in his standard work [34]. For non-strain hardening materials the Vickers hardness number HV defined as:

$$HV = \frac{\text{indenter force in kg}}{\text{surface area of the imprint in mm}^2} \quad (5)$$

The relations between strength and hardness established by Tabor [34] by the following Equation (6),

$$R_m = \left(\frac{HV}{2.9}\right) (1 - n) \left(\frac{12.5n}{1 - n}\right)^n \quad (6)$$

which relates the ultimate, nominal stress, R_m , to the Vickers hardness, HV, and the strain hardening coefficient, n . Note that the traditional unit for hardness is kgf/mm², while stress is usually given in N/mm². This leads to a unit difference of 9.81 N/kgf. Tabor assumed that the true stress, σ , could be approximated by the Ramberg and Osgood equation, also called Power law equation [34, 35]:

$$\sigma = K \varepsilon^n \quad (7)$$

where K is the Strength coefficient and ε is the true strain. This equation makes it possible to determine n from experimental results; in general for low carbon steel the strain hardening exponent is approximately 0.21 [11]. A simplified derivation results in the following expression when the curve is only fitted for the (A_{gt} , R_m)-point of the tensile curve [34, 35]:

$$n = \ln(1 + A_g) \quad (8)$$

The strain hardening coefficient can also be calculated by determining the slope of $\ln \sigma$ plotted against $\ln \varepsilon$. If the tensile curves will not produce a straight line with Equation 5, the Ludwik equation, can be used to obtain a straight line [36]:

$$\sigma = \sigma_0 + K \varepsilon^n \quad (9)$$

The relation shown in Equation (6) was improved by J.R. Cahoon [37], who presented the relation shown by Equation (10).

$$R_m = \frac{HV}{2.9} \left(\frac{n}{0.217} \right)^n \quad (10)$$

Cahoon claimed this relation to be both simpler and more accurate when compared to the relation found by Tabor. Tabor also noted that his relation showed good correlation for lower values of the strain hardening coefficient, n , but not for higher values of n [37].

There have also been attempts to establishing relations between the 0.2 % offset yield strength and the hardness of metals as well. One formula was established by Cahoon for the relation between yield strength and hardness- [38]; this result is shown by Equation (11).

$$R_{0.2} = \frac{HV}{3} (0.1)^n \quad (11)$$

The relations presented by Equations (6), (10) and (11) are good estimates for various alloys, but, since the strain hardening coefficient is a part of the expression, all are dependent on prior knowledge of the specific material [39]. But a different approximation for determining the relations between strength and hardness has also been done, the study by Pavlina and Van Tyne [39]. Their work resulted in the expressions shown by Equations (12) and (13), done by using Vickers hardness on varying steel grades for determining the yield and tensile strength for steel [39].

$$R_{0.2} = 2.876 \cdot HV - 90.7 \quad (12)$$

$$R_m = 3.734 \cdot HV - 99.8 \quad (13)$$

Their study proved more stable than the previous formula established by Tabor using the strain hardening parameter; however, the specific steel strength can vary as they have just used an average strength for giving more stable results and to reduce the standard deviation [39]. It is worth mentioning that according to offshore specifications [40], the ratio between yield and tensile strength in the base should not exceed 0.85. For the traditional class of normalized carbon-

manganese and controlled rolled low-carbon micro alloyed steels, the ratio between the base plate yield and tensile strength is about 0.7. This ratio is increased to about 0.8 for the accelerated cooled steels [41].

In 1989 there was a study done by O. M. Akselsen, G. Rorvik, M. I. Onsjøen and Ø. Grong on predictions of mechanical properties of HAZ [41]. The study was done on high strength steels where the investigation was undertaken with the objective of providing quantitative information on the strength and ductility of the grain-coarsened HAZ of modern structural steels, based on tensile testing of weld thermal simulated specimens. From stress-strain relationships and hardness measurements, empirical equations were developed to predict HAZ yield and tensile strength, as well as ductility from a knowledge of base metal chemical composition and welding parameters [41].

In the case of grain-coarsened HAZ, the regression analysis gave the following relationship [41]:

$$R_{0,2} = 3,1HV(0,1)^n - 80 \quad (14)$$

In addition to yield point, the ultimate tensile strength was developed for grain coarsened HAZ and is also related to hardness through the following equation [41]:

$$R_m = 3,5HV(1 - n) \left(\frac{12,5n}{1 - n} \right)^n - 92 \quad (15)$$

The total elongation at fracture was also plotted versus tensile strength. Although it was pointed out that there was a relatively large scatter in elongation values for the given tensile strength level, the following relationship was found (with a correlation coefficient r^2 of 0.6) [41]:

$$A_{35}(\%) = 5,75 \cdot 10^4 R_m^{-1.25} \quad (16)$$

Values calculated from equation (16) were plotted versus measured elongation illustrated in Figure 19. In general, elongation at the fracture can be predicted with a precision of $\pm 3\%$ with a small overestimation at low elongations and underestimation at high values [41].

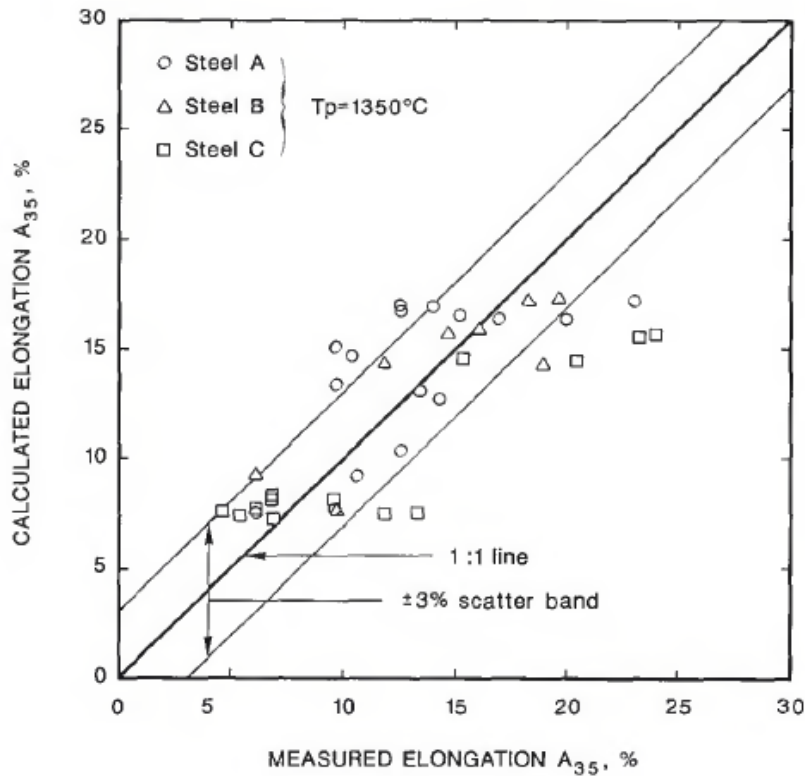


Figure 19: Correlation between measured and calculated grain-coarsened HAZ elongation, A_{35} [41].

3.15. Stress analysis of piping systems

Piping stress analyses is used to classify the static and dynamic loading resulting from temperature changes, internal and external pressures, and changes in fluid flow rate, the effects of gravity, seismic activity, fire, and other environmental conditions.

In the offshore oil and gas industry, pipe stress analysis is the important technique for engineers to design piping systems without overloading and overstressing the piping components and connected equipment. The piping stress analysis is to be performed in accordance with the requirements specified in the latest edition of the ASME B31.3 for pressure piping.

ASME B31.3 designs conditions specifically intended for pressure design. There are two main design conditions discussed in the code. These are design pressure and design temperature.

Design pressure:

A requirement when determining the design pressure, is to consider all the possible conditions of internal pressure, such as thermal expansion of trapped fluids, surge and failure of control devices. It is permitted to use a process piping system without the protection of a pressure safety relief valve. The piping systems have to be designed to withstand the maximum pressure that can occur when none of the protections are provided and it must also be safe when all the protections have failed.

Design temperature:

The design temperature mainly considers the metal temperature of the pipe. There are several internal and external conditions that can be involved in the design temperature, such as the temperature of the process fluid, ambient cooling, ambient heating, solar radiation, and maximum heat tracing temperature. Minimum design temperature is the lowest temperature that a component can be expected to reach while the system is in operation. This temperature is required to determine the design requirements and special material qualification requirements.

In the following, a brief description of the performed checks in the ASME B31.3 is presented.

Check, Internal Design Pressure

The requirement thickness of strait section of pipe shall be determine in accordance with equation(17):

$$t_m = t + C \quad (17)$$

The minimum thickness T for the pipe selected, considering the manufacturer's minus tolerance, shall not be less than t_m .

The hoop stress due to internal design pressure must fulfil the following criterion (section 304.1.2.(3a))[32]:

$$t_m = \left[\frac{PD}{2(SEW + PY)} \right] \quad (18)$$

$$t_m = \left[\frac{PD}{2(SEW + PY)} + C \right] \cdot \left[\frac{100}{100 - MT} \right] \quad (19)$$

Where,

P = Design pressure

D = Outer diameter

S = Allowable stress

E = Quality factor, here equal to 0.8, from ASME B31.3, Table A-1A[32].

W = Weld joint strength reduction factor in accordance with para. 302.3.5(e). here equal to 1.

Y = Material and temperature coefficient taken from Table 304.1.1, in ASME B31.3, or use eq(20).

t_{req} = Required wall thickness

MT = User supplied mill tolerance, percent or inches

C = Corrosion allowance, where the tolerance is not specified an assumption of 0,5 mm shall be set.

$$Y = \frac{d + 2C}{D + d + 2C} \quad (20)$$

Where,

d = Inside diameter of pipe.

Pressure Testing and Leak Testing Requirements for Process Piping

Leakage test shall be conducted after any heat treatment that has been completed, (345.2.2.b)[32].

Hydrostatic Leak Test, Test Pressure (345.4.2)

Except as provided in para. 345.4.3, the hydrostatic test pressure at EVERY POINT in a metallic piping system shall be as follows[32]:

(a) not less than 1.5 times the design pressure

(b) when the design temperature is greater than the test temperature, the minimum test pressure, at the point under consideration, shall be calculated using eq:

$$P_T = 1.5PS_T/S \quad (21)$$

Where,

P = Internal design pressure

P_T = Minimum test gauge pressure

S = Allowable stress at component design temperature for the prevalent pipe material; see table A-1 or Table A-1M in ASME B31.3.

S_T = Allowable stress at test temperature for the prevalent pipe material; see Table A-1 or Table A-1M in ASME B31.3.

(c) in those cases where the piping system may not include pipe itself, any other component in the piping system, other than pipe-supporting elements and bolting, may be used to determine the ST/S ratio based on the applicable allowable stresses obtained from Table A-1[32].

In those cases where the piping system may be made up of equivalent lengths of more than one material, the ST/S ratio shall be based on the minimum calculated ratio of the included materials.

(d) if the test pressure as defined above would produce a circumferential pressure or longitudinal stress (based on minimum pipe wall thickness) in excess of the yield strength at test temperature or a pressure more than 1.5 times the component rating at test temperature, the test pressure may be reduced to the maximum pressure that will not exceed the lesser of the yield strength or 1.5 times the component ratings at test temperature [32].

3.16. Numerical analysis in Abaqus

In this study the software Abaqus in Explicit modus is used to analyze the integrity of the pipe. This section gives a brief overview of the important features of the explicit calculation method; a more detailed overview was done in the Pre-study, *Experimental calibration of continuum damage models*[10]. The difference between Abaqus Standard and Abaqus Explicit lies in the calculation method, especially in gaining the accelerations of the nodes. In the implicit method, the global tangent stiffness matrix as well as iterations and tolerances are required, which are expensive in calculation time and can lead to numerical difficulties [42, 43].

In Abaqus Explicit the calculation method is, as the name implies, strongly explicit. The state at the end of an increment is solely based on the displacements, velocities and accelerations at the beginning of that increment in time. The calculation during that increment proceeds as follows[44]: Dynamic equilibrium is established for each node at the beginning of an increment. The acceleration of the nodes is only calculated by its mass and the net force (difference between external applied forces and internal nodal forces) acting on it. Thus, these calculations are cost-efficient. By time integration based on a central difference rule, the established equations of motion are explicitly integrated through time and obtain the node's velocities and displacements. Then the strain increments of the element, and finally its stresses, are calculated from the nodes' velocities. As the last step, the internal forces of the nodes are reset before the dynamic equilibrium at the beginning of the next increment can be solved [43, 44].

In the explicit analysis the displacement and the velocity at the beginning of each increment is known. This means that the global mass and stiffness matrix need not be added for each increment, saving much computational work. However, the size of the time increments Δt have to be smaller than a critical time increment Δt_c [42, 43, 45]

$$\Delta t \leq \Delta t_c = \frac{l_{min}^e}{c_d} \quad (22)$$

$$c_d = \sqrt{\frac{E}{\rho}} \quad (23)$$

Where l_{min}^e is the smallest element dimension on the model, and c_d is the speed of sound in the material over the element. The c_d is calculated as seen in Equation(23), where E is the Youngs modulus and ρ is the mass density. This makes the method conditionally stable, and the increments must be kept small enough to preserve the stability of the result. Since the incremental steps are small, the incremental result will never greatly deviate from the exact solution, and any inaccuracy will most likely be corrected when calculating the next increment. Due to of this, there is often no need to control the accuracy as with the implicit method [42, 43].

The explicit method is preferred over the implicit method due to the ability to convert the mass matrix to a diagonal matrix, often referred to as lumped mass. This reduces the number of calculations needed for each time increment for a three-dimensional finite element analysis (FEA). The amount of data storage needed for each increment calculation is also much smaller for the explicit method [42].

Implicit method is said to be "unconditionally stable" and is thus often preferred in structural calculations, as its results are more stable and thus believed to be more reliable. However, the stability of implicit methods comes at the price of computational recourses. For the complex problems such as excessive plasticity and fracture simulations, the more computationally efficient explicit method is often the only feasible option. Thus, the ductile damage models used in this thesis are not available in "regular" implicit Abaqus, but only in Abaqus Explicit [42].

3.17. Ductile damage in Abaqus

It is common to distinguish between brittle and ductile fracture in metals. The sudden brittle fracture is generally avoided, making the ductile fracture the preferred failure mode, where ductile materials fail as a result of nucleation, growth and coalescence of micro voids. Figure 20 displays the entire ductile fracture process [46]. In this study, the Ductile Damage model in Abaqus is used for the simulation of the damage accumulation until final fracture. More detailed use and theory behind the damage model is found in the Pre-study for this thesis [10].

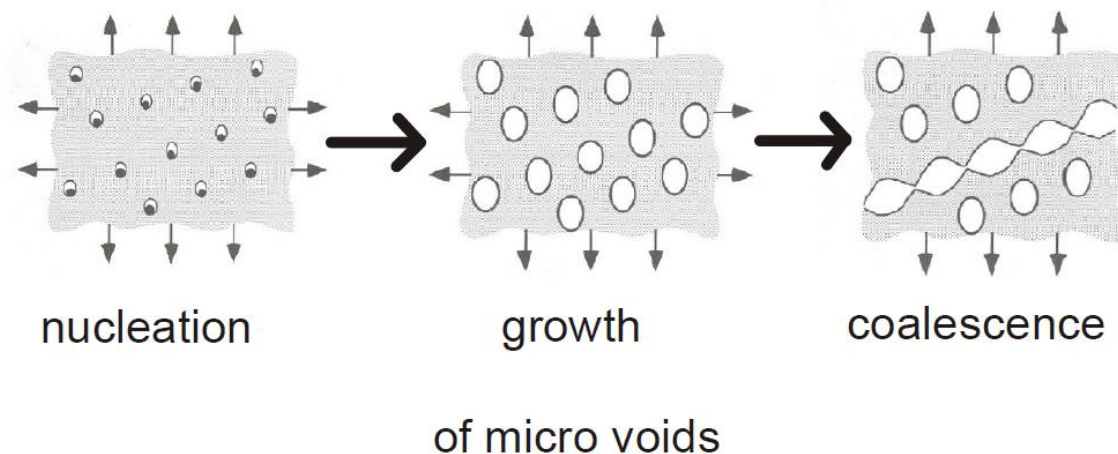


Figure 20: Ductile fracture process [46].

As described in the Abaqus user manual, ductile damage initiation criterion is a model for predicting the onset of damage due to nucleation, growth, and coalescence of voids in ductile metals. The model assumes that the equivalent plastic strain at the onset of damage is a function of stress triaxiality, and equivalent plastic strain rate at the onset of damage is a function of the stress triaxiality and strain rate [47].

The importance of triaxiality is evident, for example, in stress concentrations due to geometry and already initiated crack tips [47]. To capture the effect of triaxiality, in an experimental procedure for

estimation of the model parameters, the notched test specimen is subjected to tensile loading. In the unidirectional tension test, the stress state prior to necking is due to the 3D stress state on the sample surface. The onset of necking is accomplished by the development of a triaxial state of stress in the neck [47, 48].

The classical metal plasticity model in Abaqus defines the post-yield behavior for most metals. Abaqus approximates the smooth stress-strain behavior of the material with a series of straight lines joining the given data points. Any number of points can be used to approximate the actual material behavior. Therefore, it is possible to use a very close approximation of the actual material behavior. The plastic data define the true yield stress of the material as a function of true plastic strain. The true stress and true strain is calculated by using equation (26) and (27); these are calculated from the normal stresses and strains that can be calculated using equation (24) and (25), based on results from experimental tests. The first piece of data given for the plasticity plot defines the initial yield stress of the material and should have a plastic strain value of zero [49, 50].

$$\varepsilon = \frac{l - l_0}{l_0} = \frac{\Delta l}{l_0} \quad (24)$$

$$\sigma = \frac{F}{A_0} \quad (25)$$

$$\varepsilon_T = \ln(1 + \varepsilon) \quad (26)$$

$$\sigma_T = \sigma(1 + \varepsilon) \quad (27)$$

Figure 21 illustrates the characteristic stress-strain behavior of a material undergoing damage. In the context of an elastic-plastic material with isotropic hardening, the damage manifests itself in two forms: softening of the yield stress and degradation of the elasticity. The solid curve in the figure represents the damaged stress-strain response, while the dashed curve is the response in the absence of damage. As discussed later, the damaged response depends on the element dimensions such that mesh dependency of the results is minimized [51].

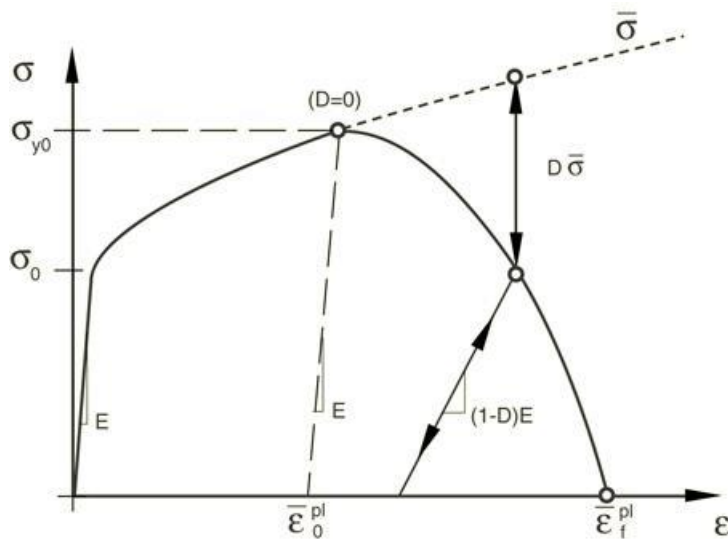


Figure 21: Stress-strain curve with progressive damage degradation [51].

In Abaqus, the specification of a failure mechanism consists of four distinct parts [52]:

- The definition of the effective (or undamaged) material response (e.g., a-b-cd'),
- A damage initiation criterion (e.g., c),
- A damage evolution law (e.g., c-d, and
- A choice of element deletion whereby elements can be removed from the calculations once the material stiffness is fully degraded (e.g., d).

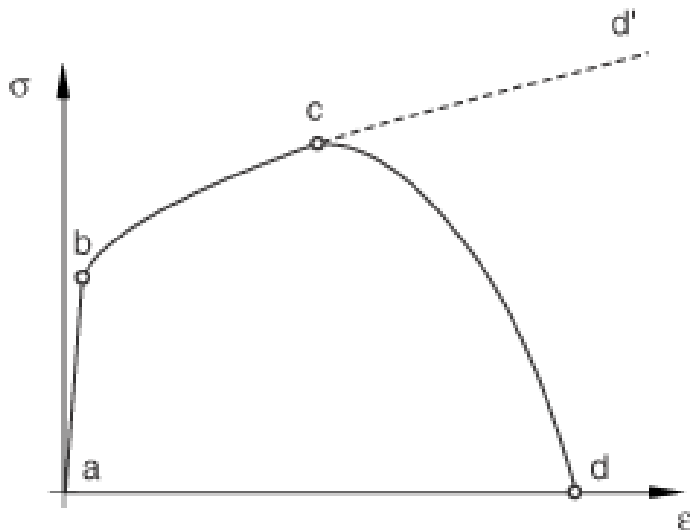


Figure 17: Failure mechanism in Abaqus[52].

In continuum mechanics the constitutive model is normally expressed in terms of stress-strain relations. When the material exhibits strain-softening behavior, leading to strain localization, this formulation results in a strong mesh dependency of the finite element results in that the energy dissipated decreases upon mesh refinement [52]. In Abaqus all the available damage evolution models use a formulation intended to alleviate the mesh dependency. This is accomplished by

introducing a characteristic length into the formulation, which in Abaqus is related to the element size, and expressing the softening part of the constitutive law as a stress-displacement relation [52].

The damage evolution is defined as mesh independent because it does not directly use any parameters that are dependent on the element size in the model. Instead of defining the deformation after damage initiation as plastic strain, it is defined as an equivalent plastic displacement \bar{u}^{pl} with the evolution expressed by [51]:

$$\dot{\bar{u}}^{pl} = L \dot{\bar{\epsilon}}^{pl} \quad (28)$$

Where L is the characteristic length of the element [51]. The evolution of damage variable with the relative plastic displacement can be specified in tabular, linear, or exponential form. Instantaneous failure will occur if the plastic displacement at failure \bar{u}_f^{pl} , is specified as 0; however, this choice is not recommended and should be used with care because it causes a sudden drop of the stress at the material point that can lead to dynamic instabilities. The linear damage evolution law defines a truly linear stress-strain softening response only if the effective response of the material is perfectly plastic (constant yield stress) after damage initiation, see Figure 22 [51].

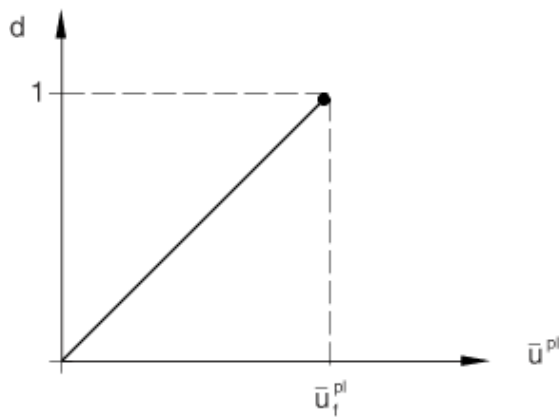


Figure 22: Linear damage evolution [51].

The characteristics of loading force on a model are with circumferential stress, axial stress and radial stress occurring at the same time, which are called the triaxial state of stress. The yield condition used in this paper is the von Mises yield condition. The von Mises yield condition considers that the yield occurred when the ratio of the maximum shape change reaches a certain value, and the expression for it is shown in equation (29)[42]:

$$\sigma_e = \frac{1}{\sqrt{2}} [(\sigma_1 - \sigma_2)^2 + (\sigma_2 - \sigma_3)^2 + (\sigma_3 - \sigma_1)^2]^{\frac{1}{2}} \quad (29)$$

In the post-processing of FEM by Abaqus, von Mises is generally called Mises equivalent stress [42]. The stress distribution for the model can be represented by the stress contour, which can make a clear description of the variation of the result for the whole simulation, to determine the failure zone for the model and the value of stress for that area. In this work, whether the welded pipe failed or not is evaluated based on the value of von Mises equivalent stress in the welded area by adopting the plastic failure criterion. The plastic failure criterion suggests that when the von Mises equivalent stress of the welded area reaches the post-yield point of the material, when the minimum stress along the wall thickness of the pipe reaches the ultimate tensile stress that will cause pipeline failure to occur, and the pressure to make this happen is called burst pressure.

3.18. Mesh density

The element mesh of a model should be good enough to capture the relevant failure modes of the structure depending on the forces acting upon it. In areas of interest, the element aspect ratio should be according to requirements for the selected element formulation. Furthermore, areas in or nearby large deformation should have an aspect ratio close to unity. Distribution of load and load type has an impact on the mesh density. And the nodes at where the load is applied needs to be correctly located [53].

It is usually necessary to run mesh sensitivity studies in order to verify that the results from the analysis are sufficiently accurate. This is also performed to make sure that the element mesh represents all the relevant failure modes in a sufficient and effective way. In general, the mesh refinement studies are completed by checking that the convergence of the results are obtained, which show that the results are stable when rerunning the analysis with decreased element size. Geometric sharp corners will have infinite small area and will therefore never converge [53].

3.19. Mass scaling

In order to obtain an economical solution for simulations with a large number of small elements, the calculation time must be shortened in some way. There are two possibilities, namely load rate scaling and mass scaling. Since load rate scaling strongly affects the time period T and, therefore, has a more lasting effect on the inertial forces, mass scaling should be preferred. Mass scaling means artificially increasing the mass of the model. Since the mass and density respectively has the important role of defining the time step for integration, see equations (22) and (23), increasing the mass will enlarge the stable time increment. Hence the analyses can be solved faster [42, 45].

There are two possibilities of mass scaling in Abaqus:

- To scale the mass by a certain factor.
- To scale the mass by defining a minimum stable time increment Δt .

As the finite element model consists of elements of different sizes, a uniform scaling with a constant factor would increase the mass, especially of the large elements, by too much. The second possibility

is preferred, where only the mass of these elements, whose stable increment Δt_{stable} is smaller than the defined one, is scaled. This is defined in Abaqus with the type BELOW MIN for the option *FIXED MASS SCALING. Hence the mass of all those elements with a stable time increment $\Delta t_{stable} = \Delta t$ are automatically scaled by a corresponding factor so that their stable time increment is redefined as $\Delta t_{stable} = \Delta t$. As a result of this kind of mass scaling, only portions of the model, where the smallest elements are located are scaled. The user has to verify that the changes in mass, and consequently the increase in inertial forces, does not influence the results of the simulation significantly. This can simplest be done by comparing it to unscaled results. In summary, the goal of mass scaling is to determine which amount of scaling will provide reasonable results while saving as much computer calculation time as possible. However, mass scaling will always reduce the quality of simulation results[42, 45].

4. Research question

Too high heat treatment temperature can cause weakening of the steel. There is an anecdotal evidence that the allowable range of heat treatment temperatures in older version the ASME B31.3 was too high and welding workshops have been reporting reduction of hardness in base material after PWHT at higher temperatures. Similar reduction of hardness was also observed by Dmitri R[1].

In 2014 PWHT temperatures were lowered in the ASME B31.3 Code for Pressure piping systems. However, this leaves the question with regard to safety of the pressure pipes that were welded in accordance to the old (prior to 2014) Code. How safe are those pipes and what consequences does the weakening of the base material might have?

Hence, the main objective for this study is to estimate the strength after different post-weld-heat-treatments (PWHT) done for AISI 4130 steel pipes; verification of strength and damage accumulation is done by numerical analysis in the software Abaqus. The study is done for welded pipe segments used for drilling fluid in the oil and gas industry.

“How has the strength of welded connections been affected by the change of PWHT procedure?”

- Are there any dangerous concerns in terms of strength of welded pipes completed before the change of PWHT procedure made in 2014 in the ASME B31.3?
- Is there any change in base material strength when it is PWHT to 705°C? How is this compared to PWHT of 650°C in terms of damage behavior?
- What are the failure mechanisms typical for this pipe segment and how can this be modeled by the finite element software Abaqus?
- What changes when using a different PWHT temperature for pipes in terms of strength integrity and failure mechanisms?

5. Case

This chapter gives an overview of the demands of the pipe that was tested and the material and equipment that was used in this study, as well as the material parameters. This study used hardness results from a previous study on the same material case. It must be mentioned that the deposited weld material from the electrodes in the study was not tensile tested, so assumptions of the material behavior were done according to the material certificate and the other material that was tested. Due to deviation of material parameters from the PWHT, it is of interest to identify what parameters may influence the failure mode of the FE model. This is of specific interest and will provide guidelines for further work. Investigations concerning the fully modeled piping system in FE analysis, will not be prioritized in this study. A closer investigation will be performed with regards to the variation of PWHT procedure and possible changes in strength.

The background for this study is the change of the PWHT procedure that was made to the ASME code in 2014, where the temperature was changed from the range 704-746°C to 650-705°C; see Figure 23, Figure 24 and Figure 25. The procedure for the tested steel in this study is marked red.

Table 331.1.1 Requirements for Heat Treatment

Base Metal P-No. [Note (1)]	Weld Metal Analysis A-Number [Note (2)]	Base Metal Group	Nominal Wall Thickness		Specified Min. Tensile Strength, Base Metal		Metal Temperature Range		Holding Time			Brinell Hardness, Max. [Note (4)]
			mm	in.	MPa	ksi	°C	°F	Nominal Wall [Note (3)]		Min. Time, h	
									min/mm	hr/in.		
1	1	Carbon steel	≤ 20 > 20	≤ ¾ > ¾	All All	All All	None 593-649	None 1,100-1,200
3	2, 11	Alloy steels, Cr ≤ ½%	≤ 20 > 20 All	≤ ¾ > ¾ All	≤ 490 All > 490	≤ 71 All > 71	None 593-718 593-718	None 1,100-1,325 1,100-1,325
4 [Note (5)]	3	Alloy steels, ½% < Cr ≤ 2%	≤ 13 > 13 All	≤ ½ > ½ All	≤ 490 All > 490	≤ 71 All > 71	None 704-746 704-746	None 1,300-1,375 1,300-1,375
5A, 5B, 5C [Note (5)]	4, 5	Alloy steels (2¼% ≤ Cr ≤ 10%) ≤ 3% Cr and ≤ 0.15% C ≤ 3% Cr and ≤ 0.15% C > 3% Cr or > 0.15% C	≤ 13 > 13 All	≤ ½ > ½ All	All All All	All All All	None 704-760 704-760	None 1,300-1,400 1,300-1,400
6	6	High alloy steels martensitic A240 Gr. 429	All All	All All	All All	All All	732-788 621-663	1,350-1,450 1,150-1,225	2.4	1	2	241
7	7	High alloy steels ferritic	All	All	All	All	None	None
8	8, 9	High alloy steels austenitic	All	All	All	All	None	None
9A, 9B	10	Nickel alloy steels	≤ 20 > 20	≤ ¾ > ¾	All All	All All	None 593-635	None 1,100-1,175
10	...	Cr-Cu steel	All	All	All	All	760-816 [Note (6)]	1,400-1,500 [Note (6)]	1.2	½	½	...

Figure 23: PWHT ASME B31.3-2012 [54].

The ASME B31.3-2012 shows that for low alloy steels with thickness over 13mm and a Chromium content as AISI 4130 the minimum holding time is set to 2.4 minutes/mm but not less than two hours. According to ASME B31.3 the heating and cooling rate shall not exceed 335°C/h[32] divided by one-half the maximum material thickness in inches at the weld, but in no case shall the temperature change rate exceed 335°C/h.

Table 331.1.1 Postweld Heat Treatment

P-No. and Group No. (BPV Code Section IX, QW/QB-420)	Holding Temperature Range, °C (°F) [Note (1)]	Minimum Holding Time at Temperature for Control Thickness [Note (2)]	
		Up to 50 mm (2 in.)	Over 50 mm (2 in.)
P-No. 1, Group Nos. 1-3	595 to 650 (1,100 to 1,200)	1 h/25 mm (1 hr/in.); 15 min min.	2 hr plus 15 min for each additional 25 mm (in.) over 50 mm (2 in.)
P-No. 3, Group Nos. 1 and 2	595 to 650 (1,100 to 1,200)		
P-No. 4, Group Nos. 1 and 2	650 to 705 (1,200 to 1,300)		
P-No. 5A, Group No. 1	675 to 760 (1,250 to 1,400)		
P-No. 5B, Group No. 1	675 to 760 (1,250 to 1,400)		
P-No. 6, Group Nos. 1-3	760 to 800 (1,400 to 1,475)		
P-No. 7, Group Nos. 1 and 2 [Note (3)]	730 to 775 (1,350 to 1,425)		
P-No. 8, Group Nos. 1-4	PWHT not required unless required by WPS		
P-No. 9A, Group No. 1	595 to 650 (1,100 to 1,200)		
P-No. 9B, Group No. 1	595 to 650 (1,100 to 1,200)		
P-No. 10H, Group No. 1	PWHT not required unless required by WPS. If done, see Note (4).		
P-No. 10I, Group No. 1 [Note (3)]	730 to 815 (1,350 to 1,500)		
P-No. 11A	550 to 585 (1,025 to 1,085) [Note (5)]		

Figure 24: PWHT ASME B31.3-2014 [33].

Table 331.1.2 Alternate Postweld Heat Treatment Requirements for Carbon and Low Alloy Steels, P-Nos. 1 and 3

Decrease in Specified Minimum Temperature, °C (°F)	Minimum Holding Time at Decreased Temperature, h [Note (1)]
30 (50)	2
55 (100)	4
85 (150) [Note (2)]	10
110 (200) [Note (2)]	20

NOTES:

- (1) Times shown apply to thicknesses ≤ 25 mm (1 in.). Add 15 min/25 mm (15 min/in.) of thickness for control thicknesses > 25 mm (1 in.) (see para. 331.1.3).
- (2) A decrease > 55 °C (100°F) below the minimum specified temperature is allowable only for P-No. 1, Group Nos. 1 and 2 materials.

Figure 25: Alternate PWHT Requirements - ASME B31.3-2014 [33].

As seen from the ASME B31.3-2014 Figure 24, the minimum holding time is set to 1/25 hour/mm but not less than 15min. Yet, as seen in Figure 25 a further reduction in minimum temperature can be made, but minimum holding time will then increase, as seen for steel with decrease of 55°C, where the minimum holding time increases to 4/25 hours/mm.

A brief overview of what was tested and analyzed in this study are as follows:

- Numerical sensitivity check of the results in terms of element size and mesh dependency of the results.
- Numerical investigation for predicting the damage accumulation and behavior of different possible material parameters in terms of softening and hardening of the HAZ after PWHT using available numerical formulas and FEA.
- Processing of material data from hardness tests from previous study and one extra numerical estimation of hardness using Holloman-Jaffe done for simulation of three different PWHT procedures that is compared in this study for comparison and verification of the behavior due to the different PWHT procedures.
- Execution experimental tensile tests and processing of material data from tensile tests done for simulation of the four different PWHT procedures that is compared in this study for comparison and final verification of the behavior due to the different PWHT procedures.

5.1. Design criteria for the pipe

This study has used the design criteria for the injection system for the drilling fluid used under deep-water drilling. The design criteria are found in Appendix J from the Piping Class Sheet KX10MH and supplied by Dimitri Rybakov in MHWirth.

Design pressure: 517 bar or 51.7 MPa

Design temperature: -29°C – 90°C

Material: Low alloy steel. (usually AISI 4130 or 4140)

Corrosion allowances: 3 mm

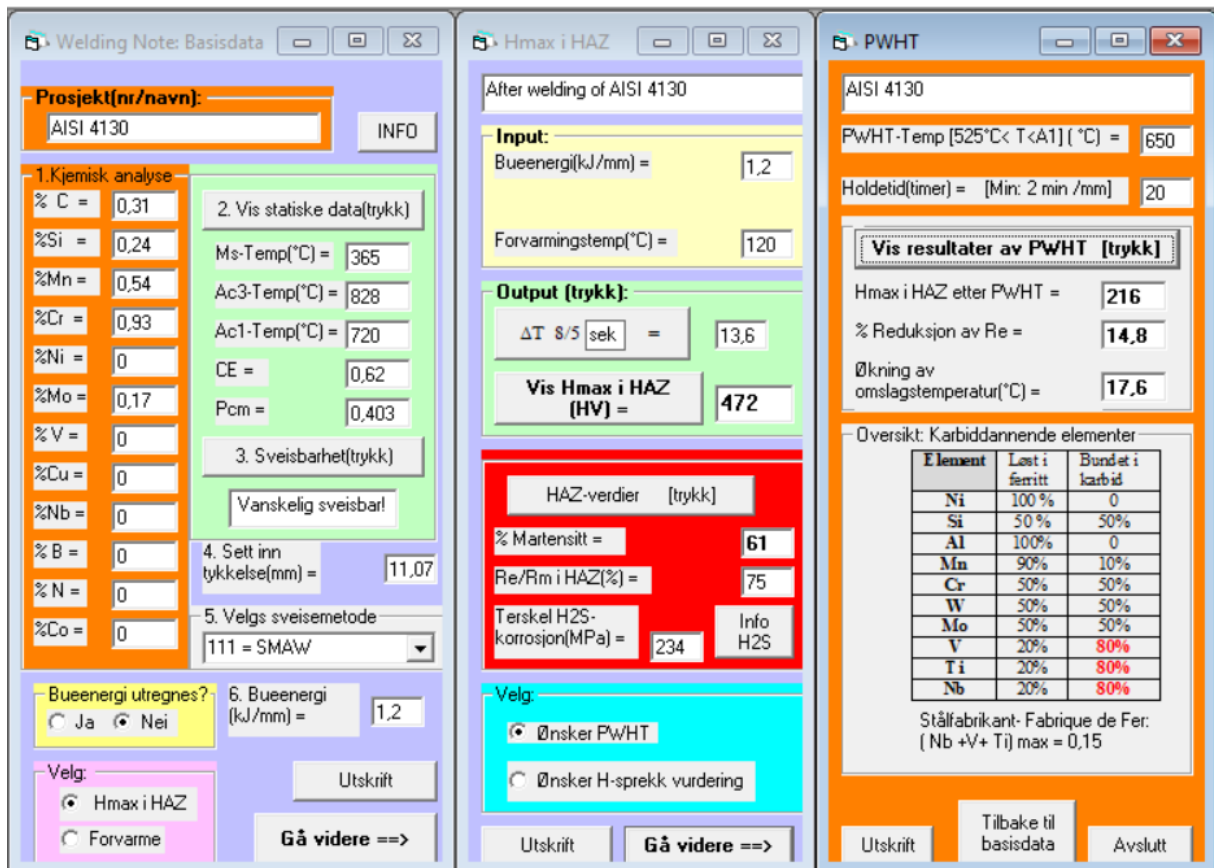
Max Design Pressure at Temperature (See note 02)					
Pressure (Barg)	517.0	517.0	517.0	517.0	517.0
Temperature (Deg. C)	-29	38	50	80	90

Figure 26: Specific design pressure from Piping Class Sheet KX10MH.

5.2. Hardness data

The hardness data in this study was taken from the study done by Dimitri Rybakov “*Post weld heat treatment of welded low alloyed steel pipes*”[1], due to current restrictions performing tests in the lab; the Vickers hardness data from this study is found in Appendix B. The steel pipes that were tested were the same as in this study AISI 4130, and the PWHT procedures were 650°C and 705°C with a holding time of twenty minutes for both procedures. Before welding, the samples were also preheated to a temperature of 120°C.

En programvare fra CorroWeld a.s. (Org. nr. 986 646 965) : Welding Note © A.T.(Rev:2016)



Welding Note: Basisdata

Prosjekt(nr/navn): AISI 4130

1. Kjemisk analyse

% C =	0,31
% Si =	0,24
% Mn =	0,54
% Cr =	0,93
% Ni =	0
% Mo =	0,17
% V =	0
% Cu =	0
% Nb =	0
% B =	0
% N =	0
% Co =	0

2. Vis statistiske data(trykk)

Ms-Temp(°C) = 365
Ac3-Temp(°C) = 828
Ac1-Temp(°C) = 720
CE = 0,62
Pcm = 0,403

3. Sveisbarhet(trykk)

Vanskelig sveisbar!

4. Sett inn tykkelse(mm) = 11,07

5. Velg sveisemetode
111 = SMAW

Bueenergi utregnes? Ja Nei

6. Bueenergi (kJ/mm) = 1,2

Velg:
 Hmax i HAZ
 Forvarme

Utskrift Gå videre ==>

Hmax i HAZ

After welding of AISI 4130

Input:
Bueenergi(kJ/mm) = 1,2
Forvarmingstemp(°C) = 120

Output (trykk):
 ΔT 8/5 sek = 13,6
Vis Hmax i HAZ (HV) = 472

HAZ-verdier (trykk)

% Martensitt = 61
Re/Rm i HAZ(%) = 75
Terskel H2S-korrosjon(MPa) = 234 Info H2S

Velg:
 Ønsker PWHT
 Ønsker H-sprekk vurdering

Utskrift Gå videre ==>

PWHT

AISI 4130
PWHT-Temp [525°C < T < A1] (°C) = 650
Holdetid(timer) = [Min: 2 min /mm] 20

Vis resultater av PWHT (trykk)

Hmax i HAZ etter PWHT = 216
% Reduksjon av Re = 14,8
Økning av omslagstemperatur(°C) = 17,6

Oversikt: Karbiddannende elementer

Element	Løst i ferritt	Bundet i karbid
Ni	100%	0
Si	50%	50%
Al	100%	0
Mn	90%	10%
Cr	50%	50%
W	50%	50%
Mo	50%	50%
V	20%	80%
Ti	20%	80%
Nb	20%	80%

Stålfabrikant: Fabrique de Fer: (Nb +V+ Ti) max = 0,15

Utskrift Tilbake til basisdata Avslutt

Figure 27: Calculation of the effects of welding and PWHT of previous study done in Weld Note.

5.3. Welded Steel pipe

The steel pipe studied is of a low-alloy AISI 4130 steel. The chemical composition of the steel pipe is presented in Figure 110 in Appendix E and the certificates for the welding electrodes are found in Appendix F and Appendix G. The properties of the AISI 4130 steel before welding are determined by the heat treatment obtained from the manufacturer. It is the hardening which gives high strength and hardness (depending on temperature and whether it is cooled down in water / oil / emulsion), then time and temperature of tempering that decreases strength and hardness and provides increased toughness. Thus, the properties of the base material are mainly determined by the heat treatment before welding.

The pipe in this study has an outer diameter of 66.33 mm and a wall thickness of 11.07 mm as can be seen from the material certificate in Figure 110 in Appendix E.

Table 1: Chemical composition of AISI 4130 steel from material certificate.

%C	%Si	%Mn	%Cr	%Ni	%Mo	%V	%Cu	%Nb	%B	%N	%Co
0.31	0.24	0.54	0.93	0	0.17	0	0	0	0	0	0

Material parameters from material certificate for the pipe:

- Yield strength, $R_e = 645 \text{ MPa}$
- Tensile strength, $R_m = 745 \text{ MPa}$
- Elongation, $\% = 22$ (Min 16)
- Hardness, HRC (Max 22) = 20 HRC (238 HV)

The material data for the steel pipe in this study that was not taken from experiments or material certificate was:

- Modulus of elasticity, $E = 2.1 \times 10^5$
- Poisson's ratio, $\nu = 0.3$
- Density of the material, $\rho = 7,8 \text{ g/cm}^3$
- Strain rate for simulations, $\dot{\epsilon}^{pl} = 0.1$
- Stress triaxiality, $\eta = 0.33$
- Tensile strain, taken from the pre-study[10] = 68% of total elongation.

<<The material in this study is considered to be isotropic >>



Figure 28: Photo of the type of welded steel pipe under study [1].

In this study, the modeled heat-affected zone (HAZ) is defined as the combination of CGHAZ and FGHAZ explained from theory. In general, when welding steel, HAZ will have a zone that has been heated above A_1 and therefore consists of untempered martensite; basically, this is an area that is hardened but not tempered. This is what the PWHT is going to take care of it is essentially a tempering of the martensite in HAZ so that it becomes more tough and ductile. It is generally unfortunate to have a zone in a component that is very brittle.

This study will simulate the pipe using two given electrodes of different strengths provided by MHWirth, to see what effect this might have on the results. The material certificates of the electrodes are found in Appendix F and G, where in this study the weak electrode refers to the OK 48.08 and the strong electrode refers to OK 74.86 Tensitrode electrode. The material of the electrodes is not tested in this study; the material data is taken from the electrode data sheets. The chemical composition and relevant material parameters are as follows:

Table 2: Chemical composition of the “weak” OK 48.08 electrode found in the certificate.

%C	%Si	%Mn	%Cr	%Ni	%Mo	%V	%Cu	%Nb	%B	%N	%Co
0.06	0.4	1.2	0	0.8	0	0	0	0	0	0	0

Material parameters from Material certificate for the electrode:

- Yield strength, Re = 540 MPa
- Tensile strength, Rm = 600 MPa
- Elongation, % = 26

Table 3: Chemical composition of the “strong” OK 74.86 Tensitrode electrode found in the certificate.

%C	%Si	%Mn	%Cr	%Ni	%Mo	%V	%Cu	%Nb	%B	%N	%Co
0.06	0.37	1.74	0.04	0.83	0.34	0	0	0	0	0	0

Material parameters from Material certificate for the electrode:

- Yield strength, Re = 630 MPa
- Tensile strength, Rm = 720 MPa
- Elongation, % = 25

5.4. Test specimens

In total there were 10 uniform samples tested in this study. All were round specimens with an outer diameter of 10mm and same gauge length of 35mm. The uniform samples had a geometry as shown in Figure 29 (B); the pipe sample provided by MHWirth is shown in Figure 29 (A). The machine drawings of the specimens are presented in Appendix L. The smallest diameter of the gauge cross section area is set to 5mm for the specimen. The test specimen was heat-treated differently as shown in Table 4, where the material parameters for the heat-affected zone (HAZ) represent samples that were first heated and quenched to form martensite, and the Base metal represents the part of the pipe that is not affected by the weldment but will be affected by the different PWHT procedure. The material parameters for the base metal and HAZ without any PWHT is also extracted, seen from the column “No PWHT”. The experimental procedure will be described in further detail in the next chapter.



Figure 29: (A) Raw steel pipe sample and (B) Uniform test specimens that were tested in this study.

This geometry of the test specimens shall fulfill the following condition from standard E8/8M-08[55]:

- Provide a uniform cylindrical gauge portion.
- Provide a uniform strain distribution over the whole gauge portion.
- Allow the extensometer to measure the strain without interference or slippage.

Table 4: Heat treatment matrix for the tensile tested specimens and number of specimens.

SECTION	NO PWHT	PWHT 600°C	PWHT 650°C	PWHT 705°C	PWHT 746°C
Base metal	2	0	1	1	1
HAZ	1	1	1	1	1

As explained from theory the PWHT temperature should always be set below the actual tempering temperature and below the A1 temperature. However, to investigate the effect of an incorrect PWHT procedure with too high a temperature, in this study experiments and simulations set on the exact temperature from the ASME B31.3 standard, as shown previously in Figure 23 and Figure 24, will be performed.

5.5. Hydraulic Tensile test machine

The test machine used for laboratory experiments in this study, was an Si-Plan 25 kN load cell. Tension tests can be performed with this test machine in a regular tension test configuration. The test speed was given as strain rate and was calculated by stroke relative to the parallel area of the test specimen. Stroke is the displacement of the crosshead on the machine measured by a linear transducer. Stroke and load are the only direct output from the test machine, but time and extension are calculated by the computer that runs the machine along with the data from extensometer.

5.6. Extensometer

For tests conducted with extensometer, an Si-Plan axial extensometer (model: 676212) applicable for gauge lengths 25 - 30mm was used. The Extensometer can read from -10% in compression to +100% in tension. The grips on this model are clip-on and were connected directly on to the specimen's gauge area on the uniform samples.



Figure 30: Si-Plan Extensometer.

5.7. Digital sliding gauge

A digital sliding gauge was used for measuring the steel specimens before and after the experimental tests.



Figure 31. Digital sliding gauge.

5.8. Furnace

To heat treat the steel samples, a Naber programmable furnace was used in order to achieve an even heating and cooling rate of max 335°C/h.



Figure 32: Furnace used for heat treatment of the steel samples.

5.9. Numerical simulation tool

The software used for numerical simulation by Finite Element Method (FEM) was Abaqus (Abaqus/Explicit). The simulation of damage was performed by using the Ductile Damage model, and the damage model was used to compare the strength and integrity of the welded pipe affected by the different material properties of the chosen PWHT procedures.

To evaluate the metal structure in the weld and heat affected zone, the program Weld Note from CorroWelds AS was used. This program can plot the corresponding microstructures in a Schaeffler diagram in terms of chemical composition of the base metal of the pipe and electrode that is joined. The corresponding A1 and A3 temperatures can also be determined by plotting the chemical composition of the base metal that is supposed to be joined, as seen from Figure 27.

Microsoft Excel was used to process the data and for calibrations and preparation of results being presented.

6. Methods

The task in this study is to evaluate possible effects of different PWHT procedures on the pipe strength and integrity, due to the change to the PWHT procedure made in the ASME Code, 2014 edition. Where the temperature range was changed from 704 - 746°C to 650 - 705°C for low-alloy steels such as AISI 4130 steel pipes, this is shown in Figure 23, Figure 24 and Figure 25 in Case [33, 54]. The method of analyzing the effect of this change is by using the available damage model Ductile Damage in the numerical finite element program Abaqus and adding material data for the different modeled sections of the weld. Abaqus is available under a student license at the University of Agder application base "Innsia".

Different methods were used to extract the necessary information to answer the research question in this study. This chapter present the methods to solve the research question.

A literature study was used to obtain the correct knowledge about the subject of heat treatment and tempering of welded steel, become familiar with the different design parameters for the welded steel pipe under investigation in this study. The methods for experimental tensile testing were performed according to the two standards E8/E8M – 08 for uniform monotonic test specimens [55]. The numerical simulations were performed using the software program Abaqus in Explicit mode (Abaqus/Explicit) to simulate the different damage accumulations from the respective PWHT procedures.

The point of the literature study is to gain an insight both into the work that has been done earlier and the results that have been presented until now on the subject. This is also important in terms of basic knowledge of the different behaviors of steel under welding and heat treatment, and what can be expected in terms of results. It has also been essential to aquire the latest and most relevant literature on the subject from reliable sources like books and standards.

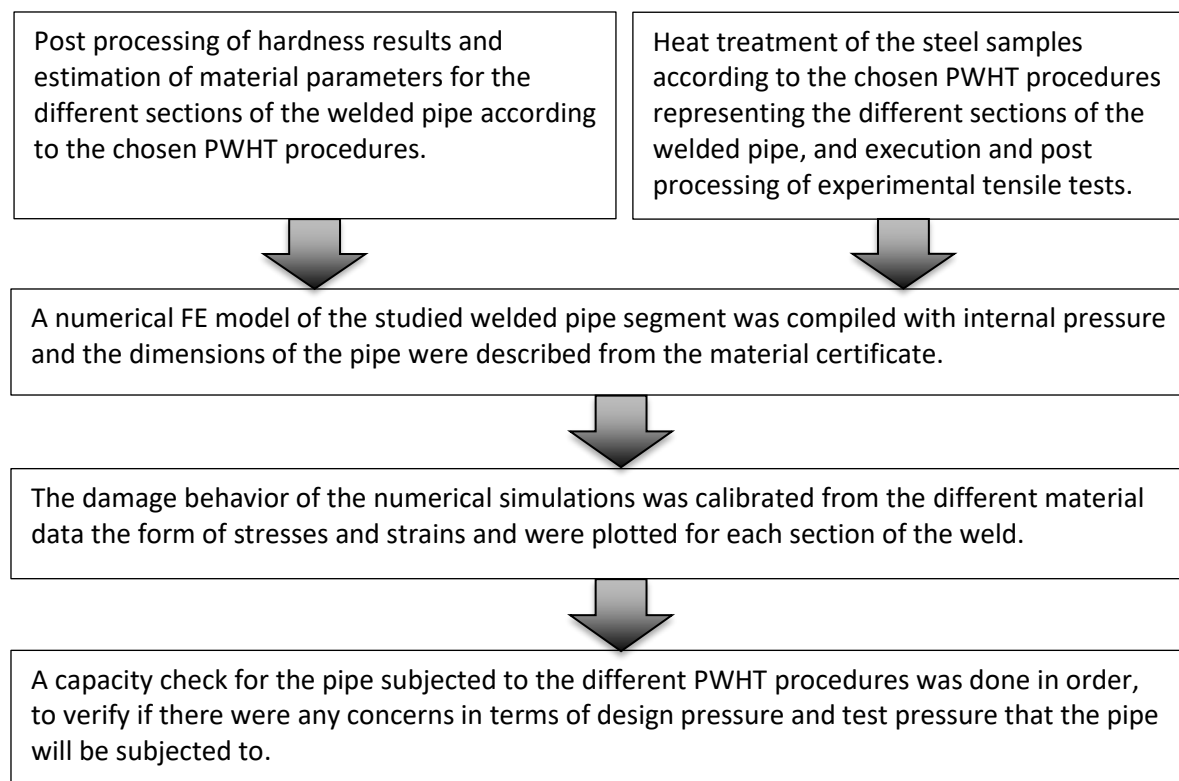
Two different approaches to deciding the material data of the welded pipe have been employed; the first using the data taken from material hardness tests and material certificates, the second using material data from experimental tensile tests for a more realistic behavior for comparison.

Two different electrodes have also been used, and these will be compared in terms of strength due to the proposed pressure load. The placement of fracture and burst pressure as well as the stresses of the modeled pipe will be of interest when analyzing the different PWHT procedures.

Different numerical formulas for material parameters after heat-treatment and for hardness were investigated so that this could be plotted numerically in Abaqus. This was so the behavior of the damage accumulation and plasticity of the welded pipe could be simulated realistically. For the calibration of the material behavior in Abaqus, the use of stresses and strains was taken from the material certificates for the pipe; material data for HAZ was set by the experimental hardness test done in the previous study done by Dimitri Rybakov[1]. One of the hardness-based simulation was performed by estimation, using Holloman-Jaffe for prediction of hardness and strength of HAZ after PWHT temperature of 600°C.

The experimental tensile tests were performed to extract more applicable material data in order to simulate the behavior of the welded pipe to a greater degree of accuracy. Elongation and behavior of the specimen's gauge area was extracted using the extensometer. The results from the experimental tests were plotted numerically in Abaqus in the same way as for the estimated material data from the use of hardness data. The results from using both the hardness data and the tensile test data have also been compared in terms of accuracy in predicting damage behavior and strength.

This chapter is thus divided into different sections in order to describe the continuous development of the study in an orderly manner. It describes the work methods used. Both the numerical and the experimental setup are explained, in addition to the extraction and post processing of the results. Due to the continuous development in the research, the respective methods was conducted as follows:



6.1. Material parameters based on hardness

In order to achieve an estimation of the possible results from the different PWHT procedures a numerical investigation of the possible outcome was performed. The results from hardness tests for the same pipe and material from the previous study by Dimitri Rybakov[1] was used and processed; the results from the previous study are found in Appendix B. Three different PWHT temperatures were tested to investigate the possible strength of the pipe based on hardness of the HAZ for the welded pipe segment. The chosen temperatures that were 600°C, 650°C and 705°C as these are the highest and lowest temperatures for the ASME B31.3-2014 and below the A1 temperature. From the results in Appendix B shown in Table 12, the mean values for HAZ were calculated by using equation (30), which was affected by the chosen PWHT procedure.

$$\bar{x} = \frac{1}{N} \sum_{i=1}^N x_i \quad (30)$$

In order to predict the hardness of the tempered martensitic structure of HAZ after PWHT of 600°C, the Holloman-Jaffe equation (4) was used together with the hardness tests for the PWHT temperatures of 650°C and 705°C. The results from this procedure are showed in Table 14 together with the estimation of the yield and tensile strength of HAZ after PWHT using equation (12) and (15) shown in Table 15. The elongation at fracture for HAZ was estimated by using equation (16) from theory and the results from the calculated tensile stress using equation (15). The formula chosen for identification of the strength hardness relation was based on comparison of the strength and hardness from the material certificate and the formulas in chapter 3.14, and is shown in Table 5.

Table 5: Comparison of hardness vs strength using hardness of 20HRC (238HV) as reference.

Formula	Yield strength, [MPa]	Tensile strength, [MPa]
Reference strength from material certificate	645	745
Tabor, Equation (6)	-	819.971664
J.R. Cahoon, Equation (11) and (10)	506.4	803.8
Pavlina and Van Tyne, Equation (12) and (13)	593.788	788.892
O. M. Akselsen, G. Rorvik, M. I. Onsjøen and Ø. Grong, Equation (14) and (15)	390.9	740.3

To find HV hardness from HRC hardness Figure 102 in the Appendix A was used. The holding time t was set according to ASME: 1/25 hour/mm but not less than 15min, and in this study set to 20 minutes. To calculate the hardness after PWHT of 600°C using Holloman-Jaffe, the c value was set to 19.5 as the recommended constant for Holloman-Jaffe, as explained from theory. To verify the phases present in the weldment before PWHT, the Schaeffler diagram was used in order to check what phases were present after welding for the material heated above the A3 temperature. As can be seen from Figure 33, the base metal of the pipe has a martensitic structure, as does the fusion zone or weld metal, albeit with some minor inclusions of ferrite.

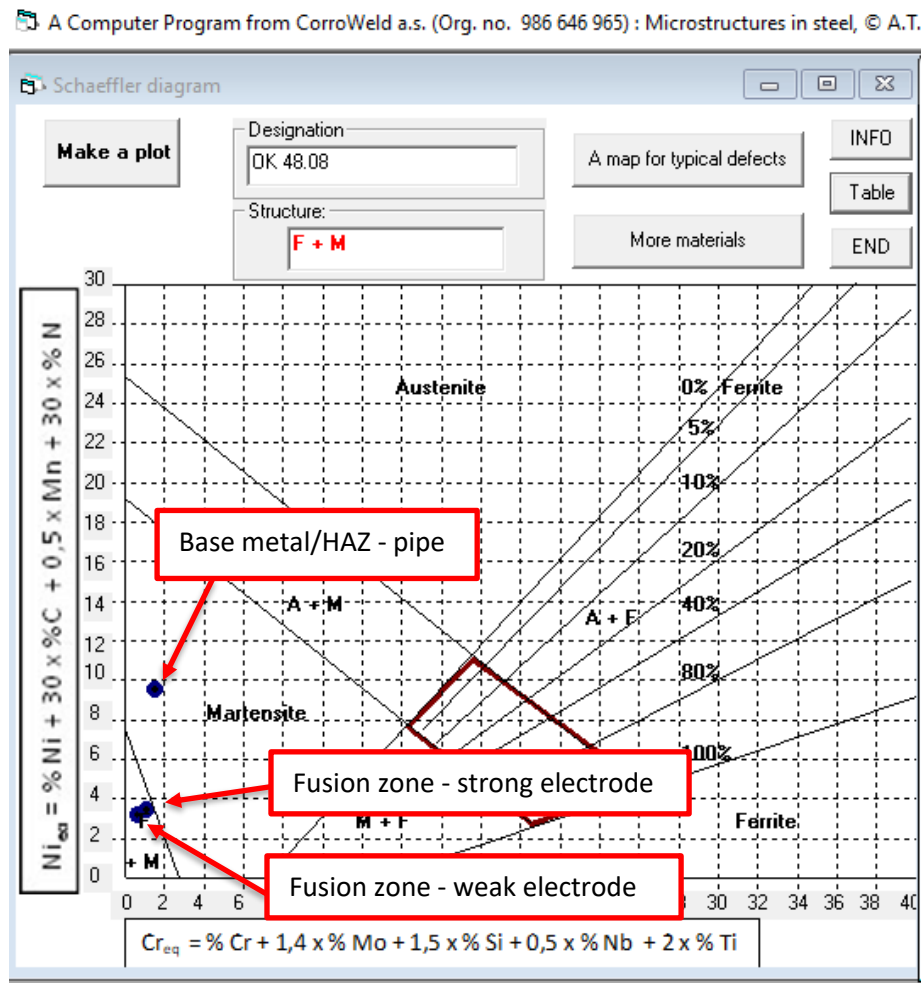


Figure 33: Check of microstructure in the welded area of the weld before PWHT using the Schaeffler diagram.

Table 6: Test Matrix based on hardness and numerical approximation.

	Temperature, [°C]	Holding time, [min]
PWHT 1	600	20
PWHT 2	650	20
PWHT 3	705	20

The PWHT was in the allowable range of the Holloman-Jaffe tempering limit of 100°C - 710°C; the procedures are shown in Table 6.

The resulting estimated yield and tensile strength was then plotted in Abaqus as parameters for the HAZ region; the material parameters for the base material as well as the weld metal was set to the same as in the material certificate. For the simulations based on hardness, the base material affected by the PWHT was set to have the same material characteristics as the rest of the pipe; see Figure 39. This is due to the minor difference in hardness that was measured, as can be seen from certificate (238 HV) and the results from the hardness tests as seen in Table 13 (241,8 and 243,8 HV). Fracture strain was calculated according to ductility from material certificates for the base metal and the electrodes as also shown in the case chapter and in the material certificate found in Appendix E, F

and G. The yield strain was thus found by using Hooks law, $\sigma = E\varepsilon$. The tensile strain was found by calculating the relation between the engineering tensile strain and engineering fracture strain from the experimental data from the Pre-study[10] by the following relation:

$$u_{tensile} = 1 - \left(\frac{\varepsilon_{fracture} - \varepsilon_{tensile}}{\varepsilon_{fracture}} \right) \quad (31)$$

By using this expression, the engineering tensile strain was found to be approximately 68% ($u_{eng,tensile}$) of the %elongation to fracture, and from this result the stress strain relations were plotted as shown in Table 16 and Figure 53 for the base material taken from the material certificate. The stress strain results from the strength-hardness data were calculated accordingly, and are found in Appendix H. The engineering fracture stress was set to the same as the yield stress estimated from the results from the Pre-study, where the engineering fracture stress was approximately the same as the yield stress [10]. From these results the true stress and strains were calculated using equation (26) and (27) from theory. The different true stress strain diagrams for each of the material parameters used for the different PWHT procedures are shown in Figure 54, Figure 55 and Figure 56.

For calibration of the damage accumulation, a data plot was made with true strain that was adjusted with zero at yield point up to ultimate strength by subtracting the strain point from yield to ultimate strength with the original true yield strain. This plot with original true stress and adjusted/effective true strain was then plotted in tabular form in Abaqus as the calibrated material plasticity data, this is shown in Figure 59. To calibrate the behavior after necking for the Ductile damage model that represents the damage stress state, the Ramberg and Osgood equation (7) was used to determine the strength coefficient K together with the strain hardening exponent, which is found by using equation (8). Figure 58 in the results shows the calibration lines that were set to match as close as possible by plotting the corresponding K and n values. This best fit calibration was done by trial and error due to the use of the linear damage evolution from necking to final failure used in Abaqus; see Figure 22 in the theory. The K and n values is decide the stress-strain curve with progressive damage degradation in linear form, as seen in Figure 21 and Figure 22 in theory. As can be seen from theory, the concept of damage assumes the growth of voids in the material that reduces the effective area. When the effective area thus equals the nominal area, the material fails. The failure criteria are decided by the calibration of the fracture strain, triaxiality and displacement at failure, as can be seen plotted in Figure 57.

As the damage accumulation after necking is different for the different PWHT procedures as well as each of the different zones of the welded pipe, the K and n values were calibrated separately for the HAZ and the base material and fusion zone so that the actual accumulation line could follow the experimental force-displacement line as close as possible. It must be mentioned that the K and n values decide the behavior and start point after necking of the damage curve; start point is shown as $D=0$ in Figure 21. The results from the processed predicted hardness data is found in chapter 7.1 and the numerical results from these material parameters is found in chapter 7.3 and 7.4 for the weak and strong electrode.

The primary focus of the validation was on failure pressure and stresses for the pipe subjected to the chosen PWHT procedure. The %deviation of the results of the pressure and stresses is calculated using the equation (32).

$$\%Deviation = \frac{S_1 - S_{reference}}{S_{reference}} \cdot 100 \quad (32)$$

Table 22 show a comparison between the burst pressure for the weak vs strong electrode relationships for the FEA model and the six simulations tested, and Table 23 shows the resulting stresses extracted from the fracture of the pipe. Figure 72 and Figure 73, show the comparison between the burst pressure and max stresses in the fracture and HAZ area of the simulated model and the weak vs strong electrode results of the FEA model for the pipe segment.

6.2. Design of experiments

To verify the results and simulation done for the material data based on hardness test, experimental tensile tests of the different sections of the weld were performed, as shown in the previous chapter in Table 4. Heat treatment for four different PWHT procedures have been performed; the three previous PWHT procedures and one additional above the A1 temperature. The additional procedure is chosen as a worst-case scenario and is set to the highest PWHT temperature of 746°C according to the ASME B31.3[54] code before the update that was introduced in 2014, shown in Figure 23. The procedures for heat treatment and experimental tensile tests were performed as follows:

6.2.1. Preparation of specimens

The first stage was the cutting and milling process of the raw steel pipe sample so it would achieve the desired shape and geometry according to the standard. Exact drawings of the two types of specimen to be tested were made before the milling process could start; see Figure 127 in Appendix L. After the milling process, the specimens were polished and checked for defects that could affect the tensile tests, such as notches and deformations on the surfaces of the specimens.



Figure 34: Cutting of the raw steel pipe sample.

6.2.2. Heat treatment procedure

To extract the material parameters of a pipe subjected to welding and the chosen PWHT procedures the steel samples had to be provided with the same material characteristics. The different material characteristics that were tested, previously shown in Table 4, were created by heating and cooling the processed steel specimens accordingly. To create the heat-affected zone (HAZ) of the weld, the samples representing this section had to acquire the same properties before PWHT as the HAZ would have after welding. This was done by heating samples to 850°C, above the A3 temperature taken from Weld Note and with a holding time of 30 minutes for full austenization. The heating was set to heat as fast as possible to 850°C. In order to create martensite, the samples were quenched in water; the procedure is also visualized in Figure 35.

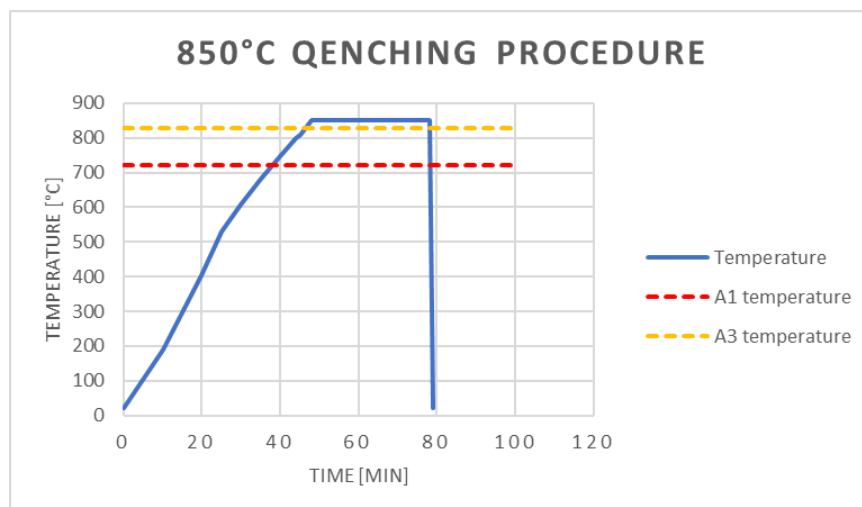


Figure 35: Time tempering procedure for creation of martensite.

Table 7: Heat treatment to make the martensitic test specimens.

	Temperature, [°C]	Holding time, [min]	Heating rate, [°C/h]	Cooling rate, [°C/h]
Martensitic test samples representing the HAZ	850	30	Approx. 996	quenched

When the martensitic samples representing the HAZ were made, the HAZ and the unaffected samples representing the part of the base metal affected by the PWHT were then heated together. The sets of samples heat treated simulating the two PWHT sections of the pipe was shown in Table 4; where four different heat treatments representing the PWHT procedures that was performed according to as shown in Table 8.

Table 8: Heat treatment matrix for the test specimen.

	Temperature, [°C]	Holding time, [min]	Heating/Cooling rate, [°C/h]
PWHT 1	600	20	Max. 335
PWHT 2	650	20	Max. 335
PWHT 3	705	20	Max. 335
PWHT 4	746	20	Max. 335

The heat treatments were also logged accordingly for approximately each 50°C, and time and temperature were noted to log the heat treatment procedures; the noted time temperature is found in Appendix M. The heating rate was easier to control in the furnace compared to the cooling rate as seen from the PWHT diagrams, shown in Figure 36. Each of the PWHT heating and cooling rates was logged with the time and temperature as shown. The heating rate that was logged was approximately 320°C/h and satisfied the requirement of 335°C/h in ASME B31.3 [32].

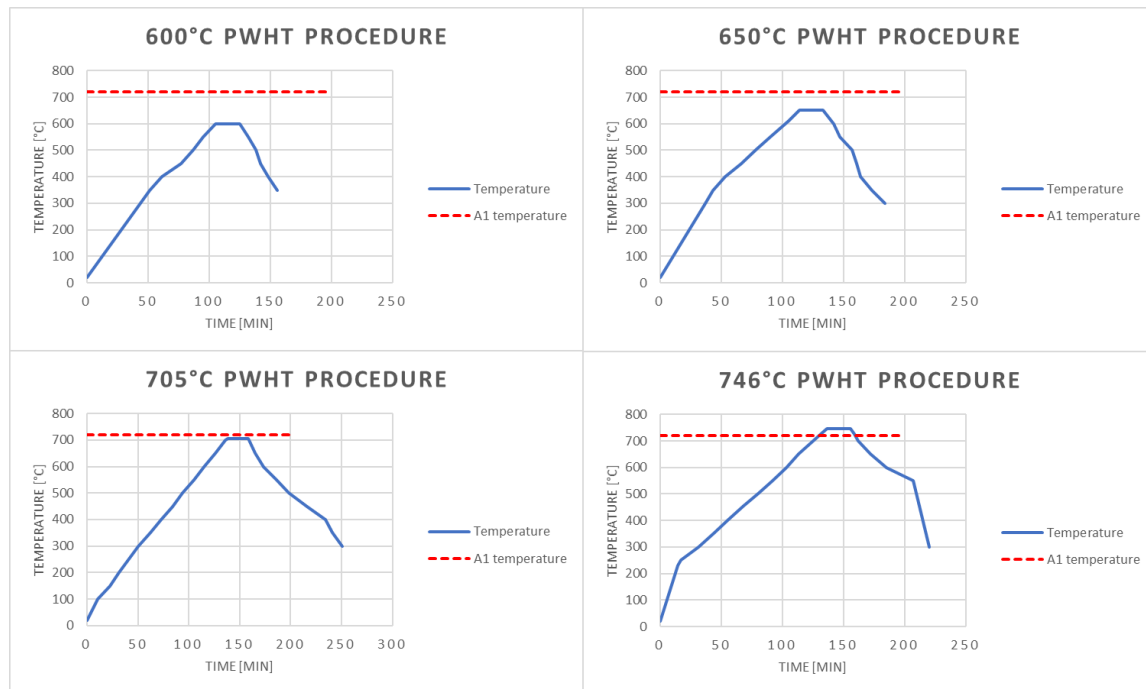


Figure 36: PWHT diagrams.

6.2.3. Quality assurance of tests

Before the actual test was performed, a check-list was made with routines for tensile testing; see Figure 125 in Appendix K. The routines were made so the quality and execution of the test would be done in the same manner for all the tested specimens. Along with the check-list for routines under testing, a sheet was also made to note information and data for the different tests performed on each specimen; see Figure 126 in Appendix K. Test specimens were labeled with appropriate numbers for reference so it would be easy to identify the specimens with the results; see Figure 124 in Appendix K. The test specimens were also carefully measured to determine the deformations, stresses and strains acting on the specimens during the experimental tests before testing.

6.2.4. Calibration of equipment

The testing machine was tested and checked before any test could begin. The wedge grip alignment was controlled on the testing machine to ensure that there was a minimum introduction of bending stress on the specimens under testing, see Figure 37. The test machine was also warmed up and aligned to normal operating temperature and positioned to minimize errors that could result from transient conditions. The testing machine was set up in a manner so that zero force indication signifies a state of zero force on the specimens.

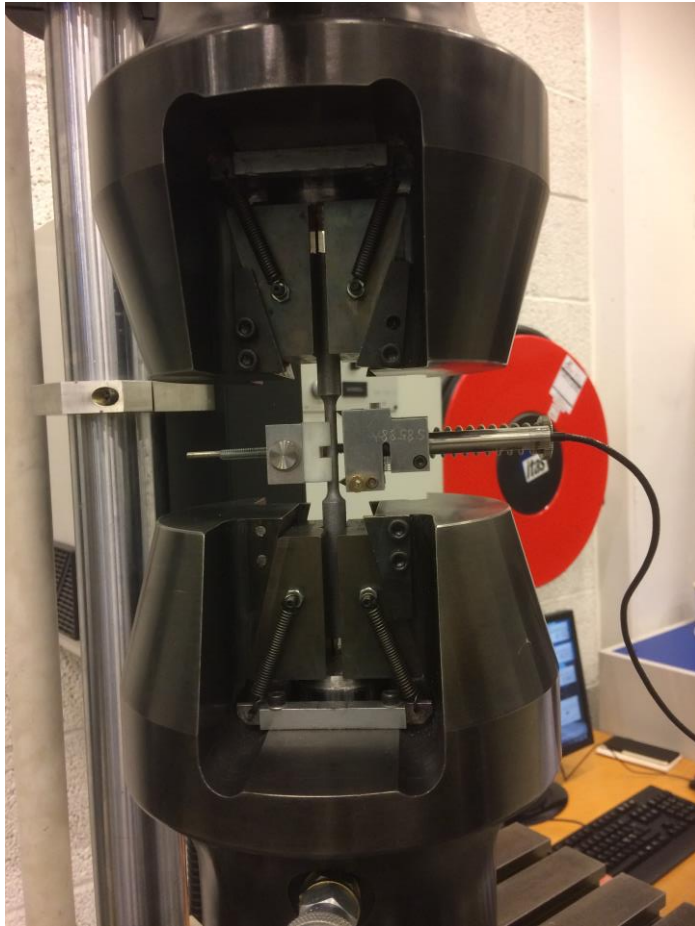


Figure 37: Tensile test frame with a specimen attached in the grip and extensometer attached to the specimen.

Before the actual mechanical test could begin, preparation of extensometer and computer for the handling of results was also checked. A clip-on extensometer was used to measure axial strain during tensile testing; see Figure 37. The gauge length (35 mm) for computing strain is a parameter intrinsic to the clip-on extensometer. The extensometer measures elongation during the testing to insured minimal drift, slippage and instrument hysteresis. It directly measured the axial strain on the gauge section of the specimens.

The strain-measuring systems, including the extensometer and its associated electronics, shall be accurate to the range of the induced strain under testing. The geometry of the contact zones and the pressure exerted by the extensometer on the specimen shall be such that they prevent slippage of the extensometer but do not damage the specimen.

6.2.5. Execution of experiments

The specimen was fit to the test machine and centered with appropriate alignment and direction of force. Maximum load is recorded during testing and noted in the information sheet made for each specimen; see Figure 126 in Appendix K. After fracture of the specimens, final diameter was measured. The tensile test was performed with a loading rate of 0.039 mm/s. This ensured that the specimens elongated plastically with a steady phase to final fracture. All testing was done at room temperature according to standards.

The test data file from the extensometer records the time, strains and the corresponding force applied to the specimen taken from the machine. This data is further postprocessed to extract the yield stress and stress at tensile strength of the uniform monotonic test specimens. The displacement is used to obtain the average strain throughout the specimen. The force applied is used to calculate the stress in the cross-sectional area of the specimens.

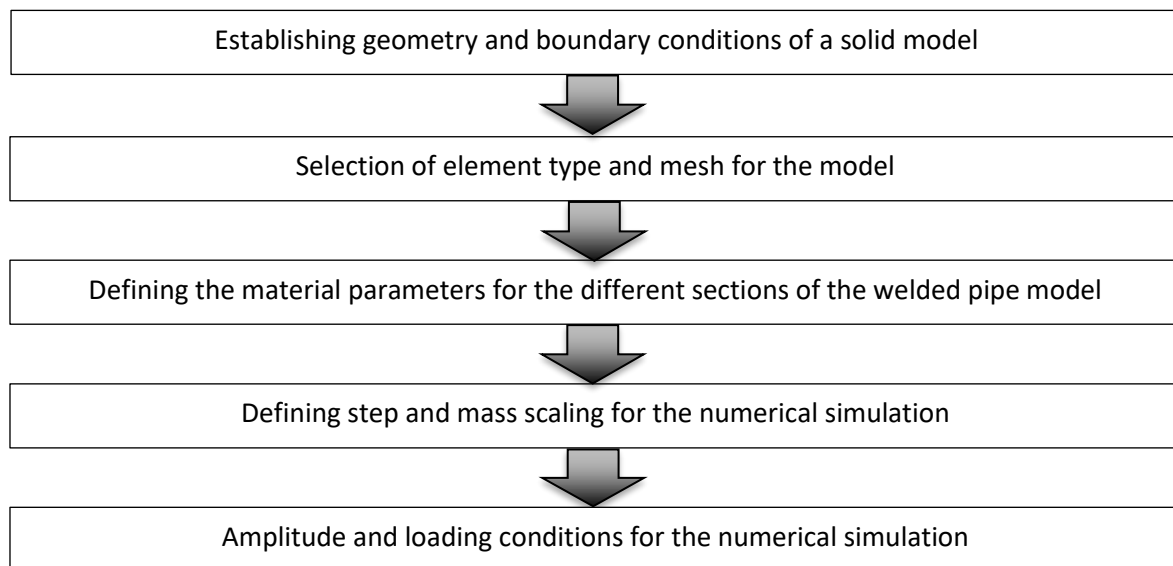
6.2.6. Processing of experimental results

The yield stresses, tensile stresses, engineering stress-strain and true stress-strain data was calculated in Excel for input parameters for the numerical analysis. The decomposition of true stress-strain curve, thus effective stress-strain, was used for calibration of the plasticity in Abaqus Explicit. This was done by converting the engineering stress-strain values to true stress-strain values using equations (24), (25), (26) and (27). This is also according to the Abaqus manual, according to which the effective true stress-strain from yielding to tensile stress should be used as input parameters[50]. The true fracture strain was determined from the fracture point from the true stress strain curves from the tensile experiments and was plotted in Abaqus.

A data plot was made with true strain that was adjusted with zero at yield point up to ultimate strength by subtracting the strain point from yield to ultimate strength with the original true yield strain. This plot with original true stress and adjusted/effective true strain was then plotted in tabular form in Abaqus as the calibrated material plasticity data, and is done in the same way as for the previous hardness data shown in Figure 59. The calibration of the behavior after necking and determining the strength coefficient K for determining the damage stress state, was also done in the same way as explained for the hardness data, and is shown in Figure 58. As seen from results, the specimen representing the heat affected base material was fracturing close to the edge of the extensometer so the strain after necking became distorted; so the damage behavior was thus assumed to be the same as for the base material after necking for this specimen; see Figure 80 and Table 26. Numerical simulations were then performed for the weak and strong electrode as for the material data based on hardness tests; this is found in chapter 7.2.2. and 7.2.3.

6.3. Numerical setup and procedure

As mentioned in this study as mentioned Abaqus Explicit is the software for the numerical simulation for finite element analysis (FEA). The geometry of the pipe was modeled according to the dimensions in Figure 109 in Appendix E. The purpose of the finite element analysis (FEA) in this study was to assess the strength and integrity of a welded pipe segment as affected by different PWHT procedures. The results from the numerical simulations with the use of material parameters estimated for the different PWHT procedures, as well as the difference between the two approaches for calibration of material data, will be analyzed and compared. The results will also be compared to the design pressure and possible test pressure described from the ASME B31.3; the procedure for the pressure check is explained in further detail later in this chapter. The establishment of the finite element model (FEM) was done as follows:



6.3.1. Geometry and boundary conditions.

The pipe was modeled as a three-dimensional solid part, as seen in Figure 38. The total length of the pipe model was set to one meter with the weld in the center. This should be appropriate to obtain good results for the weakest part of the pipe and at the same time not have too large a model that will use unnecessary much simulation time. The type of boundary conditions used are found in Figure 40, and Figure 48 displays a visualization of the applied boundaries where the arrows function as applied pressure load, corresponding to displacement in the described direction in addition to the corresponding loading conditions and amplitudes.

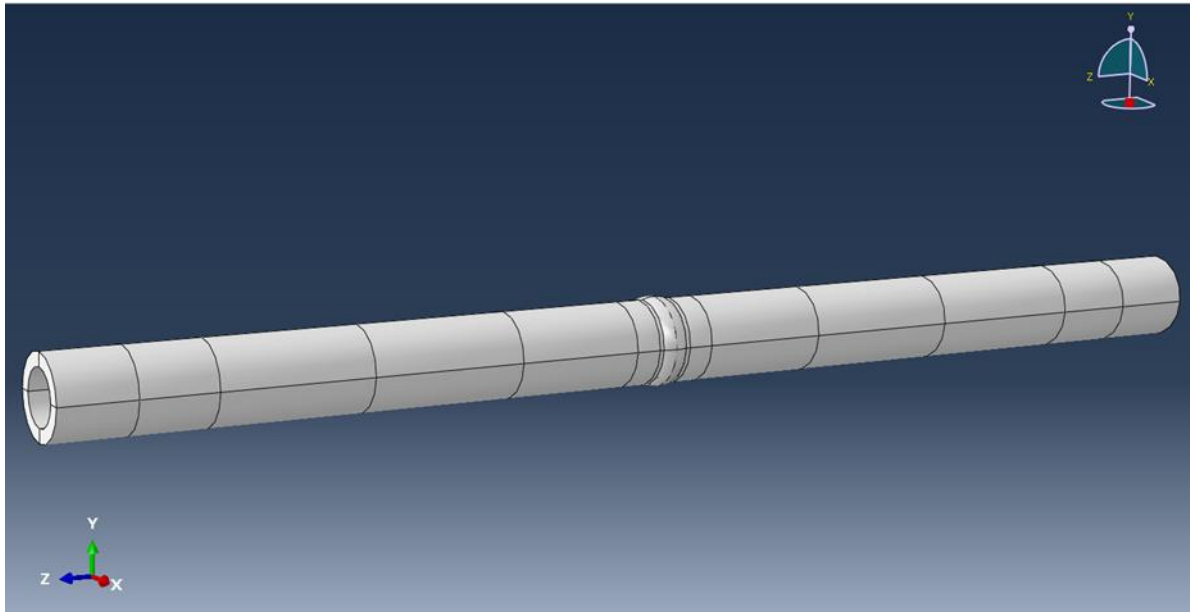


Figure 38: Modeled welded pipe segment.

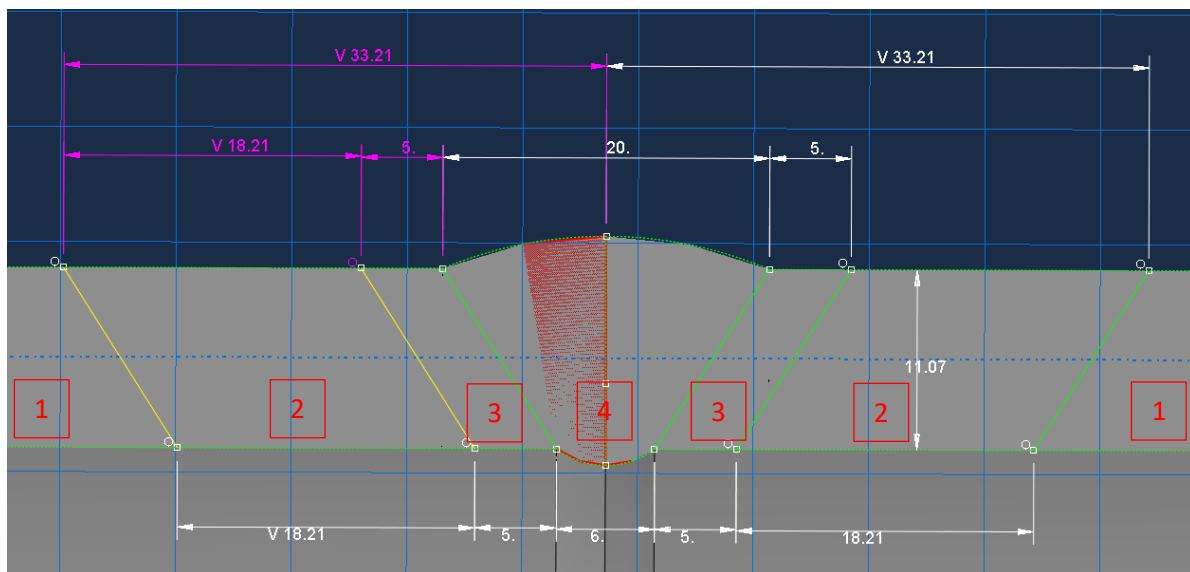


Figure 39: Design of the welded connection of the pipe. 1): unaffected base material, 2): PWHT base material, 3): HAZ, 4): Melted zone (Weld metal from electrode).

The melted weld zone and HAZ were defined by measures taken from the test piece shown in Figure 105 in Appendix B. Where the reinforcement height was set to 2mm and the root depth was set to 1mm for the weld in the simulated model, taken from the average measures of the welded pieces in Figure 105. The base metal affected by the different PWHT procedures was defined by the ASME code B31.3[32] by minimum width of local heat treatment of three times the wall thickness of the pipe from center of the weld as explained in theory.

Table 9: Boundary conditions for the welded pipe segment analyzed for pressure in Abaqus.

Type	X	Y	Z
Boundary Condition (Z= 500)	-	-	(U1=U2=U3=UR1=UR2=UR3=0)
Boundary Condition (Z= -500)	-	-	(U1=U2=U3=UR1=UR2=UR3=0)

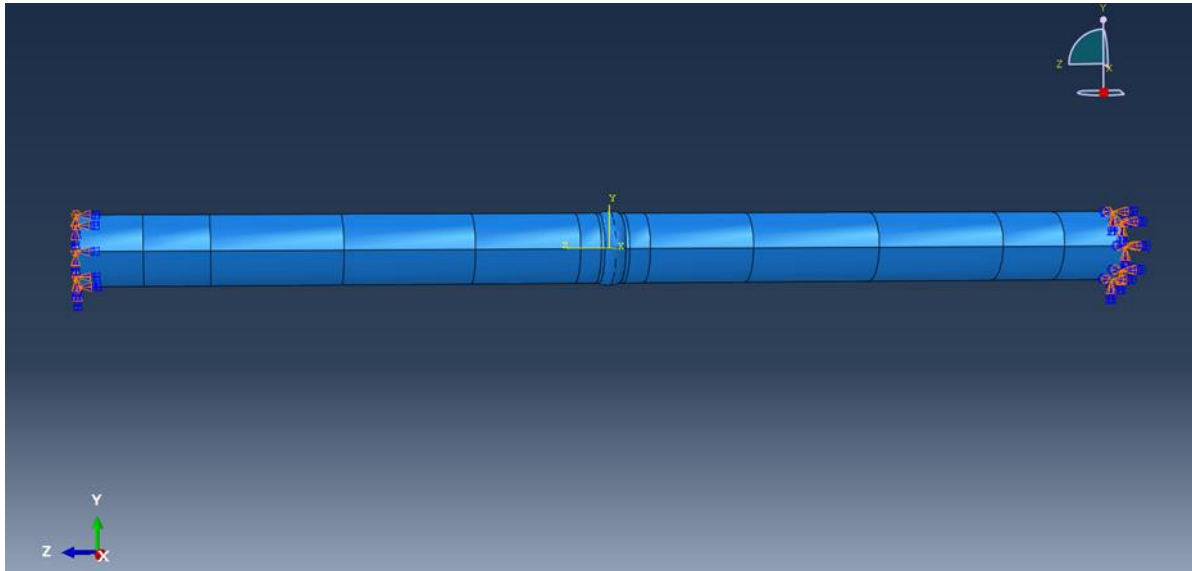


Figure 40: Applied boundary conditions for the modeled pipe segment.

6.3.2. Meshing of elements

Meshing plays a crucial role in the analysis of finite element modeling and analysis, so a verification of the mesh was performed in terms of a sensitivity study of the pipe model before analysis of the PWHT procedures. Four different mesh configurations have been tested and are presented in Table 10; Coarse, Medium, Fine and Extra fine mesh. The Hex element type was chosen for the pipe model and partitioned to achieve a more improved mesh and to reduce the running time. Both the pipe and weld region can be expected to have plastic deformations and failure, as the material defined for the regions will have different strength. Due to this only a global mesh has been considered in this study as failure is not concentrated in one specific area of the pipe, due to the chosen loading conditions and difference in material strength, see Figure 41 and Figure 44. A study has been carried out to clarify the sensitivity due to mesh refinement where a pressure deviation of approximately 2% has been considered sufficient. As defined in the pipe model, Table 10 describes the preselected element sizes of the models, where the size is approximately the same in both directions with some adjustments due to curvature and thickness.

It is important that the element size of the model where plastic deformation takes place are small enough to represent the deformation and placement of fracture in a reliable manner, even if it may not be small enough to show in detail the necking and plasticity of the fracture initiation. Linear interpolation between nodes also indicates that the element size must be small in order to properly represent the curved deformation.

Table 10: Element sizes in sensitivity procedure.

Coarse mesh [mm]	Medium mesh [mm]	Fine mesh [mm]	Extra fine mesh [mm]
10	7	5	4

The FE model of the pipe segment was modelled with a chosen mesh size of 5mm due to computational time and a reliable representation of the placement of failure and behavior of the pipe under the loading conditions.

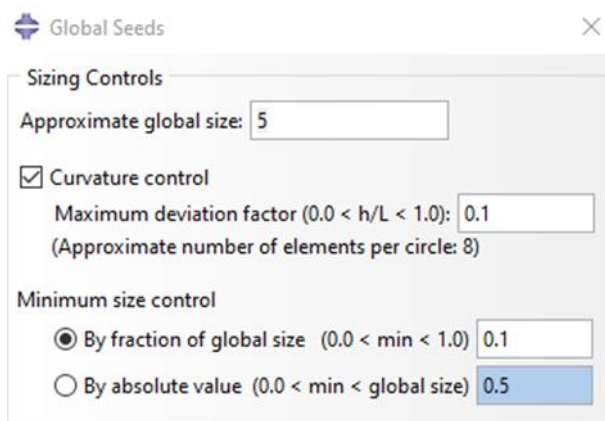


Figure 41: Mesh definition for the pipe segment.

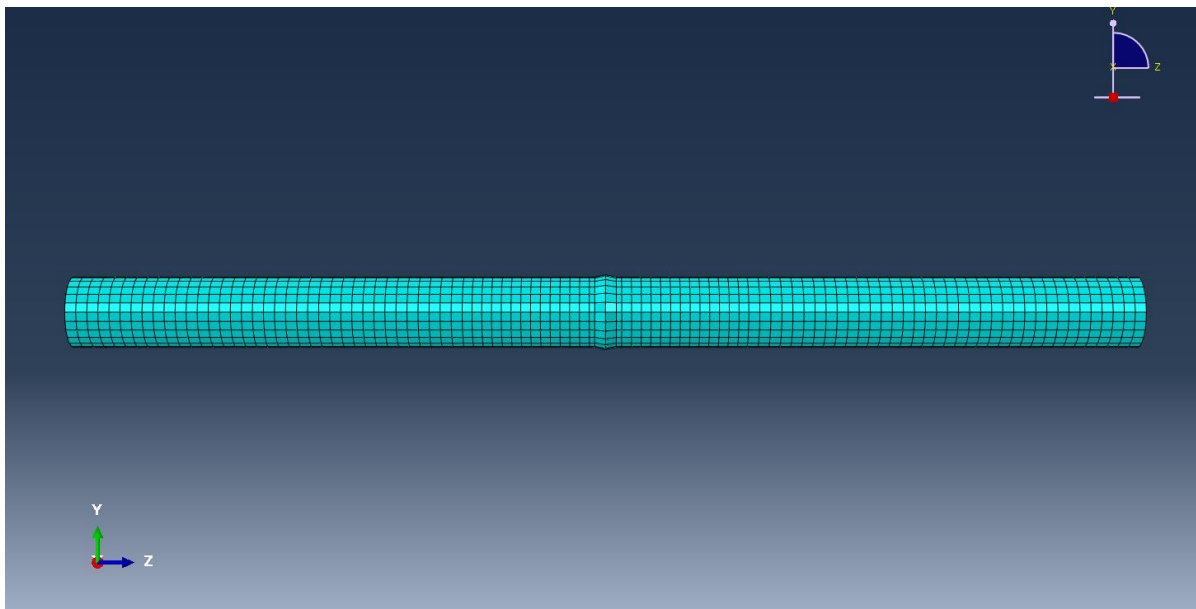


Figure 42: Applied 10mm mesh on the modeled pipe segment.

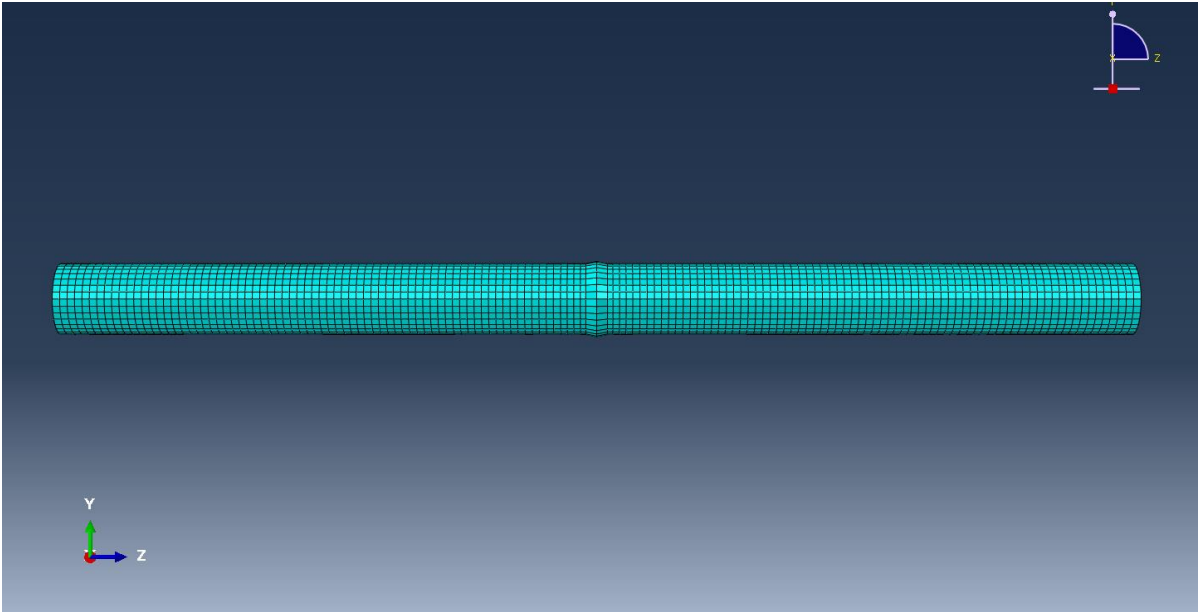


Figure 43: Applied 7mm mesh on the modeled pipe segment

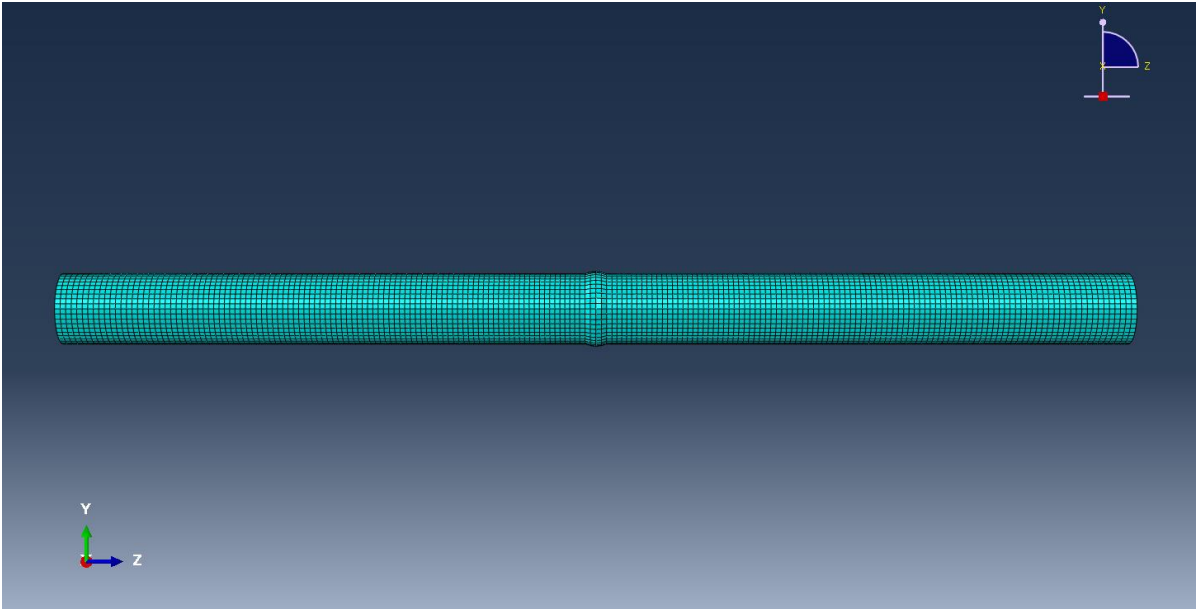


Figure 44: Applied 5mm mesh on the modeled pipe segment.

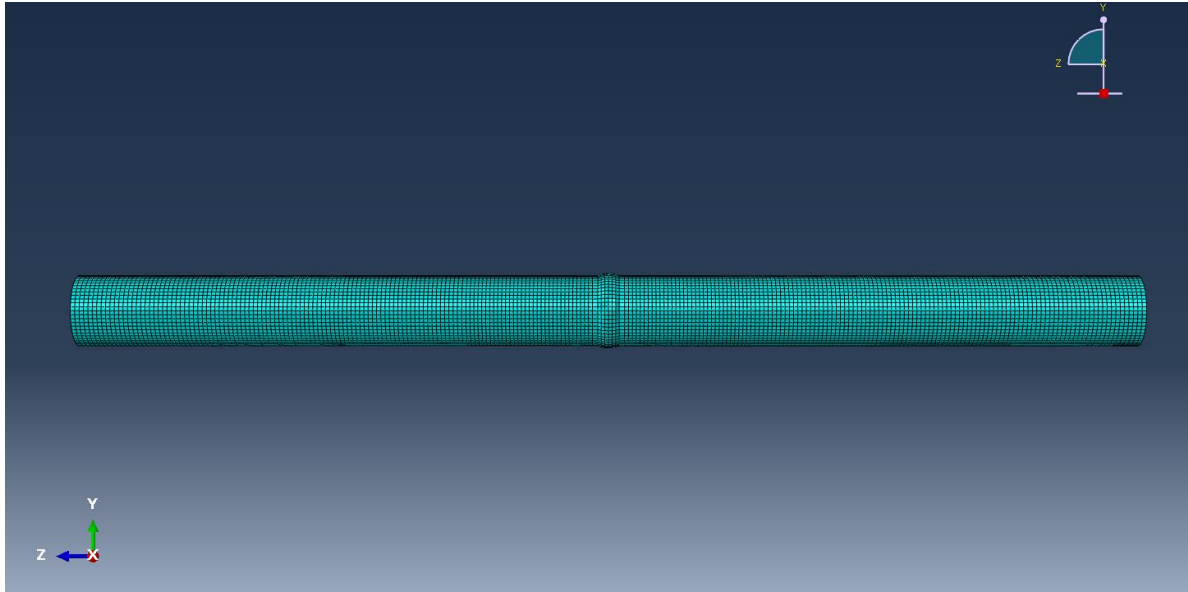


Figure 45: Applied 4mm mesh on the modeled pipe segment.

6.3.3. Material parameters in Abaqus

In this study, the Ductile Damage model was used for the numerical simulation in Abaqus, where the stress -rate, stress triaxiality and true stress and strain parameters for Ductile Damage were added, see Table 17 and Figure 57. The plasticity data from the effective true stress strain curve is added into the calibration option to the modeling of the plasticity material behavior in Abaqus, as seen in Figure 59. The damage parameters for Ductile Damage were calibrated and added in the form of fracture strain ϵ_f , stress triaxiality η and strain rate $\dot{\epsilon}i$. Strain rate was set to 0.1mm/s for the FE model, see Figure 57. The stress triaxiality was set to 0.33 as described in previous chapter and the same as in the Pre-study[10]. The isotropic hardening model in Abaqus was employed for the simulations and the yield criterion is the Von -Mises yield function was the same as that used in the Pre-study [10].

6.3.4. Step definition and Mass scaling

Dynamic Explicit analysis was used for the comparison of the damage initiation criteria chosen in this study. To reduce the running time, a time period of 1 second has been used, as shown in Figure 46, and the Mass scaling Factor was set to 10 as shown in Figure 47, as the most suitable factor done by trial and error in terms of stability and reduction of time, as described from theory.

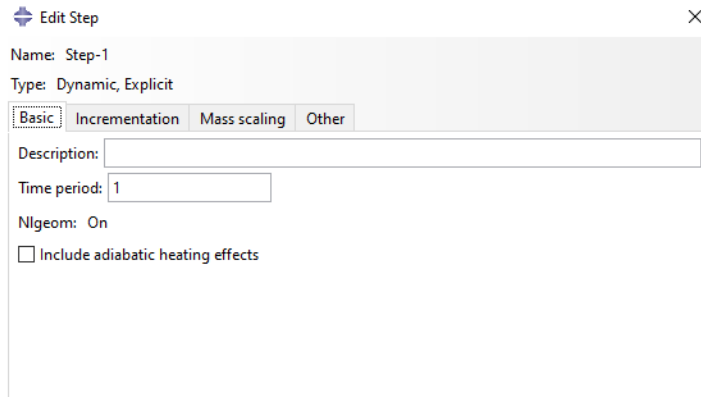


Figure 46: Time period of the defined step.

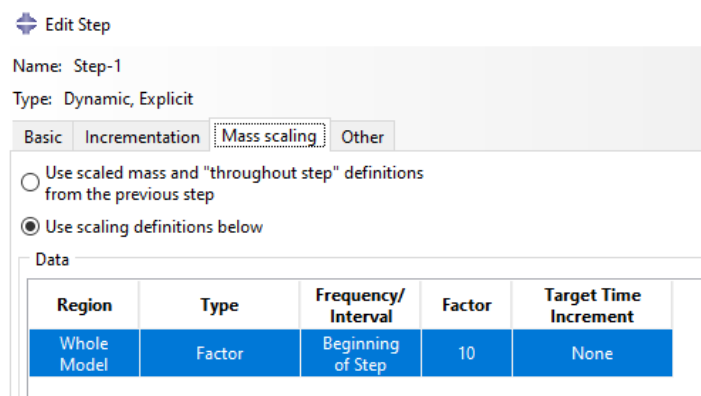


Figure 47: Mass scaling for the numerical simulation of the pipe model.

6.3.5. Amplitude and loading

The sets of numerical simulation for comparison are shown in Table 11 . The chosen loading condition was set to be pressure until failure, since the piping system referred to in this study is a high-pressure offshore piping system. The loading condition should give a good indication of the weakest part of the pipe subjected to the different PWHT procedures simulated in this study. The loading was run until failure. The burst pressure, max stresses applied on to the pipe, and placement of the failure were of interest. Table 11 shows the different numerical simulations performed based on material data from the hardness tests and experimental tensile tests.

Table 11: Numerical pressure simulation matrix for the Hardness and Tensile test properties.

	PWHT procedure 600°C	PWHT procedure 650°C	PWHT procedure 705°C	PWHT procedure 746°C
Weak electrode	*Hardness/Tensile	Hardness/Tensile	Hardness/Tensile	Tensile
Strong electrode	*Hardness/Tensile	Hardness/Tensile	Hardness/Tensile	Tensile

*Hardness estimated by using Holloman-Jaffe.

The Field output request was set with appropriate time points of 1000, set for the chosen amplitude that was run. The History output request was set at each time points, n , chosen. The amplitude plots and amplitudes are shown in Figure 49, Figure 50 and Figure 51 for the pressure load.

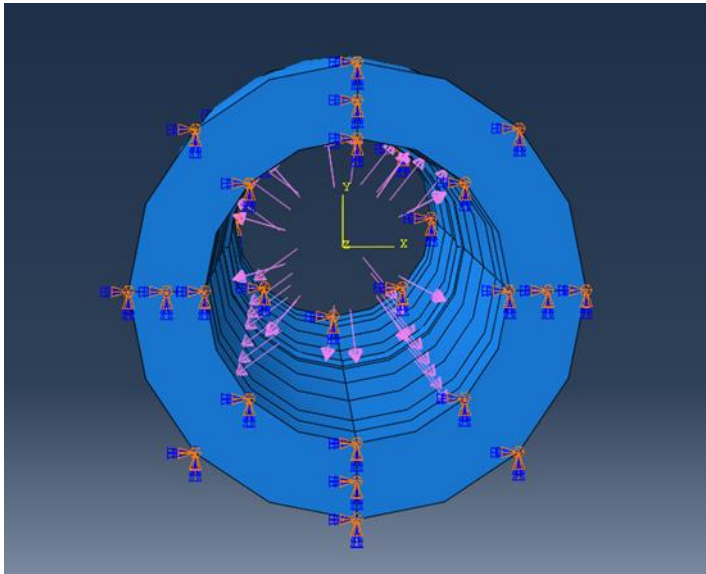


Figure 48: Pressure load applied in the pipe model.

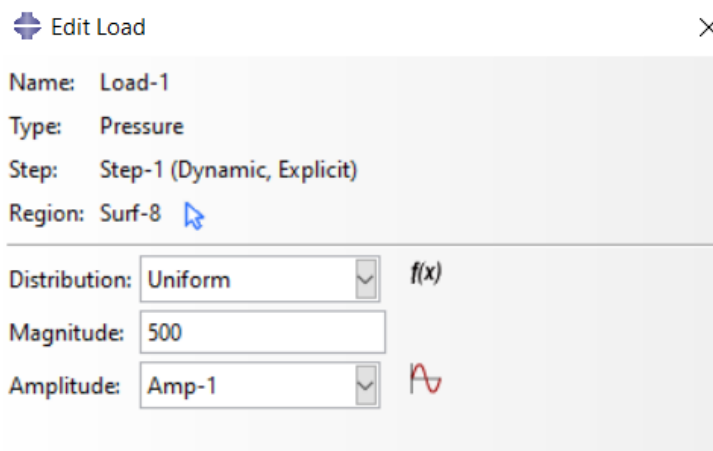


Figure 49: Load definition for the numerical pressure simulation.

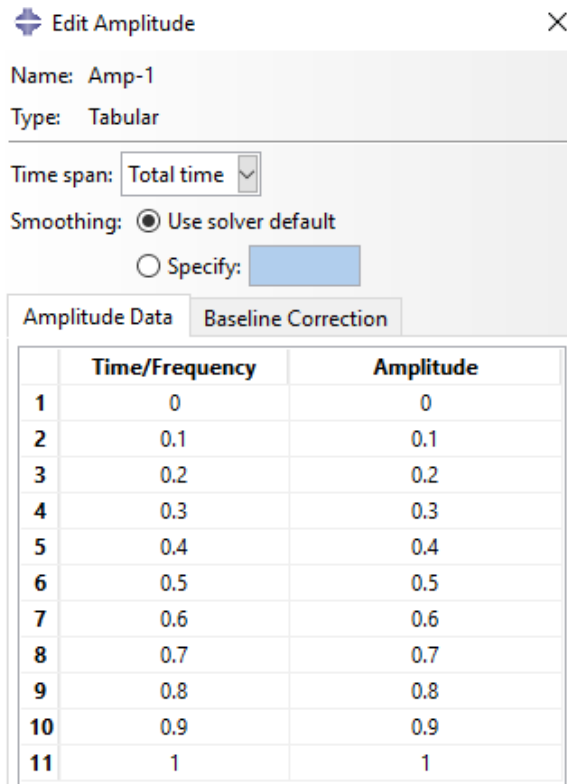


Figure 50: Time- Displacement amplitude for the applied pressure load in Abaqus.

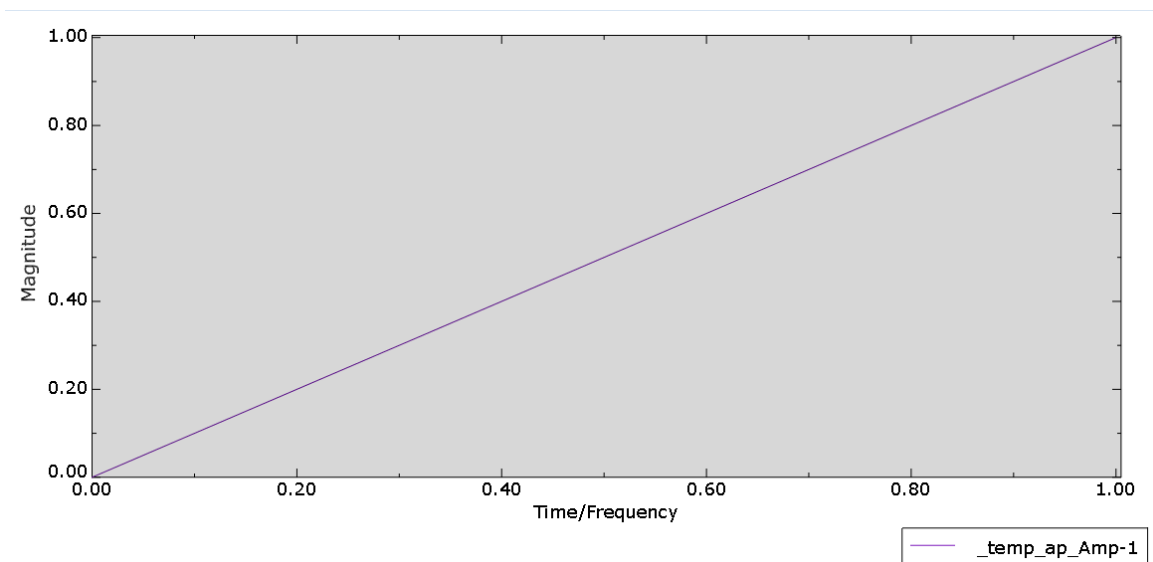


Figure 51: Loading amplitude for the pressure simulations.

6.4. Pressure checks of pipe

The results of the numerical analysis and the design criteria that were set for the pipe were checked in terms of material strength and design capacity according to the ASME B31.3. The design pressure criteria were set according to the given design pressure of 51.7 MPa, and corrosion allowance of 3mm as shown in chapter 5.1. was used to calculate the approximate stress allowance.

The design pressure was then compared against the results from the FEA of the pipe that was affected by the different PWHT procedures. The burst pressure and max stresses were of interest and compared against the design criteria and the highest-pressure loads.

For control of capacity equation (19) and (20), were used to identify the possible load cases applied to the pipe. The check was also performed for the test pressure for the pipe too, as described from theory where equation (21) was used; the resulting test pressure from this was plotted again using equations (19) and (20). The results from the calculations were performed in an Excel sheet and are shown in Table 32, Table 33, Table 34 and Table 35 in chapter 7.6.

7. Results

The purpose of this chapter is to describe and present the results of the tests and experiments in the research. The work is divided into different sections: presentation of sensitivity check, results from calculated hardness estimates for the HAZ, calibration of material, and damage parameters for the numerical simulations based on both hardness tests and experimental tensile tests. Post-processed hardness data extracted from the previous study and the experimental tensile tests done for this study are presented, along with the presentation of the results from the different numerical simulations done for two types of electrodes, together with a comparison of the results. Finally, the results from the pressure check done according to ASME B31.3 are presented for the results from the tensile tests.

7.1. Analysis based on material data from hardness tests

In this section, the results from the post processing and numerical simulations based on extracted and estimated hardness are presented. Also, the mesh sensitivity study done for the modeled pipe section is presented.

7.1.1. Results from calculation of material parameters

Table 12: Calculation of mean hardness values for the different zones of the weld before PWHT, calculated from values shown in Appendix B, the tensile stresses is found by using equation (15).

	650			705		
	Base	Haz	weld	Base	Haz	weld
	244	336	229	250	345	234
	245	349	234	244	345	213
	240	294	218	236	307	201
	246	230	220	245	245	238
	245	232	210	248	233	237
	231	274		240	270	
		273			287	
		253			271	
		235			230	
		226			237	
Sum	1451	2702	1111	1463	2770	1123
Mean	241.8	270.2	222.2	243.8	277	224.6
Tensile Strength	753.7	852.9	685.0	760.7	876.7	693.4

Table 13: Calculation of mean hardness values for the different zones of the weld after PWHT, calculated from values shown in Appendix B, the tensile stresses are found by using equation (15).

		650			705		
	Base	Haz	weld	Base	Haz	weld	
	245	271	239	230	235	216	
	246	277	238	232	230	202	
	244	245	213	226	217	184	
	249	229	212	236	209	194	
	246	231	212	232	202	195	
	227	273		231	248		
		242			213		
		234			216		
		221			208		
		229			209		
Sum	1457	2452	1114	1387	2187	991	
Mean	242.8	245.2	222.8	231.2	218.7	198.2	
Tensile Strength	757.2	765.4	687.1	716.4	672.8	601.1	

Table 14: Material hardness for HAZ using Holloman-Jaffe and hardness tests correlation.

PWHT temperature [°C]	Hp	Hardness (HRC)	Hardness (HV)
600	16.6	31	269.5
650	17.6	28	245.2
705	18.6	25	218.7

To transform from Rockwell scale HRC hardness to Vickers hardness number HV, Figure 102 shown in Appendix A has been used. As seen from Figure 52 the hardness of HAZ subjected to PWHT of 600°C is predicted to be over the H_{max} requirement of 22 HRC (250 HV) for "Sour Service"[30, 31].

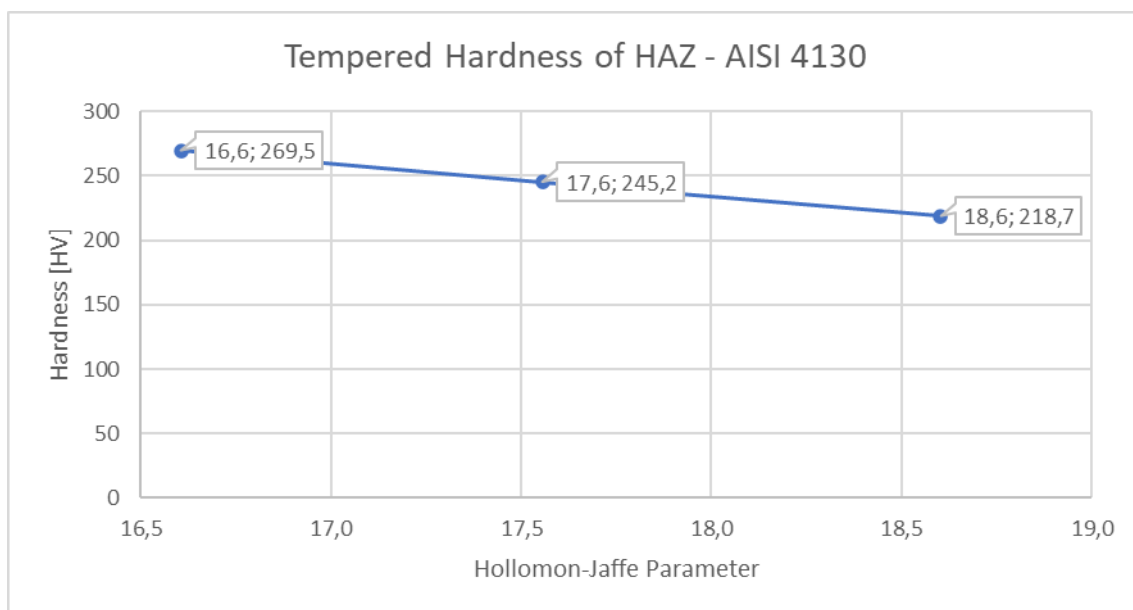


Figure 52: Tempered Hardness of HAZ for AISI 4130 steel - Tempered in 20min, constant $c = 19.5$.

Table 15: Material parameters calculated for HAZ.

PWHT temperature [°C]	Yield strength, [MPa]	Tensile Strength, [MPa]	Fracture strain, A35(%)
600	684.4	850.4	0.125
650	614.5	765.4	0.132
705	538.3	672.8	0.168

Table 16: Stress Strain results for Base-material calculated from material certificate for the pipe.

	Engineering Strength, [MPa]	Engineering Strain, [-]	True Strength, [MPa]	True Strain, [-]
Yield	645.0	0.00307	647.0	0.00307
Tensile	745.0	0.217248	906.8	0.19659
Fracture	645.0	0.32	851.4	0.27763

The stress and strain for all the sections with the different PWHT procedures was found and the stress-strain diagram was plotted as shown in Table 16 and Figure 53 for the base material of the pipe. The rest of the stress and strain data is presented in Appendix H.

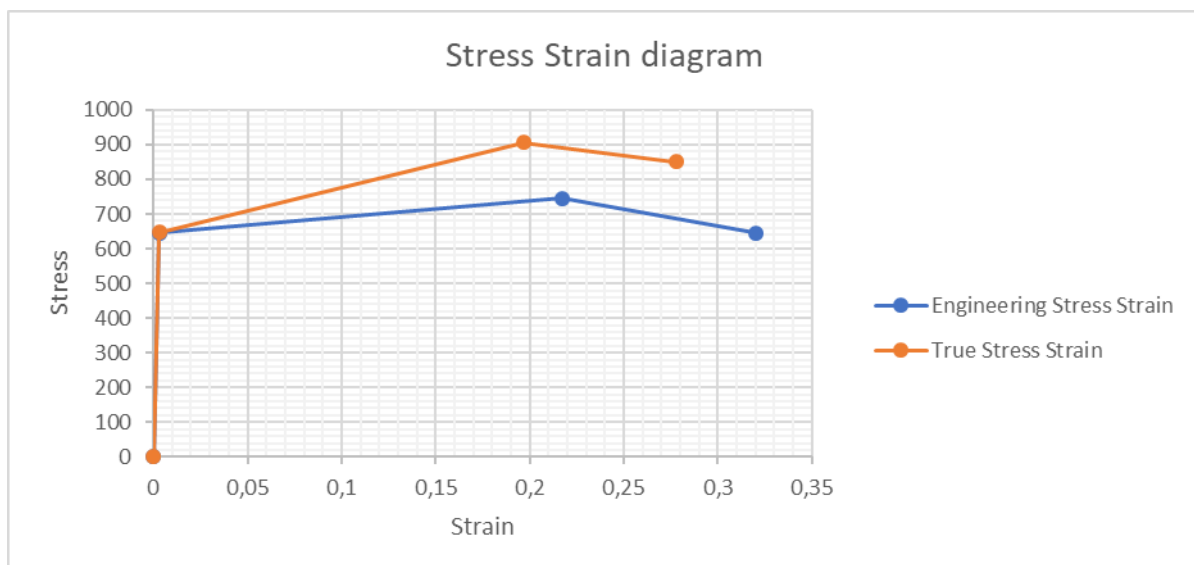


Figure 53: Stress-strain diagram for base material calculated from material certificate for the pipe.

As explained, the different sections of the weld have different material behaviors; Figure 54, Figure 55 and Figure 56 show the different true stress and strain graphs for the different sections of the pipe subjected to each of the PWHTs. We see here that the strength of HAZ is decreasing with the increase in PWHT temperature and that the strain of the HAZ is increasing with an increase in temperature. The true stress and strain for both electrodes used are also shown in the same graphs for comparison.

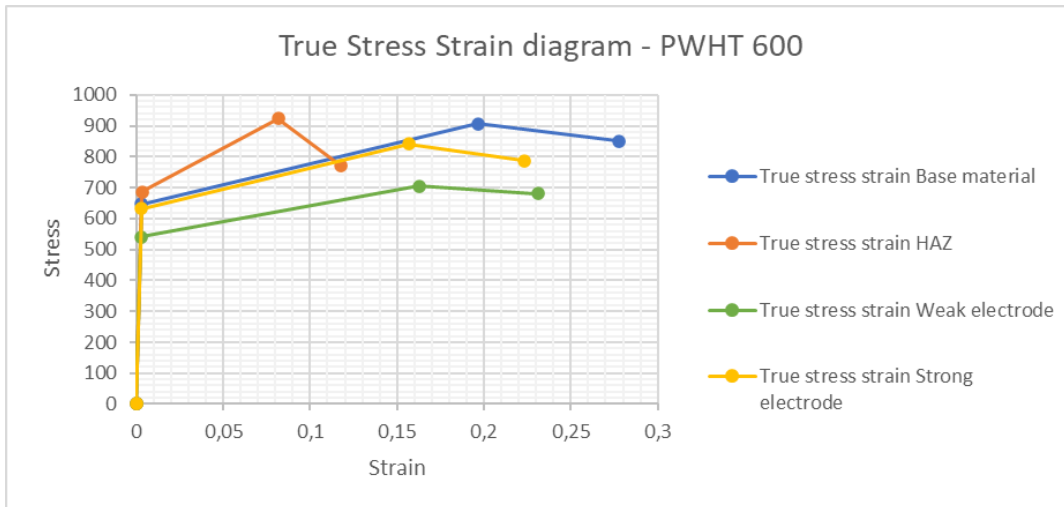


Figure 54: True stress-strain diagram for PWHT 600.

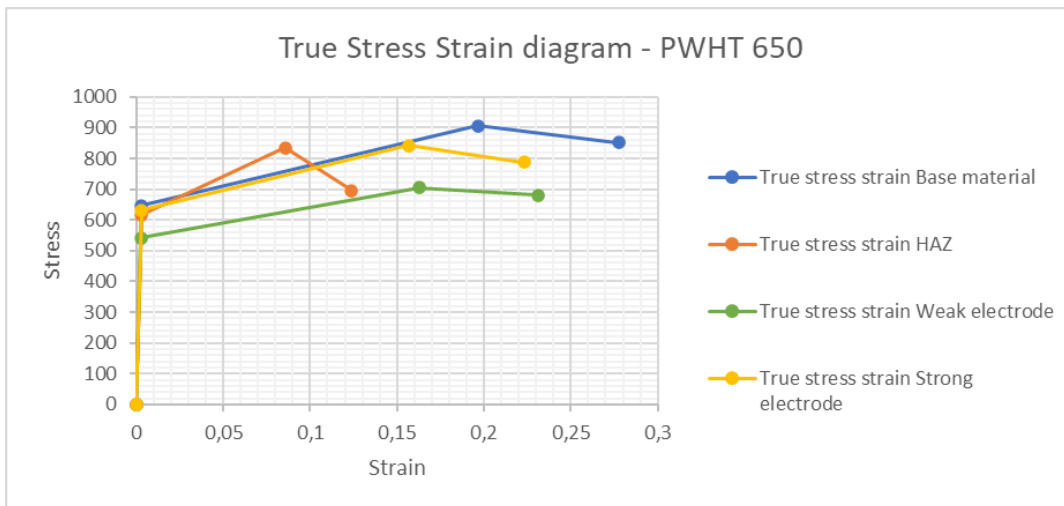


Figure 55: True stress-strain diagram for PWHT 650.

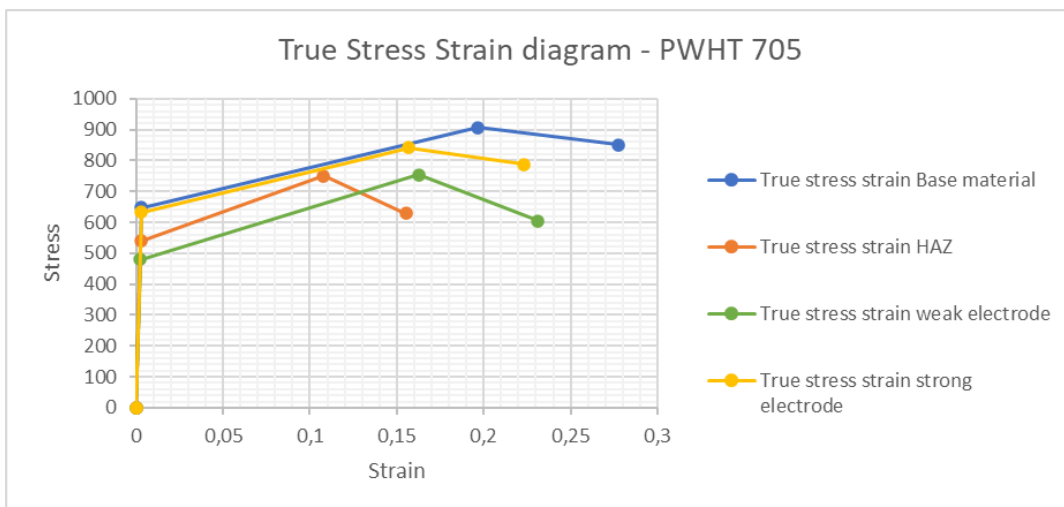
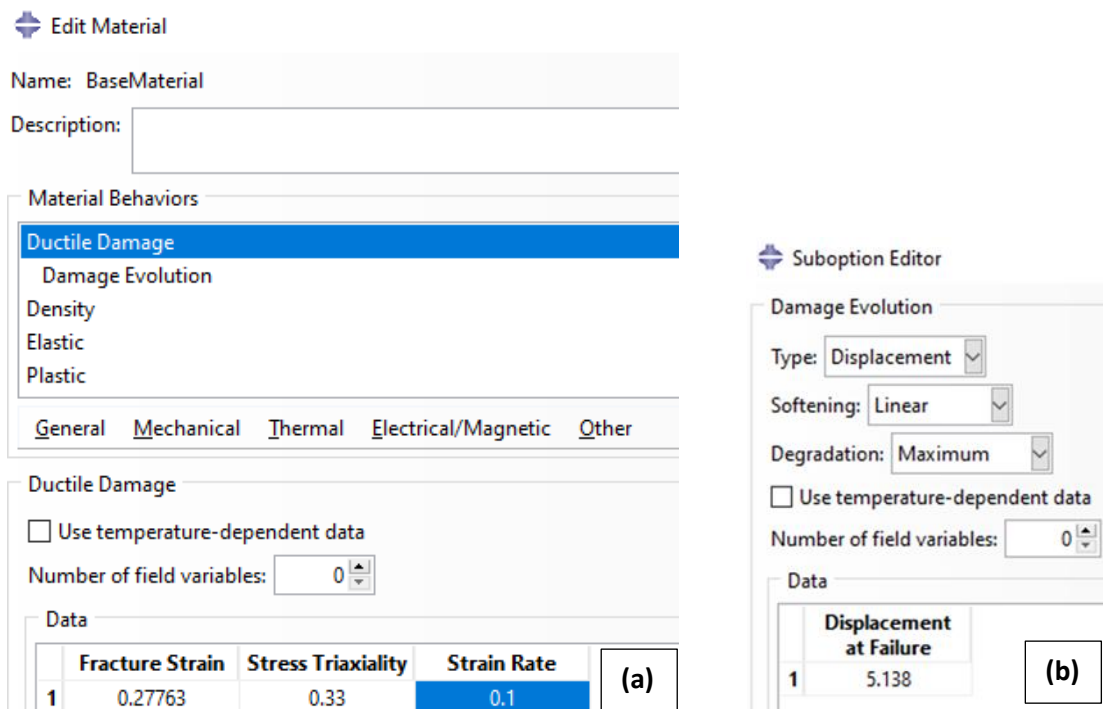


Figure 56: True stress-strain diagram for PWHT 705.

Table 17: Damage parameters calculated from certificates and hardness tests.

Material	True fracture strain $[\bar{\epsilon}_0^{pl}]$	Displacement at failure $[\bar{u}_f^{pl}]$
AISI 4130 Steel	0.27763	5.138
Weak electrode	0.23111	4.174
Strong electrode	0.22314	4.014
HAZ 600	0.11797	2.010
HAZ 650	0.12389	2.117
HAZ 705	0.15513	2.694

Table 17 shows the damage parameters for the damage accumulation from tensile strength to fracture; in Abaqus these parameters are used to define the placement of the fracture. Figure 57 shows how these damage parameters for the respective materials are plotted in Abaqus.



Edit Material

Name: BaseMaterial

Description:

Material Behaviors

- Ductile Damage
- Damage Evolution
- Density
- Elastic
- Plastic

General Mechanical Thermal Electrical/Magnetic Other

Ductile Damage

Use temperature-dependent data

Number of field variables: 0

	Fracture Strain	Stress Triaxiality	Strain Rate
1	0.27763	0.33	0.1

(a)

Suboption Editor

Damage Evolution

Type: Displacement

Softening: Linear

Degradation: Maximum

Use temperature-dependent data

Number of field variables: 0

Data

	Displacement at Failure
1	5.138

(b)

Figure 57: (a) Base material parameter plotted for Ductile Damage in Abaqus. (b) Showing the Damage evolution from necking to fracture, using linear damage evolution, plotted Displacement at Failure.

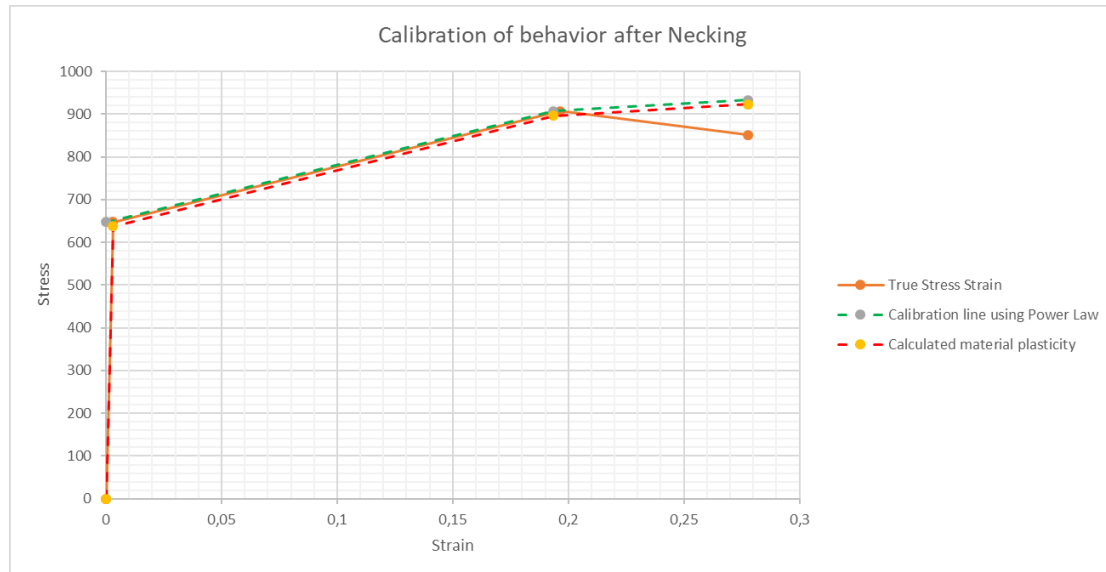


Figure 58: Visualization of calibration of strength coefficient K for unaffected base metal of the pipe.

Figure 58 shows the calibration of the strength coefficient K that is used to determine the linear damage evolution after necking for the unaffected base metal of the pipe. The green line is the plasticity curve from the true effective stress-strain curve extracted from experiments; the red line is the calibration line using the Ramberg and Osgood equation (7). This calibration was also done for the HAZ and fusion zone of the pipe with the respective PWHT procedures, as shown in Appendix I.

Table 18: Calibrated Strength coefficient, K values and hardening exponent, n .

Material	Strength coefficient, K [MPa]	Hardening exponent, n
Base material	933	0.082
Weak electrode	724	0.065
Strong electrode	865	0.073
HAZ 600	958	0.095
HAZ 650	868	0.090
HAZ 705	770	0.090

Table 18 shows the damage parameter K that is calibrated for the different sections. The hardening exponent n is calibrated too, but is not an input parameter in Abaqus; the hardening exponent is only used to calibrate the behavior of the material stress and strain graph.

Edit Material

Name: BaseMaterial

Description:

Material Behaviors

- Ductile Damage
- Damage Evolution
- Density
- Elastic
- Plastic

General Mechanical Thermal Electrical/Magnetic

Plastic

Hardening:

Use strain-rate-dependent data

Use temperature-dependent data

Number of field variables:

Data

	Yield Stress	Plastic Strain
1	647	0
2	906.8	0.19353
3	933	0.27763

Figure 59: Plotted plasticity data for the unaffected base material along with the calibrated strength coefficient K at the end that decides the start/behavior of the linear damage evolution.

7.1.2. Results sensitivity study

The choice of mesh was done after a check of the sensitivity of different mesh sizes, as described in the previous chapter. Due to the chosen loading condition affecting the whole model, a refined mesh was not chosen in this study. From simulations of the coarse mesh of 10mm, the pipe was behaving more irregularly, with an unsymmetrical behavior with considerably more simulation time. The medium to extra fine mesh was acting stiffer and had a better representation of the behavior of the fracture and loading conditions. The representation of the hardening and fracture was in any case slightly more favorable for the fine and extra fine mesh. The fracture was also occurring with a similar distance from the pipe end and the welded part of the pipe with the fine and extra fine mesh. A slight increase in the maximum load is registered with finer mesh, but the pressure level is more even, with a deviation of approximately 2% between the chosen mesh and the medium and extra fine mesh. The disturbance observed could be a reason to investigate further.

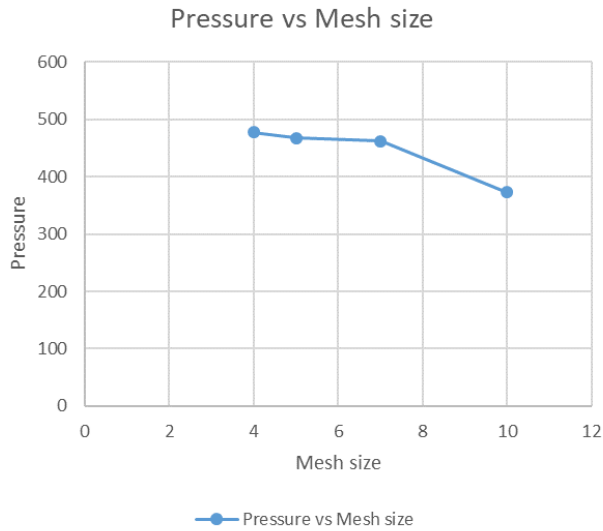


Figure 60: Pressure vs mesh size diagram for the pipe due to pressure load.

Table 19: Sensitivity results from pressure load at fracture.

Type	Mesh size [mm]	Number of elements	Number of nodes	Pressure [MPa]	Pressure Deviation [%]
Coarse	10	7344	14832	372.279	19.451
Medium	7	28416	42912	462.177	1.106
Fine	5	80784	108240	467.348	Chosen mesh
Extra Fine	4	172032	215880	477.329	2.136

Figure 61 shows the corresponding pressure vs strain curves for the different meshes that under study. There was a significant increase in stress and computational time as the mesh size was decreased.

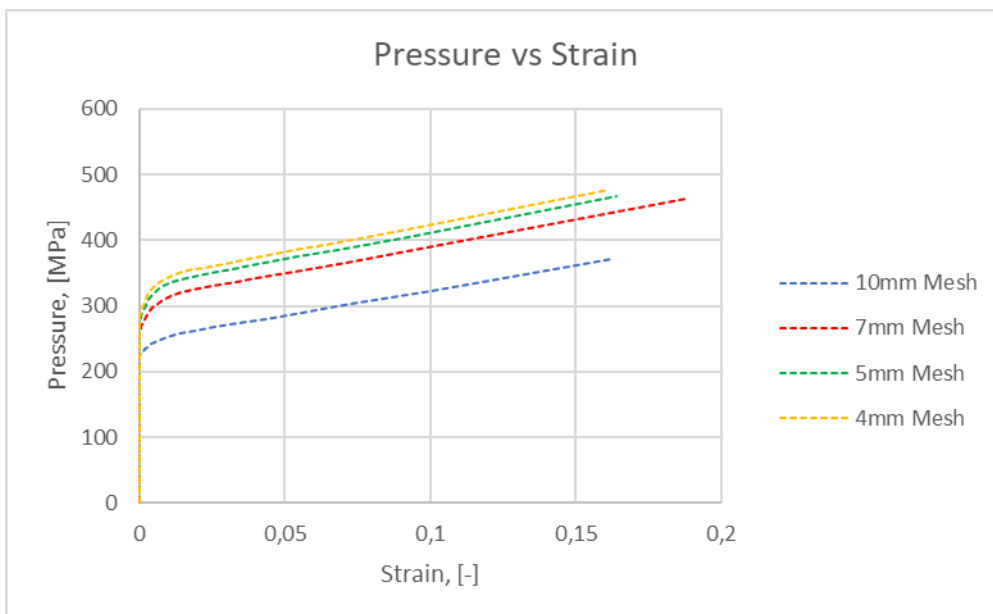


Figure 61: Pressure vs strain curve mesh sensitivity.

7.1.3. Numerical results for weak electrode

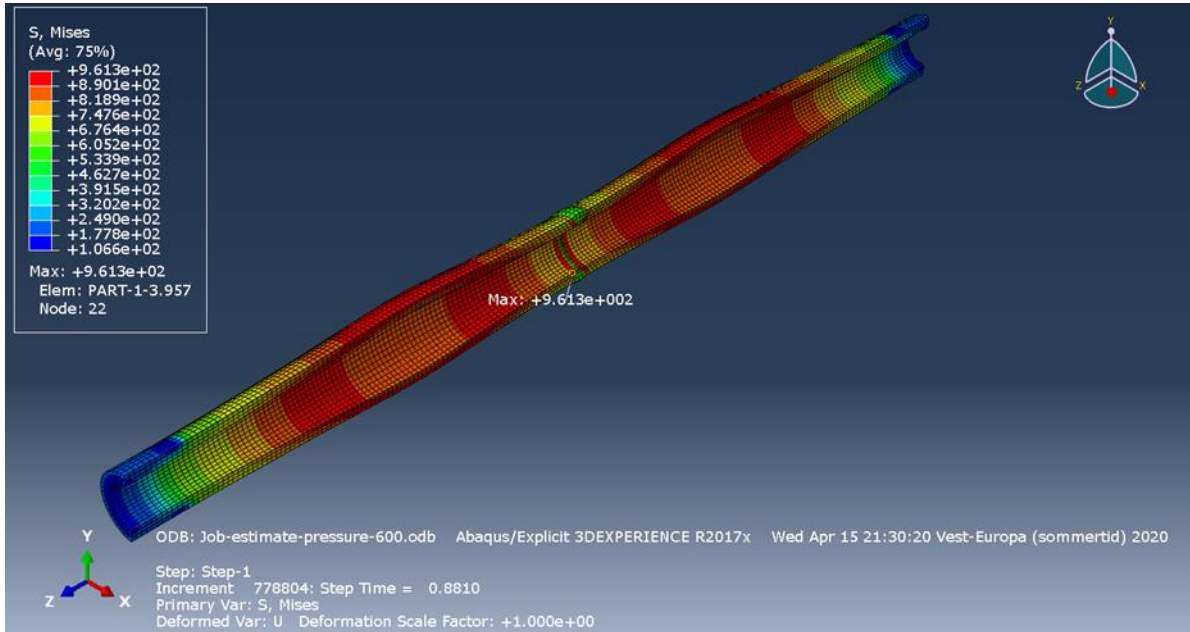


Figure 62: Numerical results for PWHT 600 weak electrode.

Figure 62 shows the simulation of the weak electrode, and as seen the fracture is occurring in the base material of the pipe.

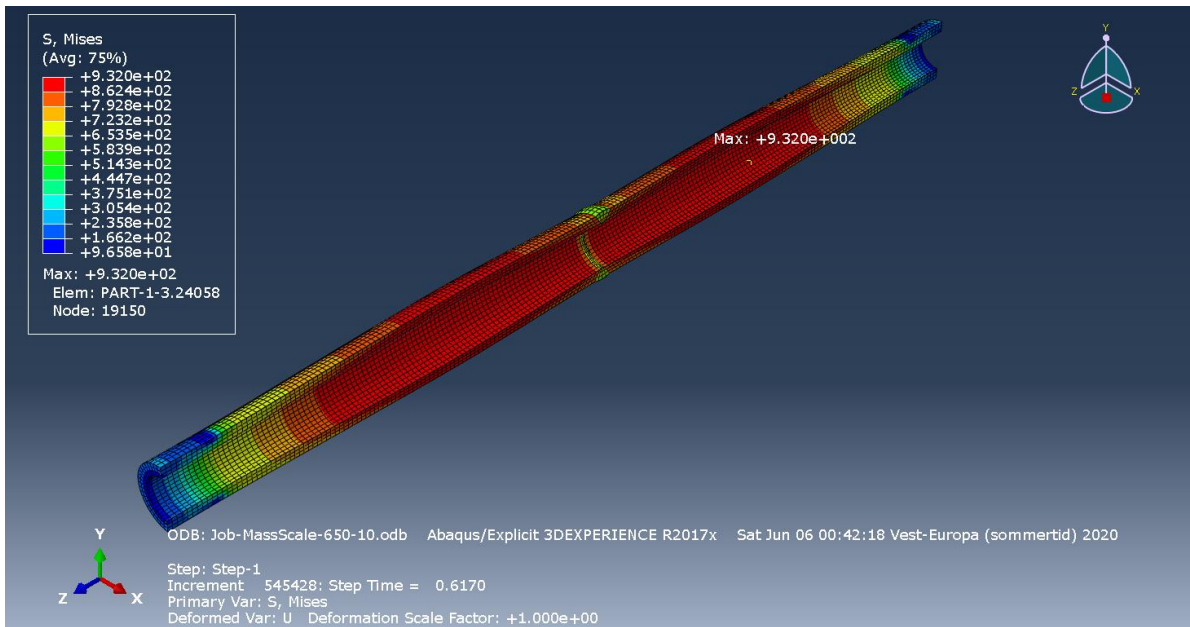


Figure 63: Numerical results from PWHT 650 weak electrode.

Figure 63 shows the simulation of the weak electrode, where the fracture is occurring in the welded area of the pipe. The visualization presented also shows the base metal deforming as well, this is due to the similar tensile strength of the materials, so placement of failure is determined by the burst pressure of the areas.

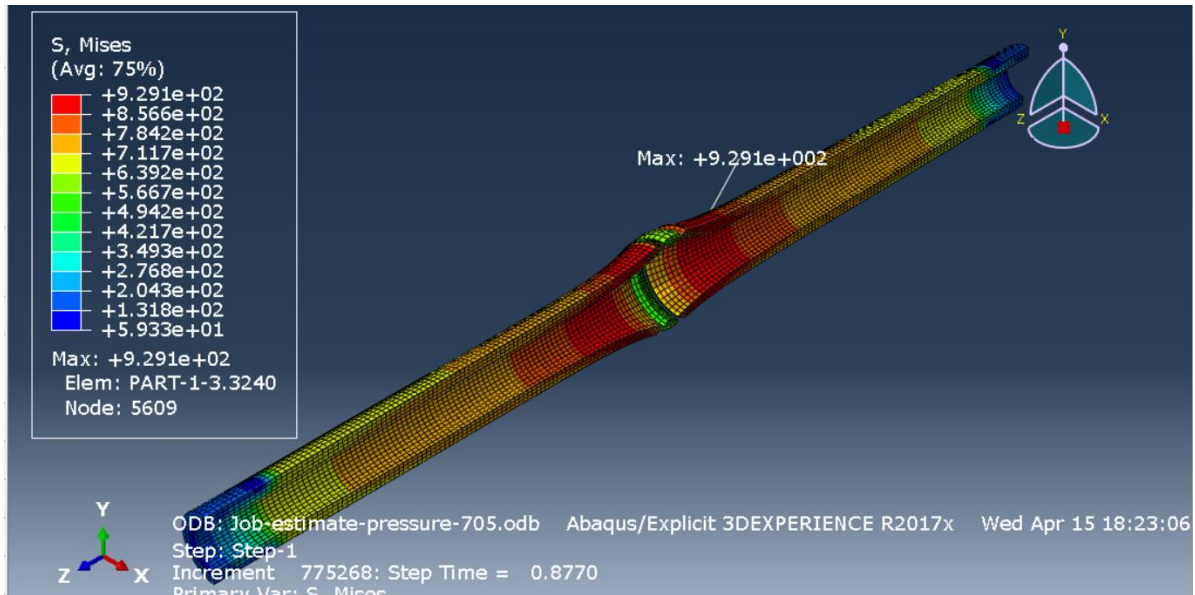


Figure 64: Numerical results from PWHT 705 weak electrode.

Figure 64 shows the simulation of the weak electrode and as seen the fracture is occurring in the welded area of the pipe. As seen from the previous simulations, the deformations around the welded section are growing larger and closer to the center of the weld with a higher PWHT temperature.

Table 20: Reaction forces on pipe with weak electrode.

PWHT procedure	Placement of fracture	Max internal stress [MPa]	Burst Pressure [MPa]
600	Base material	932.528	259.29
650	Weld	854.527	244.96
705	Weld	759.364	201.135

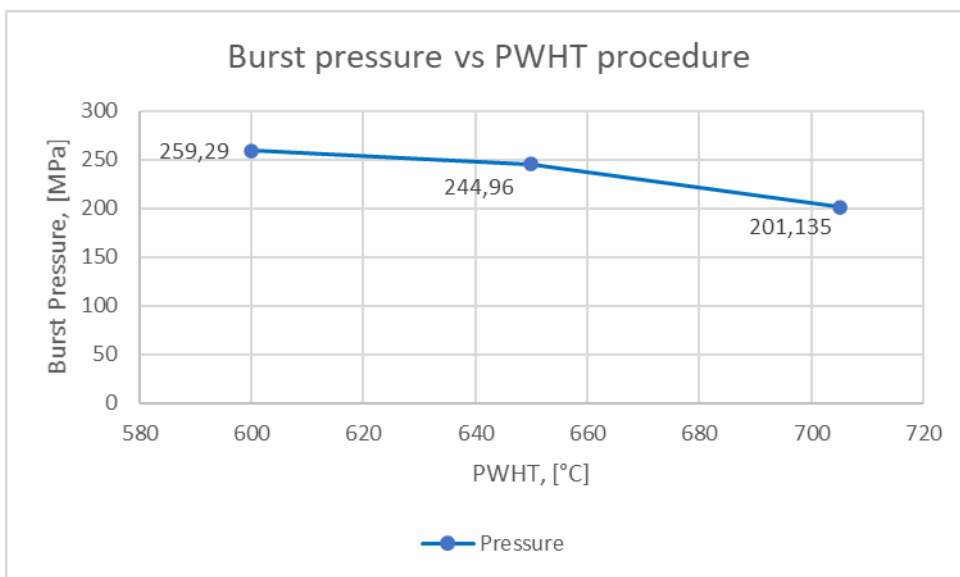


Figure 65: Resulting burst pressure based on weak electrode.

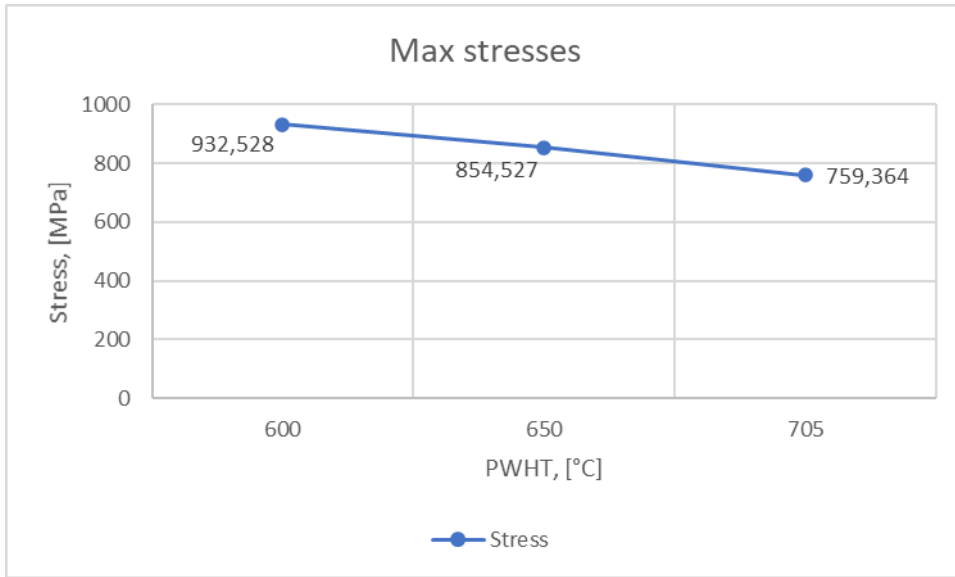


Figure 66: Highest stresses for pipe based on hardness data with weak electrode.

7.1.4. Numerical results from strong electrode

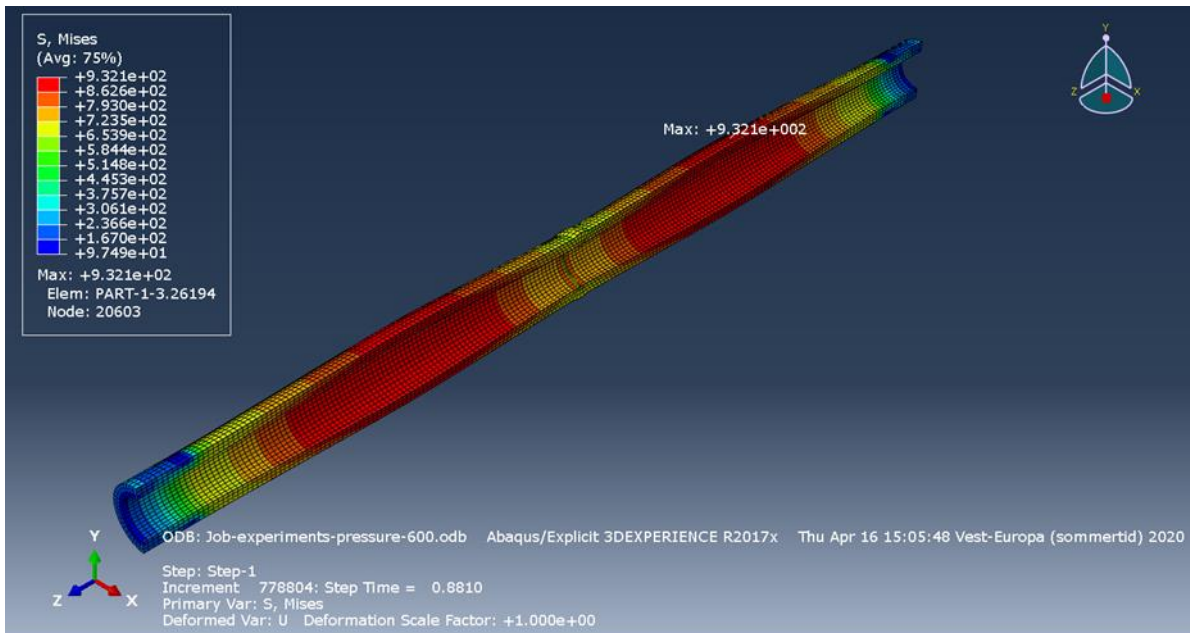


Figure 67: Pipe with pressure load until failure PWHT600 strong electrode.

Figure 67 shows the simulation of the strong electrode, and as seen the fracture is occurring in the base material of the pipe.

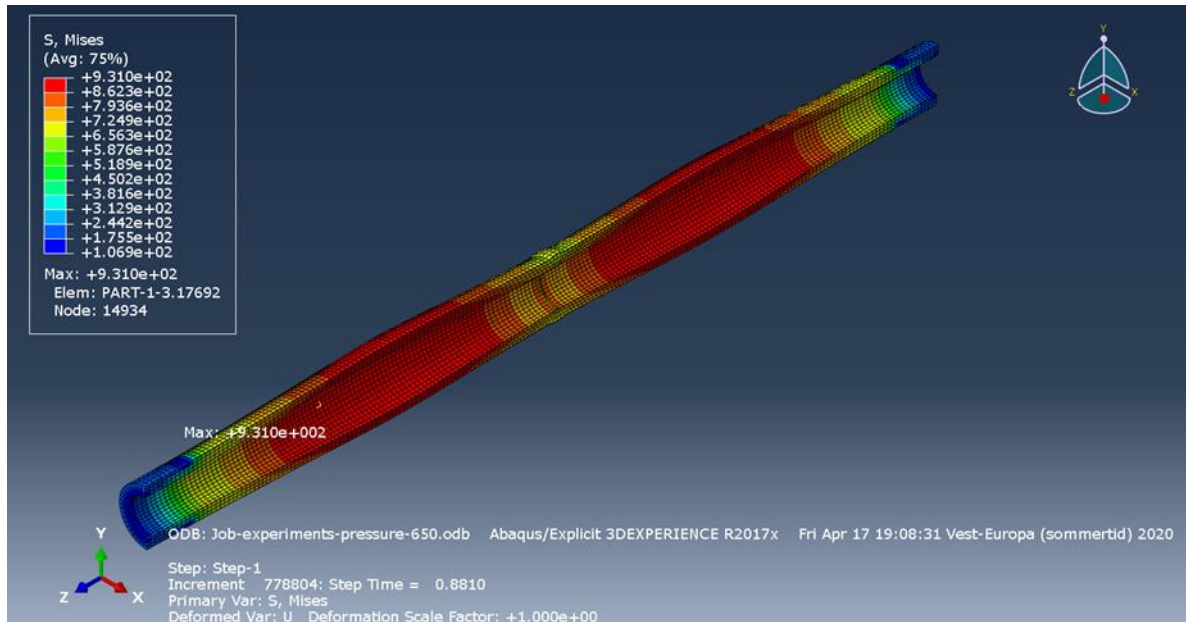


Figure 68: Pipe with pressure load until failure – PWHT650 strong electrode.

Figure 68 shows the simulation of the strong electrode and as seen the fracture is occurring in the base material of the pipe.

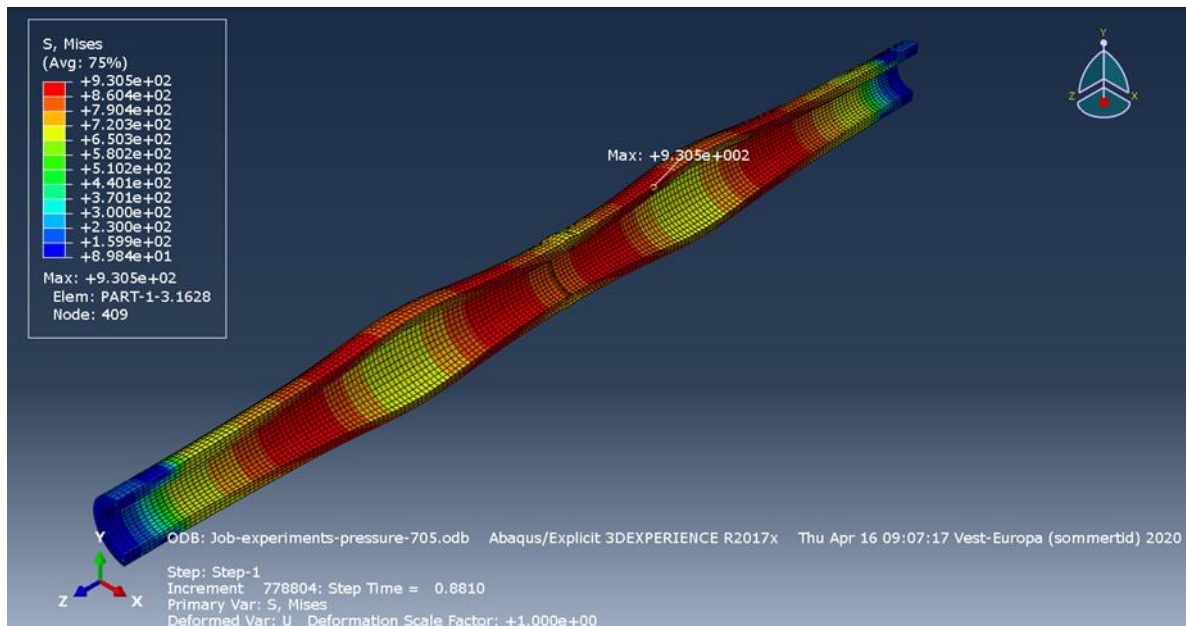


Figure 69: Pipe with pressure load until failure – PWHT705 strong electrode.

Figure 69 shows the simulation of the strong electrode, and the fracture is occurring in the welded area of the pipe. The visualization presented also shows the base metal deforming as well; this is due to the different strength and geometry of the weld, so placement of failure is determined by the burst pressure of the areas. As seen from the previous simulations, the deformations around the welded section are growing larger and closer to the center of the weld with a higher PWHT temperature also for the strong electrode.

Table 21: Reaction forces on pipe with strong electrode.

PWHT procedure	Placement of fracture	Max internal stress [MPa]	Burst Pressure [MPa]
600	Base metal	932.633	259.312
650	Base metal	906.41	255.217
705	Weld	760.271	217.091

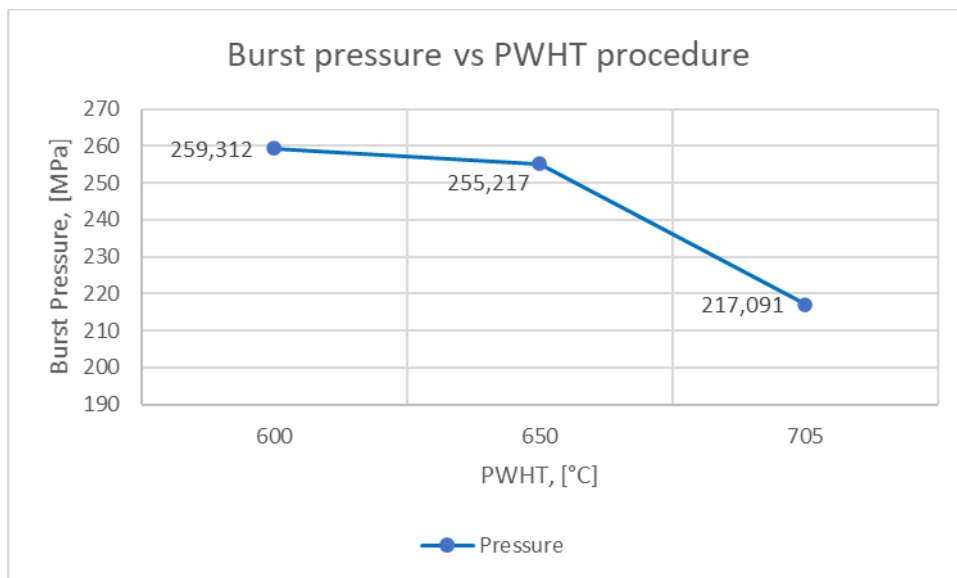


Figure 70: Burst pressure for simulations based on strong electrode.

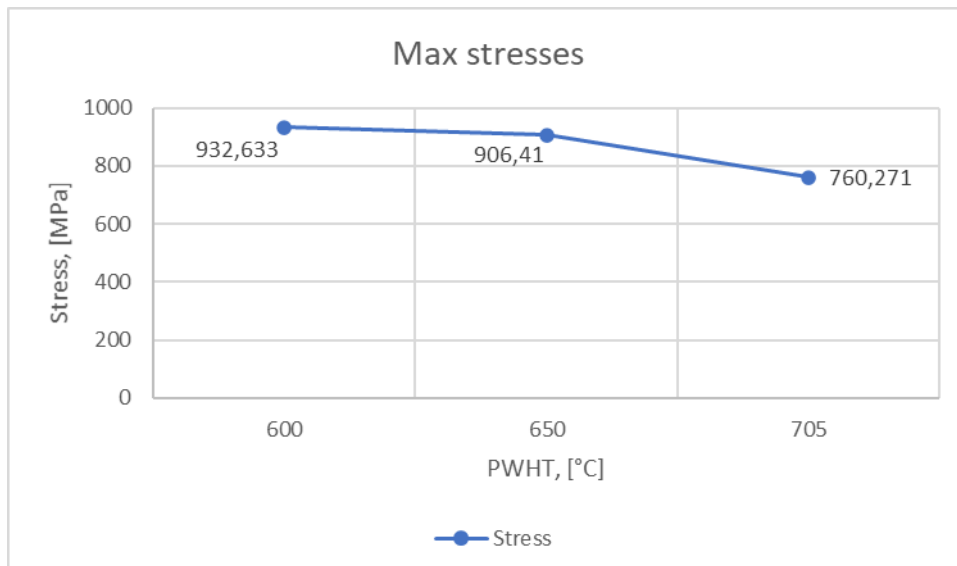


Figure 71: Highest stresses for pipe based on hardness data with strong electrode.

7.1.5. Comparison of results

Table 22: Comparison of burst pressure for the pipe.

Test procedure	Burst pressure, weak electrode [MPa]	Burst pressure, strong electrode [MPa]	Deviation [%]
PWHT 600	259.29	259.312	0.0
PWHT 650	244.96	255.217	4.2
PWHT 705	201.135	217.091	7.9

Table 23: Comparison of max stress for the fracture initiation of the pipe.

Test procedure	Max stress, weak electrode [MPa]	Max stress, strong electrode [MPa]	Deviation [%]
PWHT 600	932.528	932.633	0.0
PWHT 650	854.527	906.41	6.1
PWHT 705	759.364	760.271	0.1

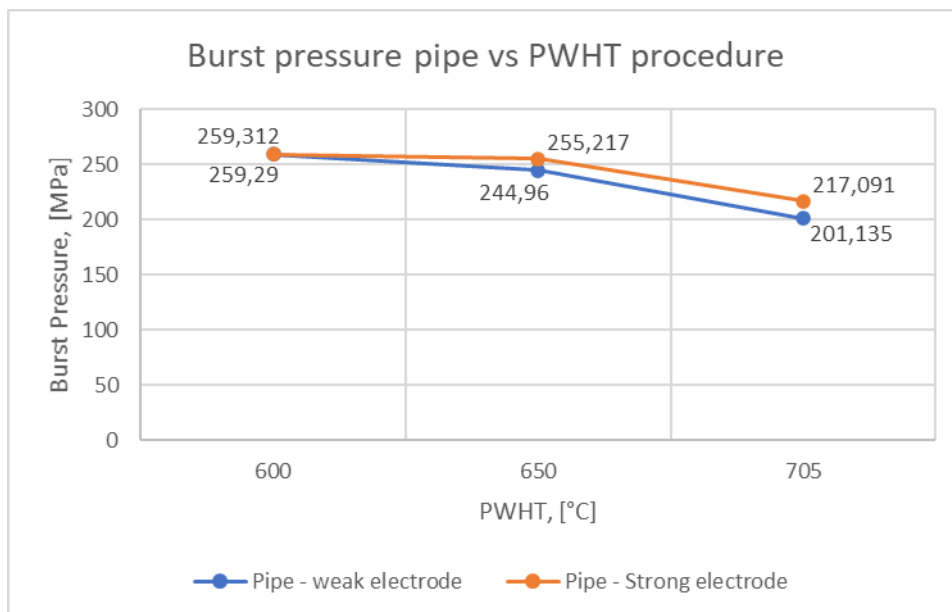


Figure 72: Weak vs strong electrode – Burst pressure results in pipe.

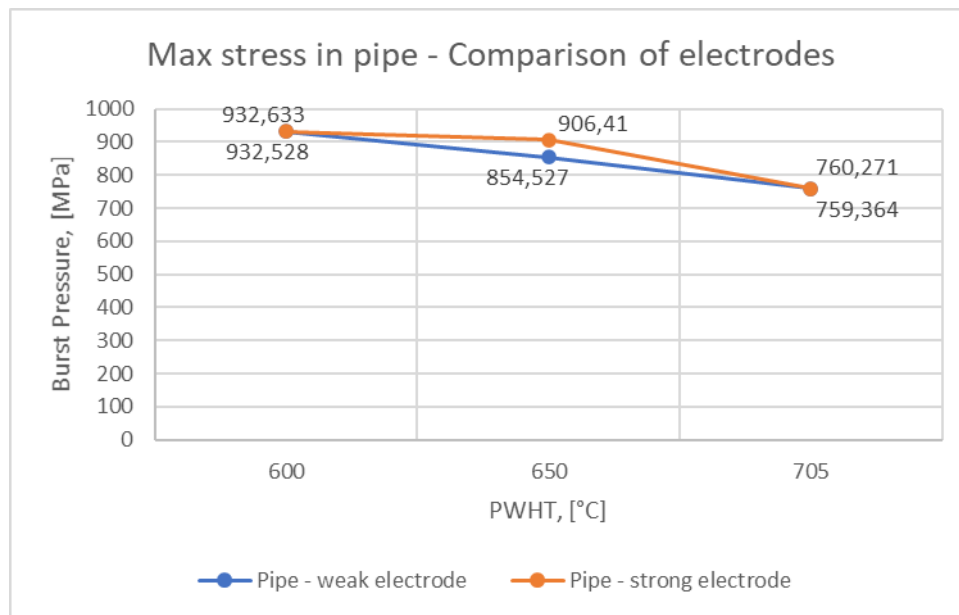


Figure 73: Weak vs strong electrode – Comparison of max stresses in pipe at fracture.

All measured pressure and stresses were taken from the elements inside the pipe that was most affected by the applied pressure load and that was failing and deforming first.

7.2. Analysis based on material data from tensile tests

All the experimental tests were conducted to fracture. For each specimen, the detailed results consist of stress-strain curves and observations made; the rest of the tests are found in Appendix N. In total there were ten specimens that were tested under a monotonic tensile load, all of which were uniformly shaped specimens. The specimens were heat-treated with the described heat treatments from previous chapter for extraction of the material parameters for the different PWHTs of the pipe.

7.2.1. Results from tension tests

The yield strength was found by identification of the lowest point in the yield plateau on the stress-strain curve for the uniformed specimens, as seen for test specimen Base 2 in Figure 75; for the rest of the samples, see Appendix O. The engineering stress-strain curves were plotted using equations (24) and (25), the strain results from the extensometer, and the force from the test machine; the stress-strain diagrams are presented in Appendix N.

As mentioned in previous chapter 6.2.6., the uniform test samples were used for calibration of the plasticity of the damage models. The value of the equivalent strain at the point of damage initiation was collected by first tuning the plasticity model and then finding the mean equivalent strain value for the damage initiation criterion. Then a damage evolution was set by defining a linear behavior of the downward curve until failure. The true strength and true strain curve are calculated according to

equations (26) and (27) respectively and plotted as seen in Figure 76. Table 25 shows the important true stress-strain data were recorded from extraction of experimental results. The tensile test of the quenched specimen is only used to show what properties the samples had before heat treatment. And as seen from Figure 133 and Figure 134 in Appendix N, the sample was substantially stronger and fractured at the maximum of the capacity of the test machine, in a brittle manner as expected.

Table 24: Collected experimental Normal/Engineering stress strain data.

Specimen	Yield stress [MPa]	Tensile stress at ultimate strength [MPa]	Tensile strain [-]	Fracture strain [-]
Base 1	626.320	744.795	0.053108	0.16192
Base 2	642.870	741.555	0.079944	0.180304
HAZ (quenched)	-	Over 1296.419	-	0.090788
HAZ 600	809.080	875.908	0.054524	0.161012
Base 650	629.680	748.126	0.048344	0.150128
HAZ 650	712.290	812.816	0.069268	0.18924
Base 705	618.090	730.912	0.075396	0.181908
HAZ 705	617.160	725.308	0.06504	0.192828
Base 746	585.190	687.692	0.087816	0.122828
HAZ 746	527.520	659.646	0.114592	0.199992

Table 25: Collected experimental true stress strain data.

Specimen	True stress at yield [MPa]	True stress at ultimate strength [MPa]	True tensile strain [-]	True fracture strain [-]
Base 1	629.221	790.016	0.063909573	0.150073809
Base 2	648.069	808.508	0.097300924	0.165772032
HAZ 600	815.228	926.733	0.059509648	0.149292039
Base 650	632.163	788.320	0.060417542	0.139873241
HAZ 650	716.468	874.386	0.077438705	0.173314448
Base 705	620.780	795.556	0.091462788	0.167130082
HAZ 705	620.075	782.551	0.084958605	0.176326958
Base 746	588.015	752.855	0.093421124	0.11587544
HAZ 746	530.257	746.630	0.14142317	0.18231489

The true stress-strain diagram was plotted for all tensile experiments and datapoints were inputted to Abaqus in tabular form to set the plasticity behavior of the material. One of the engineering stress-strain diagrams and true stress-strain diagrams is presented in Figure 74 and Figure 76, and illustration of the plasticity plot was done in the same manner as shown previously for the hardness based simulations, shown in Figure 59. The rest of the true stress-strain curves are found in Appendix N.

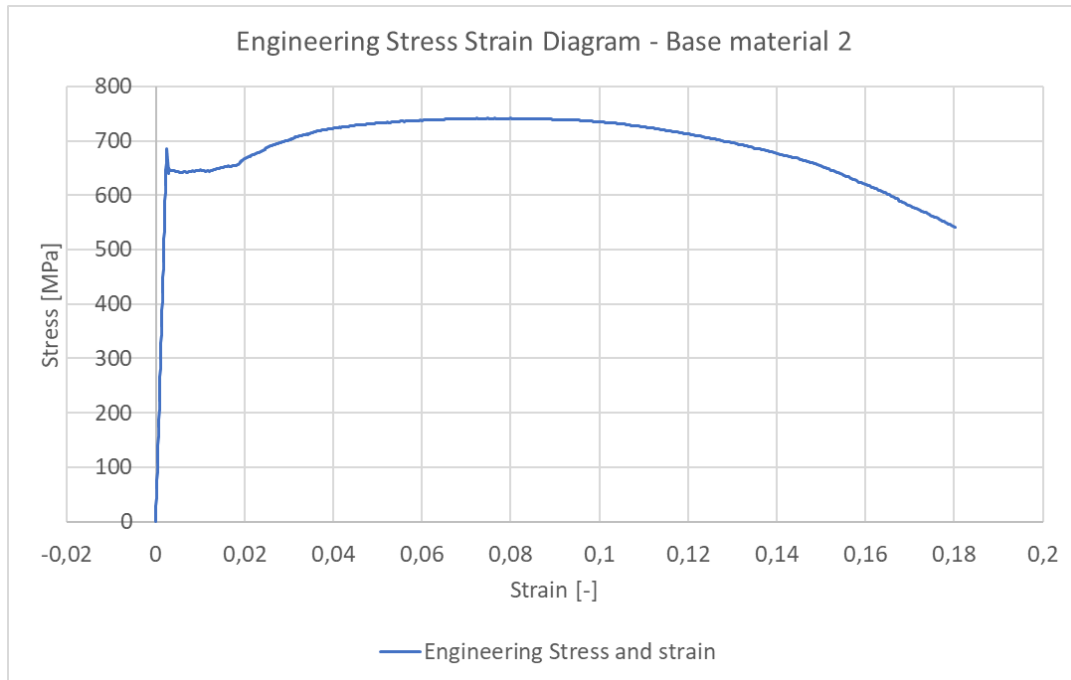


Figure 74: Engineering stress-strain diagram – Uniform specimen Base 2.

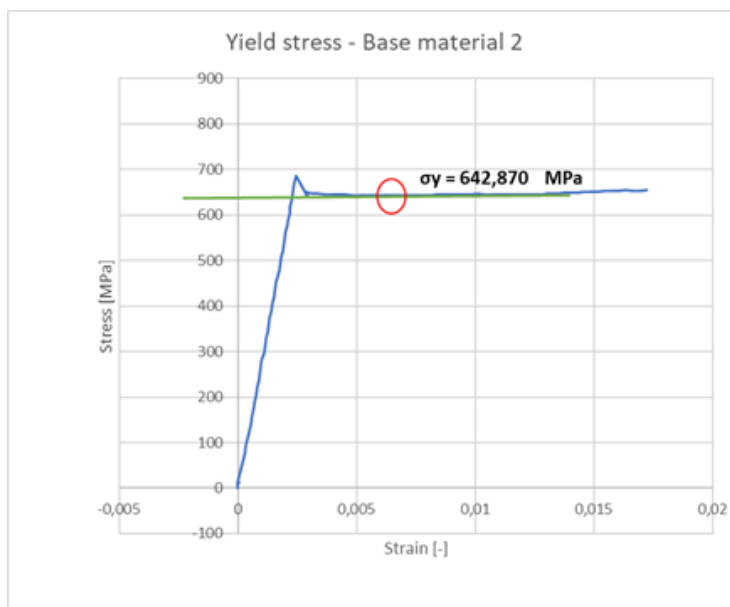


Figure 75: Illustration of determination of yield point from the experimental tensile tests – Here representing base material (Base 2).

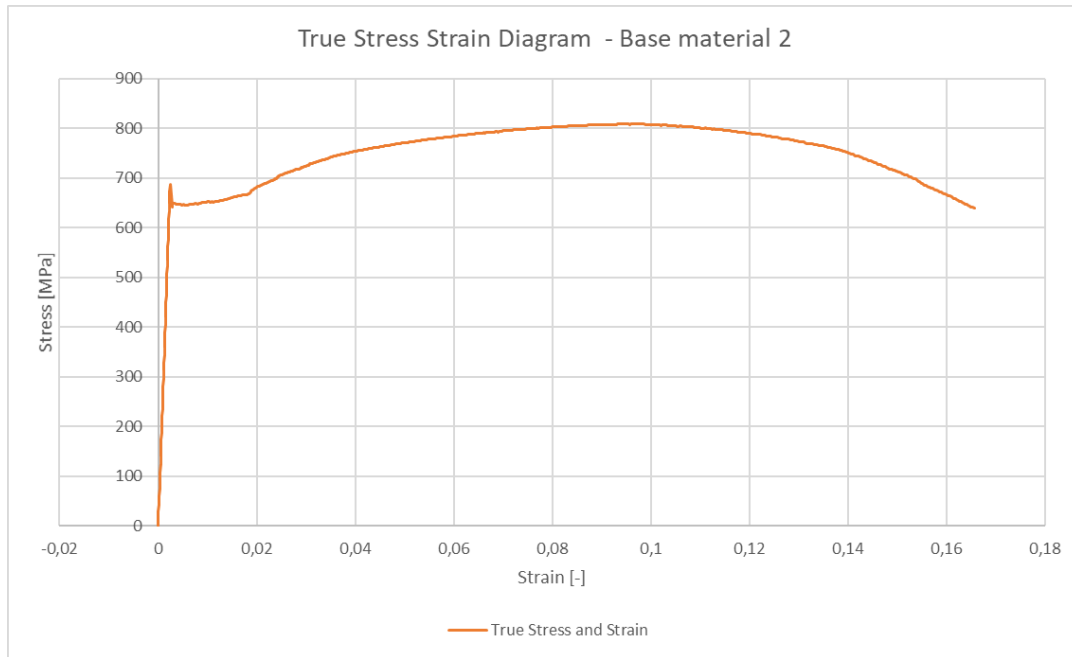


Figure 76: True stress-strain diagram – Uniform specimen Base 2.

A diagram for comparison of the different material properties of the different sections of the welded pipe was made, the same as for the hardness, as shown here by Figure 77, Figure 78, Figure 79 and Figure 80. The effect of the different heat treatments on the base material was simulated for the tensile tests as described in previous chapter, in contrast to the simulations done for the hardness test. The only base material properties affected by the PWHT procedure was PWHT 600 due to a limited amount of test specimens. The rest of the procedures had base material affected by the PWHT procedure and are labeled Base 650, Base 705 and Base 746 in the diagrams presented.

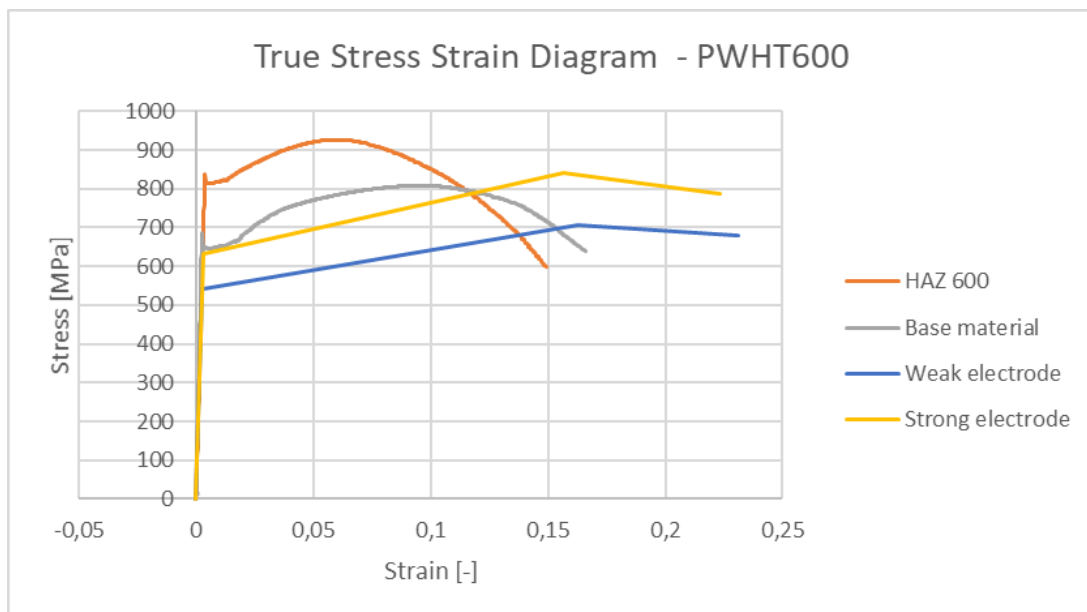


Figure 77: True stress-strain diagram for PWHT 600 based on experimental tests – Material parameters for the electrodes are estimated from certificates.

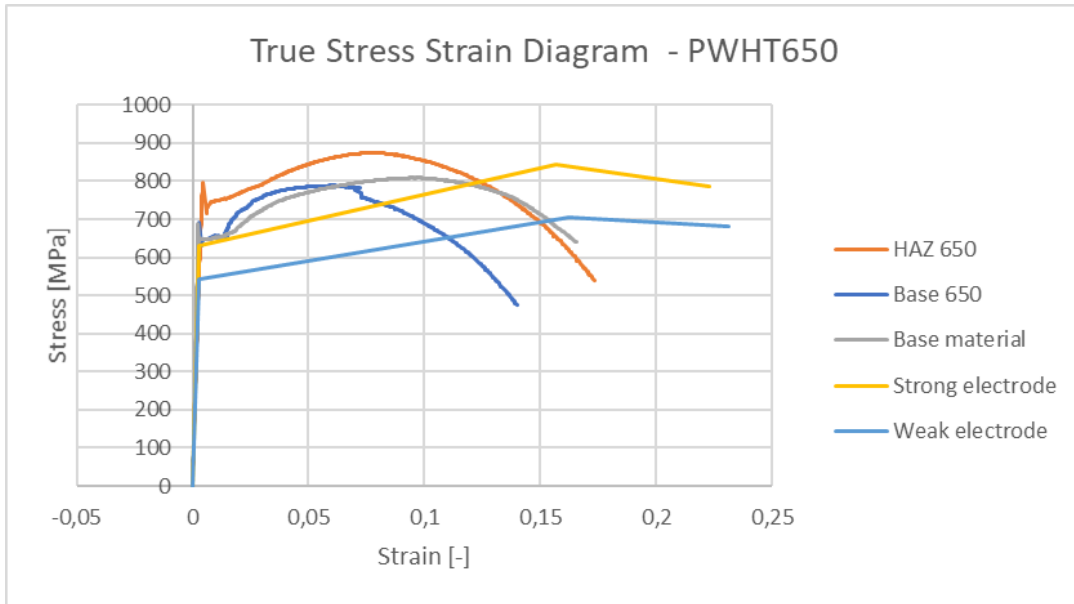


Figure 78: True stress-strain diagram for PWHT 650 based on experimental tests – Material parameters for the electrodes are estimated from certificates.

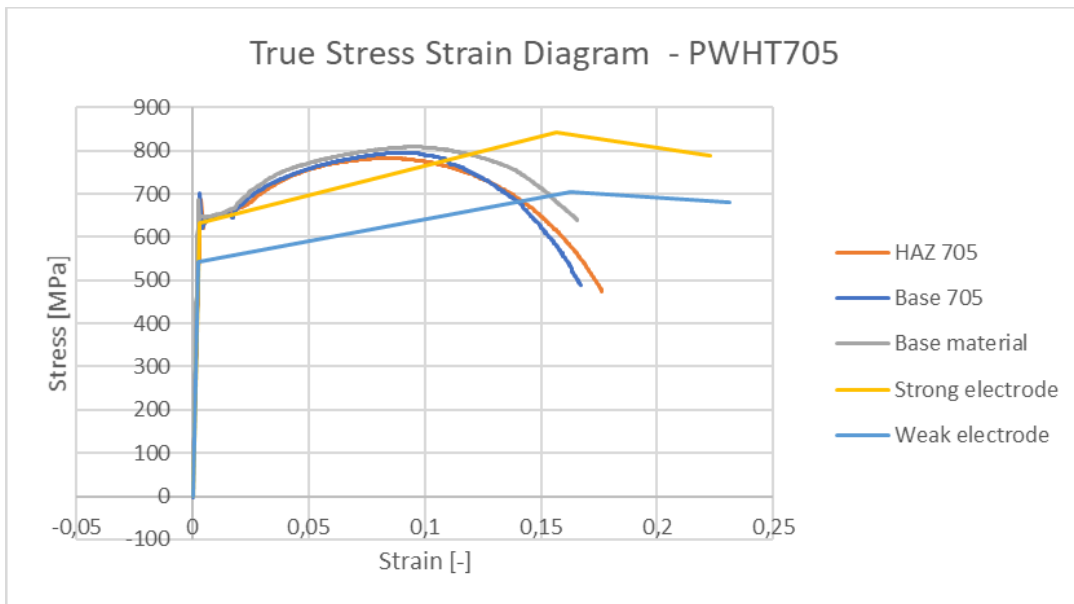


Figure 79: True stress-strain diagram for PWHT 705 based on experimental tests – Material parameters for the electrodes are estimated from certificates.

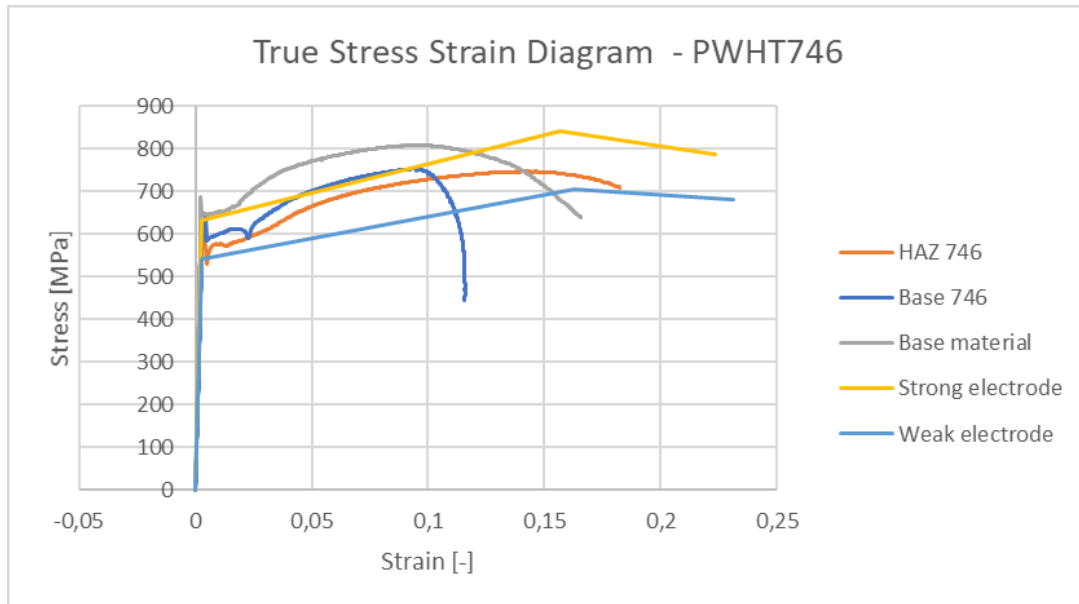


Figure 80: True stress-strain diagram for PWHT 746 based on experimental tests – Material parameters for the electrodes are estimated from certificates.

Table 26: Damage parameters calculated and run from tensile tests.

Material	True fracture strain [$\bar{\varepsilon}_0^{pl}$]	Displacement at failure [\bar{u}_f^{pl}]
Base material	0.165772032	2.509
HAZ 600	0.149292039	2.6622
Base 650	0.139873241	2.5446
HAZ 650	0.173314448	2.9993
Base 705	0.167130082	2.6628
HAZ 705	0.176326958	3.1947
*Base 746	0.11587544	0.876
HAZ 746	0.18231489	2.135

*As seen, the test specimen was fracturing close to the edge of the extensometer and the strain after necking became distorted.

Table 27: Calibrated Strength coefficient, K values and hardening exponent, n for tensile test data.

Material	Strength coefficient, K [MPa]	Hardening exponent, n
Base material	858	0.097300924
HAZ 600	988	0.059509648
Base 650	835	0.060417542
HAZ 650	935	0.077438705
Base 705	847	0.091462788
HAZ 705	838	0.084958605
Base 746	775	0.093421124
HAZ 746	780	0.14142317

The damage calibration was done in the same manner as for the hardness-based simulations as described in chapter 6.2.6.; the calibration graphs are found in Appendix P.

7.2.2. Numerical results based on weak electrode

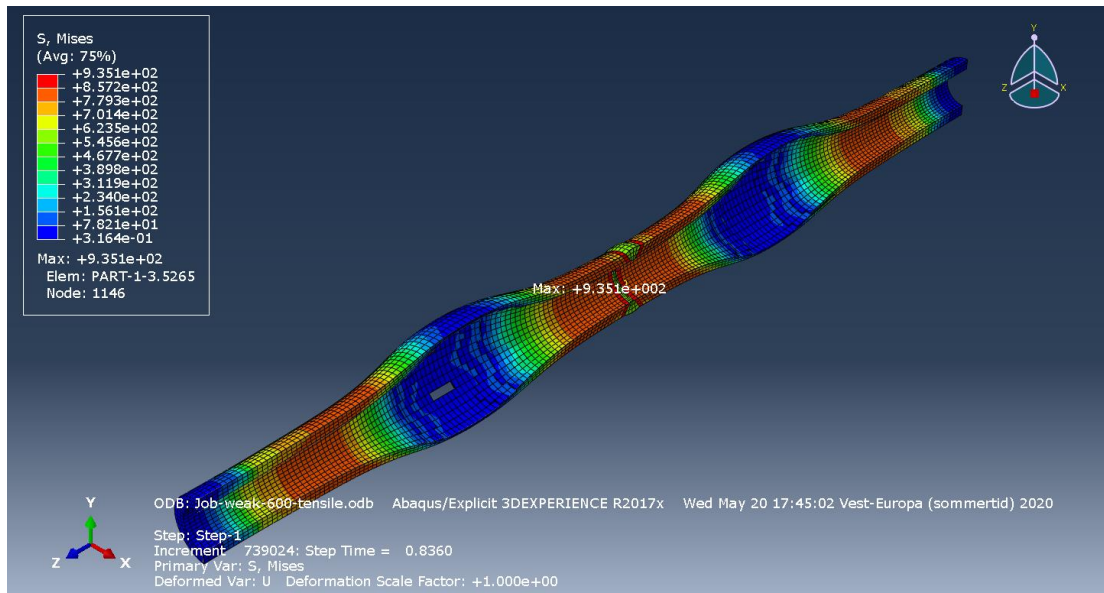


Figure 81: Numerical results for PWHT 600 weak electrode.

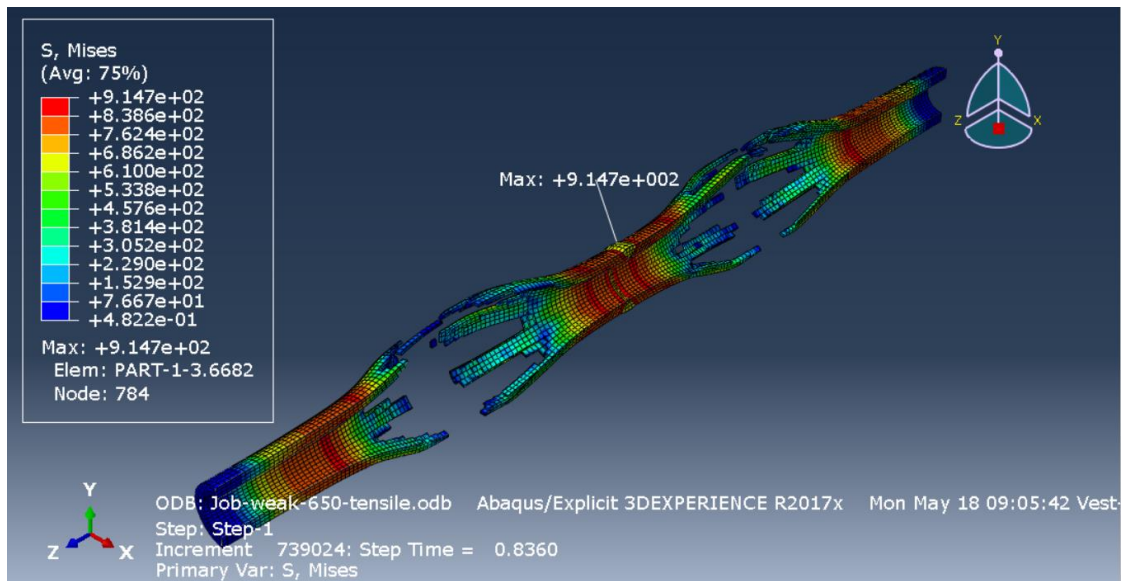


Figure 82: Numerical results from PWHT 650 weak electrode.

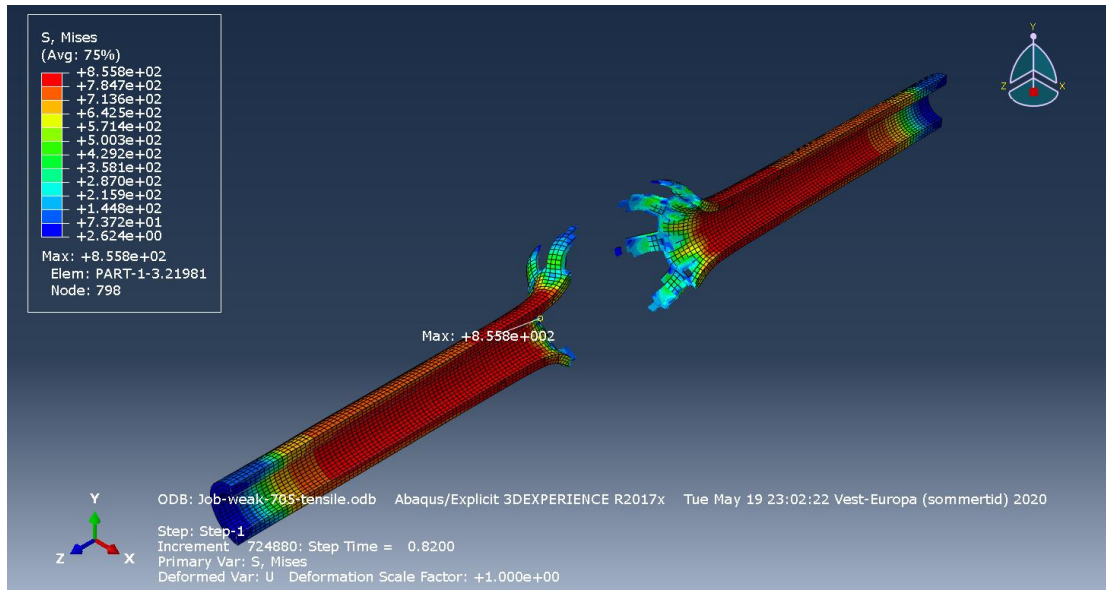


Figure 83: Numerical results from PWHT 705 weak electrode.

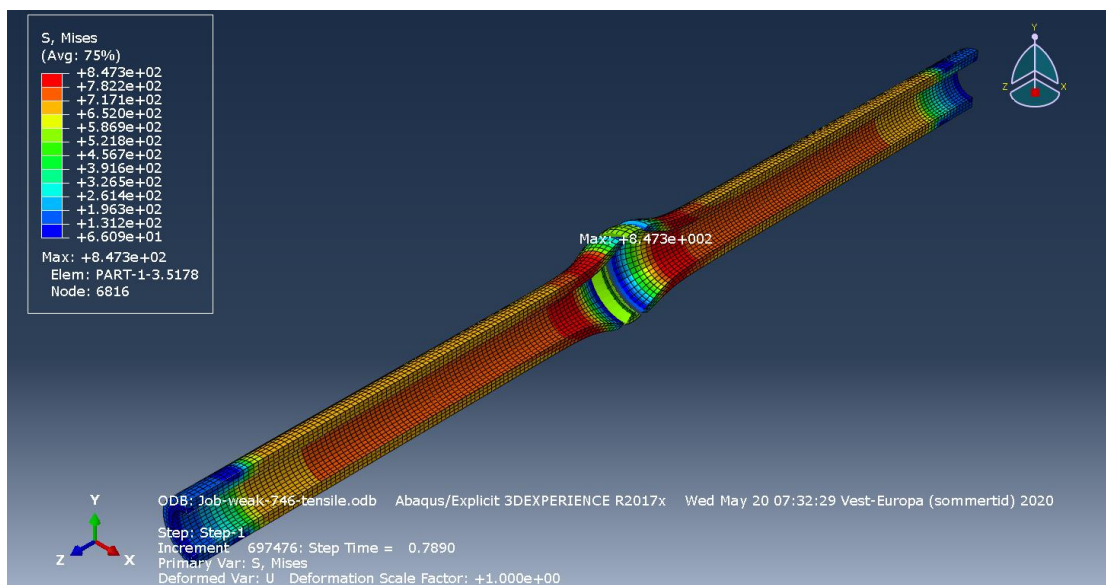


Figure 84: Numerical results from PWHT 746 weak electrode.

Table 28: Reaction forces on pipe weak electrode.

PWHT procedure	Placement of fracture	Max internal stress [MPa]	Burst Pressure [MPa]
600	Base metal	808.006	196.648
650	Base metal	811.33	198.453
705	Weld	716.249	187.474
746	Weld	685.396	159.86

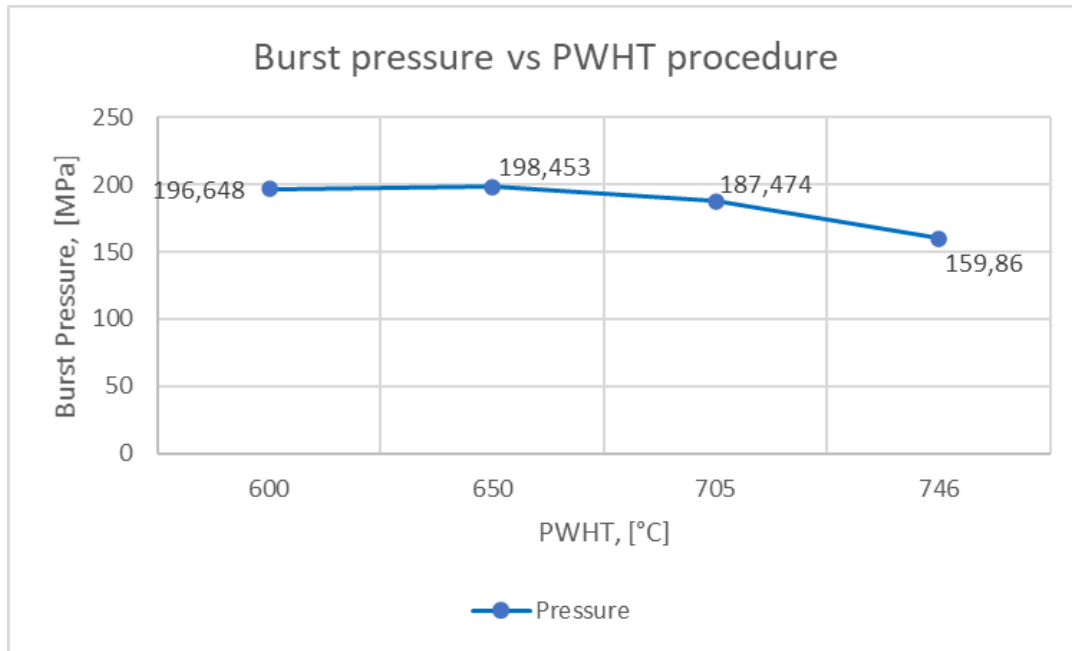


Figure 85: Resulting burst pressure based on material data from experiments and weak electrode.

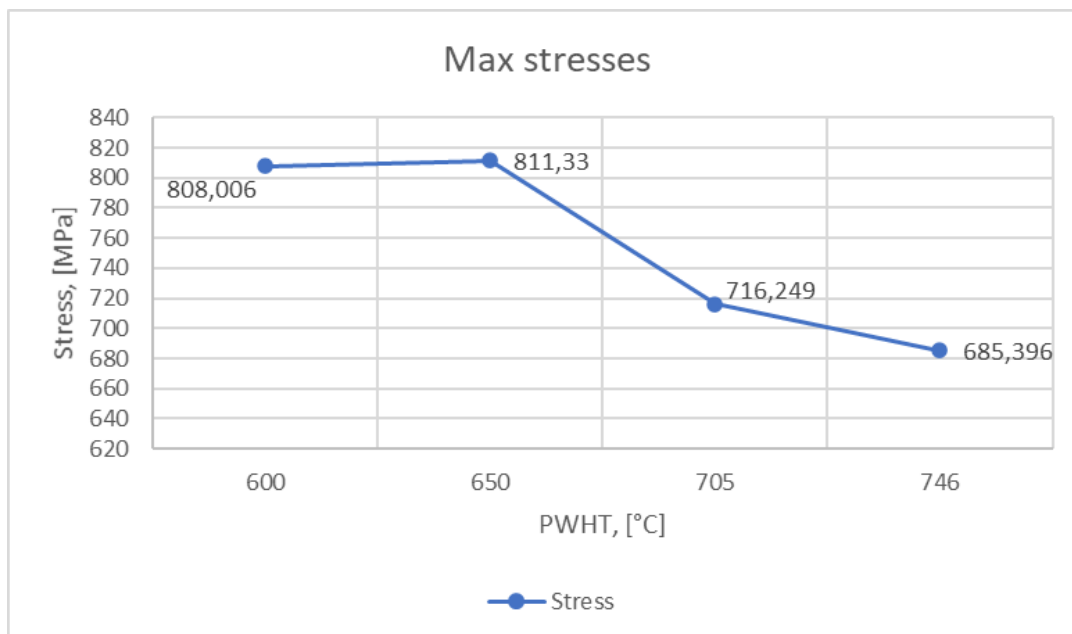


Figure 86: Highest stresses for pipe based on tensile experiment data with weak electrode.

7.2.3. Numerical results based on strong electrode

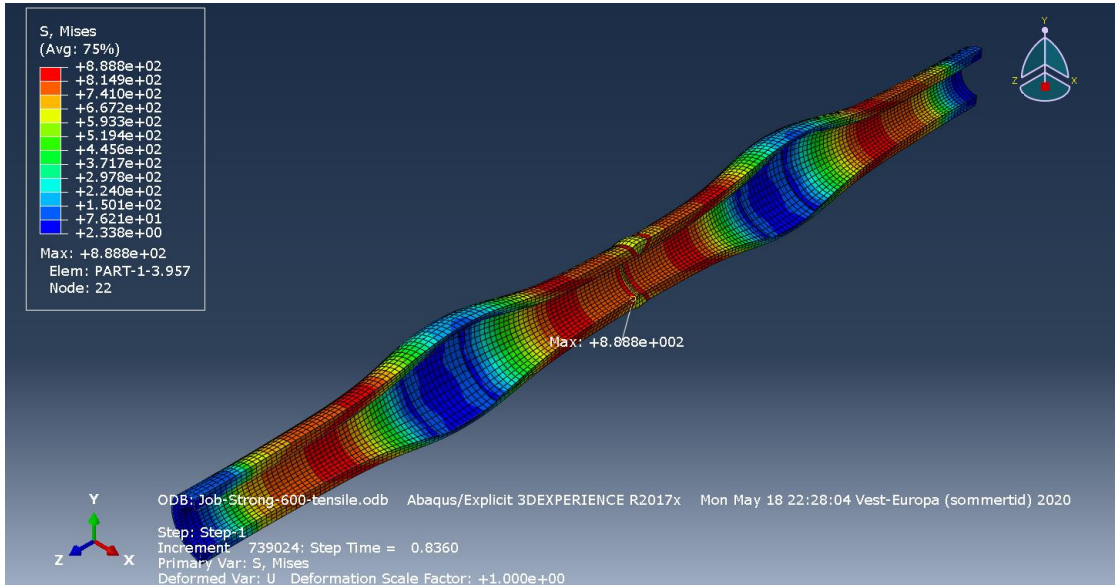


Figure 87: Numerical results from PWHT 600 strong electrode.

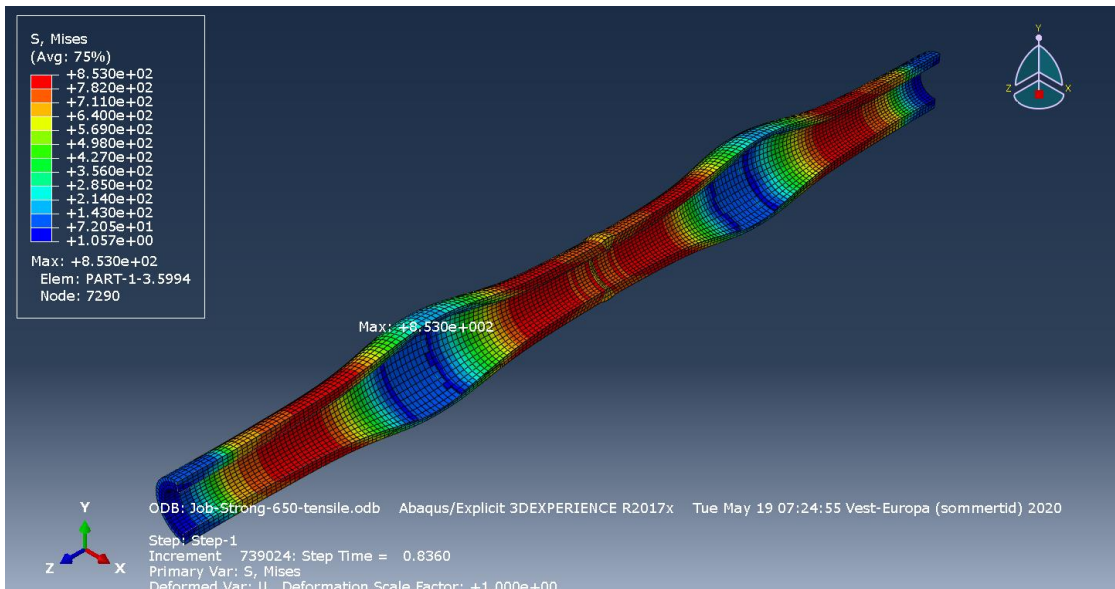


Figure 88: Numerical results from PWHT 650 strong electrode.

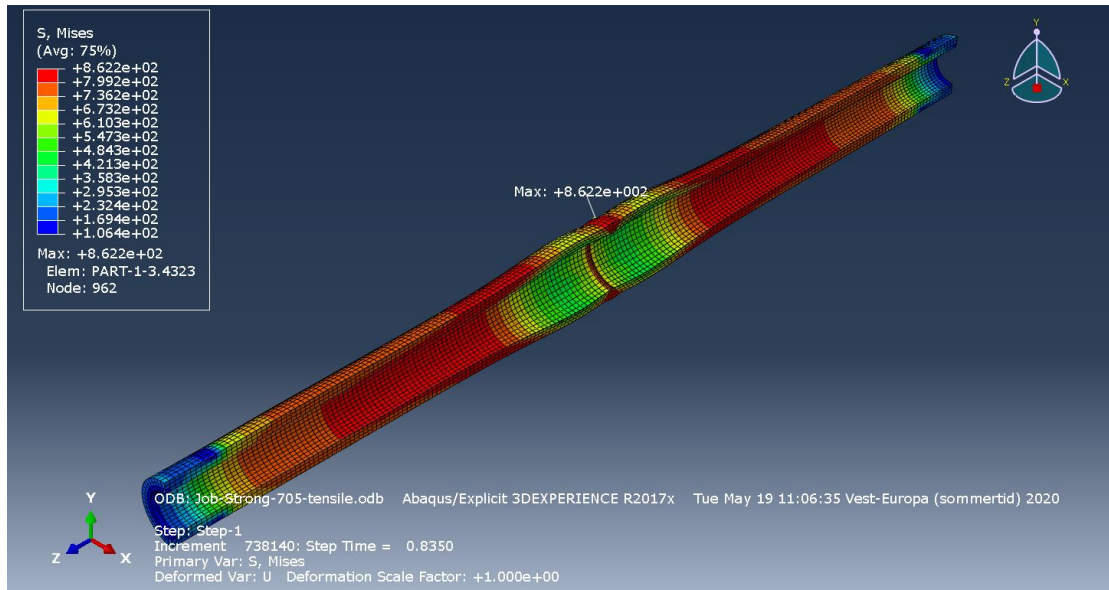


Figure 89: Numerical results from PWHT 705 strong electrode.

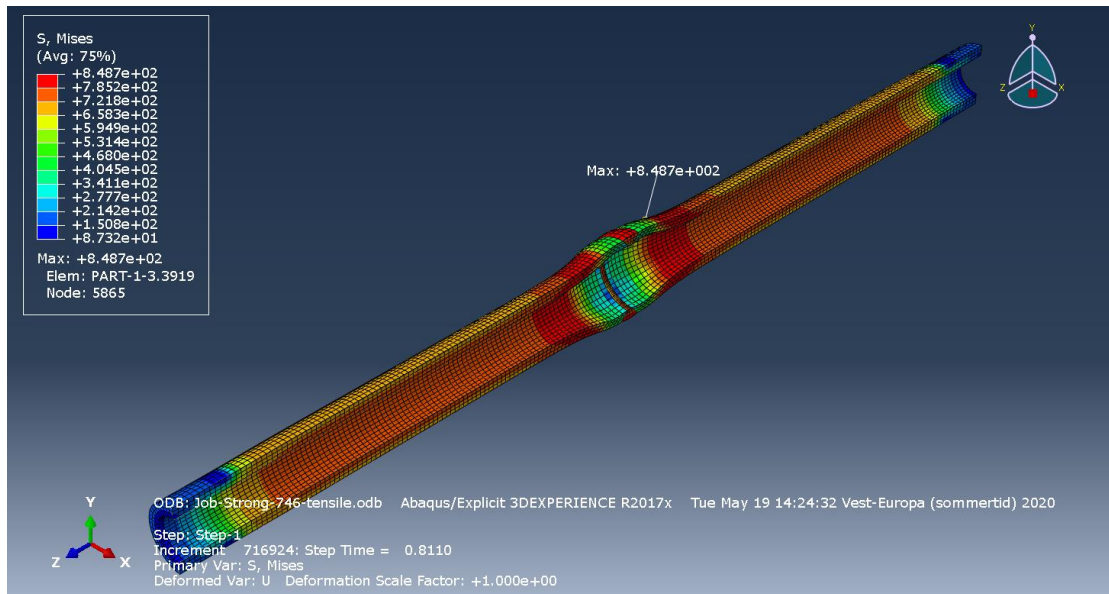


Figure 90: Numerical results from PWHT 746 strong electrode.

Table 29: Reaction forces on pipe with strong electrode.

PWHT procedure	Placement of fracture	Max internal stress [MPa]	Burst Pressure [MPa]
600	Base metal	807.425	195.923
650	Base metal	807.2	195.708
705	PWHT Base metal	805.849	194.639
746	Weld	741.357	163.642

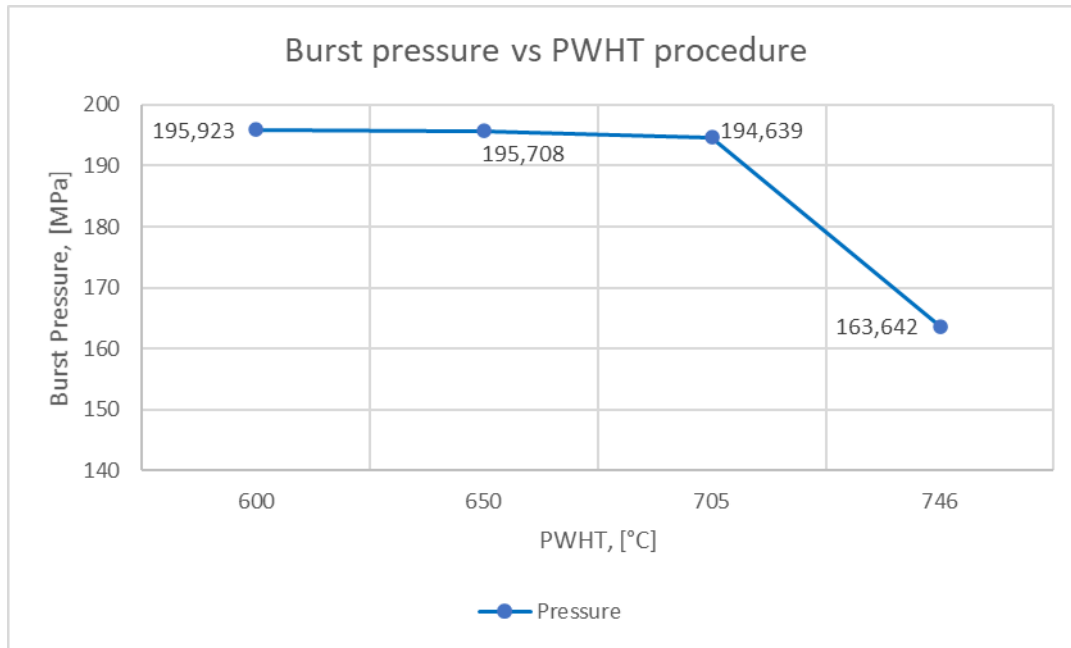


Figure 91: Resulting burst pressure based on material data from experiments and strong electrode.

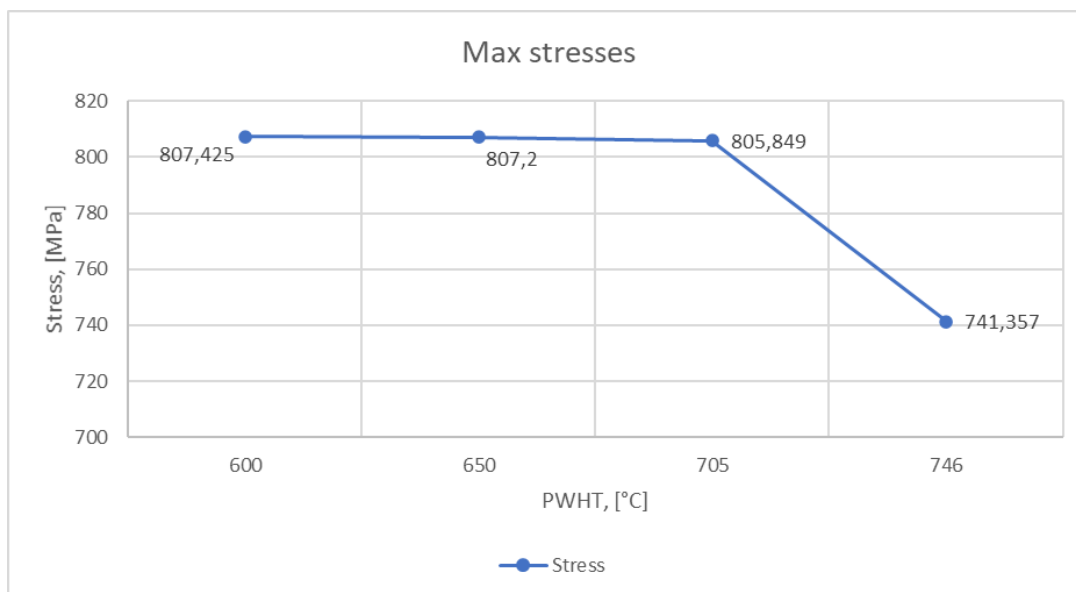


Figure 92: Highest stresses for pipe based on tensile experiment data with strong electrode.

7.2.4. Comparison of results

Table 30: Comparison of burst pressure for the pipe.

Test procedure	Burst pressure, weak electrode [MPa]	Burst pressure, strong electrode [MPa]	Deviation [%]
PWHT 600	196.648	195.923	0.4
PWHT 650	198.453	195.708	1.4
PWHT 705	187.474	194.644	3.8
PWHT 746	159.86	163.642	2.4

Table 31: Comparison of max stress for the fracture initiation of the pipe.

Test procedure	Max stress, weak electrode [MPa]	Max stress, strong electrode [MPa]	Deviation [%]
PWHT 600	808.006	807.425	0.1
PWHT 650	811.33	807.2	0.5
PWHT 705	716.249	805.849	12.5
PWHT 746	685.396	741.357	8.2

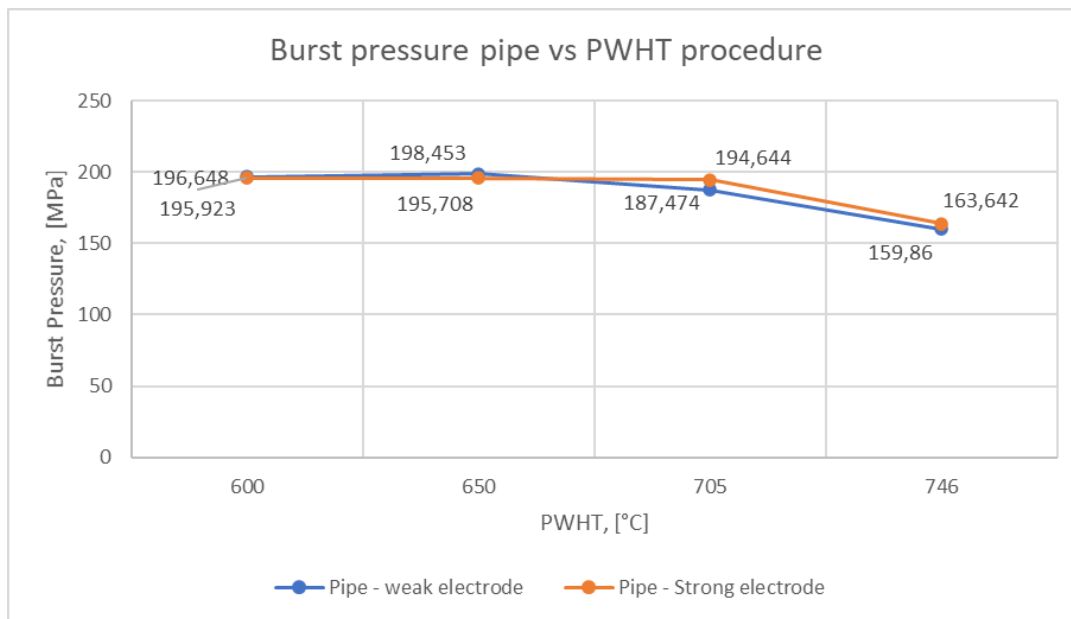


Figure 93: Weak vs strong electrode – Burst pressure based on material data from tensile tests.

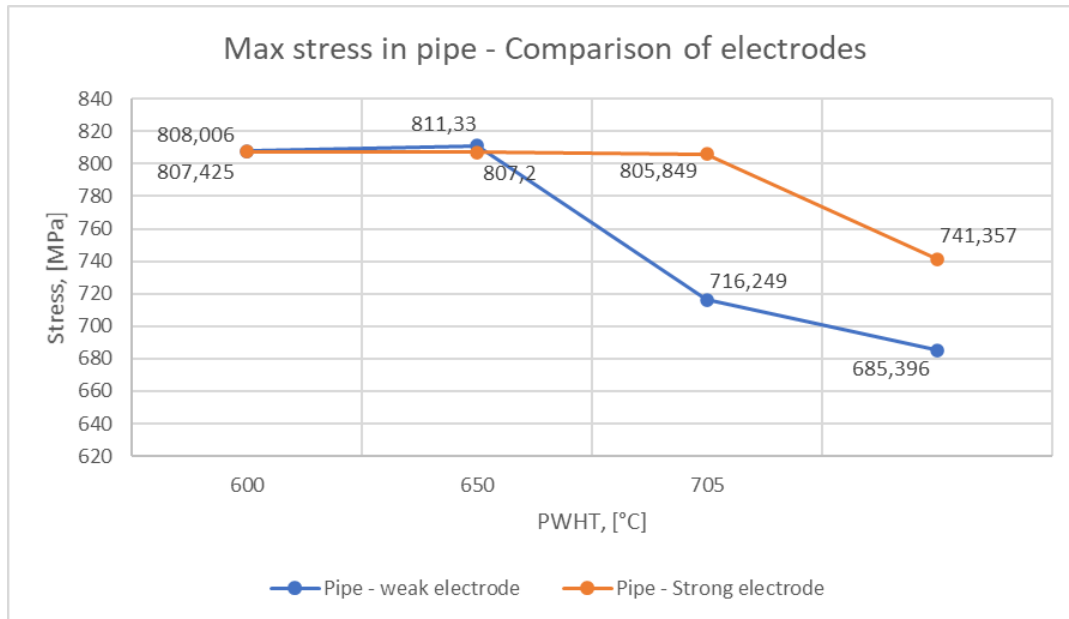


Figure 94: Weak vs strong electrode – Comparison of max stresses in pipe at fracture based on material data from tensile tests.

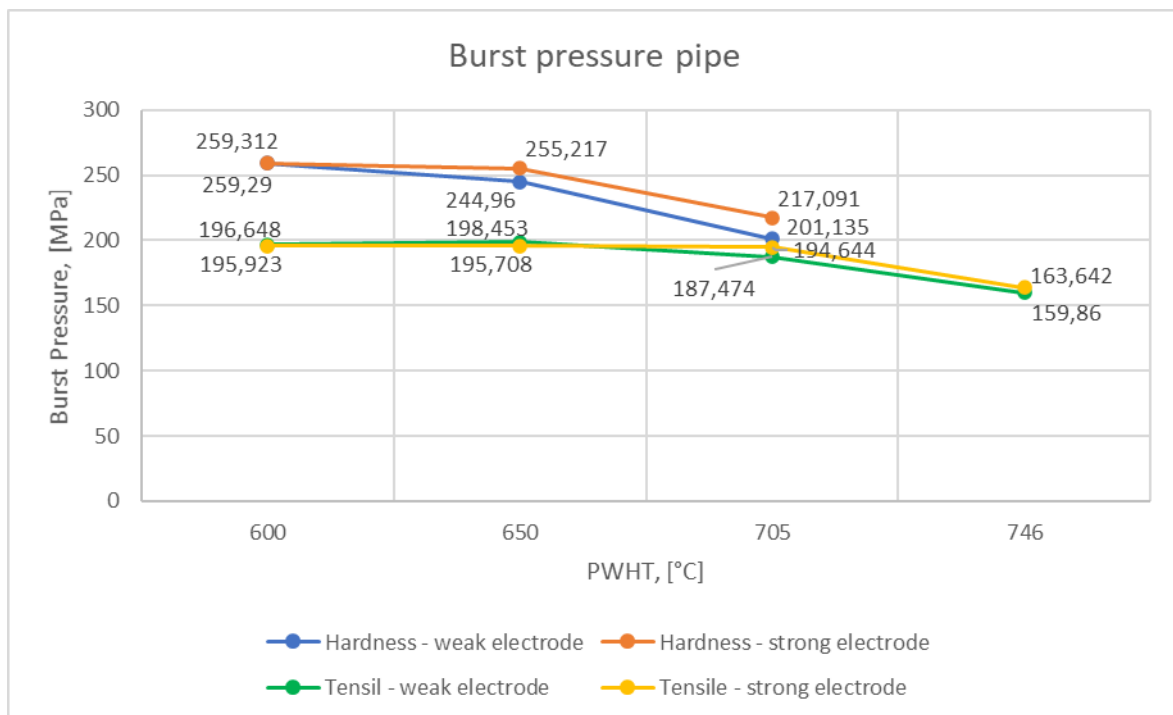


Figure 95: Presentation of burst pressure for all simulations, both based on hardness and tensile tests.

7.3. Results from pressure check

In this section the results from the control of service pressure are presented to verify the variations and if so the decrease in material strength and integrity in terms of design parameters set for pressure loads in the ASME B31.3.

Outer diameter	<i>D</i>	66,33 mm
Inside diameter of pipe	<i>d</i>	44,19 mm
Material and temperature coefficient	Y	0,43 -

Figure 96: Calculation of material and temperature coefficient, *Y*.

Applied pressure	P	51,7 MPa
Outer diameter	D	66,33 mm
Quality factor	E	0,8 -
Weld joint strength reduction factor	W	1 -
Material and temperature coefficient	Y	0,43 -
wall thickness	t	11,07 mm
User supplied mill tolerance	MT	-
Corrosion allowance	C	3 mm
Design stress	S	237,75 MPa

Figure 97: Calculation of the stress acting on the pipe with the estimated design pressure.

Internal design pressure	P	51,70 MPa
Allowable stress at component design temperature	S	25 ksi
Allowable stress at test temperature	ST	25 ksi
Minimum test gauge pressure	PT	77,55 Mpa

Figure 98: Calculation of the test pressure for the pipe with the estimated design pressure.

Test pressure	P	77,55 Mpa
Outer diameter	D	66,33 mm
Quality factor	E	0,8 -
Weld joint strength reduction factor	W	1 -
Material and temperature coefficient	Y	0,43 -
wall thickness	t	11,07 mm
User supplied mill tolerance	MT	-
Corrosion allowance	C	3 mm
Applied stress	S	356,70 MPa

Figure 99: Calculation of the stresses acting on the pipe under the estimated test pressure.

Table 32: Comparison of burst pressure and design pressure of 51.7 MPa.

Test procedure	Burst pressure [MPa]	Deviation from design pressure [MPa]	Deviation from design pressure [%]
Weak electrode - 600	196.648	144.948	280.364
Weak electrode - 650	198.453	146.753	283.855
Weak electrode - 705	187.474	135.774	262.619
Weak electrode - 746	159.86	108.16	209.207
Strong electrode - 600	195.923	144.223	278.961
Strong electrode - 650	195.708	144.008	278.545
Strong electrode - 705	194.644	142.944	276.487
Strong electrode - 746	163.642	111.942	216.522

Table 33: Comparison of max stress and design stress of 237.75 MPa.

Test procedure	Burst stress [MPa]	Deviation from design stress [MPa]	Deviation from design stress [%]
Weak electrode - 600	808.006	570.256	239.855
Weak electrode - 650	811.33	573.58	241.253
Weak electrode - 705	716.249	478.499	201.261
Weak electrode - 746	685.396	447.646	188.284
Strong electrode - 600	807.425	569.675	239.61
Strong electrode - 650	807.2	569.45	239.516
Strong electrode - 705	805.845	568.095	238.946
Strong electrode - 746	741.357	503.607	211.821

Table 34: Comparison of burst pressure and test pressure of 77.55 MPa.

Test procedure	Burst pressure [MPa]	Deviation from test pressure [MPa]	Deviation from test pressure [%]
Weak electrode - 600	196.648	119.098	153.576
Weak electrode - 650	198.453	120.903	155.903
Weak electrode - 705	187.474	109.924	141.746
Weak electrode - 746	159.86	82.31	106.138
Strong electrode - 600	195.923	118.373	152.641
Strong electrode - 650	195.708	118.158	152.364
Strong electrode - 705	194.644	117.094	150.992
Strong electrode - 746	163.642	86.092	111.015

Table 35: Comparison of max stress and test stress of 356.70 MPa.

Test procedure	Burst stress [MPa]	Deviation from test stress [MPa]	Deviation from test stress [%]
Weak electrode - 600	808.006	451.308	126.524
Weak electrode - 650	811.33	454.632	127.456
Weak electrode - 705	716.249	359.551	100.8
Weak electrode - 746	685.396	328.698	92.15
Strong electrode - 600	807.425	450.727	126.361
Strong electrode - 650	807.2	450.502	126.298
Strong electrode - 705	805.845	449.147	125.918
Strong electrode - 746	741.357	384.659	107.839

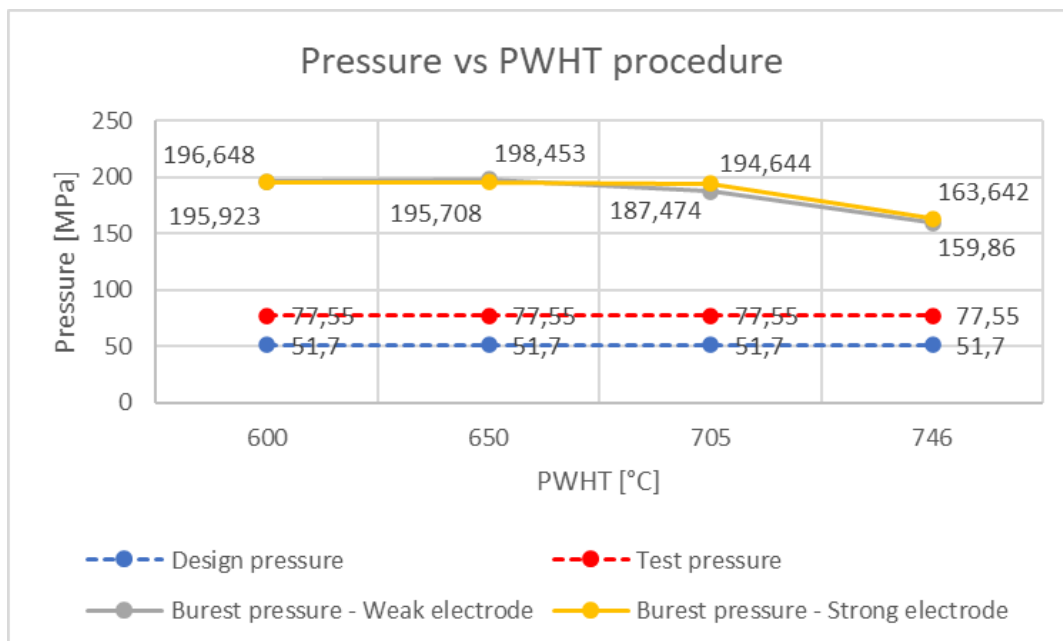


Figure 100: Visualization of service pressure and test pressure vs material burst pressure for the estimated and experimental hardness data collected.

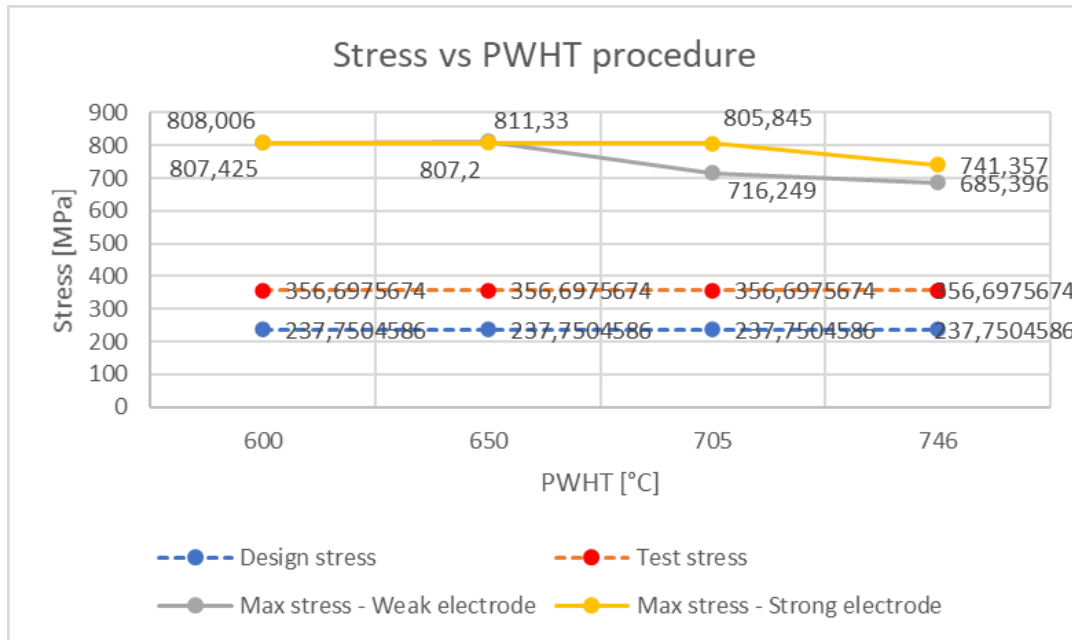


Figure 101: Visualization of service stress and test stress vs material stress capacity for the estimated and experimental hardness data collected.

8. Discussion

The focus of this thesis has been to evaluate the effect different post-weld heat treatment procedures in terms of strength and integrity of pressure pipe. The behavior of a welded pipe segment has been studied, with the material properties using different material data according to the chosen PWHT procedures and simulated in Abaqus. This chapter analyzes the results from the numerical simulations and the difference in terms of change in PWHT procedure.

8.1. Material parameters from hardness tests

In this study, the Holloman-Jaffe equation was used to estimate the hardness based on the temperature, carbon content and tempering time for the additional PWHT of 600°C based on hardness. One can also estimate the metal structures formed under heat treatment using the TTT or CCT diagram, and from this estimate the hardness of the composition of phases present, but there is uncertainty around this, so the use of the Holloman-Jaffe parameter was seen as the most preferred way to determine the outcome. As we can see from the results, the reaction from the different PWHT temperatures acts with a corresponding parallel decrease of calculated hardness and strength values, as seen in Figure 52. The prediction of the material parameters for the base material of the pipe affected by the PWHT is not possible to determine by numerical formulas as the production of steel can vary in terms of processing, such as tempering and work hardening. As a rule of thumb, it is said that the properties of the base material will not change during PWHT if the temperature does not reach the lower critical transformation temperature A1, at 720°C for AISI 4130 steel, and starts normalizing. Thus, normally only the properties of HAZ and the welding material are said to be affected by the PWHT. In the weld or fusion zone with the deposited metal from the electrode it is also hard to predict the outcome in terms of hardness due to the material composition, so the given data sheet was used in all simulations.

The weak electrode was an electrode with the minimum recommended material properties, but is not usually preferred due to its low tensile strength compared to the base metal. Normally the electrode should have a higher tensile strength than the base metal so that the weld would not have the weakest material, but given that the case in this study was the effect of different PWHTs, the point would in any case be validated to see the variation in behavior of more than one electrode if it is the case in some situations that the material has for some reason been weakened.

As can be seen from Table 12 and Table 13, the base metal and deposited weld metal subjected to the PWHT temperature 650°C has a very minor increase from 241.8 HV to 242.8 HV and is less affected by the PWHT. This is also close to the hardness in the material certificate of 238 HV (20 HRC). The HAZ has a decrease in hardness of 25 HV, from 270.2 to 245.2 HV after PWHT as preferred when tempering martensitic structures in HAZ.

The PWHT procedure with the holding temperature of 705°C shows that the hardness of the base metal subjected to the PWHT decreased 12.6 HV from 243.8 to 231.2 HV, but is still close to the value in the material certificate for the pipe. Results from the hardness test performed in the fusion zone for the deposited weld metal also have very little change - 224.6 and 198.2 HV - this is also very close

to the hardness test performed for the PWHT of 650°C. However, as for the HAZ, the reduction in hardness is larger and was shown to be approximately 58.3 HV, from 277 HV to 218.7 HV. The estimated hardness of HAZ subjected to the PWHT temperature of 600°C was estimated to be in the order of 269.5 HV, which has an estimated tensile strength of 850.4 MPa. It should also be pointed out that the H_{max} requirement of 22 HRC (250 HV) for “Sour Service” in this case is not fulfilled by this hardness.

8.2. Material parameters from tensile test

A total of ten specimens was tested under monotonic tensile load. Tests were performed to extract material data for the base material using two specimens, and one quenched specimen was tested for indication of material properties of the heat-affected zone before PWHT. All the tests were conducted until fracture with a constant strain rate of 0.039mm/s and the plasticity model could easily be made from the stress-strain data for all the uniform monotonic samples; all stress-strain diagrams from the tests samples are presented in Appendix N. The performed tensile tests were executed in a reliable manner and achieved reasonably good results except for one sample, “Base 746”, where the fracture occurred too close to the edge of the extensometer, so some adjustments were made in terms of damage behavior after necking for this sample, using the base material as reference for the damage accumulation after necking.

It must be pointed out that the samples were not preheated as would be done for an on-site weld when joining the pipe. However, what effect the preheating has to say in terms of material strength remains to be proven, but this is considered to be minor when heating to a temperature of not more than 120°C as were the hardness tested samples in the previous study. The study mainly focuses on the transformation that occurs during PWHT below the A1 temperature, but as seen from the ASME B31.3-2012, the PWHT range was set between 705°C and 746°C so to test the highest temperature would also be of interest due to the transformation of phase that occurs at 720°C (estimated in Weld Note) where the Austenite transformation takes place, if for some reason there has been a case where the PWHT has been too high. The interest in that case would then be, what occurs to the material affected by such a high PWHT temperature. However, as can be read in theory, this would rarely be the case due to the general rule that the PWHT performed should be 20°C under the PWHT temperature set in standard and not above the A1 temperature of the material used.

The results for the selected specimens were presented in the previous results section. The welded material was not tensile tested in this study. In the PWHT procedure at 600°C, only one quenched sample representing the HAZ was tested due to a lack of tensile specimens. Yet, this is the heat treatment with the lowest temperature affecting the base material and the general rule of thumb is that the base material will not change properties to a large extent. When examining the material behavior from the tested base material at 650°C and 705°C, where the deviation of material behavior is minor, when looking at the affected and unaffected base material, it is then assumed to be even less for the affected base material when PWHT is at 600°C. However, as seen for the affected base material at 746°C, there is a notable drop in strength of 55.483 MPa compared to the original base material.

The tensile test of the quenched specimen resulted in a hard and brittle fracture with a high strength, as can be expected and desired. The test reached the maximum of what the test machine could perform at approximately 25kN. From the results, it can be assumed that there is a martensitic structure after the quenching procedure, as one can expect in the HAZ after welding. From the tensile tests from the then heat-treated martensitic samples representing the HAZ, there was a clear tendency towards softer material as the temperature became higher, as expected. As can be seen from Figure 77, Figure 78, Figure 79 and Figure 80, one can see that the HAZ and heat treated base material acquires lower strength as the temperature rises. This shows the effect taking place under heat treatment with the diffusion of interstitially locked carbon, where the steel transforms from a hard and brittle structure to a tougher and more ductile structure. However, it also shows the effect of the weakening of the welded section when the temperature becomes too high, at which point the strength will be decreased unfavorably. This weakening results in the placement of fracture will change from happening in the base metal of the pipe to the heat-treated area.

8.3. Numerical setup

The calibration of the plastic behavior was done the same way for both approaches of collecting material data, by using the effective true stress-strain curve. A linear behavior was chosen in this study in terms of damage behavior after necking. The Ductile Damage model was used and calibrated to follow the degradation of all the experimental stress-strain curves after necking by using the linear damage evolution and calibration of the degradation line using Ramberg and Osgood as seen in Figure 58. Before the simulations, a control of mesh sensitivity was performed in terms of accuracy of results, the mesh size of 5mm was chosen with a deviation of approximately 2%, as seen from Table 19. However, as the investigation preferred to have a larger model and the Abaqus license maintains some restrictions in terms of number of elements, the mesh was set to 5mm with no refinements. It must be mentioned that for a better indication of the plasticity that occur in the fracture area and for a more precise view of the failure mechanisms, a much smaller mesh is needed than that which was tested in this study. In addition, the study does not focus on the brittle failure mechanisms that may occur. The mesh size of 4mm was tested but it was running slower and with errors that led to the abortion of some simulations. The indication and placement of failure were still possible to indicate in terms of the effects of the different PWHT procedures.

8.4. Numerical simulations

The results from the numerical simulations of the material data from both the hardness and tensile tests showed the tendency of the failure to occur closer to the heat-treated welded section of the pipe at higher temperature starting at around 650°C. If comparing the simulations done for material tensile test data to the simulations from the hardness tests, the failure occurs in the welded area at lower temperature, even if simulating with a stronger electrode due to the material data also for the PWHT base material. In terms of numerical simulations, it is obvious to see that with a higher PWHT temperature the placement of fracture is occurring in the weld due to the lower strength of the HAZ

and affected base material, owing to loss of stiffness and strength close to the weld due to the heat treatment.

For the simulations based on hardness test, the fracture was occurring in the base metal of the pipe in the simulations for PWHT 600°C with strong and weak electrode at pressure around 259 MPa, and for the PWHT 650°C with strong electrode at pressure around 255.217 MPa. For the rest of the PWHT procedures the fracture occurred in the weld, where the welds refer both to the area of HAZ and weld material. The PWHT at 650°C with the weak electrode the pressure was approximately 244.96 MPa, while with the PWHT at 705°C the weak and strong electrode failed with a burst pressure of 201.135 and 217.091 MPa.

As can be seen based on material data from the tensile test, the fracture occurs in the base material for PWHT of 600°C with a burst pressure of 196.648 and 195.923 MPa and 650°C with burst pressure of approximately 198.453 and 195.708 MPa for both electrodes. For PWHT procedure 705°C and 746°C using the weak electrode, the weld metal fails first at approximately 187.474 and 195.86 MPa. Using the strong electrode, the failure occurs in the affected base material and for PWHT 705°C at a pressure of 194.644 MPa and for the PWHT 746°C the HAZ fails first at approximately 159.86 MPa and is the lowest burst pressure for all the simulations. One must also bear in mind that because the weld has a thicker section, this will compensate for some of the lower strength of the material in the way the geometry is conducted in this study. However, this is perhaps not the case in a real scenario where the weld has variations in its geometry and potential minor defects that can cause stress concentrations in other places around the welded area. Examples of this can be undercut or a too high a reinforcement in the weld toe area. As can be seen from Figure 79, the strength of the HAZ for PWHT 705°C is slightly lower than both weld material and affected base material, but is strengthened by the weld, and results in the affected base material failing first.

Overall, the different PWHTs simulated in this study shows that the material capacity in terms of burst pressure and fracture stress for the welded pipe is above the design pressure and stress by approximately 209.207% to 188.284% for the simulations based on material data from tensile tests, shown in Table 32 and Table 33. The test pressure for the pipe was also evaluated since the pipe will be tested under higher pressure when heat treatment has been performed; the result from this shows that the test pressure is also below the burst pressure and fracture stress by approximately 106.138% to 92.150% in this case, shown in Table 34 and Table 35. Only the tensile-tested results were checked in terms of capacity due to the lower strength and, more importantly, the more realistic material data.

8.5. Comparison of material parameters

The results show that the base material that was tested had a lower yield and tensile strength compared to what is shown in the material certificate for the pipe. However, the greatest impact on the difference in material parameters was the strain and ductility since, when calculating the true tensile stress using the elongation from the certificate, the strength is shown to be too high compared to the real case. From the tensile tests the approximate tensile strength was 98.292 MPa and 116.784 MPa under the true tensile strength estimated from the certificate. The results from the

tensile-tested specimens representing the HAZ showed that the yield and tensile stress were higher than that estimated for all PWHT procedures, as seen collated in Table 36, where the deviation just also got larger with the higher temperature. The estimated fracture strain was actually not that far from the actual strain of the tempered HAZ, but there was a difference in terms of stress at ultimate strength. The estimated hardness and strength of the PWHT procedure at 600°C by using Holloman-Jaffe turned out to be a reasonable indication of strength, at least when comparing the ultimate strength where the deviation was 25.508 MPa. If the hardness turns out to also be accurate when the HAZ undergoes PWHT at 600°C, one shall than keep in mind that the H_{max} requirement may not be fulfilled and a longer tempering time is needed to reduce the hardness accordingly. The results show the tendency towards reduction of strength with an increase in temperature, and so by using the hardness one is at least on the conservative side in terms of strength indication using hardness data, as can be seen from Table 36.

Table 36: Comparison of stress at ultimate tensile strength for HAZ.

PWHT procedure	Hardness data, true tensile stress, [MPa]	Tensile tests, true tensile stress, [MPa]	Deviation, [MPa]
600°C	850.4	875.908	25.508
650°C	765.4	812.816	47.416
705°C	672.8	725.308	52.508

Even if there was only one tensile sample for the tested material that represented each PWHT procedure, it is a good indication of how the material reacts to the PWHT procedures in a more realistic manner. It should also be pointed out that the ratio between the yield and tensile stresses is above the limit of 0.85 in the certificate and for the tests for the base material as mentioned in chapter 3.14..

8.6. Sources of error

When using numerical formulas based on hardness for approximating strength and ductility that cannot be exactly verified, there are errors in the predictions of data that are calculated for that part of this study. The numerical mesh sensitivity analysis was performed with a deviation of approximately 2%. Still, other errors may occur as well, such as with the mass scaling. When calculating the hardness using the Holloman-Jaffe equation, the c parameter is not possible to know exactly without having the exact curve for the steel grade used and, in this case, it must be adjusted after experimental hardness tests. The calculation of the tensile and yield stresses also comes with deviations in terms of accuracy compared to the actual strength and strain shown from tensile tests of the material used.

9. Conclusion

The aim of this study was to investigate how different post-weld heat treatment (PWHT) procedures would affect the welded pipe connection in terms of strength and integrity, based on the change made to ASME B31.3 in 2014. The verification of strength and damage accumulation has been conducted using Abaqus Explicit and the damage model Ductile Damage. To investigate the effect of the PWHT procedures, two approaches have been employed: one using material parameters from hardness results from a previous study and a second using material parameters from experimental tensile tests. Numerical formulas have been used to calculate the corresponding yield and tensile stresses for the material when based on hardness, together with material data from the material certificate to evaluate the material properties. The plasticity of the material for both the base metal of the pipe, HAZ and weld metal has been plotted in Abaqus to investigate the effects of the PWHT as realistically as possible. The pipe was investigated numerically by means of internal pressure load to failure. As there are several different welding electrodes, two typical electrodes have also been used in the simulations; only the material properties from the certificate have been used. When analyzing the effect of heat treatments, only one tempering time has been considered in this study. One shall also bear in mind that there is a risk of not getting the hardness requirements fulfilled if using too low a temperature.

Based on the results achieved, the following conclusions can be drawn:

- 1) It can be concluded that with a high PWHT temperature below but close to the A1 temperature, the risk of failure occurring in the heat-treated part is present due to decrease in strength compared to a lower temperature.
- 2) As can be seen from the results from the pressure check performed according to ASME B31.3 of the simulated pipe in this study, it can be concluded that the strength capacity for the pipe is satisfied, but not without consequences in terms of placement of failure.
- 3) There is a change in terms of placement of failure due to the decrease in strength of the base material subjected to the PWHT procedure of 705°C compared to 650°C, where failure is occurring in the heat-treated part of the pipe as a result of the higher temperature.
- 4) The failure mechanisms of the pipe segment that was simulated and analyzed were of a ductile manner - "ductile rupture" - where the weakest part of the modeled pipe expanded like a balloon until a uniform rupture occurring by element deletion around the expanding part of the pipe. The defined material strength, thickness, and geometry defines the placement of failure.
- 5) When using a higher PWHT temperature, the study shows that the welded section of the pipe achieves a lower strength, especially in the HAZ as it undergoes the heat treatment. The FE analysis shows that the mid-section loses stiffness as the strength decreases, gaining ductility and toughness.

10. Suggestions for further work

Suggestions for future work from this study include the following:

- This study has been limited to using the hardness test performed in a previous study due to current lab restrictions; a suggestion is to investigate the hardness of the tensile test specimen that was used in this study to see if these could be numerically calculated more precisely in terms of strength- hardness correlation.
- Due to the limited amount of tensile test specimens in this study to verify the material behavior, a further verification of the material properties after post-weld heat treatment is recommended; further testing is also recommended due to potential errors during testing.
- In this study two types of typical electrode were used, but all material behavior was estimated from the material certificates of the electrodes. In order also to simulate the effect and behavior of the welding material that is deposited and affected by the heat treatment more realistically, material testing would be recommended.
- The numerical simulations performed in this study were not intended to simulate the behavior of the fracture or of crack initiation. This would also be of interest for further work in terms of failure initiation of a welded pipe. Interesting scenarios to investigate would typically be flaws or hydrogen cracks near the weld or areas affected by corrosion attacks.
- Only one loading scenario on a straight pipe segment was investigated in this study, but further numerically investigating the behavior also of different pipe geometries and perhaps different loading scenarios could be of interest. This is in order to investigate if there are welded connections that will be affected at higher stress concentrations that may be more critical if subjected to the incorrect heat treatment. This also involves other structures, not only piping systems.

Bibliography

Uncategorized References

- [1] D. Rybakov, "Post weld heat treatment of welded low alloyed steel pipes," Master, Department of Engineering Sciences, University of Agder, Norway, 2018. [Online]. Available: <https://uia.brage.unit.no/uia-xmlui/handle/11250/2617141>
- [2] K. Masubuchi, *Analysis of welded structures : residual stresses, distortion, and their consequences*, 1st ed. (International series on materials science and technology v 33). Oxford ; New York: Pergamon Press, 1980, pp. xi, 642 p.
- [3] R. H. Leggatt, "Residual stresses in welded structures," (in English), *Int J Pres Ves Pip*, vol. 85, no. 3, pp. 144-151, Mar 2008, doi: 10.1016/j.ijpvp.2007.10.004.
- [4] K. J. Ahmed Khaleel, "Post-Weld Heat Treatment – Case Studies,," *BARC Newsletter*, no. Founder's Day Special Issue, pp. 111-115, 2002. [Online]. Available: <http://barc.gov.in/publications/nl/2003/200310-17.pdf>.
- [5] R. S. Funderburk, "Key Concepts in Welding Engineering: Postweld Heat Treatment," *Welding Innovation*, vol. Vol XV, No. 2., no. Postweld Heat Treatment, 1998. [Online]. Available: <http://www.jlff.org/v/vspfiles/assets/pdf/wi298.pdf>.
- [6] A. A. Fernandes, A. M. P. d. Jesus, and R. N. Jorge, F. o. E. o. P. PortoPortugal, Ed. *Monotonic and Ultra-Low-Cycle Fatigue Behaviour of Pipeline Steels*. 6330 Cham, Switzerland: Springer, 2018.
- [7] I. JOURNAL, "The Power of Proper Post-Weld Heat Treatment," *INSPECTIONEERING JOURNAL*, May/June 2017. [Online]. Available: <https://inspectioneering.com/journal/2017-06-21/6562/the-power-of-proper-post-weld-heat-treat>.
- [8] N. Bailey, *Weldability of Ferritic Steels*. England: Woodhead Publishing Ltd 1994.
- [9] WelderDestiny. "Post Weld Heat Treatment (PWHT)." WelderDestiny. <https://www.welderdestiny.com/post-weld-heat-treatment.html> (accessed 2016).
- [10] E. Englund, "Experimental calibration of continuum damage models," Master, Department of Engineering sciences, University of Agder,, Norway, 2019.
- [11] D. G. R. William D Callister, *Materials Science and Engineering*, 9th Edition SI Version ed. New York, United States: John Wiley & Sons Inc (in English), 2014.
- [12] D. o. S. T. Diagrams. "AISI 4130 Steel." Copyright © 2019 by Steel Data. All Rights Reserved. <http://www.steeldata.info/std/demo/data/4970.html> (accessed.
- [13] S. Kou, *WELDING METALLURGY*, SECOND EDITION ed. New Jersey: A JOHN WILEY & SONS, INC., PUBLICATION, 2003.
- [14] H. K. D. H. B. a. R. W. K. Honeycombe, *Steels: Microstructure and Properties*, Fourth edition ed. Butterworth-Heinemann, 2006.
- [15] H. K. D. H. Bhadeshia and J. W. Christian, "Bainite in Steels," (in English), *Metall Trans A*, vol. 21, no. 4, pp. 767-797, Apr 1990, doi: Doi 10.1007/Bf02656561.
- [16] G. R. Speich and W. C. Leslie, "Tempering of Steel," (in English), *Metall Trans*, vol. 3, no. 5, pp. 1043-&, 1972, doi: Doi 10.1007/Bf02642436.
- [17] Y. Y. Song, X. Y. Li, L. J. Rong, and Y. Y. Li, "The influence of tempering temperature on the reversed austenite formation and tensile properties in Fe-13%Cr-4%Ni-Mo low carbon martensite stainless steels," (in English), *Mat Sci Eng a-Struct*, vol. 528, no. 12, pp. 4075-4079, May 15 2011, doi: 10.1016/j.msea.2011.01.078.
- [18] R. C. HIBBELER, *MECHANICS OF MATERIALS*, NINTH EDITION ed. Pearson Prentice Hall, 2014.

- [19] X. Y. Lauralice C.F. Canale, Jianfeng Gu, George E. Totten "A historical overview of steel tempering parameters " *Int. J. Microstructure and Materials Properties*, vol. 3, 2008. [Online]. Available: http://mmm.sjtu.edu.cn/userfiles/1/files/2008-96_Canale.pdf. Inderscience Enterprises Ltd.
- [20] C. R. Brooks, *Principles of the Heat Treatment of Plain Carbon and Low Alloy Steels*. USA: ASM International, 1996.
- [21] J. D. Verhoeven, *Steel Metallurgy for the Non-Metallurgist*. ASM International, 2007.
- [22] M. F. Ashby and K. E. Easterling, "A 1st Report on Diagrams for Grain-Growth in Welds," (in English), *Acta Metallurgica*, vol. 30, no. 11, pp. 1969-1978, 1982, doi: Doi 10.1016/0001-6160(82)90100-6.
- [23] D. S. P. T. Bipin kumar Srivastava, Prakash Jyoti, "A Review on Effect of Preheating and/or Post Weld Heat Treatment (Pwht) on Mechanical Behaviour of Ferrous Metals.," *International Journal of Engineering Science and Technology*, vol. Vol. 2(4), 2010. [Online]. Available: https://www.researchgate.net/publication/50273836_A_Review_on_Effect_of_Preheating_andor_Post_Weld_Heat_Treatment_Pwht_on_Mechanical_Behaviour_of_Ferrous_Metals.
- [24] N. E. Hannerz and Dekazinc.F, "Kinetics of Austenite Grain Growth in Steel," (in English), *J Iron Steel I*, vol. 208, pp. 475-&, 1970. [Online]. Available: <Go to ISI>://WOS:A1970G346000015.
- [25] J. C. L. John N. DuPont, Samuel D. Kiser, *Welding Metallurgy and Weldability of Nickel-Base Alloys*. New Jersey: John Wiley & Sons, Inc. , 2009.
- [26] R. M. Miranda and M. A. Fortes, "Austenite Grain-Growth, Microstructure and Hardness in the Heat-Affected Zone of a 2.25cr-1mo Steel," (in English), *Mat Sci Eng a-Struct*, vol. 108, pp. 1-8, Feb 1989, doi: Doi 10.1016/0921-5093(89)90399-7.
- [27] K. Easterling, *Introduction to the Physical Metallurgy of Welding*, 2nd ed ed. Oxford: Butterworth Heinemann, , 1992.
- [28] G. Agarwal, H. Gao, M. Amirthalingam, and M. Hermans, "Study of Solidification Cracking Susceptibility during Laser Welding in an Advanced High Strength Automotive Steel," (in English), *Metals-Basel*, vol. 8, no. 9, Sep 2018, doi: ARTN 673 10.3390/met8090673.
- [29] W. F. Savage, E. F. Nippes, and E. S. Szekeres, "Study of Weld Interface Phenomena in a Low-Alloy Steel," (in English), *Weld J*, vol. 55, no. 9, pp. S260-S268, 1976. [Online]. Available: <Go to ISI>://WOS:A1976CD50200010.
- [30] *Petroleum and natural gas industries - Materials for use in H2S-containing environments in oil and gas production*, N. I. I. 2005, U.S.A. , 2005-09-01 2005. [Online]. Available: <http://www.antaressoffshore.com/internal/engineering/stds/nace/NACE%20MRO175.pdf>
- [31] Å. Gunleiksrud, *Materialteknikk offshore -Transportrør for olje og gass*. Norway: Norwegian Steel Association, 2010.
- [32] *ASME Code for Pressure Piping, B31.3*, T. A. S. O. M. ENGINEERS, USA, 2016.
- [33] *ASME Code for Pressure Piping, B31*, T. A. S. O. M. ENGINEERS, USA, 2014.
- [34] D. Tabor, "The Hardness and Strength of Metals," (in English), *J I Met*, vol. 79, no. 7, pp. 1-18, 1951. [Online]. Available: <Go to ISI>://WOS:A1951XR08300001.
- [35] Z. P. Zhang, Q. Sun, C. W. Li, and W. Z. Zhao, "Theoretical calculation of the strain-hardening exponent and the strength coefficient of metallic materials," (in

- English), *J Mater Eng Perform*, vol. 15, no. 1, pp. 19-22, Feb 2006, doi: 10.1361/10599490524057.
- [36] J. George E. Dieter, *Mechanical Metallurgy*. USA: McGraw-Hill Book Company, 1961.
- [37] J. R. Cahoon, "Improved Equation Relating Hardness to Ultimate Strength," (in English), *Metall Trans*, vol. 3, no. 11, pp. 3040-&, 1972, doi: Doi 10.1007/Bf02652880.
- [38] J. R. Cahoon, W. H. Broughton, and A. R. Kutzak, "Determination of Yield Strength from Hardness Measurements," (in English), *Metall Trans*, vol. 2, no. 7, pp. 1979-+, 1971. [Online]. Available: <Go to ISI>://WOS:A1971J748000032.
- [39] E. J. Pavlina and C. J. Van Tyne, "Correlation of Yield Strength and Tensile Strength with Hardness for Steels," (in English), *J Mater Eng Perform*, vol. 17, no. 6, pp. 888-893, Dec 2008, doi: 10.1007/s11665-008-9225-5.
- [40] *Rules for the Design, Construction and Inspection of Offshore Structure*, D. N. Veritas, Høvik, Norway, 1977.
- [41] O. M. Akselsen, G. Rorvik, M. I. Onsoien, and O. Grong, "Assessment and Predictions of Haz Tensile Properties of High-Strength Steels - an Investigation into the Grain-Coarsened Haz of Single-Pass Weldments Reveals a Means of Predicting Haz Strength and Ductility," (in English), *Weld J*, vol. 68, no. 9, pp. S356-S362, Sep 1989. [Online]. Available: <Go to ISI>://WOS:A1989AM81900012.
- [42] R. D. Cook, *Concepts and applications of finite element analysis*. Wiley, 2001.
- [43] A. M.-. MIT. "Types of problems suited for Abaqus/Explicit." MIT. <https://abaqus-docs.mit.edu/2017/English/SIMACAEGSARefMap/simagsa-c-ovwtypes.htm> (accessed).
- [44] A. M.-. MIT. "Quasi-Static Analysis with Abaqus/Explicit." <https://abaqus-docs.mit.edu/2017/English/SIMACAEGSARefMap/simagsa-m-Quasi-sb.htm> (accessed).
- [45] A. M.-. MIT. "Mass scaling." (accessed).
- [46] T. L. Anderson, *FRACTURE MECHANICS (Fundamentals and Applications)*. UIS: Taylor & Francis Group, LLC, 2005.
- [47] A. M.-. MIT. "Damage initiation for ductile metals." <https://abaqus-docs.mit.edu/2017/English/SIMACAEMATRefMap/simamat-c-damageinitductile.htm> (accessed).
- [48] D. A. a. D. R. M. S. R. Hiremath, *Stress Triaxiality in Damage Models*. Springer, Singapore, 2017.
- [49] SIMULA. "Getting started with Abaqus: Interactive Edition." SIMULA. <http://dsk.ippt.pan.pl/docs/abaqus/v6.13/books/usb/default.htm> (accessed 25.09, 2019).
- [50] A. M.-. MIT. "Defining plasticity in Abaqus." <https://abaqus-docs.mit.edu/2017/English/SIMACAEGSARefMap/simagsa-c-matdefining.htm> (accessed).
- [51] A. M.-. MIT. "Damage evolution and element removal for ductile metals." <https://abaqus-docs.mit.edu/2017/English/SIMACAEMATRefMap/simamat-c-damageevolductile.htm> (accessed).
- [52] A. M.-. MIT. "About progressive damage and failure." <https://abaqus-docs.mit.edu/2017/English/SIMACAEMATRefMap/simamat-c-damageoverview.htm> (accessed).

- [53] *DNV-RP C208: DETERMINATION OF STRUCTURAL CAPACITY BY NON-LINEAR FE ANALYSIS METHODS*, D. N. VERITAS, 2013.
- [54] *ASME Code for Pressure Piping, B31*, T. A. S. O. M. ENGINEERS, USA, 2012.
- [55] *Standard Test Methods for Tension Testing of Metallic Materials1, Designation: E 8/E 8M – 08*, A. Internationa, March 2008 2008. [Online]. Available: https://faculty.engr.utexas.edu/sites/default/files/astm_e8_08_0.pdf

Appendix A

Table 5.3 Approximate equivalent hardness numbers for several hardness tests on steels

HRC	HV	HB(a)	HRA	HRB	Ultimate tensile strength	
					MPa	ksi
68	940	...	85.6
67	900	...	85.0
66	865	...	84.5
65	832	(739)	83.9
64	800	(722)	83.4
63	772	(705)	82.8
62	746	(688)	82.3
61	720	(670)	81.8
60	697	(654)	81.2
59	674	(634)	80.7
58	653	615	80.1
57	633	595	79.6
56	613	577	79.0
55	595	570	78.5	...	2075	301
54	577	543	78.0	...	2013	292
53	560	525	77.4	...	1951	283
52	544	512	76.8	...	1882	273
51	528	496	76.3	...	1820	264
50	513	481	75.9	...	1758	255
49	498	469	75.2	...	1696	246
48	484	455	74.7	...	1634	237
47	471	443	74.1	...	1579	229
46	458	432	73.6	...	1531	222
45	446	421	73.1	...	1482	215
44	434	409	72.5	...	1434	208
43	423	400	72.0	...	1386	201
42	412	390	71.5	...	1338	194
41	402	381	70.9	...	1296	188
40	392	371	70.4	...	1248	181
39	382	362	69.9	...	1213	176
38	372	353	69.4	...	1179	171
37	363	344	68.9	...	1158	168
36	354	336	68.4	(109.0)	1117	162
35	345	327	67.9	(108.5)	1082	157
34	336	319	67.4	(108.0)	1055	153
33	327	311	66.8	(107.5)	1027	149
32	318	301	66.3	(107.0)	1000	145
31	310	294	65.8	(106.0)	979	142
30	302	286	65.3	(105.5)	951	138
29	294	279	64.7	(104.5)	931	135
28	286	271	64.3	(104.0)	910	132
27	279	264	63.8	(103.0)	883	128
26	272	258	63.3	(102.5)	862	125
25	266	253	62.8	(101.5)	841	122
24	260	247	62.5	(101.0)	827	120
23	254	243	62.0	100.0	807	117
22	248	237	61.5	99.0	786	114
21	243	231	61.0	98.5	772	112
20	238	226	60.5	97.8	758	110
(18)	230	219	...	97.8	731	106
(16)	222	212	...	95.5	703	102
(14)	213	203	...	93.9	676	98
(12)	204	194	...	92.3	648	94
(10)	196	187	...	90.7	621	90
(8)	188	179	...	89.5	600	87
(6)	180	171	...	85.5	579	84
(4)	173	165	...	85.5	552	80
(2)	166	158	...	83.5	531	77
(0)	160	152	...	81.7	517	75

Figure 102: Hardness conversion table [21].

Appendix B

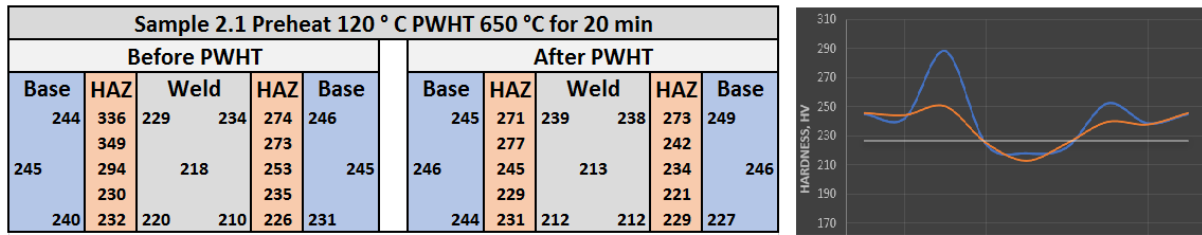


Figure 103: Hardness test results for PWHT procedure at 650°C [1].

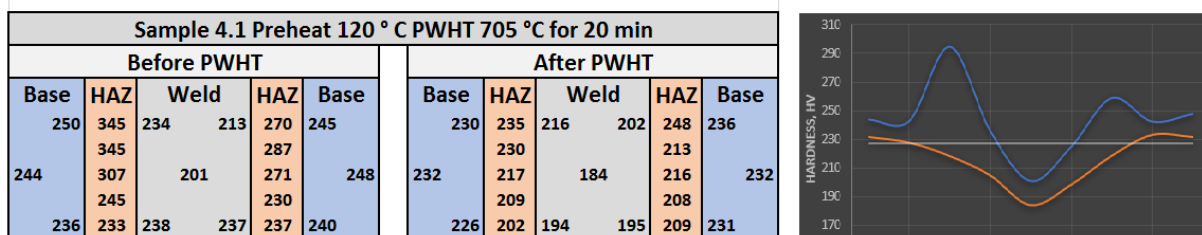


Figure 104: Hardness test results for PWHT procedure at 705°C [1].

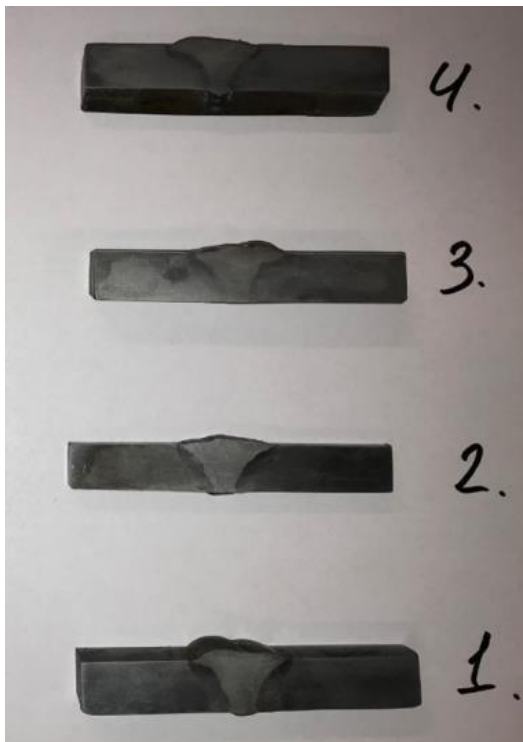


Figure 105: Some of the welded pipe sections that were hardness tested in the previous study [1].

Appendix C

Table 331.1.1 Requirements for Heat Treatment

Base Metal P-No. [Note (1)]	Weld Metal Analysis A-Number [Note (2)]	Base Metal Group	Nominal Wall Thickness		Specified Min. Tensile Strength, Base Metal		Metal Temperature Range		Holding Time			Brinell Hardness, Max. [Note (4)]
									Nominal Wall [Note (3)]		Min. Time, h	
			mm	in.	MPa	ksi	°C	°F	min/mm	hr/in.		
1	1	Carbon steel	≤ 20	≤ ¾	All	All	None	None
			> 20	> ¾	All	All	593-649	1,100-1,200	2.4	1	1	...
3	2, 11	Alloy steels, Cr ≤ 1/2%	≤ 20	≤ ¾	≤ 490	≤ 71	None	None
			> 20	> ¾	All	All	593-718	1,100-1,325	2.4	1	1	225
			All	All	> 490	> 71	593-718	1,100-1,325	2.4	1	1	225
4 [Note (5)]	3	Alloy steels, 1/2% < Cr ≤ 2%	≤ 13	≤ 1/2	≤ 490	≤ 71	None	None
			> 13	> 1/2	All	All	704-746	1,300-1,375	2.4	1	2	225
			All	All	> 490	> 71	704-746	1,300-1,375	2.4	1	2	225
5A, 5B, 5C [Note (5)]	4, 5	Alloy steels (2 1/4% ≤ Cr ≤ 10%) ≤ 3% Cr and ≤ 0.15% C ≤ 3% Cr and ≤ 0.15% C > 3% Cr or > 0.15% C	≤ 13	≤ 1/2	All	All	None	None
			> 13	> 1/2	All	All	704-760	1,300-1,400	2.4	1	2	241
			All	All	All	All	704-760	1,300-1,400	2.4	1	2	241
6	6	High alloy steels martensitic A240 Gr. 429	All	All	All	All	732-788	1,350-1,450	2.4	1	2	241
			All	All	All	All	621-663	1,150-1,225	2.4	1	2	241
7	7	High alloy steels ferritic	All	All	All	All	None	None
8	8, 9	High alloy steels austenitic	All	All	All	All	None	None
9A, 9B	10	Nickel alloy steels	≤ 20	≤ ¾	All	All	None	None
			> 20	> ¾	All	All	593-635	1,100-1,175	1.2	1/2	1	...
10	...	Cr-Cu steel	All	All	All	All	760-816 [Note (6)]	1,400-1,500 [Note (6)]	1.2	1/2	1/2	...

Figure 106: PWHT procedure ASME B31.3-2012-Page 68[54].

Table 331.1.1 Requirements for Heat Treatment (Cont'd)

Base Metal P-No. [Note (1)]	Weld Metal Analysis A-Number [Note (2)]	Base Metal Group	Nominal Wall Thickness		Specified Min. Tensile Strength, Base Metal		Metal Temperature Range		Holding Time			Brinell Hardness, Max. [Note (4)]
									Nominal Wall [Note (3)]		Min. Time, h	
			mm	in.	MPa	ksi	°C	°F	min/mm	hr/in.		
10H	...	Duplex stainless steel	All	All	All	All	Note (7)	Note (7)	1.2	1/2	1/2	...
10I	...	27Cr steel	All	All	All	All	663-704 [Note (8)]	1,225-1,300 [Note (8)]	2.4	1	1	...
11A SG 1	...	8Ni, 9Ni steel	≤ 51	≤ 2	All	All	None	None
			> 51	> 2	All	All	552-585 [Note (9)]	1,025-1,085 [Note (9)]	2.4	1	1	...
11A SG 2	...	5Ni steel	> 51	> 2	All	All	552-585 [Note (9)]	1,025-1,085 [Note (9)]	2.4	1	1	...
15E	5	Alloy steels 9Cr-1Mo-V	All	All	All	All	732-774	1,350-1,425	2.4	1	2	250
62	...	Zr R60705	All	All	All	All	538-593 [Note (10)]	1,000-1,100 [Note (10)]	Note (10)	Note (10)	1	...

NOTES:

- (1) P-Number from BPV Code, Section IX, QW/QB-422.
- (2) A-Number from Section IX, QW-442.
- (3) For holding time in SI metric units, use min/mm (minutes per mm thickness). For U.S. units, use hr/in. thickness.
- (4) See para. 331.1.7.
- (5) See Appendix F, para. F331.1.
- (6) Cool as rapidly as possible after the hold period.
- (7) Postweld heat treatment is neither required nor prohibited, but any heat treatment applied shall be as required in the material specification.
- (8) Cooling rate to 649°C (1,200°F) shall be less than 56°C (100°F)/h; thereafter, the cooling rate shall be fast enough to prevent embrittlement.
- (9) Cooling rate shall be > 167°C (300°F)/h to 316°C (600°F).
- (10) Heat treat within 14 days after welding. Hold time shall be increased by 1/2 h for each 25 mm (1 in.) over 25 mm thickness. Cool to 427°C (800°F) at a rate ≤ 278°C (500°F)/h, per 25 mm (1 in.) nominal thickness, 278°C (500°F)/h max. Cool in still air from 427°C (800°F).

Figure 107: PWHT procedure ASME B31.3-2012-Page 69[54].

Appendix D

Table 331.1.1 Postweld Heat Treatment

P-No. and Group No. (BPV Code Section IX, QW/QB-420)	Holding Temperature Range, °C (°F) [Note (1)]	Minimum Holding Time at Temperature for Control Thickness [Note (2)]	
		Up to 50 mm (2 in.)	Over 50 mm (2 in.)
P-No. 1, Group Nos. 1–3	595 to 650 (1,100 to 1,200)	1 h/25 mm (1 hr/in.); 15 min min.	2 hr plus 15 min for each additional 25 mm (in.) over 50 mm (2 in.)
P-No. 3, Group Nos. 1 and 2	595 to 650 (1,100 to 1,200)		
P-No. 4, Group Nos. 1 and 2	650 to 705 (1,200 to 1,300)		
P-No. 5A, Group No. 1	675 to 760 (1,250 to 1,400)		
P-No. 5B, Group No. 1	675 to 760 (1,250 to 1,400)		
P-No. 6, Group Nos. 1–3	760 to 800 (1,400 to 1,475)		
P-No. 7, Group Nos. 1 and 2 [Note (3)]	730 to 775 (1,350 to 1,425)		
P-No. 8, Group Nos. 1–4	PWHT not required unless required by WPS		
P-No. 9A, Group No. 1	595 to 650 (1,100 to 1,200)		
P-No. 9B, Group No. 1	595 to 650 (1,100 to 1,200)		
P-No. 10H, Group No. 1	PWHT not required unless required by WPS. If done, see Note (4).		
P-No. 10I, Group No. 1 [Note (3)]	730 to 815 (1,350 to 1,500)		
P-No. 11A	550 to 585 (1,025 to 1,085) [Note (5)]		
P-No. 15E, Group No. 1	730 to 775 (1,350 to 1,425) [Notes (6) and (7)]	1 h/25 mm (1 hr/in.); 30 min min.	1 h/25 mm (1 hr/in.) up to 125 mm (5 in.) plus 15 min for each addi- tional 25 mm (in.) over 125 mm (5 in.)
P-No. 62	540 to 595 (1,000 to 1,100)	...	See Note (8)
All other materials	PWHT as required by WPS	In accordance with WPS	In accordance with WPS

GENERAL NOTE: The exemptions for mandatory PWHT are defined in Table 331.1.3.

NOTES:

- (1) The holding temperature range is further defined in para. 331.1.6(c) and Table 331.1.2.
- (2) The control thickness is defined in para. 331.1.3.
- (3) Cooling rate shall not be greater than 55°C (100°F) per hour in the range above 650°C (1,200°F), after which the cooling rate shall be sufficiently rapid to prevent embrittlement.
- (4) If PWHT is performed after welding, it shall be within the following temperature ranges for the specific alloy, followed by rapid cooling:
 - Alloys S31803 and S32205 — 1 020°C to 1 100°C (1,870°F to 2,010°F)
 - Alloy S32550 — 1 040°C to 1 120°C (1,900°F to 2,050°F)
 - Alloy S32750 — 1 025°C to 1 125°C (1,880°F to 2,060°F)
 - All others — 980°C to 1 040°C (1,800°F to 1,900°F).
- (5) Cooling rate shall be >165°C (300°F)/h to 315°C (600°F)/h.
- (6) The minimum PWHT holding temperature may be 720°C (1,325°F) for nominal material thicknesses [see para. 331.1.3(c)] ≤½ in. (13 mm).
- (7) The Ni + Mn content of the filler metal shall not exceed 1.2% unless specified by the designer, in which case the maximum temperature to be reached during PWHT shall be the A₁ (lower transformation or lower critical temperature) of the filler metal, as determined by analysis and calculation or by test, but not exceeding 800°C (1,470°F). If the 800°C (1,470°F) limit was not exceeded but the A₁ of the filler metal was exceeded or if the composition of the filler metal is unknown, the weld must be removed and replaced. It shall then be rewelded with compliant filler metal and subjected to a compliant PWHT. If the 800°C (1,470°F) limit was exceeded, the weld and the entire area affected by the PWHT will be removed and, if reused, shall be renormalized and tempered prior to reinstallation.
- (8) Heat treat within 14 days after welding. Hold time shall be increased by 1.2 h for each 25 mm (1 in.) over 25 mm (1 in.) thickness. Cool to 425°C (800°F) at a rate ≤280°C (500°F).

Figure 108: PWHT procedure ASME B31.3-2014-Page 70[33].

Appendix E

REVIEWED BENTELER
 By stein roar egge at 6:44 am, Dec 17, 2012

Benteler Steel/Tube GmbH - Postfach 13 40 - 33043 Paderborn - Deutschland Tel.: + 49.5254.81-0 Fax: + 49.5254.13666		ABNAHMEPRÜFZEUGNIS EN 10204-3.1 INSPECTION CERTIFICATE EN 10204-3.1 CERTIFICAT DE RECEPTION EN 10204-3.1 EN 10204:2005-01		Dokument-Nr.: 65-706733/001/P Document No.: No. du document:		Prüf-Nr.: Inspection No.: No. du certificat:		Blatt: 1 / 3 Page:	
Benteler Steel/Tube GmbH - Postfach 1340 - 33043 Paderborn - Deutschland National Oilwell Varco UK Ltd., Telford Court, Unit 15 MORPETH Northumberland NE61 2DB UNITED KINGDOM		Kunden-Bestell-Nr.: 10383/0000 Purchase Order No.: No. de commande du client:		Hersteller: Warmrohrwerk Dinslaken Manufacturer: (DIN EN ISO 9001, ISO/TS-16949 CERTIFIED BY TÜV NORD CERT) Producteur: (PED 97/23/EC CERTIFIED BY TÜV NORD SYSTEMS)		Herstellerzeichen: Manufacturer's brand: Marque du producteur:		Stempel des Abnahmebeauftragten: WA Stamp of the inspection representative: Poignon du contrôleur:	
Benteler Auftrags-Nr.: 1568398 Benteler Order No.: No. de commande Benteler:		Versandanzeigen-Nr.: 6565471 Dispatch Note No.: No. d'avis d'expédition:		Produkt: NAHTLOSE STAHLROHRE Product: SEAMLESS STEEL TUBES Produit: TUBES D'ACIER SANS SOUDURE		Stahlschmelzungsverfahren: ELEKTROSTAHL Steelmaking process: ELECTRIC FURNACE Procédé d'élaboration de l'acier: FOUR ELECTRIQUE		ITEM 69	
Lieferbedingungen: Terms of delivery: Conditions de livraison:		Techdrill Specification No. TDA519-4130 rev. C with agreed deviations: Without pt. 3, tensile strength, protection, NDT, ASTM-A 519-2006, NACE Standard MR0175-97							
Maße - Toleranzen: Dimensions-tolérances:		Techdrill specification no. TDA519-4130 rev. B							
Stahlsorte: Steel grade: Nuance d'acier:		GRADE 4130							
Lieferzustand: Delivery condition: État de livraison:		QT							
Produktkennzeichen: Product marking: Marquage du produit:		FS: BENTELER SIGN 4130 DIMENSION HEAT-NO.							
ABZ = Azulienbeschriftung, Etching ink marking, Gravure à l'encre - FK = Farbkennzeichnung, colour marking, marquage par couleur - FS = Farbstrahlbeschriftung, paint etching, marquage par peinture - FSD = Farbstrahlprüfer, Colour jet printer, imprimante à jet d'encre de couleur - LK = Laserkennzeichnung, Laser marking, Marquage laser - PKE = Etikettkennzeichnung, tag marking, marquage sur étiquette - PS = Prägestempel, die stamp, marquage par poinçonnage - TS = Tintenstrahlkennzeichnung, ink jet spray marking, imprimante à jet d'encre -									
Pos.	Stück	Maße	Länge	Gewicht	Schmelzen-Nr.	Prüfdruck	Rohr-Nr.-Gruppe	Vielfachlängen	
Item	Number	Dimensions	Length	Weight	Heat No.	Test pressure	Tube number group	Multiple lengths	
Poste	Nombre	Dimensions	Longueur	Poids	No. de coulée	Pression d'épreuve	Série de no. des tubes	Longueurs multiples	
0010	22	60,330 X 11,070 mm	5000 - 7000	134,29	1811	571644			

Figure 109: Material Certificate.

Benteler Steel/Tube GmbH Postfach 13 40 33043 Paderborn Deutschland Tel.: + 49.5254.81-0 Fax: + 49.5254.13666		BENTELER Steel/Tube						
ABNAHMEPRÜFZEUGNIS EN 10204-3.1 INSPECTION CERTIFICATE EN 10204-3.1 CERTIFICAT DE RECEPTION EN 10204-3.1		Dokument-Nr.: 65-706733/001/P Document No.: No. du document:		Prüf-Nr.: Inspection No.: No. du certificat:		Blatt: 2 / 3 Page:		
Schmelzenanalyse [%] / Heat analysis [%] / Analyse sur coulée [%]								
Pos.	Schmelzen-Nr.	C	SI	MN	P	S	CR	MO
Item	Heat No.							
Poste	No. de coulée							
0010	571644	0,310	0,240	0,54	0,006	0,001	0,93	0,17
Prüfergebnisse / Test results / Résultats des essais								
Die Rohre wurden zerstörungsfrei geprüft: The tubes are non destructive tested: Les tubes ont passé un essai non destructif:		UT-long.imperfections: acc. to API 5L 42nd Edition, SR 4.3; Outside notch depth: 12,5 %; Inside notch depth: 12,5 %						PASSED
Augensichtkontrolle: Visual inspection: Examen visuel:		PASSED		Maßkontrolle: Dimensions examination: Vérification des dimensions:		PASSED		
Ergebnisse der mechanischen Prüfung / Results of mechanical testing / Résultats des essais mécaniques								
Die Probenahme erfolgte an Vielfachlängen. The sampling was carried out on multiple lengths. L'échantillonnage était réalisé aux longueurs multiples.								
Zugversuch längs Streifenprobe / Tensile test longitudinal Strip test specimen / Essai de traction longitudinale Bande decoupee sur tube								
Pos.	Proben-Nr.	Schmelzen-Nr.	Probenabmessung	Streckgrenze	Zugfestigkeit	Dehnung	Einschnürung	
Item	Specimen No.	Heat No.	Specimen dimensions	Yield strength	Tensile strength	Elongation	Area reduction	
Poste	No. de l'éprouvette	No. de coulée	Dimensions de l'éprouv.	Limite élastique	Résistance à la traction	Allongement	Coefficient de striction	
Anforderungen			mm	ReH	Rm	A2"	1. Formel	
Requirements				N/mm²	N/mm²	%	1. Formula	
Exigences				MIN 586	MIN 690	MIN 18	1. Formule	
0010	000002	571644	19,00 X 10,70	645	745	32	MIN 35	
Härteprüfung / Hardness test / Essai de dureté								
Pos.	Proben-Nr.	Schmelzen-Nr.	Härte					
Item	Specimen No.	Heat No.	Hardness					
Poste	No. de l'éprouv.	No. de coulée	Dureté					
Anforderungen			HRC	HB	HV	HRB	HBW	
Requirements								
Exigences			MAX 22,0					
0010	000002	571644	020					

Figure 110: Material Certificate.


Benteler Steel/Tube GmbH Postfach 13 40 33043 Paderborn Deutschland Tel.: + 49.5254.81-0 Fax: + 49.5254.13666			BENTELER  Steel/Tube								
ABNAHMEPRÜFZEUGNIS EN 10204-3.1 INSPECTION CERTIFICATE EN 10204-3.1 CERTIFICAT DE RECEPTION EN 10204-3.1			Dokument-Nr.: 65-706733/001/P Document No.: No. du document:		Prüf-Nr.: Inspection No.: No. du certificat:		Blatt: 3 / 3 Page: Page:				
Kerbschlagbiegeversuch Notched bar impact test / Essai de flexion par choc (résilience) [1 CHARPY_V]											
Pos. Item	Proben-Nr. Specimen No.	Schmelzen-Nr. Heat No.	Probenabmessung Specimen dimensions Dimensions de l'éprouvette			Probenlage Specimen position Position de l'éprouvette	Prüftemperatur Test temperature Température d'essai	Kerbschlagarbeit Absorbed energy Energie absorbée		Kerbschlagzähigkeit Impact strength Résistance au choc	Laterale Breitung Lateral expansion Expansion latérale
Anforderungen Requirements Exigences	Länge Length Longueur	Breite Width Largeur	Höhe Height Hauteur	längs (L) longitudinal (L) longitudinal (L)		GRAD °C	einzel single individuelle	mittel average moyenne	einzel single individuelle	mittel average moyenne	mm min. 0,38
	mm	mm	mm	quer (Q) transversal (Q) transversal (Q)			J	J	J/cm²	J/cm²	
	55	7,50	10,00	L		-50	MIN 024	MIN 032			
0010 000004	571644	7,50	10,00			-50	123				
		7,50	10,00				126				1,80
		7,50	10,00				130	126			
Wärmebehandlung / Heat treatment / Traitement thermique Hardening temperature: 850°C, Holding time: 1 min, Cooling: water / Tempering temperature: 740°C, Holding time: 3 min, Cooling: air											
Verkäufer(in) / Salesman/ woman in charge / Personne chargée : Mr Pospischil, Tel.: 05254/81-4348, Fax: 4394											
NOV 2012 Dinslaken, 25.07.2012, TEL.: 02064.623-537 FAX: 02064.623-539						Abnahmebeauftragter Inspection representative Contrôleur DR. BASEL KEITA / Thei Es wird bestätigt, daß die gelieferten Erzeugnisse den techn. Lieferbedingungen des Auftrages entsprechen. Dieses Dokument wurde mittels EDV erstellt und ist ohne Unterschrift rechtsgültig. We certify that the supplied products comply with the order specification. This document was prepared by means of electronic data processing and is valid without signature. Nous attestons que les produits livrés sont conformes aux stipulations de la commande. Ce document a été établi par traitement électronique de l'information et est valide sans signature.					

Figure 111: Material Certificate.

Appendix F



C03

OK 48.08

SMAW

OK 48.08 is an LMA electrode with very good mechanical properties suitable for demanding applications, such as offshore. The weld metal contains approximately 1% Ni for high impact values down to -40°C. The coating is of the latest LMA type for optimum resistance to porosity and hydrogen cracking. OK 48.08 is CTOD tested.

Recovery

125%

Welding Current

AC, DC + (-) OCV 65 V



PACKING/ORDERING INFORMATION				
Part Number	Dia (mm)	Inner Carton (kg)	Carton Weight (kg)	Pallet Weight (kg)
VacPac				
4808253INV0	2.5	2.9	11.6	580.0
480832HNV0	3.2	3.5	14.0	700.0
480840HNV0	4.0	3.7	14.8	740.0
480850HNV0	5.0	4.0	16.0	800.0

CLASSIFICATIONS	APPROVALS	TYPICAL ALL WELD METAL COMPOSITION (%)		TYPICAL MECH. PROPERTIES ALL WELD METAL	
SFA/AWS A5.5 E7018-G	ABS 3H5 3Y H5 DNV 4 Y40H10	C	0.06	Yield Stress, Mpa 540	
EN ISO 2560-A E 46 S Ni B 32 H5	GL 4YH5 LR 4Y40M H5	Si	0.4	Tensile Strength, Mpa 600	
		Mn	1.2	Elongation, % 26	
		Ni	0.8	Charpy V Test Temps, °C Impact Values, J	
				-20	160
				-40	130
				-50	100
				-60	60

WELDING PARAMETERS							
Diameter (mm)	Length (mm)	Welding Current, A	Arc Voltage, V	N. Kg Weld Metal/(kg) Electrodes	B. No. Of Electrodes/(kg) Weld Metal	H. Kg Weld Metal/(hour) Arc Time	T. Burn-off time, (secs)/ Electrode
2.0	300	55-80	22	0.57	135.1	0.6	42
2.5	350	75-110	27	0.57	88.2	1.0	41
3.2	350	110-150	22	0.62	42.3	1.3	66
3.2	450	110-150	22	0.66	30.0	1.4	85
4.0	350	150-200	22	0.66	26.5	2.0	68
4.0	450	150-200	22	0.69	20.3	2.0	90
5.0	450	190-275	23	0.69	14.0	3.0	85
6.0	450	220-360	26	0.66	10.0	3.8	95



TEL : +608-907 4962 FAX : +609-900 4459
EMAIL : sales@netlite.com.my

Figure 112: Weak electrode 48.08 electrode used for the welded pipe [1].

Appendix G

COVERED (STICK) ELECTRODES (SMAW) LOW ALLOY ELECTRODES



OK 74.86 Tensitrode



A basic coated electrode for steels and castings with U.T.S. of min. 690 MPa.

Classifications:	SFA/AWS A5.5:E10018-D2, EN ISO 18275-A:E 62 4 Mn1NiMo B T 32 H5
Approvals:	CE EN 13479, Saproz UNA 272580, NAKS/HAKC 3.2-4.0 mm

Approvals are based on factory location. Please contact ESAB for more information.

Welding Current:	AC, DC+
Alloy Type:	1.8%Mn, 0.4%Mo
Coating Type:	Basic

Typical Tensile Properties			
Condition	Yield Strength	Tensile Strength	Elongation
ISO			
Stress relieved 1 hr 590 °C	630 MPa	720 MPa	25 %

Typical Charpy V-Notch Properties		
Condition	Testing Temperature	Impact Value
ISO		
Stress relieved 1 hr 590 °C	-40 °C	75 J
Stress relieved 1 hr 590 °C	-50 °C	60 J

Typical Weld Metal Analysis %					
C	Mn	Si	Ni	Cr	Mo
0.06	1.74	0.37	0.83	0.04	0.34

Deposition Data						
Diameter	Current	Voltage	kg weld metal/ kg electrodes	Number of electrodes/kg weld metal	Fusion time per electrode at 90% I max	Deposition rate 90% I max
2.5 x 350 mm	75-100 A	21.6 V	0.61	69.4	60.1 s	0.86 kg/h
3.2 x 450 mm	110-140 A	22 V	0.65	35	85.6 s	1.2 kg/h
4.0 x 450 mm	150-190 A	22.8 V	0.62	22.4	93.4 s	1.72 kg/h
5.0 x 450 mm	190-260 A	22.8 V	0.68	14.3	92.6 s	2.72 kg/h

Figure 113: Strong electrode – 74.86 electrode used for the simulation of the welded pipe.

Appendix H

Table 37: Stress-strain results for the weak electrode calculated from the electrode data sheet.

	Engineering Stress	Engineering Strain	True Stress	True Strain
Yield	540,0	0,00257	541,4	0,00257
Tensile	600,0	0,176514	705,9	0,16256
Fracture	540,0	0,26	680,4	0,23111

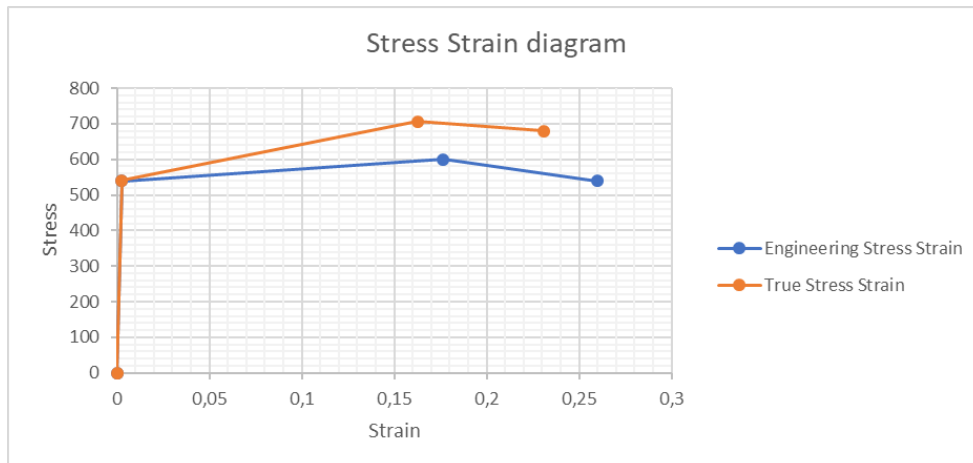


Figure 114: Stress-strain diagram for the weak weld calculated from the electrode data sheet.

Table 38: Stress-strain results for the strong electrode calculated from the electrode data sheet.

	Engineering Stress	Engineering Strain	True Stress	True Strain
Yield	630,0	0,00300	631,9	0,00300
Tensile	720,0	0,169725	842,2	0,15677
Fracture	630,0	0,25	787,5	0,22314

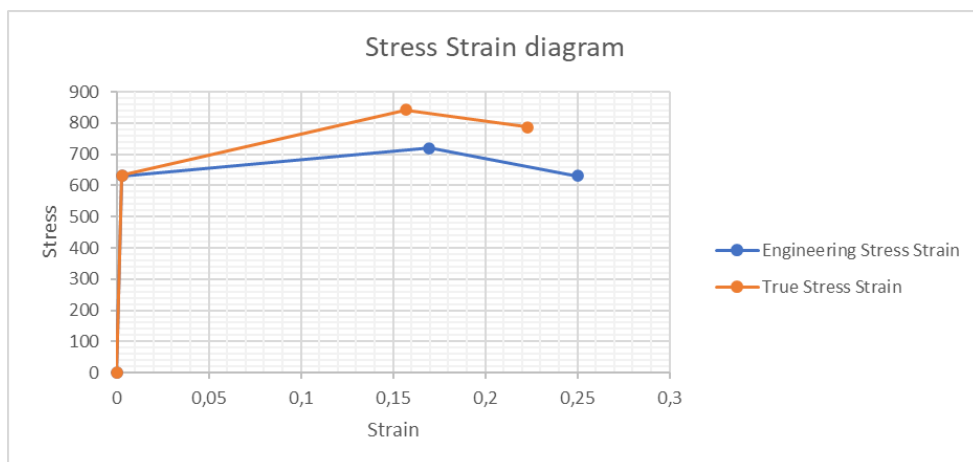


Figure 115: Stress-strain diagram for the strong weld calculated from the electrode data sheet.

Table 39: Approximated HAZ Stress-strain results for PWHT 600.

	Engineering Stress	Engineering Strain	True Stress	True Strain
Yield	684,4	0,00326	686,6	0,00325
Tensile	850,4	0,085001926	922,7	0,08158
Fracture	684,4	0,125205371	770,1	0,11797

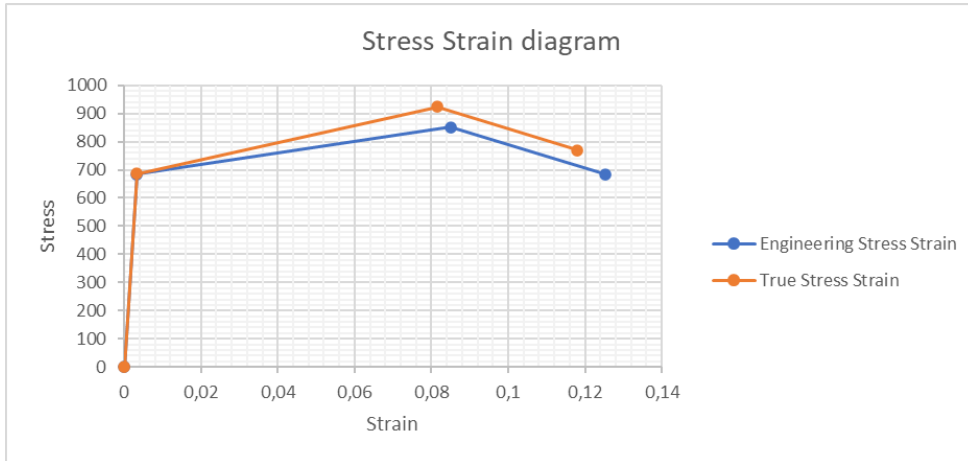


Figure 116: HAZ Stress-strain diagram for the approximated results for PWHT 600.

Table 40: Approximated HAZ Stress-strain results for PWHT 650.

	Engineering Stress	Engineering Strain	True Stress	True Strain
Yield	614,5	0,00293	616,3	0,00292
Tensile	765,4	0,089538428	834,0	0,08575
Fracture	614,5	0,131887506	695,5	0,12389

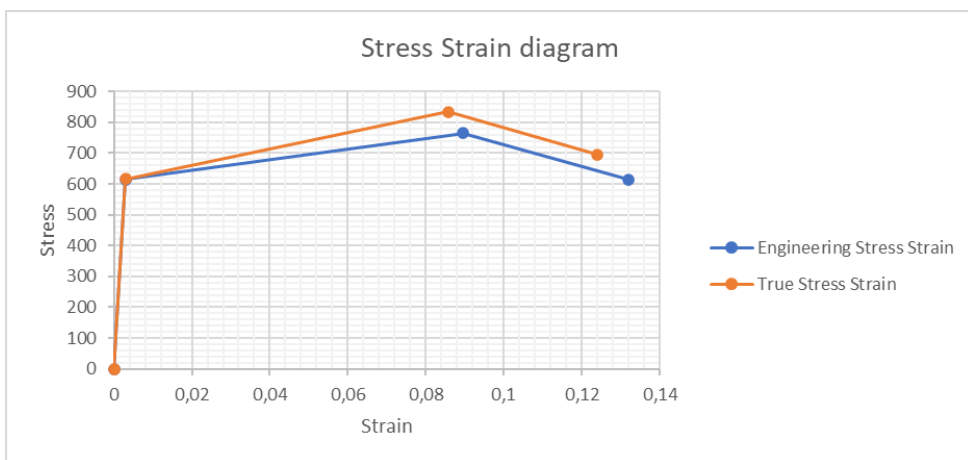
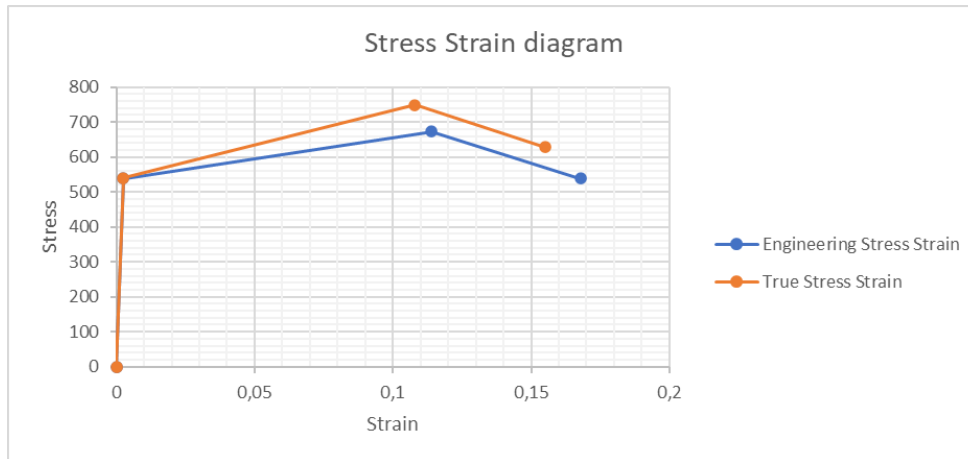


Figure 117: HAZ Stress-strain diagram for the approximated results for PWHT 650.

Table 41: Approximated HAZ Stress-strain results for PWHT 705.

	Engineering Stress	Engineering Strain	True Stress	True Strain
Yield	538,3	0,00256	539,7	0,00256
Tensile	672,8	0,113928411	749,4	0,10789
Fracture	538,3	0,167813244	628,6	0,15513

*Figure 118: HAZ Stress-strain diagram for the approximated results for PWHT 705.*

Appendix I

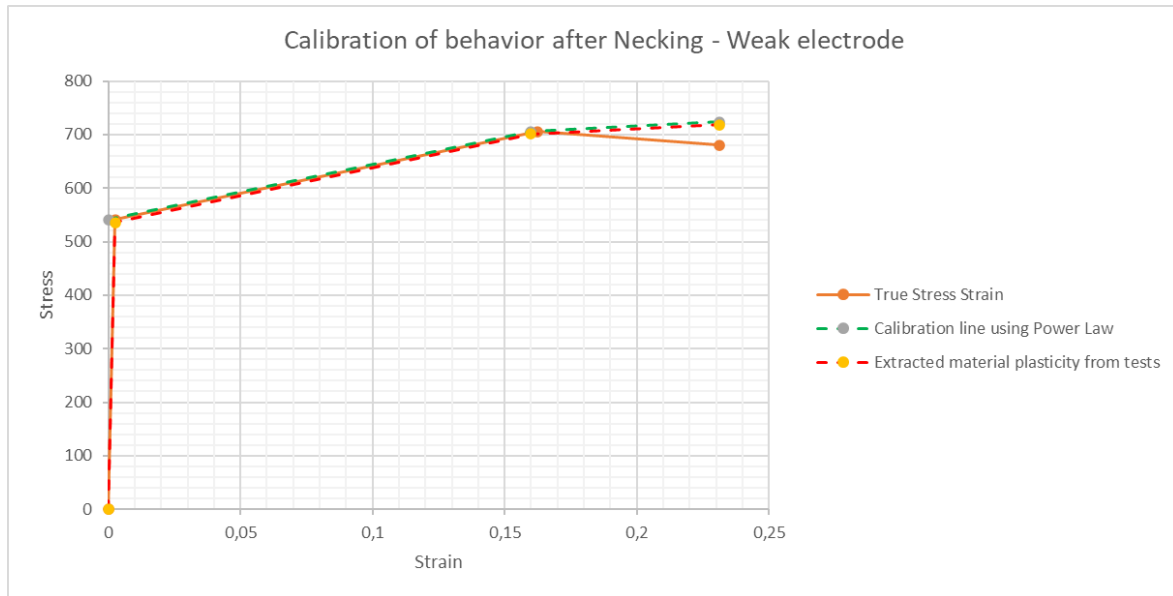


Figure 119: Visualization of calibration of strength coefficient K for the weak electrode.

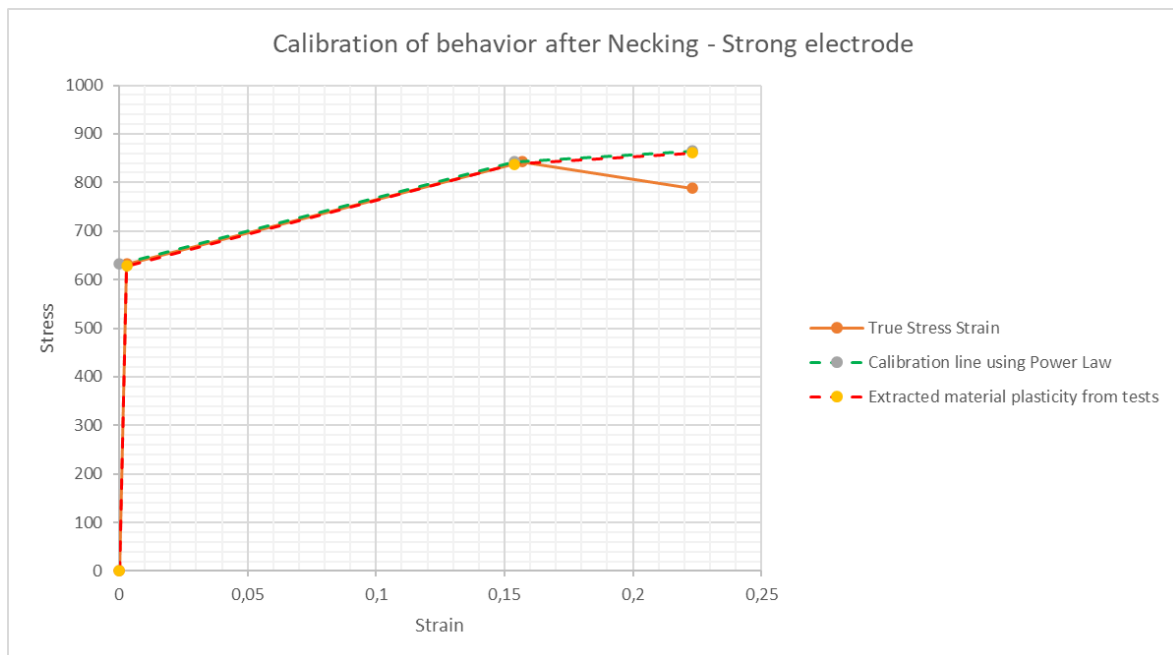


Figure 120: Visualization of calibration of strength coefficient K for the strong electrode.

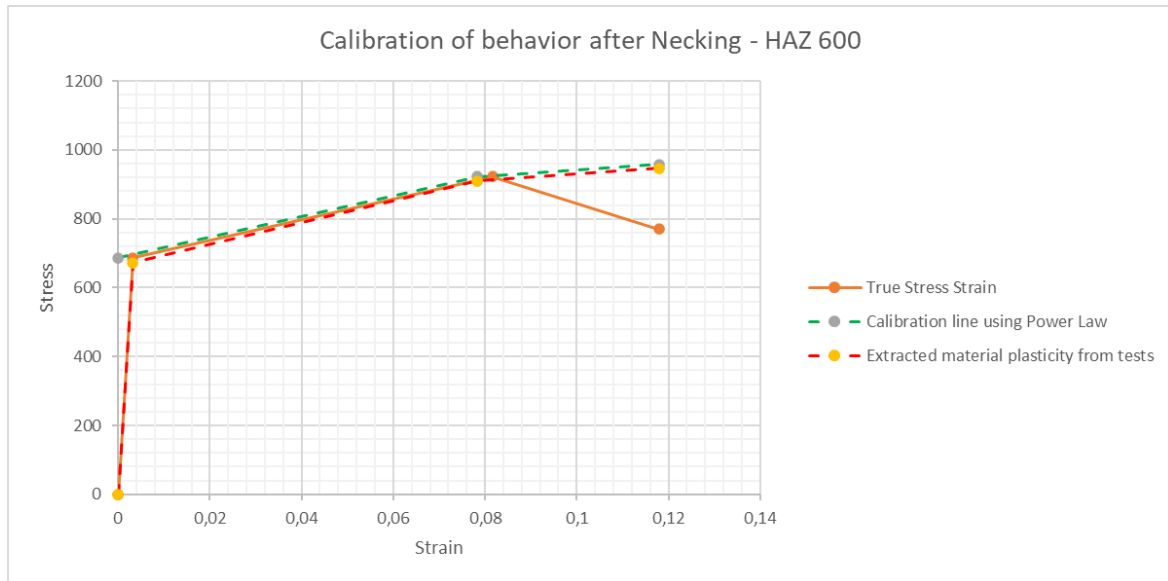


Figure 121: Visualization of calibration of strength coefficient K for the HAZ with PWHT temperature 600°C.

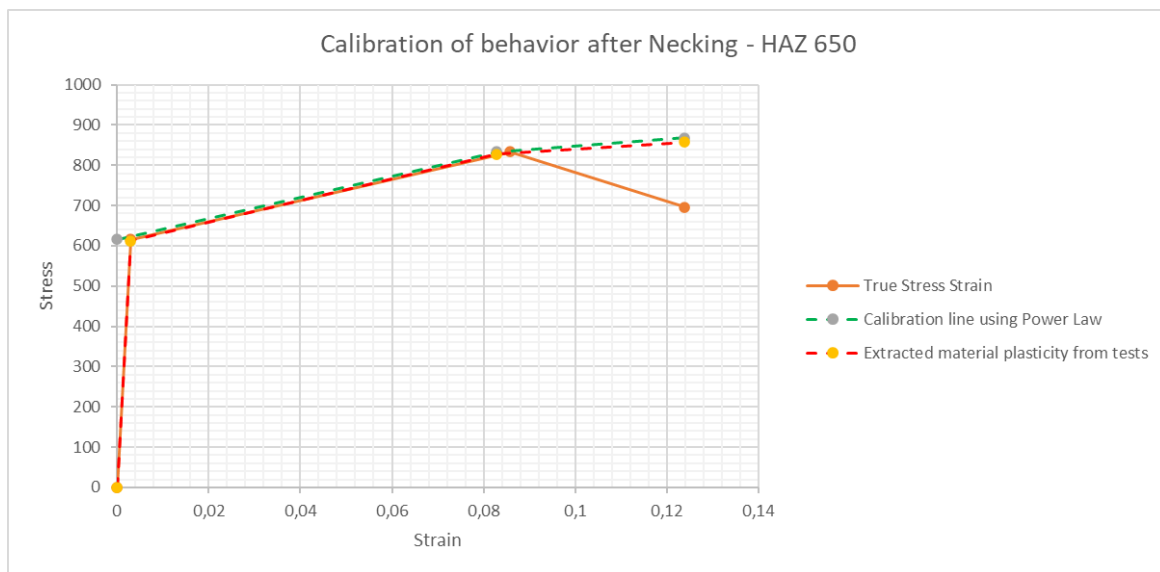


Figure 122: Visualization of calibration of strength coefficient K for the HAZ with PWHT temperature 650°C.

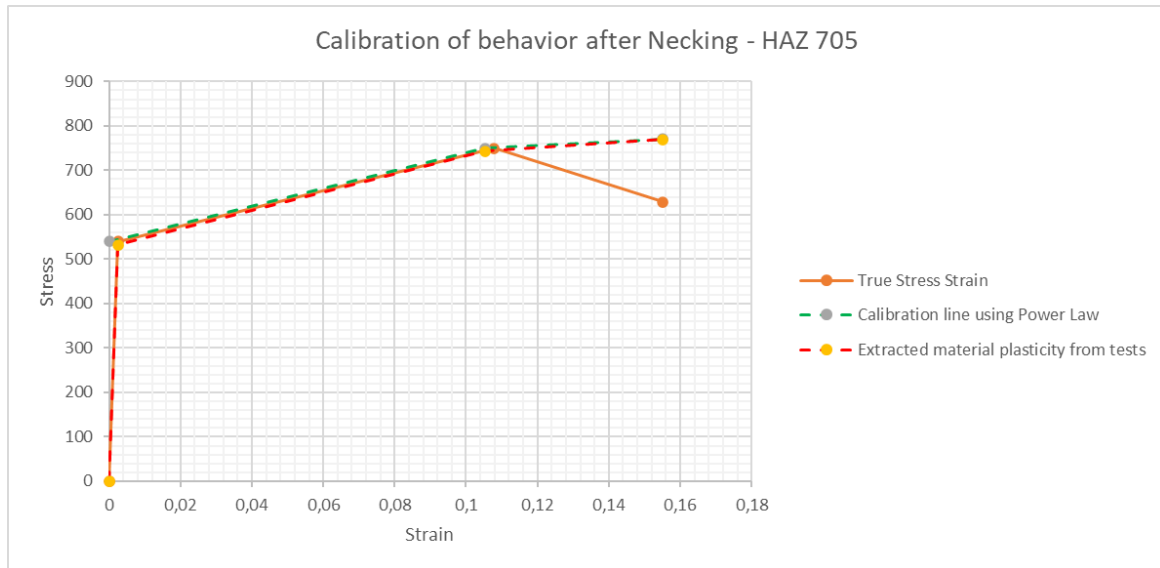


Figure 123: Visualization of calibration of strength coefficient K for the HAZ with PWHT temperature 705°C.

Appendix J



Title:	Piping Class Sheet	Doc. No.	MHSTD-L-ZZ50-SA17-0001	Appendix:	1	Class	KX10MH
Project: MHWirth Standard Piping Specification		Company: MHWirth		Rev. Date:	25.09.18	Rev.:	05

Max Design Pressure at Temperature (See note 02)					API Pressure rating	7 500 psi	
Pressure (Barg)	517.0	517.0	517.0	517.0	-	-	
Temperature (Deg. C)	-29	38	50	80	90	Service Code	Chap. 4.4

Design Code	ASME B31.3 Chapter IX High Pressure Piping (See note 52)
Corr. Allow. (mm)	3.0
Wall Thickness Under Tolerance	12.5 %, (See note 01)
Longitudinal Weld Efficiency	1
PWHT	Yes
NDT Class	3
Painting	MHSTD-Z-ZZ50-SA16-0001, SYSTEM No. 1 (See note 49)

ND (inch)	2	3	4	5	6
OD (mm)	60.30	88.90	114.30	141.30	168.30
ID (mm)	38.16	58.42	80.06	103.20	124.40
THK (mm)	11.07	15.24	17.12	19.05	21.95
SCH	-	-	-	-	-
WEIGHT	XXS	XXS	XXS	XXS	XXS

ITEM TYPE	RANGE FROM TO (inch)	GEOMETRIC STANDARD	EDS/ VDS	END CONN #1 #2	MATERIAL DESCR.	MDS	RATING	SCHD.	NOTES
PIPE SMLS	2 6	ASME B36.10M		BE BE	A519 AISI 4130	X21			
MANIFOLD FITTINGS	2 6	MANUFACTURERS STANDARD	HMF1	BE BE	API 6A 75K AISI 4130	X24			03
CAP	2 6	ASME B16.9		BE	A234 AISI 4130	X21			
CONCENTRIC REDUCER	2 6	ASME B16.9		BE BE	A234 AISI 4130	X21			
ECCENTRIC REDUCER	2 6	ASME B16.9		BE BE	A234 AISI 4130	X21			
ELBOW LONG RADIUS 45 DEG	2 6	ASME B16.9		BE BE	A234 AISI 4130	X21			03
ELBOW LONG RADIUS 90 DEG	2 6	ASME B16.9		BE BE	A234 AISI 4130	X21			03
STRAIGHT TEE	2 6	ASME B16.9		BE BE	A234 AISI 4130	X21			03
REDUCING TEE	2 6	ASME B16.9		BE BE	A234 AISI 4130	X21			03
FLANGE BLIND	2 6	API 6A TYPE 6BX		RJ	API 6A 75K AISI 4130	X24	10000psi		17
FLANGE WN	2 6	API 6A TYPE 6BX		RJ BE	API 6A 75K AISI 4130	X24	10000psi		15, 17
SPADE	2 6	API 6A TYPE 6BX		RJ RJ	API 6A 75K AISI 4130	X24	10000psi		17
SPACER	2 6	API 6A TYPE 6BX		RJ RJ	API 6A 75K AISI 4130	X24	10000psi		15, 17
GASKET	2 6	API 6A TYPE BX RING			316SS HB83 PRESS. ENERGIZED				
MECHANICAL JOINT BLIND HUB	2 6	GRAYLOC TYPE	NMJ1		API 6A 75K AISI 4130	X24			
MECHANICAL JOINT HUB	2 6	GRAYLOC TYPE	NMJ1	BE	API 6A 75K AISI 4130	X24			
MECHANICAL JOINT CLAMP	2 6	GRAYLOC TYPE	NMJ1		A788 AISI 4130	X02			

Appendix K

Material course test samples				
#	Notation	Diameter [mm]	Geometry type	Load
1	Base 1	4,95	Uniform	Monotonic
2	Base 2	5,0275	Uniform	Monotonic
3	HAZ	4,955	Uniform	Monotonic
4	HAZ 600	4,89	Uniform	Monotonic
5	HAZ 650	4,985	Uniform	Monotonic
6	Base 650	4,93	Uniform	Monotonic
7	HAZ 705	4,97	Uniform	Monotonic
8	Base 705	4,9725	Uniform	Monotonic
9	HAZ 746	4,962	Uniform	Monotonic
10	Base 746	5,003	Uniform	Monotonic

Figure 124: Material course test samples.

Check list			
Specimen name:		Date: / /	
1	fill data sheet for previous test		
2	take photo of previous tested sample		
3	check specimen alignment		
4	zero preload		
5	attach label on specimen and it is visible		
6	extensometer installation		
7	take photo of sample		
8	camera connection		
9	image quality and reflection		
10	extensometer connection		
11	load cell connection		
12	check load protocol and rate in software		
13	check and fill specimen data sheet		
14	check extensometer pin is released		
15	zero extensometer		
16	push recording button		
17	Run		

Figure 125: Check list for tensile testing.

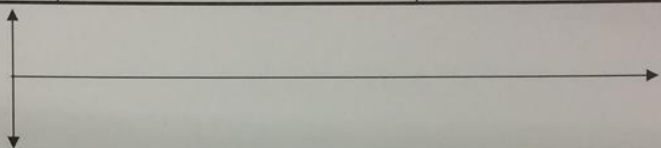
Test data sheet			
Smample Name:		Date of test: / /	
Data:			
Gage length(mm) :	50		
Sample diamter(mm):			
Sample type:	Uniform <input type="radio"/>	Hourglass <input type="radio"/>	
Load type:	Monotonic <input type="radio"/>	Cyclic <input type="radio"/>	
Loading rate:	0.041mm/s-0.41mm/s		
Cyclic load amplitude:	%		mm
Loading protocol:			
Results:			
Fu:			
εu:			
2Nf:			
File name:			
Note:			

Figure 126: Test data sheet -There is one test data sheet that is filled out for each sample.

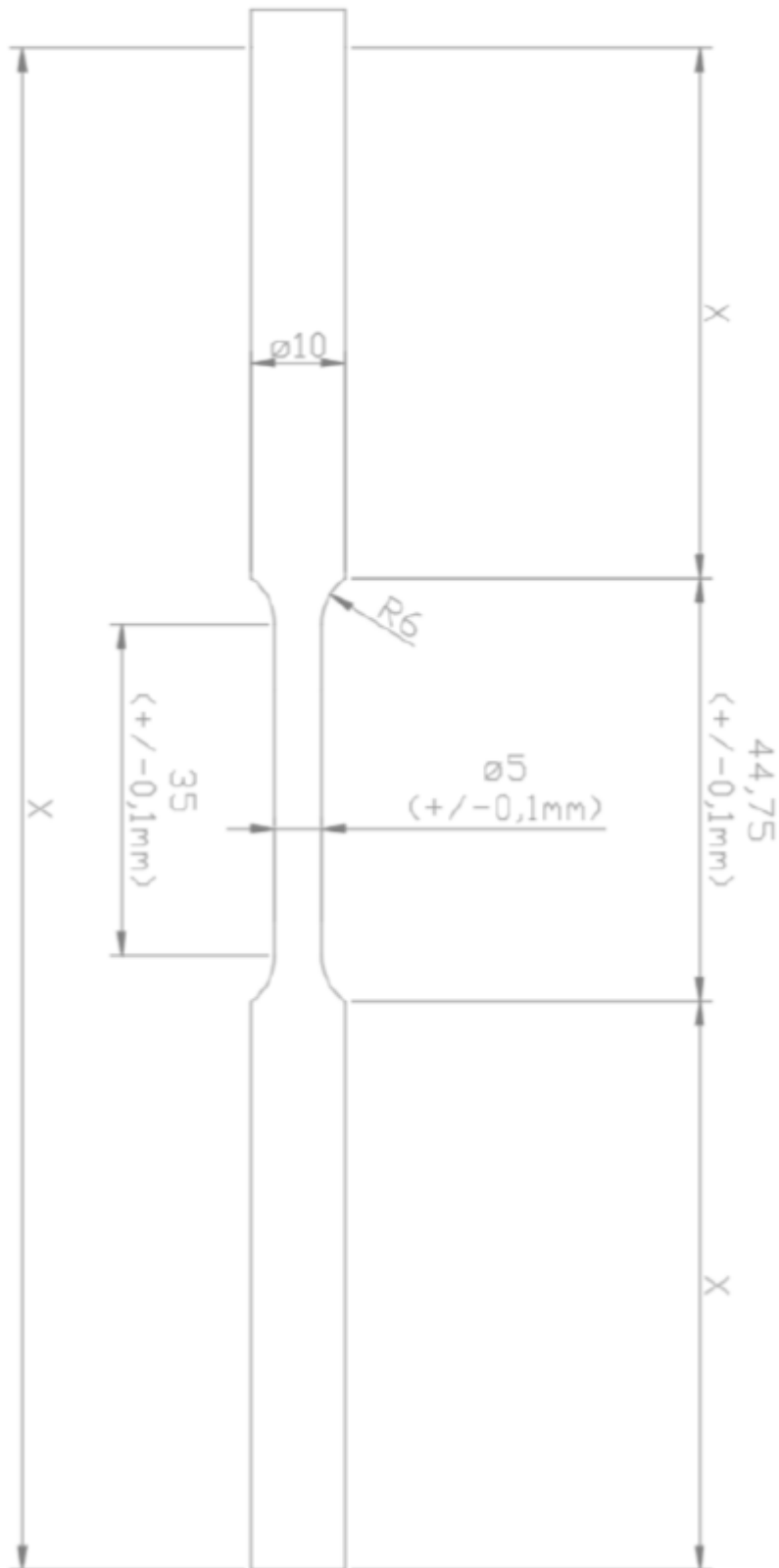
Appendix L

Figure 127: Drawing of the tested specimen -The total length varies between 150 and 170mm, but the gauge section is always centered accordingly.

Appendix M

HAZ (quenched)		PWHT 600		PWHT 650	
30 min holding time		20 min holding time		20 min holding time	
Temp [°C]	time [min]	Temp [°C]	time [min]	Temp [°C]	time [min]
20	0	20	0	20	0
189	10	350	51	300	37
296	15	400	61	350	43
403	20	450	77	400	53
529	25	500	87	450	66
607	30	550	95	500	78
682	35	600	105	550	90
748	40	600	125	610	105
800	44	550	132	650	114
809	45	500	138	650	133
850	48	450	142	600	142
850	78	400	148	550	147
20	79	350	156	500	157
				450	161
				400	164
				350	173
				300	184

PWHT 705		PWHT 746	
20 min holding time		20 min holding time	
Temp [°C]	time [min]	Temp [°C]	time [min]
20	0	20	0
100	10	230	14
150	22	250	17
200	31	300	31
300	50	355	44
350	62	400	55
400	73	455	68
450	84	500	80
500	94	550	92
550	105	600	103
600	115	650	113
650	126	700	125
700	136	727	131
705	138	746	136
705	158	746	156
700	159	727	159
650	165	700	162
600	173	650	172
550	186	600	185
500	198	550	207
450	216	300	220
400	234		
350	241		
300	251		

Figure 128: Time temperature rate noted for each of the PWHT procedures.

Appendix N

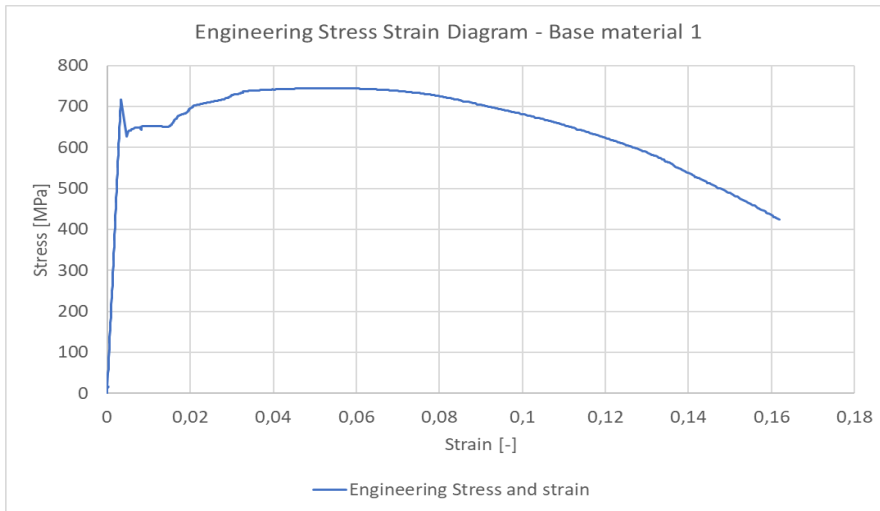


Figure 129: Engineering stress-strain diagram – Uniform specimen Base 1.

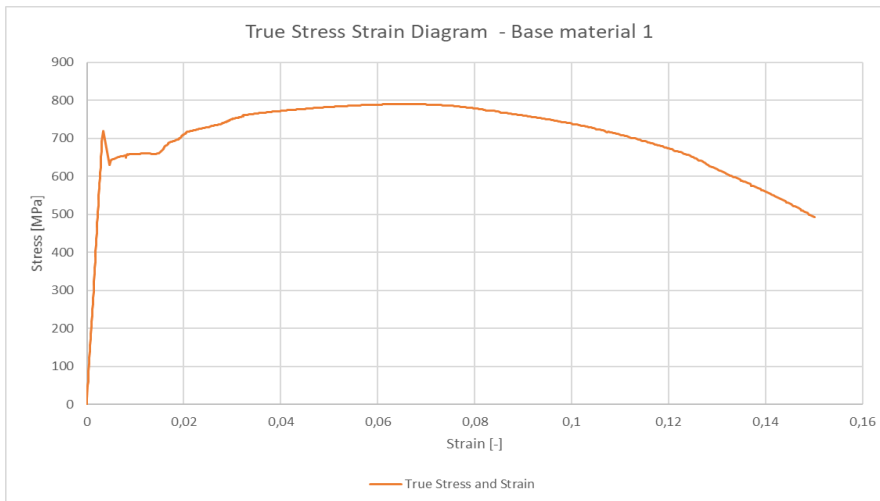


Figure 130: True stress-strain diagram – Uniform specimen Base 1.

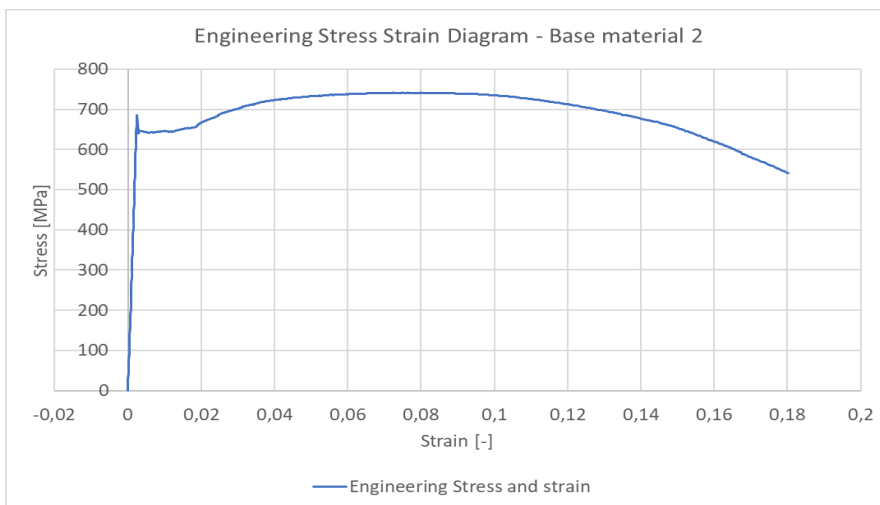


Figure 131: Engineering stress-strain diagram – Uniform specimen Base 2.

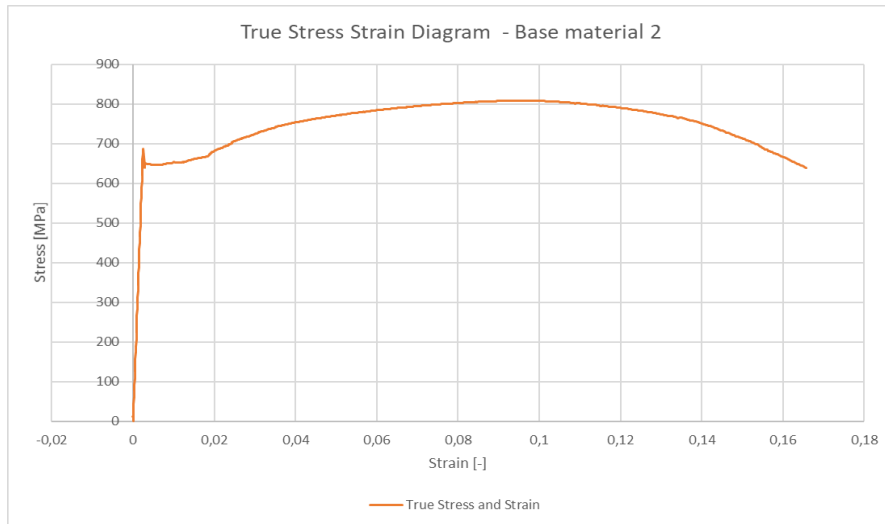


Figure 132: True stress-strain diagram – Uniform specimen Base 2.

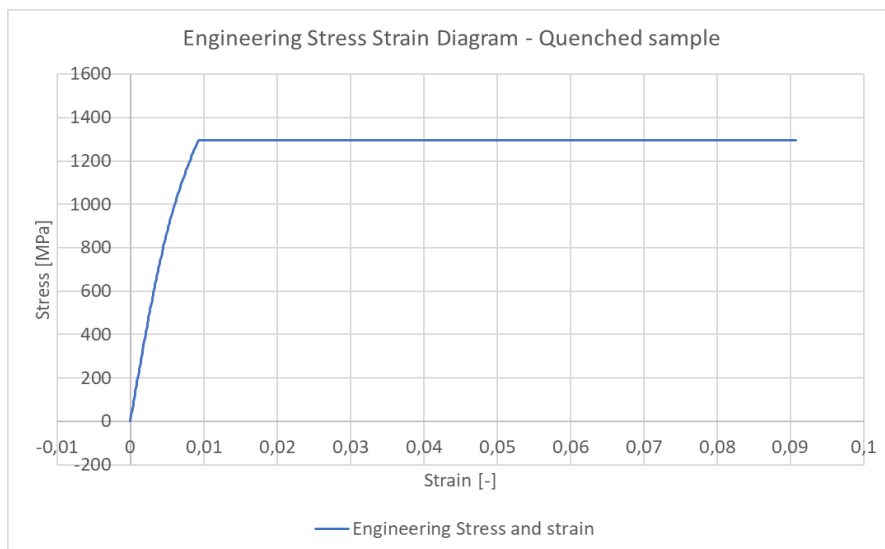


Figure 133: Engineering stress-strain diagram – Uniform specimen HAZ - Quenched.

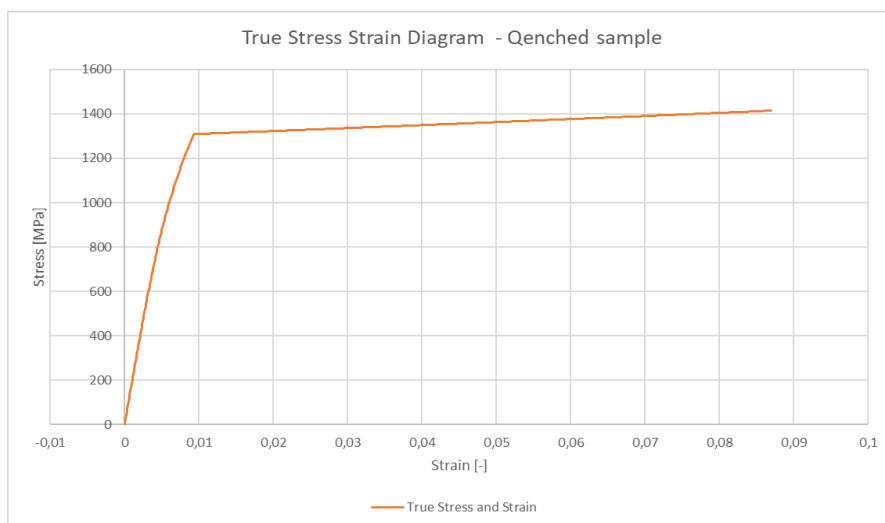


Figure 134: True stress-strain diagram – Uniform specimen HAZ - Quenched.

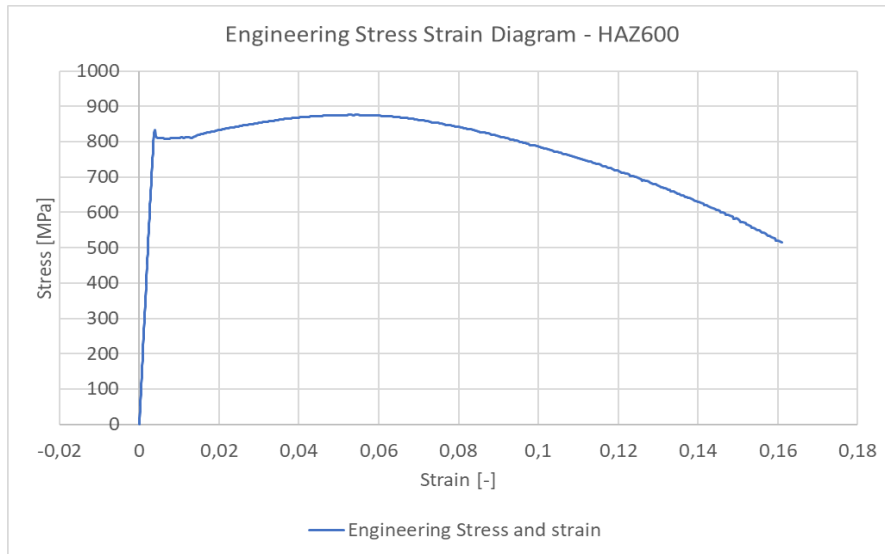


Figure 135: Engineering stress-strain diagram – Uniform specimen HAZ 600.

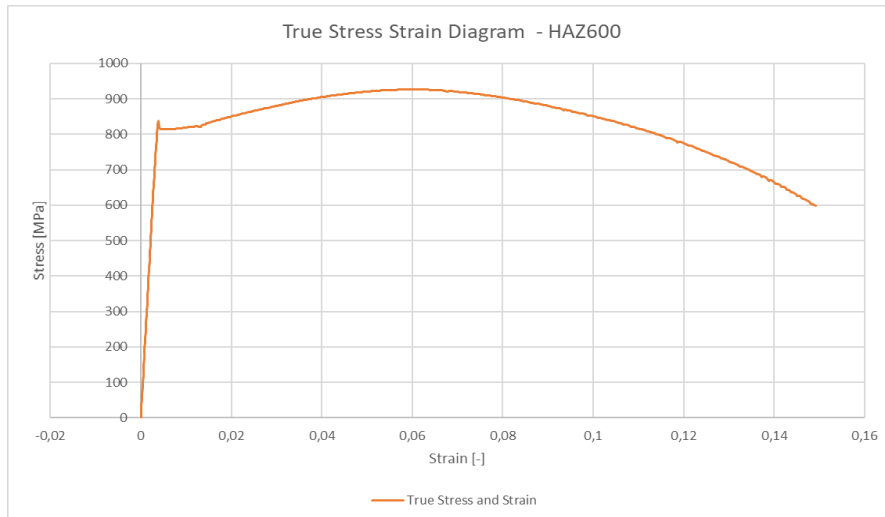


Figure 136: True stress-strain diagram – Uniform specimen HAZ 600.

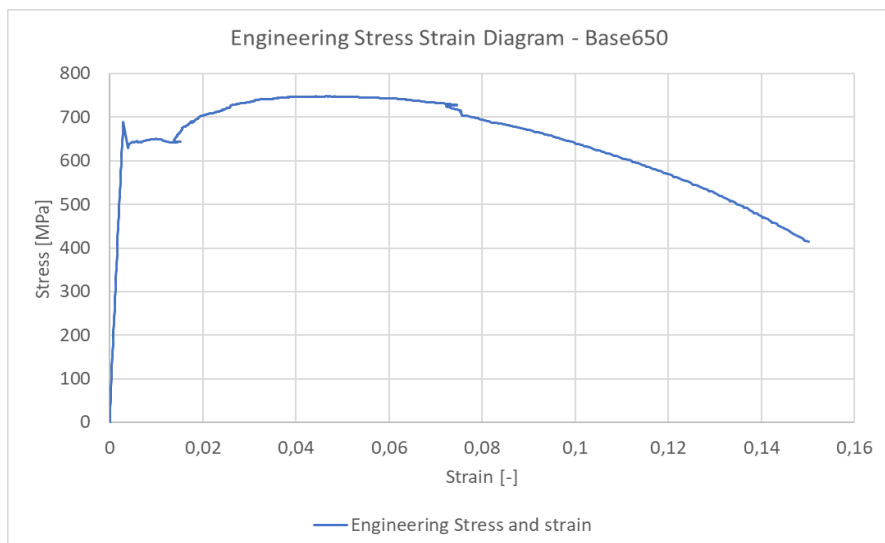


Figure 137: Engineering stress-strain diagram – Uniform specimen Base 650.

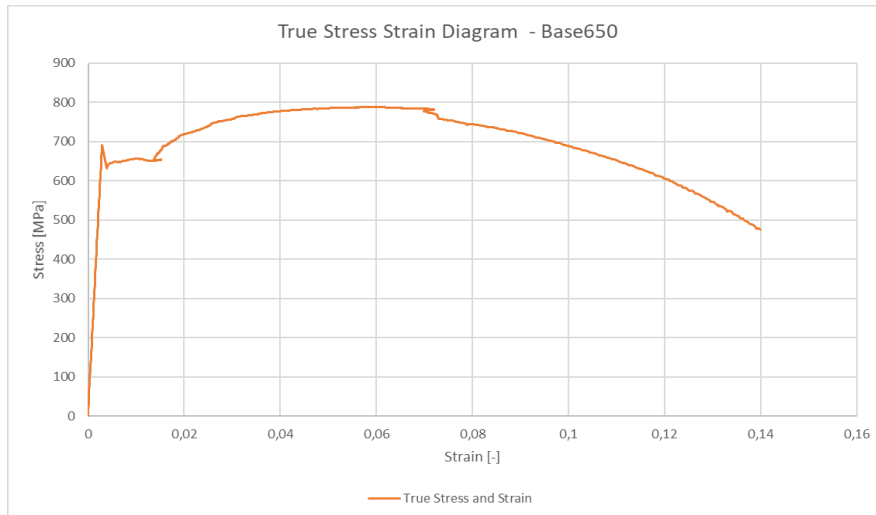


Figure 138: True stress-strain diagram – Uniform specimen Base 650.

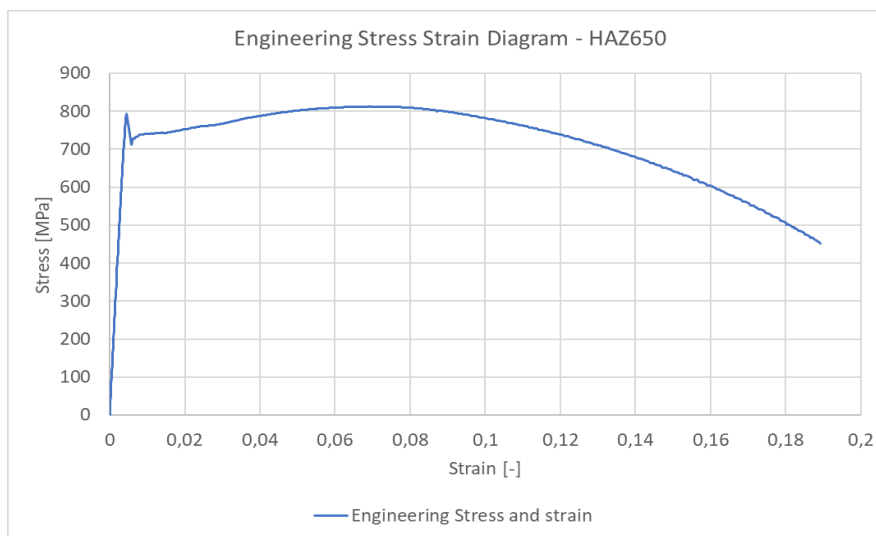


Figure 139: Engineering stress-strain diagram – Uniform specimen HAZ 650.

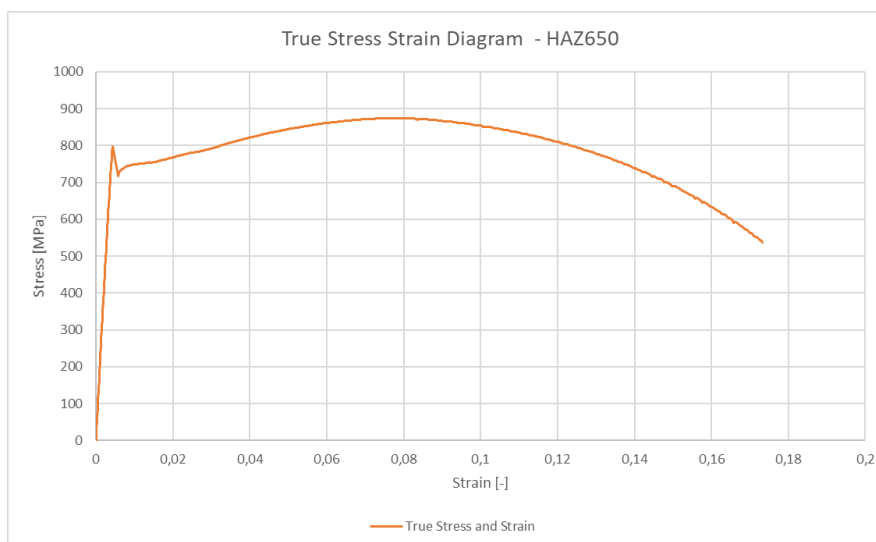


Figure 140: True stress-strain diagram – Uniform specimen HAZ 650.

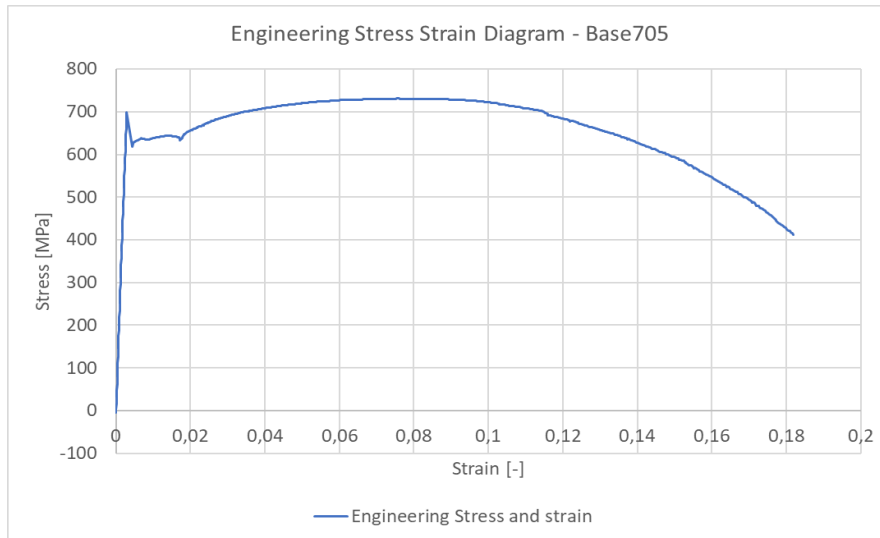


Figure 141: Engineering stress-strain diagram – Uniform specimen Base 705.

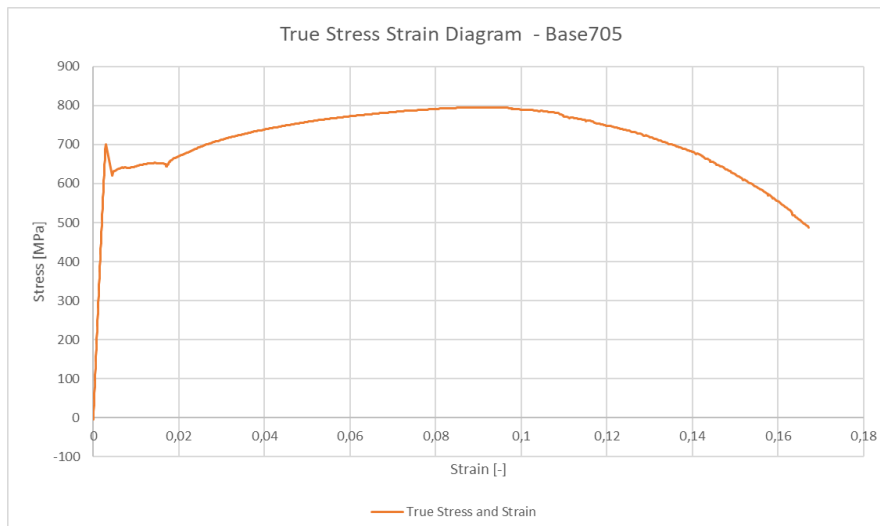


Figure 142: True stress-strain diagram – Uniform specimen Base 705.

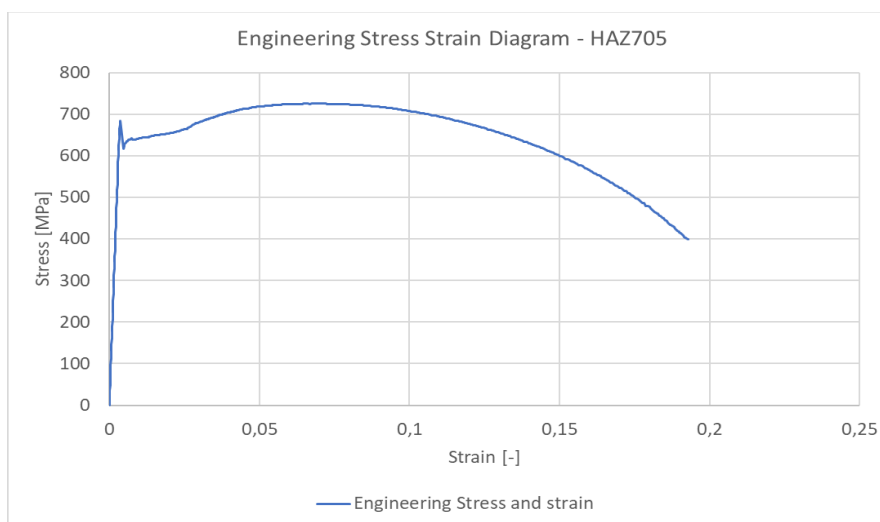


Figure 143: Engineering stress-strain diagram – Uniform specimen HAZ 705.

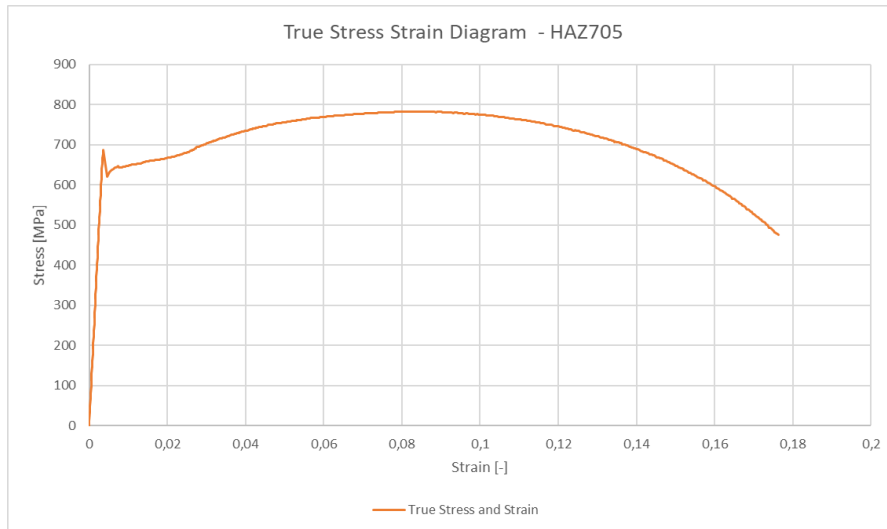


Figure 144: True stress-strain diagram – Uniform specimen HAZ 705.

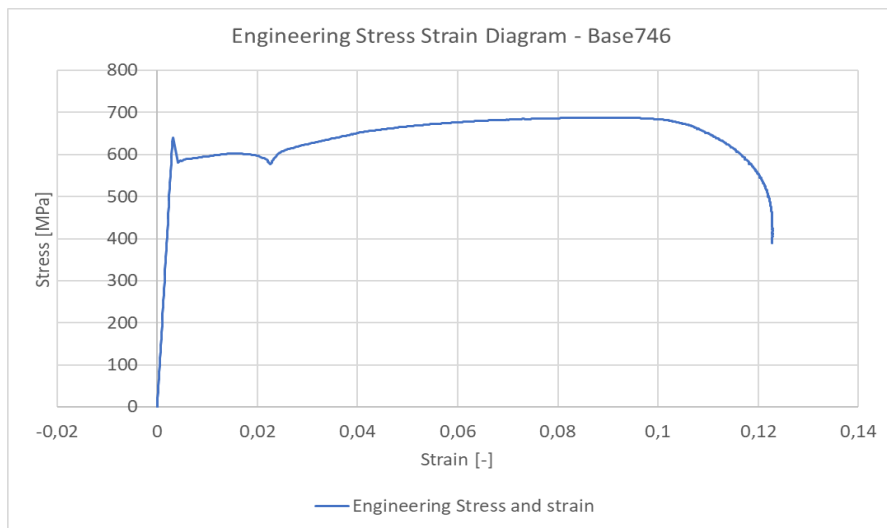


Figure 145: Engineering stress-strain diagram – Uniform specimen Base 746.

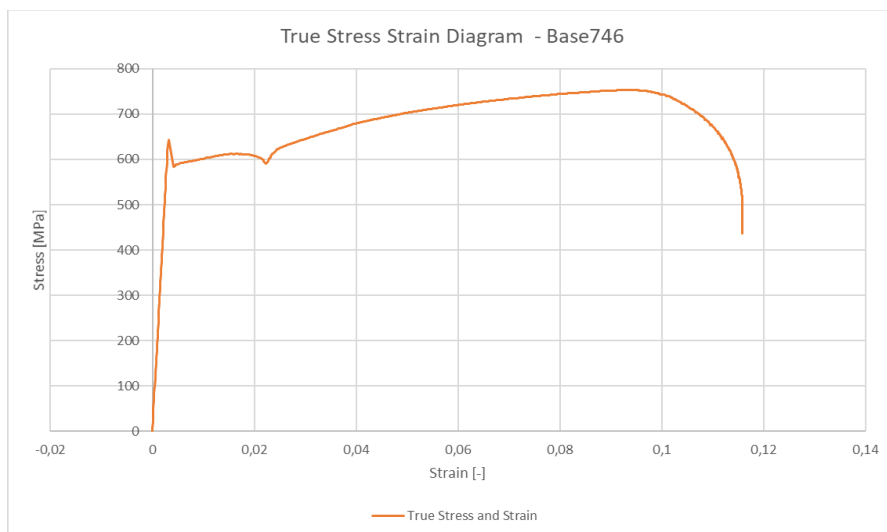


Figure 146: True stress-strain diagram – Uniform specimen Base 746.

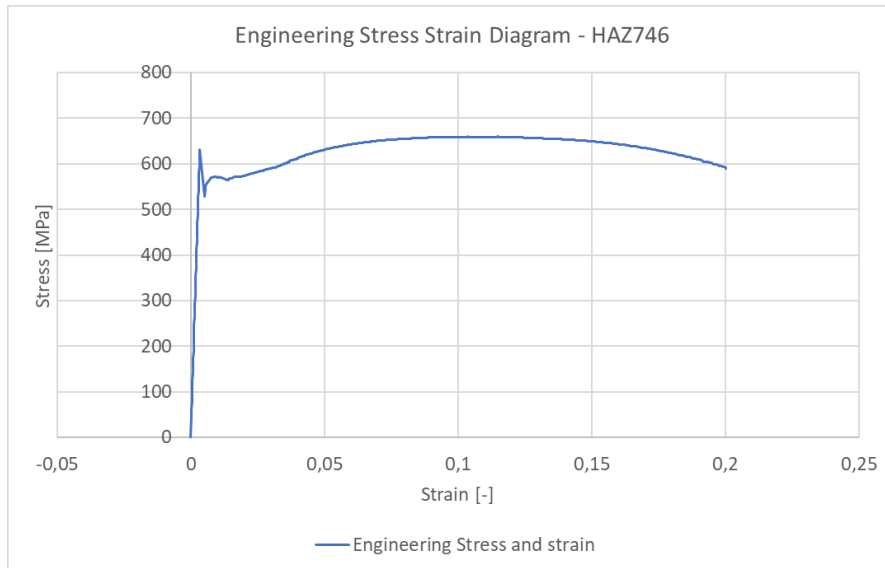


Figure 147: Engineering stress-strain diagram – Uniform specimen HAZ 746.

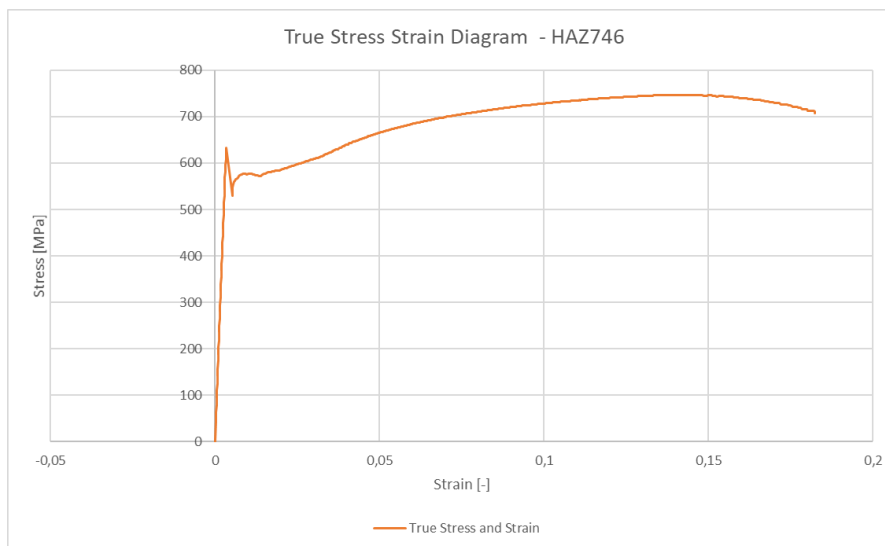
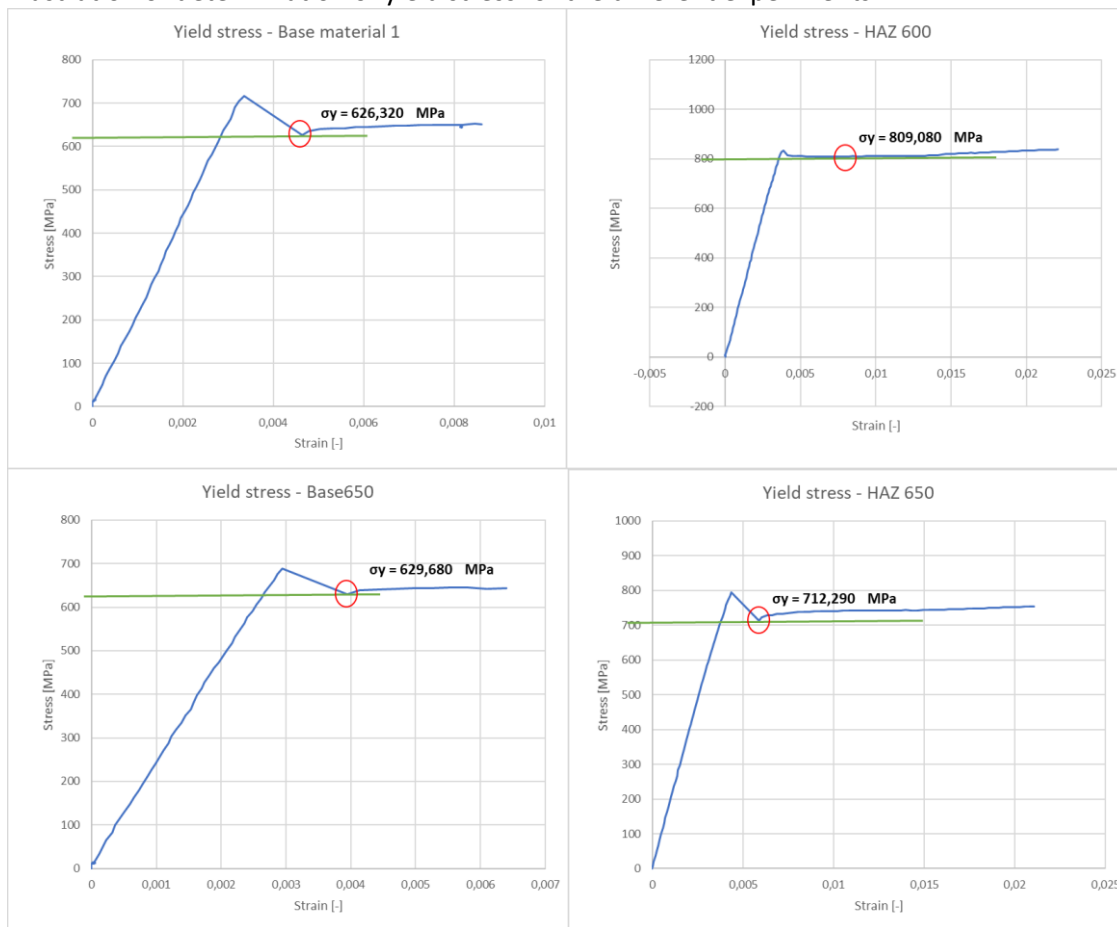
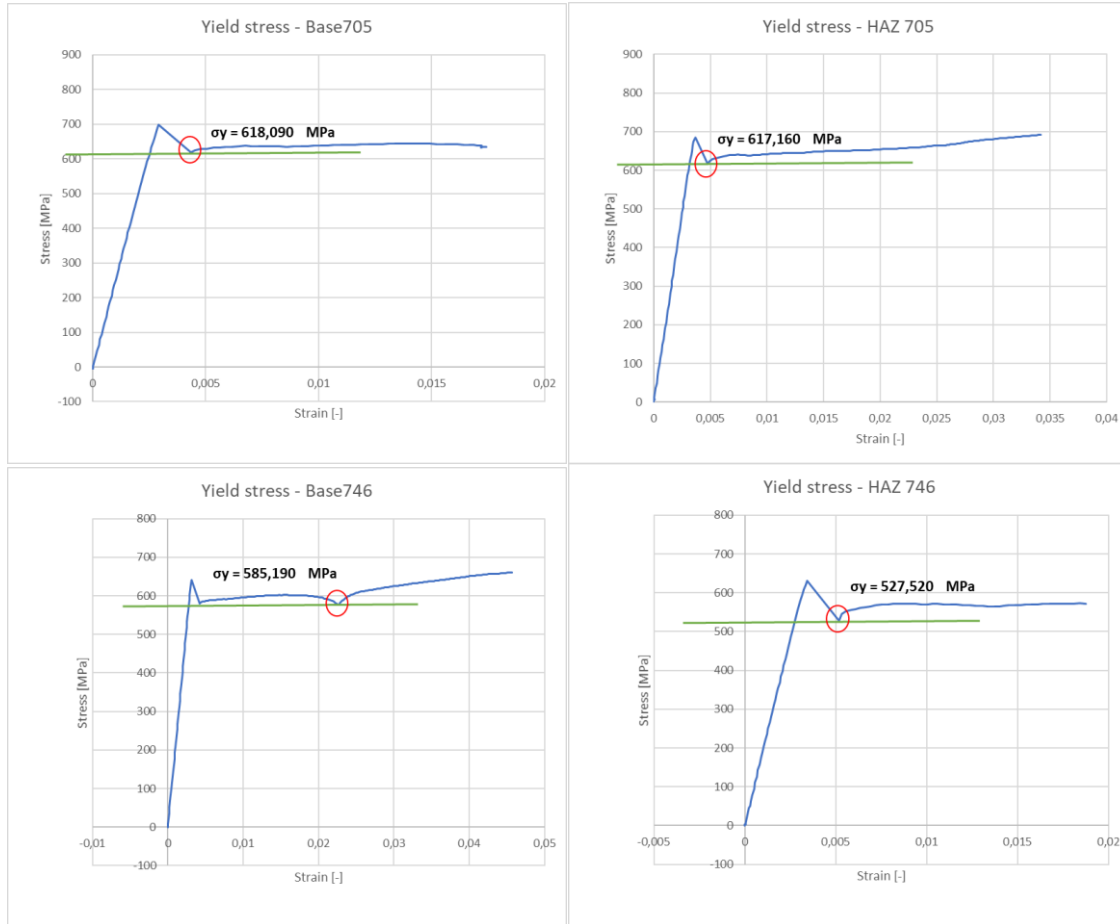


Figure 148: True stress-strain diagram – Uniform specimen HAZ 746.

Appendix O

Illustration of determination of yield stress for the different experiments.





Appendix P

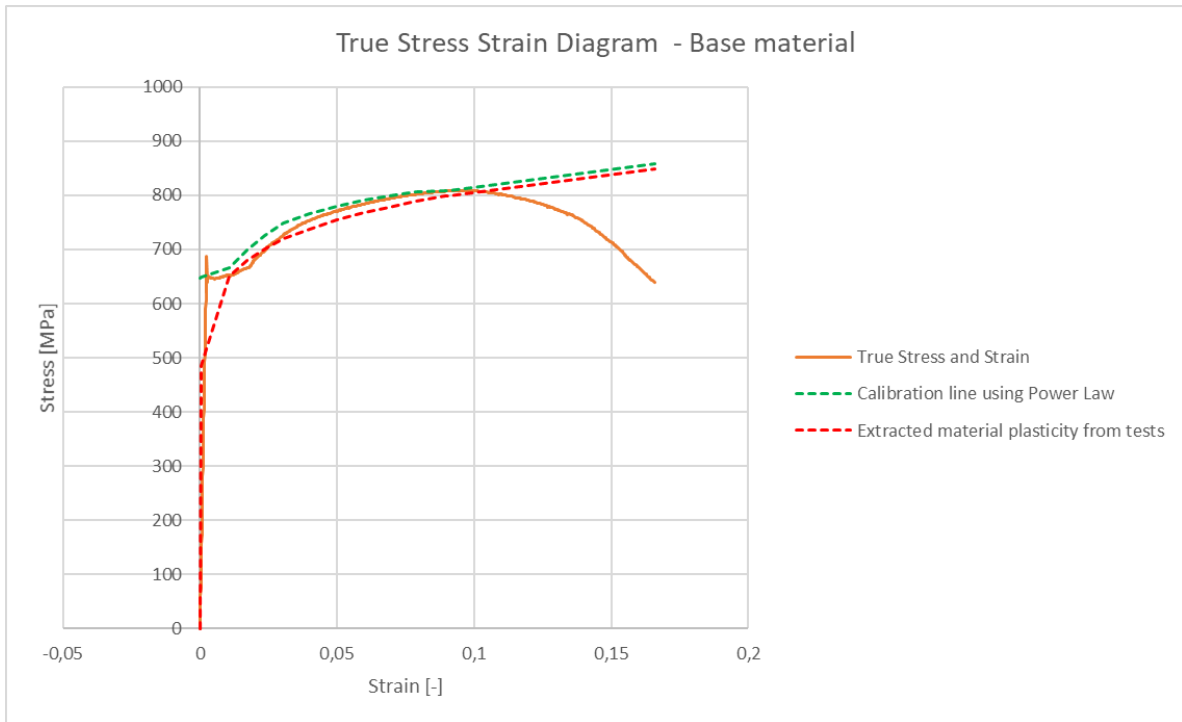


Figure 149: Visualization of calibration of strength coefficient K for the tensile tested base material.



Figure 150: Visualization of calibration of strength coefficient K for the tensile tested HAZ 600.

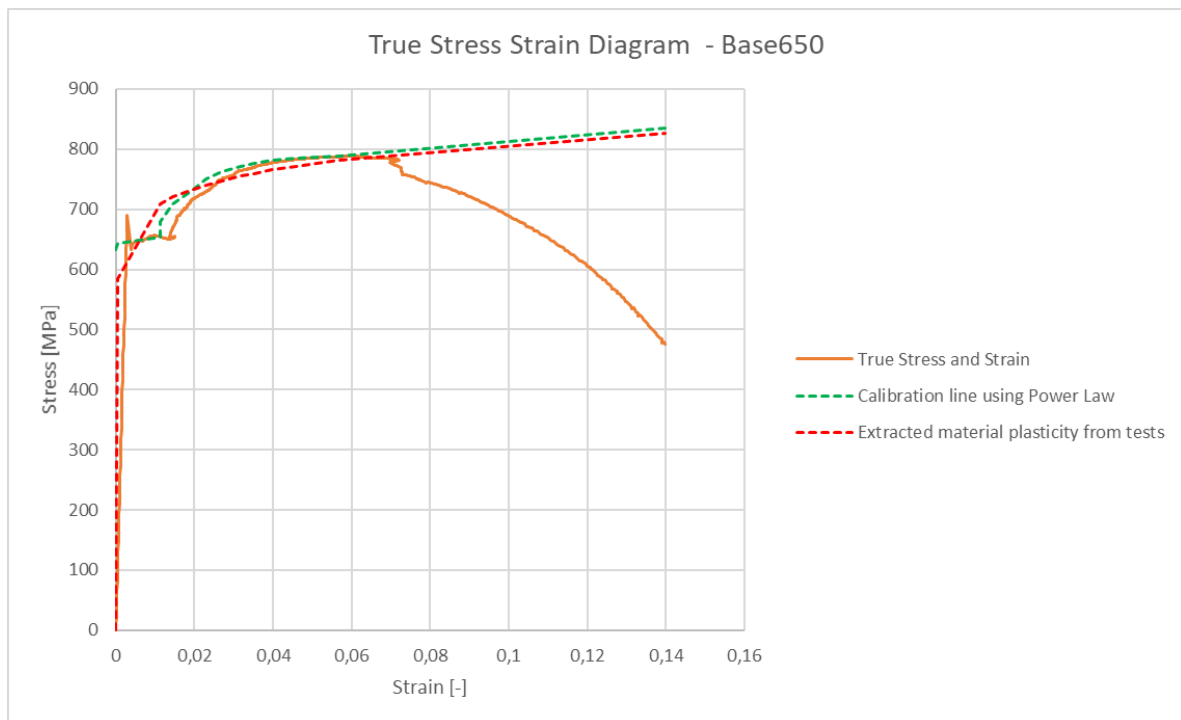


Figure 151: Visualization of calibration of strength coefficient K for the tensile tested base material affected by PWHT temperature of 650°C.



Figure 152: Visualization of calibration of strength coefficient K for the tensile tested HAZ 650.

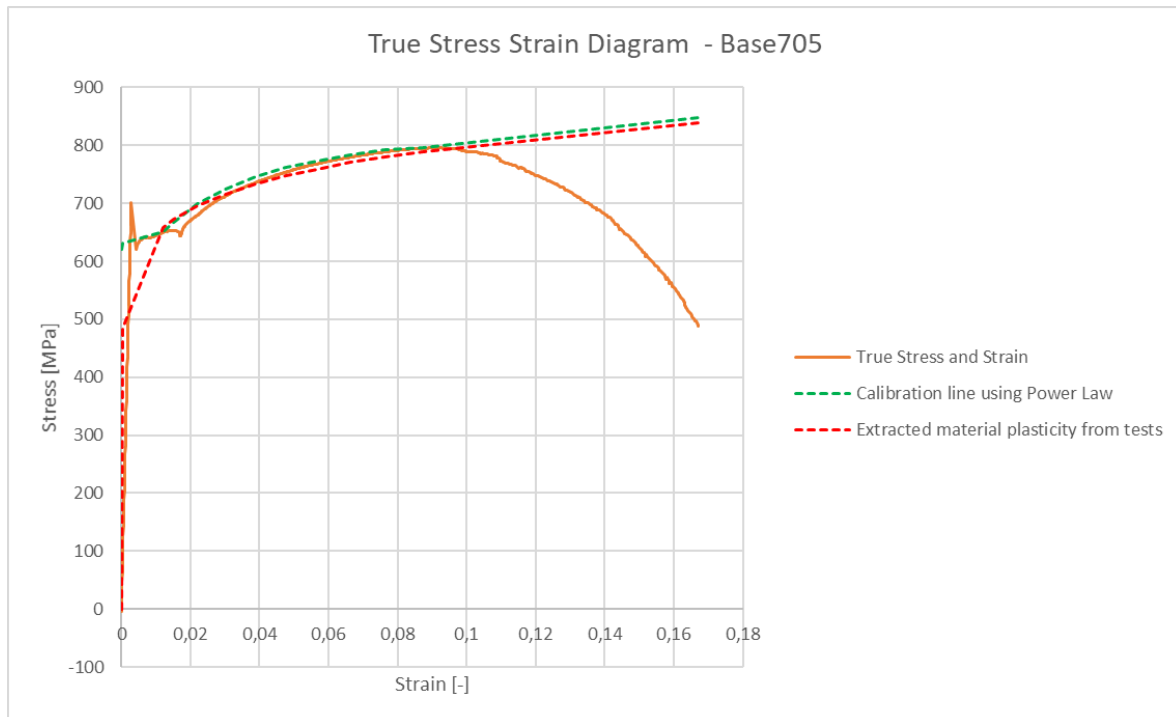


Figure 153: Visualization of calibration of strength coefficient K for the tensile tested base material affected by PWHT temperature of 705°C.

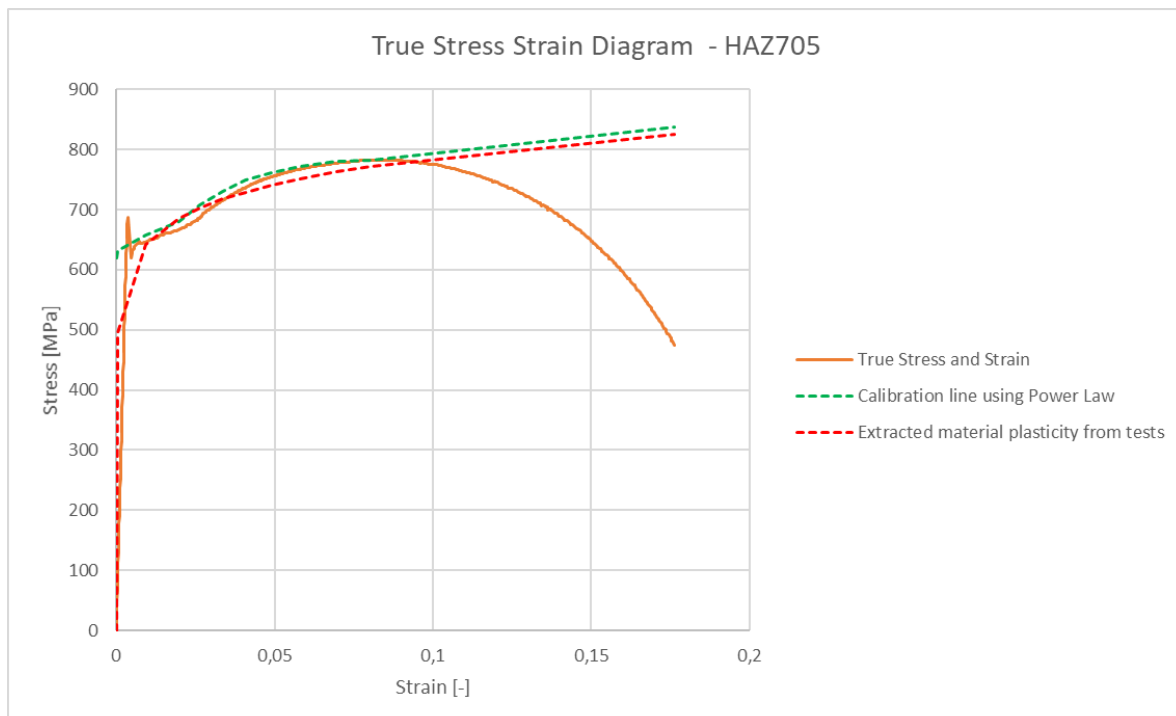


Figure 154: Visualization of calibration of strength coefficient K for the tensile tested HAZ 705.

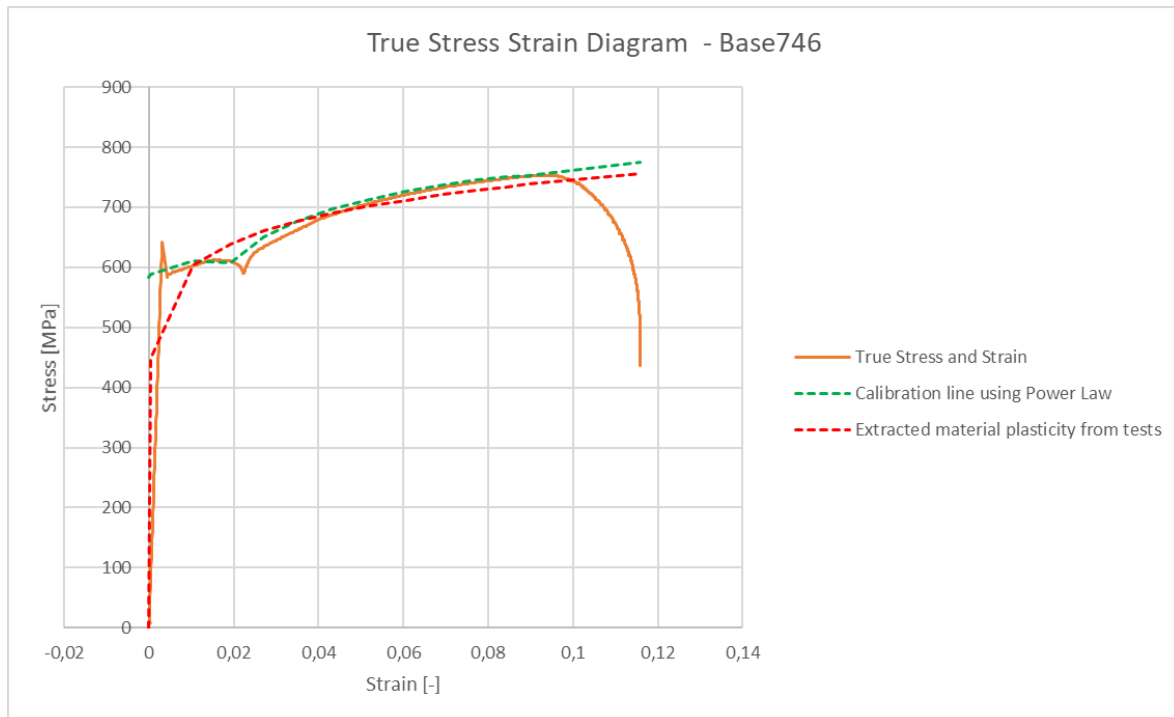


Figure 155: Visualization of calibration of strength coefficient K for the tensile tested base material affected by PWHT temperature of 746°C.



Figure 156: Visualization of calibration of strength coefficient K for the tensile tested HAZ 746.

Appendix Q

Project meetings:

Project meeting 1-2020		
Date: 10.01.2020	Time: 10.30	Place: MHWirth, KRS A317 Frikstad
Referent: Even Englund		
Name Dr. Dmitry Vysochinskiy Even Englund	Role: Supervisor Master student	
Dmitri Rybakov	Company contact (MHW)	
TASKS		
<ul style="list-style-type: none"> - Strength reduction under heat treatment of pipes. - Received literature; get an understanding of the subject post weld heat treatment (PWHT). - Dmitri Rybakov form MHWirth will supply the pipe that shall be tested. 		

Project meeting 2-2020		
Date: 16.01.2020	Time: 12.45	Place: UIA Grimstad
Referent: Even Englund		
Name Dr. Dmitry Vysochinskiy Even Englund	Role: Supervisor Master student	
TASKS		
<ul style="list-style-type: none"> - Status progress ; get an understanding of the subject PWHT, pipe design and ASME B31.3. - New PWHT procedure in ASME B31.3 2014 revision. - Start design of experiments for the pipe, heat treatment and numbers of tensile tests. - Start modeling a section of the pipe in Abaqus that is going to be tested, the pipe is used in sour service. - The Ductile Damage model will be used to simulate the damage accumulation until fracture. - The burst pressure is the focus in this study. 		

Project meeting 3-2020		
Date: 23.01.2020	Time: 12.45	Place: UIA Grimstad Referent: Even Englund
Name Dr. Dmitry Vysochinskiy Even Englund	Role: Supervisor Master student	
TASKS		
	<ul style="list-style-type: none"> - Martensite in the weld and heat affected zone will be of focus due to the unwanted material properties this will have. - Test matrix for the tensile specimens must be ready until next meeting. 	

Project meeting 4-2020		
Date: 30.01.2020	Time: 12.45	Place: UIA Grimstad Referent: Even Englund
Name Dr. Dmitry Vysochinskiy Even Englund	Role: Supervisor Master student	
TASKS		
	<ul style="list-style-type: none"> - Make a simpler test matrix to present to Dmitri Rybakov. - Make more deadlines in the project plan in MS Project. 	

Project meeting 5-2020		
Date: 03.02.2020	Time: 14.45	Place: UIA Grimstad Referent: Even Englund
Name Dr. Dmitry Vysochinskiy Even Englund	Role: Supervisor Master student	
Dmitri Rybakov	Company contact (MHW)	
TASKS		
	<ul style="list-style-type: none"> - The HAZ will need to have to sets of heat treatments one first for creation of martensite with quenching, and a second to simulate the PWHT. - The material properties of the base material affected by the different PWHT will be the focus and interest in this study. - Dmitri Rybakov also wants that there will be performed a new set of hardness tests for the tested material. 	

Project meeting 6-2020		
Date: 07.02.2020	Time: 10.00	Place: UIA Grimstad Referent: Even Englund
Name Dr. Dmitry Vysochinskiy Even Englund	Role: Supervisor Master student	
TASKS		
	<ul style="list-style-type: none"> - There will have to be made an appointment for cutting and preparation of the tested pipe section, and how many test pieces that can be extracted from the pipe. - Revision of the test matrix. - Figure out what the design parameters for the pressurized pipe section. - Presentation of the modeled section of the pipe in Abaqus. 	

Project meeting 7-2020		
Date: 13.02.2020	Time: 12.45	Place: UIA Grimstad Referent: Even Englund
Name Dr. Dmitry Vysochinskiy Even Englund	Role: Supervisor Master student	
TASKS		
<ul style="list-style-type: none"> - As UIA don't have capacity to cut the pipe section for extraction of the test specimens, an external company has to be contacted for this task. 		

Project meeting 8-2020		
Date: 20.02.2020	Time: 12.45	Place: UIA Grimstad Referent: Even Englund
Name Dr. Dmitry Vysochinskiy Even Englund	Role: Supervisor Master student	
TASKS		
<ul style="list-style-type: none"> - Prepare and work with a review of theory of the study for next meeting as well as the Significance of the work for the thesis. - Also send price for cutting of pipe to Paul before ordering of cutting of the pipe. 		

Project meeting 9-2020		
Date: 27.02.2020		Time: 14.45 Place: UIA Grimstad
Referent: Even Englund		
Name Dr. Dmitry Vysochinskiy Even Englund	Role: Supervisor Master student	
TASKS		
<ul style="list-style-type: none"> - Investigate hardness testing and material data that can be extracted. - Test the modeled pipe section with the extracted hardness test done by Dmitri Rybakov to see what result this will give. - Prepare for heat treatment of the test specimens and book time for tensile tests in the lab (contact Cecilie Ødegår). - Dmitry Vysochinskiy will get the piece that has been cut from the pipe milled in HiOF. 		

Project meeting 10-2020		
Date: 05.03.2020		Time: 14.45 Place: UIA Grimstad
Referent: Even Englund		
Name Dr. Dmitry Vysochinskiy Even Englund	Role: Supervisor Master student	
TASKS		
<ul style="list-style-type: none"> - Make a simple numerical test matrix for the simulations in Abaqus. - Prepare a PWHT procedure matrix and procedure for the experimental tests. - Make a sensitivity study of the pipe before testing of the PWHT procedures. 		

Project meeting 11-2020	
Date: 19.03.2020 Time: 10.30 Place: Microsoft Teams Referent: Even Englund	
Name Dr. Dmitry Vysochinskiy Even Englund	Role: Supervisor Master student
TASKS	
<ul style="list-style-type: none"> - CORONA VIRUS – <i>possibly the experimental test will not be performed, new focus for the study must be made.</i> - Investigate: Design criteria for the pipe, Hardness parameters, heat treatment. - Use the experimental hardness results from Dmitri Rybakov master thesis to simulate the failure of the pipe for PWHT temperatures 650°C and 705°C. - Test different electrodes as the one used by Dmitri Rybakov was not maybe not the most appropriate one in all cases. 	

Project meeting 12-2020	
Date: 26.03.2020 Time: 10.15 Place: Microsoft Teams Referent: Even Englund	
Name Dr. Dmitry Vysochinskiy Even Englund	Role: Supervisor Master student
TASKS	
<ul style="list-style-type: none"> - Focus on Max force applied on the pipe and max stresses as this is the important design criteria's in ASME B31.3. - Make a design check of the pipe to verify if there are any concerns. - Make a simple Numerical test matrix for the numerical simulations that now will be performed. - Also preform simulation for PWHT temperature 600°C using Holloman-Jaffe. 	

Project meeting 13-2020		
Date: 02.04.2020 Time: 10.00 Place: Microsoft Teams Referent: Even Englund		
Name Dr. Dmitry Vysochinskiy Even Englund	Role: Supervisor Master student	
TASKS		
	<ul style="list-style-type: none"> - Start adding results from the simulations into the report and finish the Case and Method chapter for next meeting. - Start writhing the Discussion and Conclusion. 	

Project meeting 14-2020		
Date: 08.04.2020 Time: 10.00 Place: Microsoft Teams Referent: Even Englund		
Name Dr. Dmitry Vysochinskiy Even Englund	Role: Supervisor Master student	
TASKS		
	<ul style="list-style-type: none"> - Make ready a preview of the report for Dmitry Vysochinskiy until next meeting. - Make a flow chart for the progress of the work and work methods used, for better get an overview of the report – <u>Try not to have more steps than three max five steps.</u> 	

Project meeting 15-2020		
Date: 15.04.2020 Time: 09.15 Place: Microsoft Teams Referent: Even Englund		
Name Dr. Dmitry Vysochinskiy Even Englund	Role: Supervisor Master student	
TASKS		
	<ul style="list-style-type: none"> - Verification of the background of new and old PWHT in ASME B31.3, must be of focus and well presented. - See over the structure of the report – <u>Make a natural flow stepwise in the report.</u> 	

Project meeting 16-2020		
Date: 23.04.2020 Time: 09.30 Place: Microsoft Teams Referent: Even Englund		
Name Dr. Dmitry Vysochinskiy Even Englund	Role: Supervisor Master student	
TASKS		
	<ul style="list-style-type: none"> - Waiting for final decision of the experimental testing, Dmitry Vysochinskiy is contacting Rino at HiOF to ask if he has milled the specimens. 	

Project meeting 17-2020		
Date: 30.04.2020 Time: 09.30 Place: Microsoft Teams Referent: Even Englund		
Name Dr. Dmitry Vysochinskiy Even Englund	Role: Supervisor Master student	
TASKS		
<ul style="list-style-type: none"> - Contact Rino for collecting of the test samples - New agreement and schedule for heat treatment and experimental testing - Finish the report based on the results from hardness tests and prepare for validation by adding the experimental tensile tests later. - Prepare the heat treatment (07.05 and 08.05) and experimental test program (14.05). 		

Project meeting 18-2020		
Date: 12.05.2020 Time: 18.00 Place: Microsoft Teams Referent: Even Englund		
Name Dr. Dmitry Vysochinskiy Even Englund	Role: Supervisor Master student	
TASKS		
<ul style="list-style-type: none"> - Make separate part in the report for the tensile tests to validate the hardness tests - Further improvements of setup and structure in the report. 		

Project meeting 19-2020		
Date: 28.05.2020 Time: 10.30 Place: Microsoft Teams Referent: Even Englund		
Name Dr. Dmitry Vysochinskiy Even Englund	Role: Supervisor Master student	
TASKS		
	<ul style="list-style-type: none"> - Make sure that it is clear that the material data for the electrodes is taken from certificates - True stress at yielding, True stress at UTS - Only show the normal stress for the quenched test specimen. - 	

Project meeting 20-2020		
Date: 04.06.2020 Time: 18.00 Place: Microsoft Teams Referent: Even Englund		
Name Dr. Dmitry Vysochinskiy Even Englund	Role: Supervisor Master student	
TASKS		
	<ul style="list-style-type: none"> - Show the difference in pressure in a clear and simple manner. - Show the max stresses as well in the fracture but not the other places "less is more". - Mention the limitations. - We do not focus on the formation of cracks or brittle fracture, just ductile failure. - Simple; what changes when temperature is changed, is the failure in the base metal or the weld. 	